

## **INFORMATION TO USERS**

**This manuscript has been reproduced from the microfilm master. UMI films the text directly from the original or copy submitted. Thus, some thesis and dissertation copies are in typewriter face, while others may be from any type of computer printer.**

**The quality of this reproduction is dependent upon the quality of the copy submitted. Broken or indistinct print, colored or poor quality illustrations and photographs, print bleedthrough, substandard margins, and improper alignment can adversely affect reproduction.**

**In the unlikely event that the author did not send UMI a complete manuscript and there are missing pages, these will be noted. Also, if unauthorized copyright material had to be removed, a note will indicate the deletion.**

**Oversize materials (e.g., maps, drawings, charts) are reproduced by sectioning the original, beginning at the upper left-hand corner and continuing from left to right in equal sections with small overlaps.**

**Photographs included in the original manuscript have been reproduced xerographically in this copy. Higher quality 6" x 9" black and white photographic prints are available for any photographs or illustrations appearing in this copy for an additional charge. Contact UMI directly to order.**

**ProQuest Information and Learning  
300 North Zeeb Road, Ann Arbor, MI 48106-1346 USA  
800-521-0600**

**UMI<sup>®</sup>**



**The Pennsylvania State University**

**The Graduate School**

**Department of Materials Science and Engineering**

**QUALITY ISSUES IN LASER WELDING OF AUTOMOTIVE  
ALUMINUM AND MAGNESIUM ALLOYS**

**A Thesis in**

**Materials Science and Engineering**

**by**

**Hailiang Zhao**

**Submitted in Partial Fulfillment  
of the Requirements  
for the Degree of**

**Doctor of Philosophy**

**December 2001**

UMI Number: 3036140

**UMI<sup>®</sup>**

---

UMI Microform 3036140

Copyright 2002 by ProQuest Information and Learning Company.

All rights reserved. This microform edition is protected against  
unauthorized copying under Title 17, United States Code.

---

ProQuest Information and Learning Company

300 North Zeeb Road

P.O. Box 1346

Ann Arbor, MI 48106-1346

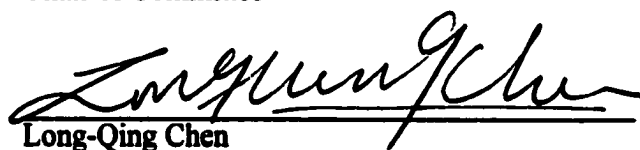
We approve the thesis of Hailiang Zhao.

Date of Signature



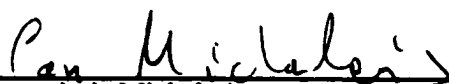
24 October 2001

Tarasankar DebRoy  
Professor of Materials Science and Engineering  
Thesis Advisor  
Chair of Committee



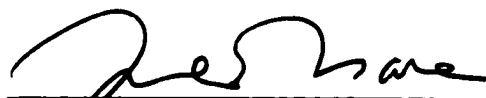
Oct. 25, 2001

Long-Qing Chen  
Associate Professor of Materials Science and  
Engineering  
Coordinator of Graduate Programs in Materials  
Science and Engineering



Oct. 25, 2001

Panagiotis Michaleris  
Assistant Professor of Mechanical Engineering



Oct. 25, 2001

Kwadwo Osseo-Asare  
Professor of Metallurgy

## ABSTRACT

Achievement of defect-free and structurally sound welds based on scientific principles has been a goal of contemporary welding research. In the welding of automotive aluminum and magnesium alloys, alloying element loss and porosity formation have been two major concerns. The presence of porosity and loss of alloying elements in the weld metal weaken the strength of the weldment. The loss of certain alloying elements may also increase hot cracking susceptibility and decrease corrosion resistance of the weldment. The present research focuses on the alleviation of these problems through quantitative understanding of alloying element loss and porosity formation during laser welding.

Loss of alloying elements can be affected by many interdependent factors such as the temperature distribution and size of the molten weld pool and the vaporization rate of each alloying element. An experimental and theoretical study was carried out to seek a quantitative understanding of the influences of various welding variables on vaporization and composition change during conduction mode laser welding of aluminum alloy 5182. A comprehensive model for the calculation of vaporization rate and weld metal composition change was developed based on the principles of transport phenomena, kinetics and thermodynamics. The calculations showed that the vaporization was concentrated in a small high temperature region under the laser beam where the local vapor pressure exceeded the ambient pressure. The convective vapor flux driven by the pressure gradient was much higher than the diffusive vapor flux driven by the concentration gradient. The computed weld pool geometry, vaporization rates and composition changes for different welding conditions agreed well with the corresponding experimental data. The good agreement demonstrates that the comprehensive model can serve as a basis for the quantitative understanding of the influences of various welding variables on heat transfer, fluid flow, and vaporization occurring during conduction mode laser welding of automotive aluminum alloys.

The instability of the keyhole is an important cause of macro pores during laser welding of thin plates of aluminum alloys. In this study, we seek to present computational and experimental results that demonstrate that applications of transport phenomena can lead to better understanding of the formation and prevention of macro porosity during laser welding of aluminum alloys 5182 and 5754. The modeling approach is based on the fact that during laser welding of thin plates of aluminum alloys, macroporosity is formed when the beam intensity is just above the threshold value for keyhole formation, where the keyhole is unstable. Macroporosity does not form during welding in either conduction mode or in keyhole mode. In the modeling, the keyhole profile was calculated based on point-by-point energy balance on the keyhole wall where the temperature was assumed to be equal to the boiling point of the alloy. The three-dimensional temperature field of the weld pool was calculated based on principles of thermal conduction. The model predictions of the stability of the keyhole and weld pool geometry were compared with the experimental data to validate the model. A key feature of this model is its ability to determine geometric stability of the keyhole for a given set of welding parameters. The model can be used to determine the operating window of welding parameters where a stable keyhole can be formed and macroporosity could be avoided.

Unlike laser welding of aluminum alloys, there was significant amount of pre-existing pores in die-cast magnesium alloy AM60B base metal. Experimental observation and theoretical analysis showed that coalescence and expansion to pre-existing pores caused the formation of large pores during laser welding of this alloy. The stability of keyhole was not a major factor in pore formation for this alloy. The porosity in the fusion zone increased with heat input, i.e., increase in the laser power and decrease in the welding speed. Well controlled remelting of the welded metal led to removal of gas bubbles and reduced porosity in the welded metal.

## TABLE OF CONTENTS

	Page
LIST OF FIGURES.....	x
LIST OF TABLES.....	xviii
ACKNOWLEDGEMENTS.....	xix
CHAPTER 1. INTRODUCTION.....	1
1.1 General Background.....	1
1.2 Statement of Objectives.....	5
1.3 Organization of the Thesis.....	6
1.4 References.....	7
CHAPTER 2. LITERATURE REVIEW.....	11
2.1 Energy Absorption.....	11
2.1.1 Energy Transfer Efficiency.....	11
2.1.2 Melting Efficiency.....	18
2.2 Heat Transfer and Fluid Flow.....	20
2.2.1 Background.....	20
2.2.2 Temperature and Velocity Fields.....	21
2.2.3 Effect of Turbulence in Weld Pool.....	25
2.2.4 Relative Importance of Conduction and Convection.....	27
2.2.5 Effect of Power Density Distribution.....	32
2.2.6 Effect of Convection on Weld Pool Shape.....	35
2.2.7 Surface Tension of Aluminum Alloys.....	35
2.2.8 Fluid Flow and Heat Transfer in Keyhole Mode of Welding.....	39
2.3 Vaporization at the Weld Pool Surface.....	44
2.3.1 Factors Affecting Vaporization.....	44
2.3.1.1 Temperature and Composition.....	44



2.3.1.2 Role of Plasma.....	48
2.3.1.3 Role of Surface Active Elements.....	49
2.3.2 Mechanism of Vaporization.....	49
2.3.3 Calculation of Vaporization Rate and Composition Change.....	51
2.4 Weldment Structure and Properties.....	52
2.4.1 Microstructural Features.....	52
2.4.1.1 Fusion Zone.....	53
2.4.1.2 Partially Melted Zone.....	55
2.4.1.3 Heat Affected Zone.....	56
2.4.1.4 Role of Filler Metals.....	56
2.4.1.5 Fractography.....	61
2.4.2 Effect of Welding on Mechanical Properties.....	62
2.4.3 Mechanical Characterization.....	62
2.4.3.1 Tensile Properties.....	65
2.4.3.2 Formability and Fracture Toughness.....	66
2.4.3.3 Other Properties.....	67
2.5 Hot Cracking.....	67
2.5.1 Mechanism of Solidification Cracking.....	68
2.5.2 Solidification Cracking Susceptibility.....	71
2.5.3 Prevention of Solidification Cracking.....	73
2.6 Porosity.....	75
2.6.1 Porosity due to Absorption and Entrapment of Gases.....	76
2.6.1.1 Solubility of Oxygen.....	76
2.6.1.2 Solubility of Nitrogen.....	78
2.6.1.3 Solubility of Hydrogen.....	79
2.6.1.4 Effect of Alloying Elements on the Solubility of Hydrogen in Aluminum.....	84
2.6.1.5 Nucleation and Growth of Hydrogen Bubbles in Weld Metal...	84
2.6.2 Porosity due to Collapse of the Keyhole.....	88
2.6.3 Summary.....	96

2.7 A Selection of Important Unanswered Questions.....	100
2.8 References.....	102
<b>CHAPTER 3. WELD METAL COMPOSITION CHANGE DURING CONDUCTION MODE LASER WELDING OF ALUMINUM ALLOY 5182.....</b>	<b>112</b>
3.1 Background.....	112
3.2 Experimental Procedure.....	115
3.3 Mathematical Modeling.....	117
3.3.1 Turbulent Fluid Flow and Heat Transfer in the Weld Pool.....	117
3.3.1.1 Governing equations.....	117
3.3.1.2 Boundary Conditions.....	121
3.3.1.3 Solution Procedure.....	125
3.3.2 Vaporization Rate and Composition Change in the Weld Metal.....	128
3.3.2.1 Vaporization Flux due to Concentration Gradient.....	129
3.3.2.2 Vapor Flux due to Pressure Gradient.....	130
3.3.3 Vaporization Rate and Composition Change.....	134
3.3.4 Data Used for the Calculations.....	135
3.4 Results and Discussion.....	142
3.4.1 Temperature and Velocity Fields in the Weld Pool.....	142
3.4.2 Vaporization and Composition Change.....	145
3.4.3 Influence of Laser Power.....	151
3.4.4 Influence of Welding Speed.....	156
3.5 Summary and Conclusions.....	159
3.6 References.....	160
<b>CHAPTER 4. MATHEMATICAL MODELING OF MACROPOROSITY FORMATION DURING LASER WELDING OF ALUMINUM ALLOYS.....</b>	<b>164</b>
4.1 Background.....	164

4.2 Mathematical Model.....	171
4.2.1 Energy Balance on the Keyhole Wall.....	171
4.2.2 Keyhole Stability and Keyhole Wall Profile.....	177
4.2.3 Three-dimensional Temperature Field.....	184
4.3 Results and Discussion.....	187
4.3.1 Keyhole Profile and Temperature Field.....	187
4.3.2 Keyhole Stability and Macroporosity Formation.....	194
4.4 Summery and Conclusions.....	203
4.5 References.....	204
4.6 List of Symbols.....	208
4.7 Appendix: Calculation of Various Absorption Coefficients.....	210
<b>CHAPTER 5. PORE FORMATION DURING LASER WELDING OF DIE-CAST MAGNESIUM ALLOY AM60B – MECHANISM AND REMEDY</b> .....	<b>214</b>
5.1 Background.....	214
5.2 Experimental Procedure.....	217
5.3 Results and Discussion.....	219
5.3.1 Enhanced Porosity due to Melting of the Base Metal.....	219
5.3.2 Enhanced Porosity in Welded Metal.....	222
5.3.3 Pore Coalescence and Expansion.....	222
5.3.4 Keyhole Stability.....	230
5.3.5 Reduction of Weld Metal Porosity.....	232
5.4 Summary and Conclusions.....	236
5.5 References.....	237
5.6 Appendix I: Estimation of Pore Expansion during Welding.....	239
5.7 Appendix II: Weld Geometry, Microstructure and Microhardness.....	242
<b>CHAPTER 6. CONCLUDING REMARKS.....</b>	<b>259</b>
<b>Appendix A. Program for the Calculation of Vaporization Rates and Composition Change during Laser Welding of 5000 Series Aluminum Alloys.....</b>	<b>264</b>

<b>Appendix B. Program for the Calculation of Keyhole Geometry and Weld Pool Temperature Field during Laser Welding.....</b>	<b>281</b>
<b>Appendix C. Animation of Transient Weld Pool Temperature Field during Laser Welding.....</b>	<b>300</b>
<b>Appendix D. Programs for the Calculation of Turbulent Fluid Flow and Heat Transfer during Laser Welding.....</b>	<b>309</b>

## LIST OF FIGURES

Figure	Page
2.1 Effect of laser beam intensity on the measured heat transfer efficiency for CO <sub>2</sub> laser welding of 1018 steel, 304 stainless steel, and tin [13].....	17
2.2 Dependence of laser melting efficiency on the dimensionless parameter, $R_y$ , for CO <sub>2</sub> laser welding of 1018 steel, 304 stainless steel, and tin [13]....	19
2.3 Calculated velocity and temperature fields in a laser weld pool of 6063 aluminum alloy using a CO <sub>2</sub> laser power of 1.3 kW and welding speed of 10 ipm [32].....	24
2.4 Contour plots of effective viscosity as calculated from the K- $\epsilon$ model for GTA stationary welding of AISI 304 stainless steel with different currents [34]: (a) 50 A; (b) 100 A; (c) 150 A. The numbers on the contour lines represent the ratios of effective viscosity to molecular viscosity.....	28
2.5 Comparison of weld pool shapes for: (a) experimental results, (b) numerical results based on laminar properties, (c) numerical results using a constant effective viscosity and thermal conductivity which are 30 times of the molecular values, (d) numerical results based on the K- $\epsilon$ turbulence model [34].....	29
2.6 Four different power density profiles of the heat source and their resultant welds with heat source power of 860 W and welding speed of 5.5 mm/s [41].....	33
2.7 Cross sections of Nd:YAG laser welded 1.45 mm thick 5754 aluminum alloy for several beam defocusing values with laser power of 3.0 kW and welding speed of 150 ipm [37].....	34
2.8 Spot weld pool geometries of Bohler S705 high-speed steel using CO <sub>2</sub> laser with a power of 1900 W for the heats containing (a) 20 ppm and (b) 150 ppm of sulfur; and with a power of 5200 W for the heats containing (c) 20 ppm and (d) 150 ppm of sulfur [42]. Plate thickness: 15 mm, irradiation time: 5 s, and shielding gas: 20 L/min of argon.....	36
2.9 Effect of added elements on the surface tension of 99.99% aluminum at 973 to 1013 K in argon [46].....	38
2.10 Correlation between tensile yield, elongation, and magnesium content for some commercial alloys [72].....	45

2.11	Equilibrium vapor pressure as a function of temperature for various elements [74].....	47
2.12	Typical microstructure of laser welded 5754-O aluminum alloy using a 3 kW CW Nd:YAG laser at welding speed of 200 ipm [88].....	54
2.13	Microstructure showing equiaxed grain structure along the weld center of 6061 laser weld [93].....	57
2.14	Solidification cracking along the cellular dendritic grain boundary of 6111-T4 aluminum alloy welded using a 3 kW CO <sub>2</sub> laser at a speed of 400 ipm [87].....	58
2.15	Photomicrograph showing evidence of liquation at the grain boundaries during welding of 6013-T6 aluminum alloy using a 7 kW CO <sub>2</sub> laser at 100 mm/s travel speed [85].....	59
2.16	A fractograph showing two distinct fracture modes in different regions of a tensile specimen of CO <sub>2</sub> laser welded 6111-T4 aluminum alloy tested in the longitudinal direction [89].....	63
2.17	SEM micrograph of a typical fracture surface of laser welded 6013-T6 aluminum alloy tensile specimen that fractured in the fusion zone [84].....	64
2.18	Weld metal ductility during and following solidification [104]. Weld metal ductility during and following solidification [104].....	69
2.19	Effect of constitutional features on cracking susceptibility in binary systems [109].....	70
2.20	Effect of chemical composition of weld metal on crack susceptibility in various aluminum binary alloys [111].....	72
2.21	Effect of weld porosity on tension test performance (P = passed bend test, F = failed bend test) [124].....	77
2.22	The calculated equilibrium partial pressure of diatomic nitrogen and monatomic nitrogen in forming aluminum nitride, as a function of temperature.....	80
2.23	The calculated hydrogen solubility in aluminum based on the results of Ransley and Neufeld [131].....	81

2.24	The calculated hydrogen solubility in aluminum in the environments of diatomic hydrogen and monatomic hydrogen [131,140].....	82
2.25	Effect of alloying elements on the solubility of hydrogen in liquid aluminum at 973 K and 1 atm partial pressure of hydrogen [141].....	85
2.26	Pore volume fraction as a function of the cooling rate in Al-4.7% Mg alloy [142].....	87
2.27	Addition of alloying elements on viscosity of aluminum [46].....	89
2.28	A schematic diagram showing the formation of void at the weld root due to imperfect collapse of the keyhole [146].....	90
2.29	The keyhole wall profiles during CO <sub>2</sub> laser welding of 1.0 mm thick aluminum sheet with a power of 2 kW and welding speed of 10 mm/s at time $t = 0.1$ ms, 0.15 ms, 0.2 ms and 0.25 ms following the extinction of the laser beam [150].....	92
2.30	Calculated values for surface tension pressure and vapor pressure in an 1100 aluminum EB welding cavity as a function of cavity depth [153].....	94
2.31	Liquid projection formation at location where surface tension force is nearly in balance with vapor pressure force [153].....	95
2.32	Typical porosity observed during Nd:YAG laser welding of 5754 aluminum alloy [37].....	97
2.33	Porosity produced at several beam defocusing values during Nd:YAG laser welding of 5754 aluminum alloy with a power of 3.0 kW and welding speed of 150 ipm, and shielding gas of pure helium at a flow rate of 200 ft <sup>3</sup> /h [146].....	98
2.34	Solubility of hydrogen in magnesium [154].....	99
3.1	Schematic diagram of coordinate system used in the 3D heat transfer and fluid flow model.....	118
3.2	Schematic diagram of laser beam profile and its position relative to the workpiece.....	124
3.3	Velocity distribution functions of vapor molecules at various locations.....	131
3.4	Flow chart of the comprehensive model.....	136

3.5	Experimental and calculated weld pool cross sections for laser power of (a) 1.5 kW, (b) 2.0 kW, (c) 2.5 kW, and (d) 3.0 kW. Welding speed 105.8 mm/s Welding speed 105.8 mm/s, beam defocusing +1.5 mm, and other parameters are listed in Table 3.4.....	143
3.6(a)	Distributions of ratio of effective to molecular viscosity in weld pool cross section. Laser power 3.0 kW, welding speed 105.8 mm/s, beam defocusing +/-1.5 mm, and other parameters are listed in Table 3.4.....	146
3.6(b)	Distribution of ratio of effective to molecular thermal conductivity in weld pool cross section. Laser power 3.0 kW, welding speed 105.8 mm/s, beam defocusing +/-1.5 mm, and other parameters are listed in Table 3.4.....	147
3.7	Distributions of temperature and various vapor fluxes on the weld pool surface. Laser power 3.0 kW, welding speed 105.8 mm/s, and beam defocusing +/-1.5 mm.....	148
3.8	Typical magnesium concentration profile across the weld pool width. The data were taken on three weld pool cross sections made using the same welding conditions: laser power 3.0 kW, welding speed 105.8 mm/s, and beam defocusing +1.5 mm.....	150
3.9(a)	Influence of laser power on weld pool size and vaporization rate. Welding speed 105.8 mm/s and beam defocusing +/-1.5 mm.....	154
3.9(b)	Influence of laser power on weld metal composition change. Welding speed 105.8 mm/s and beam defocusing +/-1.5 mm.....	155
3.10(a)	Influence of welding speed on melting rate and vaporization rate. Laser power 3.0 kW and beam defocusing +/-2.0 mm.....	157
3.10(b)	Influence of welding speed on weld metal composition change. Laser power 3.0 kW and beam defocusing +/-2.0 mm.....	158
4.1	Effect of weld porosity on tension test performance (P = passed bend test, F = failed bend test) of aluminum alloy 5086-H116 welded with 5356 electrodes [16].....	165
4.2	Typical keyhole shape for high-speed CO <sub>2</sub> laser welding of glass observed using in situ X-ray transmission imaging system [43].....	168



4.3	Typical keyhole shape for high-speed laser welding of ice observed using in situ X-ray transmission imaging system [44]. Laser power: 70 W.....	169
4.4	Typical keyhole shape for high speed pulsed Nd:YAG laser welding of stainless steel 304 observed using in situ X-ray transmission imaging system [45].....	170
4.5	The relationship between the locally absorbed beam energy flux, $I_a$ , the heat loss due to heat of evaporation, $I_v$ , and the heat flux conducted into the metal, $I_c$ , determines the keyhole wall angle $\theta$ .....	173
4.6	Schematic diagram of the coordinate system used in the model.....	175
4.7	The laser beam location and the keyhole profile on the top surface of the workpiece.....	179
4.8	From the current keyhole wall position, $(x_i, z_i)$ and the local angle, $\theta_i$ , the next position, $(x_{i+1}, z_{i+1})$ , at a distance, $dz$ , below the current point can be obtained.....	180
4.9	Determination of front and rear keyhole wall positions on top surface along x-axis.....	183
4.10	Beam profile, line source location, and keyhole profile. Alloy: 5182, laser power: 2.5 kW, welding speed: 300 ipm (127 mm/s), and beam defocus: 0 mm.....	188
4.11	Calculated three-dimensional temperature field in the weld pool. Alloy: 5182, laser power: 2.5 kW, welding speed: 300 ipm (127 mm/s), and beam defocus: 0mm.....	189
4.12	Comparing of the experimentally obtained weld pool cross sections at several welding speeds with the calculated results. Alloy: 5182, plate thickness: 1.0 mm, laser power: 2.5 kW, beam defocus: 0 mm, and shielding gas flow rate: 200 ft <sup>3</sup> /h (5.66 m <sup>3</sup> /h) of helium.....	190
4.13	Porosity produced at several defocus values in alloys (a) 5182 and (b) 5754. Nominal power: 3.0 kW, welding speeds: 250 ipm (106 mm/s) and 150 ipm (63.5 mm/s) for alloys 5182 and 5754, respectively, and shielding gas flow rate: 200 ft <sup>3</sup> /h (5.66 m <sup>3</sup> /h) of helium [21].....	195

4.14(a) Calculated keyhole depth for laser welded 1.0 mm-thick aluminum alloy 5182 plates at several beam defocus values. Laser power: 2.5 kW, welding speeds: 250 ipm (106 mm/s), and shielding gas flow rate: 200 ft<sup>3</sup>/h (5.66 m<sup>3</sup>/h) of helium..... 197

4.14(b) Experimental [21] and calculated weld pool depth for laser welded 1.0 mm-thick aluminum alloy 5182 plates at several beam defocus values. Laser power: 2.5 kW, welding speeds: 250 ipm (106 mm/s), and shielding gas flow rate: 200 ft<sup>3</sup>/h (5.66 m<sup>3</sup>/h) of helium..... 198

4.15 The experimental [21] and calculated weld pool depths for laser welded 1.45 mm-thick aluminum alloy 5754 plates at several defocus values. Laser power: 3.0 kW, welding speed: 150 ipm (63.5 mm/s), and shielding gas flow rate: 200 ft<sup>3</sup>/h (5.66 m<sup>3</sup>/h) of helium..... 200

4.16(a) The calculated weld pool depth and measured porosity [21] at several defocus values in alloy 5182. Laser power: 2.5 kW, welding speed: 250 ipm (106 mm/s), and shielding gas flow rate: 200 ft<sup>3</sup>/h (5.66 m<sup>3</sup>/h) of helium.... 201

4.16(b) The calculated weld pool depth and measured porosity [21] at several defocus values in alloy 5754. Laser power: 3.0 kW, welding speed: 150 ipm (63.5 mm/s), and shielding gas flow rate: 200 ft<sup>3</sup>/h (5.66 m<sup>3</sup>/h) of helium..... 202

4.17 Schematic diagram showing the angles among the initial incident beam, the reflected beam and the keyhole wall..... 212

5.1 Solubility of hydrogen in magnesium [13]..... 216

5.2(a) Micrograph showing features of porosity on an unetched sample of 2 mm-thick alloy AM60B plate base metal before heat treatment..... 220

5.2(b) Micrograph showing features of porosity on an unetched sample of 2 mm-thick alloy AM60B plate after heat treatment at 863 K for 2 hours..... 221

5.3 Typical pores observed in weld pool of laser welded alloy AM60B. Plate thickness 6 mm, laser power 1.5 kW, welding speed 250 ipm (106 mm/s), beam defocusing +1.0 mm, and shielding gas flow rate 200 ft<sup>3</sup>/h (5.7 m<sup>3</sup>/h) of helium..... 223

5.4 Formation of large pores in the fusion zone (the black background) due to the expansion and coalescence of the pre-existing pores in the base metal (the gray background) of alloy AM60B. All the figures have the same magnification as shown in (a)..... 224

5.5(a)	Pore size distribution in 2 mm-thick alloy AM60B base metal.....	226
5.5(b)	Pore size distribution in the fusion zone of laser welded alloy AM60B using a focused beam. Plate thickness 2 mm, laser power 1.5 kW, welding speed 125 ipm (53 mm/s), and shielding gas flow rate 200 ft <sup>3</sup> /h (5.7 m <sup>3</sup> /h) of helium.....	227
5.6	Porosity formed in laser welds of alloy AM60B at several beam defocusing values. Plate thickness 6 mm, laser power 1.5 kW, welding speed 250 ipm (106 mm/s), and shielding gas flow rate 200 ft <sup>3</sup> /h (5.7 m <sup>3</sup> /h) of helium.....	231
5.7(a)	Porosity formed in laser welds of 2 mm-thick alloy AM60B plates for different welding speeds and laser powers using focused beam and shielding gas flow rate 200 ft <sup>3</sup> /h (5.7 m <sup>3</sup> /h) of helium.....	233
5.7(b)	Porosity formed in laser welds of 6 mm-thick alloy AM60B plates for different welding speeds and laser powers using focused beam and shielding gas flow rate 200 ft <sup>3</sup> /h (5.7 m <sup>3</sup> /h) of helium.....	234
5.8	Area percent porosity produced on as-welded (single-run) and re-melted (double-run) samples of alloy AM60B with a focused beam. Plate thickness 6 mm, laser power 1.5 kW for first run and 1.0 kW for second run and shielding gas flow rate 200 ft <sup>3</sup> /h (5.7 m <sup>3</sup> /h) of helium.....	235
5.9	Measurement of weld pool width, depth, and cross section area.....	243
5.10(a)	Area percent of porosity (gay bars) and area percent of overfill (black bars) in laser welds of AM60B alloy at several welding speeds for 2 mm-thick plates. Nominal laser power: 3 kW, laser beam: at focus, and shielding gas flow rate: 200 ft <sup>3</sup> /h (5.7 m <sup>3</sup> /h) of helium.....	244
5.10(b)	Area percent of porosity (gay bars) and area percent of overfill (black bars) in laser welds of AM60B alloy at several welding speeds for 6 mm-thick plates. Nominal laser power: 3 kW, laser beam: at focus, and shielding gas flow rate: 200 ft <sup>3</sup> /h (5.7 m <sup>3</sup> /h) of helium.....	245
5.11(a)	Width and depth of the weld pools produced at several welding speeds and laser powers in AM60B alloy for 2 mm-thick plates. Laser beam: at focus, shielding gas flow rate: 200 ft <sup>3</sup> /h (5.7 m <sup>3</sup> /h) of helium.....	246
5.11(b)	Width and depth of the weld pools produced at several welding speeds and laser powers in AM60B alloy for 6 mm-thick plates. Laser beam: at focus, shielding gas flow rate: 200 ft <sup>3</sup> /h (5.7 m <sup>3</sup> /h) of helium.....	247

5.12(a)	Width and depth of the weld pools produced at several beam defocus values in AM60B alloy for 2 mm-thick plates. Nominal power: 1.5 kW, welding speed: 105.8 mm/s, and shielding gas flow rate: 200 ft <sup>3</sup> /h (5.7 m <sup>3</sup> /h) of helium.....	248
5.12(b)	Width and depth of the weld pools produced at several beam defocus values in AM60B alloy for 6 mm-thick plates. Nominal power: 1.5 kW, welding speed: 105.8 mm/s, and shielding gas flow rate: 200 ft <sup>3</sup> /h (5.7 m <sup>3</sup> /h) of helium.....	249
5.13(a)	Weld pool area produced in laser welds of 2 mm-thick alloy AM60B plates for different welding speeds and laser powers using focused beam and shielding gas flow rate 200 ft <sup>3</sup> /h (5.7 m <sup>3</sup> /h) of helium.....	250
5.13(b)	Weld pool area produced in laser welds of 6 mm-thick alloy AM60B plates for different welding speeds and laser powers using focused beam and shielding gas flow rate 200 ft <sup>3</sup> /h (5.7 m <sup>3</sup> /h) of helium.....	251
5.14	Microstructures in the fusion zone and base metal of laser welded alloy AM60B. The Microstructures consist of cored grains of magnesium-rich solid solution (gray) surrounded by Mg <sub>17</sub> Al <sub>12</sub> intermetallic (unetched) in both the fusion zone and the base metal. Porosity (black) is also observed. Nominal power: 1.5 kW, welding speed: 74.1 mm/s. Chemically etched with 10% HF aqueous solution.....	253
5.15	Grain morphologies of magnesium-rich solid solution (gray) in (a) the base metal, (b) the fusion zone welded at a welding speed lower than 74 mm/s, and (c) the fusion zone produced at a welding speed higher than 74 mm/s. Specimen thickness: 6 mm, nominal power: 1.5 kW. Chemically etched with 10% HF aqueous solution.....	254
5.16	Variation of the grain size in the fusion zone as a function of the welding speed for laser welds of AM60B alloy. Nominal power: 1.5 kW, shielding gas flow rate: 200 ft <sup>3</sup> /h (5.7 m <sup>3</sup> /h) of helium.....	255
5.17	Microhardness profile across the fusion zone of laser welded AM60B alloy. Nominal power: 1.5 kW, laser beam: at focus, welding speed: 105.8 mm/s, and shielding gas flow rate: 200 ft <sup>3</sup> /h (5.7 m <sup>3</sup> /h) of helium. Test load: 100 g, time of loading 15 s.....	257
5.18	Dents (black) of microhardness test showing the influence of porosity on hardness. The regions with the presence of porosity have larger dent sizes and smaller hardness readings than the regions without porosity.....	258

## LIST OF TABLES

Table	Page
2.1 Percent power absorbed from a 200 joule, 2 second laser pulse [4].....	14
2.2 Thermophysical properties of aluminum and iron [158,159].....	31
3.1 Composition of aluminum alloy 5182.....	116
3.2 Welding parameters used in the study.....	116
3.3 Data used for the calculations of weld pool temperature and velocity fields [1,47-49].....	139
3.4 Welding conditions and the corresponding beam radius and absorption coefficient used for the calculations.....	140
3.5 Data used for the calculations of vaporization rates [48,53-55].....	141
3.6(a) Calculated and experimental weld pool geometry, vaporization rate and loss of magnesium in the weld pool for different laser powers at welding speed of 105.8 mm/s and beam defocusing of +/-1.5 mm.....	152
3.6(b) Calculated and experimental weld pool geometry, vaporization rate and loss of magnesium in the weld pool for different welding speed and beam defocusing at laser power of 3.0 kW.....	153
4.1 Material properties and process parameters.....	187
5.1 Chemical composition (wt%) of alloy AM60B.....	217
5.2 Power density on the specimen surface at different beam defocusing at a nominal laser power of 1.5 kW.....	218
5.3 Pore number density, average pore radius, and area percent porosity in the base metal and weld metal of 2 mm-thick alloy AM60B plates. Welding conditions: laser power 1.5 kW, focused beam, shielding gas flow rate 200 ft <sup>3</sup> /h (5.7 m <sup>3</sup> /h) of helium, and various welding speeds.....	229

## **ACKNOWLEDGEMENTS**

I would first like to offer my deep gratitude to my thesis advisor, Dr. Tarasankar DebRoy, for his valuable guidance, encouragement, and suggestions throughout the course of this research. I also wish to thank Dr. Long-Qing Chen, Dr. Panagiotis Michaleris, and Dr. Kwadwo Osseo-Asare for serving on my thesis committee and giving their valuable time to read and comment on this thesis. I would like to thank Dr. Stan David and Dr. Dawn White for their support and helpful discussions. I am very thankful to my colleagues Tao Hong, Todd Palmer, Mario Pastor, Sarang Sista, and Zhishang Yang for their help and discussions.

I am extremely grateful to my parents for their love and support throughout my life. I am deeply indebted to wife, Bei Wu, for her love, encouragement, and support during the course of my study.

I would like to acknowledge the financial support of the United States Department of Energy, Office of Basic Energy Sciences, Division of Materials Science, under Grant No. DE-FG02-96ER45602 and DE-FG02-84ER45158.

## **Chapter 1**

### **INTRODUCTION**

#### **1.1 General Background**

As environmental awareness grows among consumers as well as government agencies, attempts to improve fuel economy in automobiles are accelerating. In addition to improved powertrain efficiency, vehicle weight reduction is an important factor. Since the ability of a steel body structure to deliver weight savings is limited, the use of light-weight materials including aluminum and magnesium alloys in autobody structures is increasing, and is projected to expand further in the next decade.

Body architecture is also likely to undergo change in the near future. Tailor welded blanks are becoming increasingly common; most commonly implemented in steel today, the need for tailor welded blanks in aluminum is growing. Tailor welded blanks offer reduced weight with increased design flexibility, and can reduce material usage. Since safety is also a growing public concern, some vehicle architecture changes may be needed to offset issues surrounding the relationship between vehicle weight and safety, with increasing use of space frames, or space frame subassemblies expected. Increased use of technologies such as hydroforming, which can be used to produce complex single piece sections, further decreasing weight, while enhancing structural strength and stiffness, will also be seen. All of these technologies are likely to be implemented in aluminum as well as in steel, as the weight of the body structure drops.

Inevitably, this will lead to needs for new joining technologies for automotive aluminum and magnesium alloys. Resistance spot welding (RSW) is the most important welding process now used in autobody construction. While RSW is a nearly ideal process for the assembly of stamped steel body structures, offering robustness and low cost, it is

more costly and less robust when used on aluminum structures. Further, increased use of closed sections made via hydroforming will require processes other than RSW. Implementing tailor welded blanks in aluminum will also require new joining capability to support high volume production.

Laser welding is a particularly interesting approach to the construction of advanced automotive body structures because of its high speed, low heat input, and flexibility. Among potential benefits of laser welding are thinner flanges, tailor welded blanks, and reduced distortion in hydroformed frame structures. New developments in laser technology such as fiber optic delivery of YAG laser energy, have enhanced its ability to be used in high volume automation, while solid state laser diodes promise lower prices in the near future. Since future vehicle structures are likely to be composed of a much wider variety of materials than today, including mild steel, high strength steel and aluminum, a single power source will reduce capital investment, and increase flexibility in an age of increasing "mass customization".

Application of laser welding to aluminum and magnesium is far from a mature technology. Fundamental questions remain open, ranging from laser coupling with the material to the composition, structure, and properties of the resulting joints. These questions need to be addressed in order to obtain structurally sound and defect free welds.

The 2000, 5000, and 6000 series aluminum alloys chosen for automotive applications, provide substantial specific strength, good crash-worthiness, and excellent corrosion resistance [1]. Currently, weld metal composition change, porosity, and hot cracking are major concerns in the welding of aluminum alloys for automotive applications. The present study will address the issues of weld metal composition change and porosity formation.

During laser welding, the interaction between the material and the laser beam leads to rapid heating and melting of the material. The temperatures near the center of the



interaction zone on the weld pool surface are much higher than the melting point of the material. As a result, pronounced vaporization of alloying elements takes place on the weld pool surface. Weld metal composition change caused by selective vaporization of volatile alloying elements, especially magnesium, may affect the mechanical properties, corrosion resistance and hot crack susceptibility of aluminum weldment [2-4]. In the last decade significant progress has been made in understanding the vaporization of various species from the weld pool during fusion welding of several important engineering alloys and pure metals [5-14]. It is known that the weld metal composition change depends on the vaporization flux and the melting rate, the latter often being an important factor in determining the composition change [14]. However, these understandings are qualitative in nature. A comprehensive model is needed to achieve quantitative understanding of vaporization and weld metal composition change. The modeling can also provide a basis of controlling the process parameters to get a desired weld composition. The existing models [11-13] have been developed and used for predicting the vaporization rates and composition changes of steels or pure metals. These models are limited to spot welding or welding at low speeds. A more realistic three dimensional model needs to be developed to accurately predict the vaporization rates of alloying elements and weld metal composition changes during laser welding.

Accurate determination of the temperature field of the weld pool is a prerequisite for the realistic prediction of weld metal compositional changes and other physical processes. Although measurement of the weld pool temperature field is still a formidable task, mathematical modeling of transport phenomena in the weld pool provided detailed insight about the welding processes [15-24]. Calculations of heat transfer and fluid flow are commonly used to determine the resulting weld pool size and shape and thermal cycles at different locations in the weldment. These calculations have proven to be reliable in predicting weld pool characteristics in a number of different welding processes. The transport phenomena models have been incorporated with other models to quantitatively understand the development of weldment microstructures of C-Mn steels and titanium [25,26], the growth and dissolution of various inclusions in arc welding of low alloy

steels [27,28], and dissolution of gaseous species in GTA welding of steels [29,30]. However, so far very little research has been done to use the accurate heat transfer and fluid flow calculations to quantitatively understand the vaporization of alloying elements and compositional changes in the weldment. No quantitative investigations on weld metal composition change during laser welding of automotive aluminum alloys have been reported in the literature.

The detrimental effect of porosity on the mechanical properties of aluminum welds has been documented in the literature [31-33]. However, the mechanism of porosity formation during laser beam welding is less well understood. Pore formation has been linked to hydrogen rejection from the solid phase during solidification [34-37] and imperfect collapse of the keyhole [34, 38-40]. Sources of hydrogen in the weld metal include the filler metal, and to a lesser extent, the shielding gas and the base metal [41]. Controlling the hydrogen content in the metal to below the threshold level can effectively control hydrogen porosity in arc welding of aluminum alloys [37]. However, severe porosity has been observed consistently [42] during autogenous laser welding of aluminum alloys even when hydrogen contamination was minimized. A recent study [10] showed that during laser welding of thin plates of aluminum alloys 5182 and 5754, porosity was minimum when welding was conducted in either keyhole or conduction mode. In contrast, a large volume of macro-pores in the weld metal was observed when the welding mode shifted between keyhole and conduction modes. In this transition region, the keyhole was not stable. Therefore, the formation of macro-porosity was caused by instability of the keyhole. Hydrogen rejection played a minor role on porosity formation in laser welding of these alloys.

Magnesium alloys show particular promise for the construction of lightweight structures because of their low weight and high specific strength (tensile strength divided by specific gravity). Most magnesium alloys are used for parts that operate at high rotational speeds in order to minimize inertial forces. Current structural applications of magnesium alloys include industrial machinery, automotive components, and aerospace

equipment. Although joining of these alloys are important for their use, very little work has been reported on the laser welding of these alloys. It is known that magnesium alloys are difficult to weld due to pore formation [43-45] and liquation cracking [46]. Die cast magnesium alloys are more prone to porosity formation than cast or wrought magnesium alloys [44]. However, the mechanism of pore formation in laser welded die cast magnesium alloys is not well understood. Understanding the mechanism of pore formation and establishing the science-based remedies for laser welding of die-cast magnesium alloys are also important goals in this study.

## **1.2 Statement of Objectives**

The overall goal of this research is to seek better understanding of alloying element loss and macro porosity formation during laser welding of automotive aluminum and magnesium alloys. In particular, a quantitative understanding of the weld metal composition change due to selective vaporization of alloying elements will be achieved through theoretical and experimental study. Furthermore, the mechanisms of porosity formation during laser welding of these alloys will be investigated so that an appropriate remedy can be developed based on scientific principles. In order to achieve the overall goal, the following primary objectives of this research are listed here:

- (a) To develop a comprehensive mathematical model from the fundamentals of transport phenomena to predict fluid flow and heat transfer in the weld pool, vaporization rates of alloying elements, and the resulting weld metal composition changes for conduction mode laser welding of automotive aluminum alloys.
- (b) To investigate the effects of changes in welding parameters on weld pool geometry, vaporization rates of alloying elements, and the resulting weld metal composition change for laser welding of automotive aluminum alloys.

- (c) To develop a mathematical model to predict geometric features of welds in both keyhole and conduction modes, predict the weld pool temperature field, and investigate the effect of welding mode on the macroporosity formation during laser welding of automotive aluminum alloys.
- (d) To investigate the effects of changes in welding parameters on volume percentage, average size, and number density of porosity for laser welding of die-cast magnesium alloy AM60B.
- (e) To determine the mechanism of pore formation in laser welded die-cast magnesium alloy AM60B and establish the science-based measures to prevent pore formation for laser welding of this alloy.

### **1.3 Organization of the Thesis**

The thesis consists of six chapters. Chapter 1 describes the general background, objectives, and contents of the thesis. Chapter 2 is a critical literature review on current questions and problems in laser welding of automotive aluminum and magnesium alloys. The subject matter includes energy absorption, heat transfer and fluid flow in the weld pool, vaporization of alloying elements, weldment structure and properties, and mechanisms and remedies for the most commonly observed weld defects such as porosity.

Chapter 3 presents the experimental and theoretical study of weld metal composition change during conduction mode laser welding of aluminum alloy 5182. Based on the principles of transport phenomena, kinetics, and thermodynamics, a comprehensive model is developed for calculations of turbulent heat transfer and fluid flow, vaporization, and weld metal composition change for conduction mode laser welding. The model is used to predict the weld pool geometry, vaporization rates of alloying elements, and the resulting welding metal composition change. The calculated results are compared with experimental results. As a result this study, a quantitative understanding on the influences

of welding parameters including laser power and welding speed on weld metal composition change is achieved.

In chapter 4, a model is developed to predict the weld pool geometry for keyhole mode laser beam welding. The keyhole profile was calculated based on point-by-point energy balance on the keyhole wall where the temperature was assumed to be equal to the boiling point of the alloy. This keyhole profile was then used to calculate the three-dimensional temperature field of the weld pool. The temperature field was calculated by solving the heat conduction equation with appropriate boundary conditions. A key feature of this model is its ability to determine if a stable keyhole can be formed based on the welding conditions used. Therefore, the model can be used to determine the operation window of welding parameters where macroporosity caused by unstable keyhole can be avoided. The model has been used to predict the mode of welding, the keyhole profile, and weld pool temperature field for laser beam welding of aluminum alloys 5182 and 5754. The calculated results are compared with the experimental results.

The influences of welding parameters and the mechanism of pore formation during laser welding of die-cast magnesium alloy AM60B are studied and the science-based remedies are presented in chapter 5. A summary of the present study and suggestions for future research are given in chapter 6. Finally, several important computer programs used in this study are described in Appendix A through Appendix D.

#### **1.4 References**

1. L. Griffing: '*Welding Handbook*', Section 4, *Metals and Their Weldability*, American Welding Society, Miami, FL, 1972.
2. J. E. Hatch: '*Aluminum: Properties and Physical Metallurgy*', American Society for Metals, Metals Park, OH, 1984.
3. M. J. Cieslak and P. W. Fuerschbach: *Metallurgical Transactions*, 1988, 19B, pp. 319-329.

4. J. H. Dudas and F. R. Collins: *Welding Journal*, 1966, 45, pp. 241s-249s.
5. A. Block-Bolten and T. W. Eagar: *Metallurgical Transactions*, 1984, 15B, pp. 461-469.
6. M. Cullur, A. Paul, and T. DebRoy: *Metallurgical Transactions*, 1987, 18B, pp. 733-740.
7. P. A. A. Khan and T. DebRoy: *Metallurgical Transactions*, 1984, 15B, pp. 641-644.
8. P. Sahoo, M. M. Collur, and T. DebRoy: *Metallurgical Transactions*, 1988, 19B, pp. 967-972.
9. P. A. A. Khan, T. DebRoy and S. A. David: *Welding Journal*, 1988, 67, 1, pp. 1s-7s.
10. M. Pastor, H. Zhao, R. P. Martukanitz, and T. DebRoy: *Welding Journal*, 1999, 78, 6, pp. 207s-216s.
11. C. L. Chan and J. Mazumder: *Journal of Applied Physics*, 1987, 62, pp. 4579-4586.
12. T. DebRoy, S. Basu, and K. Mundra: *Journal of Applied Physics*, 1991, 70, pp. 1313-1319.
13. K. Mundra and T. DebRoy: *Metallurgical Transactions*, 1993, 24B, pp. 145-155.
14. S. A. David and T. DebRoy: *Science*, 1992, 257, pp. 497-502.
15. G. M. Oreper and J. Szekely: *Journal of Fluid Mechanics*, 1984, 147, pp. 53-79.
16. S. Kou and Y. H. Wang: *Metallurgical Transactions*, 1986, 17A, pp. 2265-2270.
17. S. Kou and Y. H. Wang: *Welding Journal*, 1986, 65, 3, pp. 63s-70s.
18. M. C. Tsai and S. Kou: *Welding Journal*, 1990, 69, 6, pp. 241s-246s.
19. T. Zacharia, A. H. Eraslan, and D. K. Aidun: *Welding Journal*, 1988, 67, 3, pp. 53s-62s.
20. T. Zacharia, S. A. David, J. M. Vitek, and T. DebRoy: *Welding Journal*, 1989, 68, 12, pp. 499s-509s.
21. K. Mundra, T. DebRoy, T. Zacharia, and S. A. David: *Welding Journal*, 1992, 71, 9, pp. 313s-320s.
22. K. Mundra, T. DebRoy, and K. M. Kelkar: *Numerical Heat Transfer, Part A*, 1996, 29, 2, pp. 115-129.
23. R. T. C. Choo and J. Szekely: *Welding Journal*, 1994, 73, 2, pp. 25s-31s.
24. K. Hong: Ph.D. Thesis, 1996, University of Waterloo, Waterloo, Ontario, Canada.

25. K. Mundra, T. DebRoy, S.S. Babu, and S.A. David: *Welding Journal*, 1997, 76, 4, pp. 163s-171s.
26. Z. Yang, J. W. Elmer, J. Wong, and T. DebRoy: *Welding Journal*, 2000, 79, 4, pp. 97s-112s.
27. S. S. Babu, S. A. David, T. Hong, and T. DebRoy: *Minerals, Metals and Materials Society/AIME, Fluid Flow Phenomena in Metals Processing (USA)*, March 1999, pp. 221-228.
28. T. Hong, T. DebRoy, S. S. Basu, and S. A. David: *Metallurgical and Materials Transactions*, 2000, 31B, pp. 161-169.
29. K. Mundra, J. M. Blackburn, and T. DebRoy: *Science and Technology of Welding and Joining (UK)*, 1997, 2, 4, pp. 174-184.
30. T. A. Palmer and T. DebRoy: *Metallurgical and Materials Transactions*, 2000, 31B, pp. 1371-1385.
31. F. V. Lawrence and W. H. Munse: *WRC Bulletin 181*, 1973, pp. 1-23.
32. R. F. Ashton and R. P. Wesley: *Welding Journal*, 1975, 54, 3, pp. 95s-98s.
33. M. Kato: *Welding International (UK)*, 1996, 10, 10, pp. 771-777.
34. S. Katayama: *Journal of Light Metal Welding and Construction (Japan)*, 1996, 34, 4, pp. 31-41.
35. I. Masumoto and M. Kutsuna: *International Institute of Welding*, IIW Doc. IV-566-91, 1991.
36. M. Kutsuna: *Welding in the World*, IIW 31, 1993, pp. 126-135.
37. R. A. Woods: 'Hydrogen in Metals', eds. I. M. Bernstein and A. W. Thompson, 1974, pp. 713-725, ASM, Metals Park, OH.
38. D. A. Schauer and W. H. Giedt: *Welding Journal*, 1978, 57, 7, pp. 189s-195s.
39. I. R. Whitaker, D. G. McCartney, and W. M. Steen: *ICALEO '92*, 1992, pp. 565-573.
40. R. P. Martukanitz and D. J. Smith: *Proceedings of the Sixth International Conference on Aluminum Weldments*, 1995, pp. 309-323, AWS, Cleveland, OH.
41. R. P. Martukanitz and P. R. Michnuk: *Aluminum*, 1982, 58, 5, pp. 276-279.
42. T. Marsico: M. S. Thesis, The Pennsylvania State University, University Park, 1988.

43. H. Haferkamp, Fr.-W. Bach, I. Burmester, K. Kreuzburg, and N. Niemeyer: *Proceedings of the Third International Magnesium Conference*, 1997, pp. 89-98, ed. G.W. Lorimer, The Institute of Materials, Cambridge, UK.
44. A. Weisheit, R. Galun, and B. L. Mordike: *Welding Journal*, 1998, 77, 4, pp. 149s-154s.
45. P. G. Sanders, J. S. Keske, K. H. Leong, and G. Kornecki: *Journal of Laser Applications*, 1999, 11, 2, pp. 96-103.
46. W. A. Baeslack, III, S. J. Savage, and F. H. Froes: *Journal of Materials Science Letters*, 1986, 5, pp. 935-939.



## **Chapter 2**

### **LITERATURE REVIEW**

In this chapter, the current issues and problems in the laser welding of automotive aluminum and magnesium alloys are critically reviewed. First, the current understanding of the important physical processes occurring during laser welding of these alloys, including energy absorption, fluid flow and heat transfer in the weld pool, and vaporization of alloying elements at the weld pool surface are examined. Second, the microstructural features and mechanical properties of the weldment are critically evaluated. Third, the commonly encountered defects, including porosity and hot cracking, found in laser welded automotive grade aluminum and magnesium alloys and their science based remedies are analyzed considering both the physical processes in the welding and the structure of these alloys. Finally, several important unanswered questions related to this welding are identified.

#### **2.1 Energy Absorption**

##### **2.1.1 Energy Transfer Efficiency**

Energy transfer efficiency is defined as the ratio of the energy absorbed by the irradiated materials to the laser energy available for absorption. During conduction mode laser welding, the energy transfer efficiency is equivalent to the absorptivity of the metal. On the other hand, when a keyhole is formed during laser welding, the energy transfer efficiency can be much larger than the absorptivity of the metal because of multiple reflections within the keyhole.

The absorption of laser energy by metals depends largely on conductive absorption by free electrons. For clean metal surfaces the absorptivity can be calculated from

the electrical resistivity of the metal substrate. Hagen and Rubens [1] first developed an approximate formula for calculating the emissivity of polished metals from experimental study. Combined with Kirchhoff's law that the emissivity is equal to the absorptivity at the same temperature and wavelength for internally non-reflecting media, their findings led to the following relation for absorptivity in the normal direction:

$$\eta_{\lambda}(T) = \varepsilon_{\lambda}(T) = 0.365 \left( \frac{r}{\lambda} \right)^{1/2} \quad (2.1)$$

where  $\eta_{\lambda}(T)$  and  $\varepsilon_{\lambda}(T)$  are the absorptivity and emissivity at temperature  $T$  and wavelength  $\lambda$ ,  $r$  is the resistivity in  $\Omega$ -cm at temperature  $T$ , and  $\lambda$  is the wavelength in cm. Bramson [2] developed a more accurate formula for absorptivity using the series expansion:

$$\eta_{\lambda}(T) = \varepsilon_{\lambda}(T) = 0.365 \left( \frac{r}{\lambda} \right)^{1/2} - 0.0667 \left( \frac{r}{\lambda} \right) + 0.006 \left( \frac{r}{\lambda} \right)^{3/2} \quad (2.2)$$

Calculations using Eqn. (2.2) are accurate during vertical laser irradiation of clean metal surfaces in vacuum when a plasma plume is not formed. Eqn. (2.2) indicates that the absorption of laser energy is determined by the wavelength of the laser and the resistivity of the metal. However, several other factors such as the nature of the surface, the joint geometry, the size and nature of the plasma existing above the weld pool, and the concentration of volatile alloying elements in the metal also affect the absorption of laser energy during welding. The absorption of laser energy by materials becomes more efficient as the laser wavelength decreases. The solid state Nd:YAG laser with a characteristic wavelength of 1.06  $\mu\text{m}$  provides better coupling with aluminum than CO<sub>2</sub> laser with a characteristic wavelength of 10.6  $\mu\text{m}$  [3].

Experiments [4,5] show that the absorption of laser beam energy by aluminum is very low. The poor coupling of the laser energy is due in part to the high density of free electrons in the solid. The free electrons in aluminum absorb and reemit the light energy efficiently making it one of the best reflectors of light. Huntington and Eagar [4] studied the absorption of CO<sub>2</sub> laser beam energy by pure aluminum and Al-5456 alloy by calorimetry. Table 2.1 illustrates the extent of absorption of a 200 joule, 2 second pulse laser beam by pure aluminum and Al-5466 alloy with different surface preparations. It is noted that the energy absorption is low on the as-received samples and considerable scatter in the measured absorption exists due to local differences in oxide thickness and surface roughness. Compared to as-received samples, sandblasting and anodizing significantly increase, whereas electropolishing somewhat decreases, the absorption of the laser beam energy. It was believed that the increased absorption of the anodized sample was due to the decreased free electron concentration at the surface, while in the case of the sandblasted sample, the increased absorption was thought to be due to light absorption by glass particles embedded in the surface [4]. The electropolished sample reduced the absorption apparently due to high reflectivity of the smooth surface. It is also observed from the data in Table 2.1 that Al-5456 alloy has an absorption coefficient of about 20 to 25% higher than that of pure aluminum with the same surface preparation, which can be explained by lower free electron concentration in the Al-5456 alloy [4]. Marsico [5] measured the absorption of a CO<sub>2</sub> laser beam by Al-5083 and Al-7039 alloys. The absorption of a 220 joule, 2 second pulse was found to be in the range of 12% to 15% by Al-5083 alloy and 6.9% to 9.0% by Al-7039 alloy. The difference in absorption was attributed to the difference in composition of the two alloys. All the above results were obtained when a flat surface was irradiated by a laser beam without any keyhole formation. Under such conditions, the absorption of laser beam energy by aluminum and its alloys is very low.

The formation of a keyhole greatly increases the absorption. The minimum power density required for keyhole formation is about  $10^6$  W/cm<sup>2</sup> for the CO<sub>2</sub> laser welding of aluminum alloys [3]. This threshold power density is considerably lower for the Nd:YAG laser welding of the same materials [3]. The enhanced absorption is believed to be

**Table 2.1 Percent power absorbed from a 200 joule, 2 second laser pulse [4]**

<b>Surface preparation</b>	<b>5456 aluminum alloy</b>	<b>99.999% pure aluminum</b>
<b>Anodized</b>	27	22
<b>Sandblasted</b>	22	20
<b>As-received</b>	5 - 12	7
<b>Electropolished</b>	4	5

contributed by the multiple reflections of the laser beam in the cavity [6]. Huntington and Eagar [4] studied the effects of keyhole formation and joint geometry on laser beam absorption by pure aluminum and Al-5456 alloy. They found that the absorption increased drastically as the laser beam power increased to a certain level. They showed that the dramatic increase in absorption was due to the formation of a keyhole rather than the onset of melting as commonly believed [7,8].

Experiments [9-11] on laser welding of aluminum alloys show that there exists a threshold laser power density above which a keyhole is formed and coupling of the laser beam with the welded materials drastically increases. Since a keyhole is formed primarily by the recoil force of the vaporizing atoms, high concentration of volatile elements in weld metal is helpful in the formation of a keyhole. Katayama [12] reviewed the melting of aluminum alloys by laser beam and rated the melting of aluminum alloys from easy to difficult to be in the following order: 2090 < (5456, 5083, and 5182) < (7075 and 7N01) < 5052 < (2024, 6061, and 6N01) < (2219 and 3003) < (1100 and 1050). These results indicate that alloys with higher concentrations of volatile elements such as Li in Al-2090, Mg in Al-5xxx, and Zn in Al-7xxx, are more easily melted by the laser beam. The volatile alloying elements, owing to their high vapor pressures, aid in the establishment of the keyhole and reduce the threshold power density required to achieve satisfactory coupling between laser beam and aluminum alloys.

Fuerschbach [13] measured the energy absorption during CO<sub>2</sub> laser welding of 1018 steel, 304 stainless steel, and tin. Most of the measurements were carried out using power densities which were well above the keyhole formation. It was observed that the energy transfer efficiency was less dependent on the laser irradiance, defined as the laser power divided by the beam spot area at the focal point, than on the laser intensity, defined as the laser power divided by the diameter of the beam spot at the focal point. Therefore, the energy transfer efficiency was plotted [13] as a function of the laser intensity as shown in Fig. 2.1. Despite the great differences in composition and physical properties of

these three materials, the measured values of energy transfer efficiency were found to be independent of material. The absorptivity increased from 0.20 to 0.90 with the increase in laser beam intensity and stabilized at approximately 0.90 at intensities greater than 30 kW/cm for the three materials as shown in Fig. 2.1. The results indicate that the absorption of laser energy is similar for different materials in the regime of keyhole mode of welding. An empirical relationship between the energy transfer efficiency and laser power intensity was obtained for the three materials as shown in Fig. 2.1. However, the applicability of this formula to the CO<sub>2</sub> laser welding of aluminum alloys has not been examined.

Independent of the mode of welding, pronounced vaporization of the volatile alloying elements may result in the formation of a plasma plume that can absorb [14] and scatter [15] a part of the laser beam energy. The plasma re-radiates [16,17] the laser energy in all directions by shorter-wavelength photons which are more readily absorbed by the material than the original laser light. When the plasma is small in size and is confined near the weld pool surface, it may aid in the coupling of the laser beam with the workpiece due to efficient absorption of the re-radiated energy by the workpiece. However, when the plasma plume grows in size, it absorbs a significant amount of laser energy [18,19], resulting in less absorption by the workpiece.

Huntington and Eagar [4] showed that optimizing joint geometry can improve the absorption of laser energy. To study the effect of joint geometry on absorption, welds were made on bead-on-plate, V-groove, and square groove with the same laser beam power. The fusion zone cross section areas on V-groove and square groove were much greater than that of bead-on-plate welds, indicating better absorption of laser beam energy in grooved joints. The square groove joints were found to be very sensitive to geometric changes, which could significantly alter the beam absorption. On the other hand, V-groove joints were found to be desirable for both weld consistency and efficient use of laser beam energy.

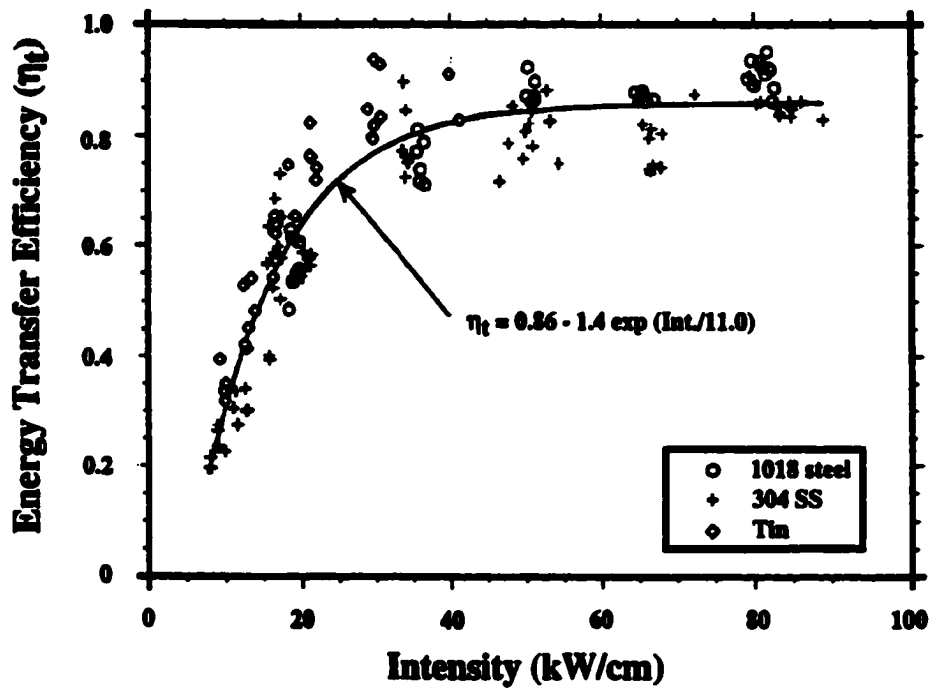


Fig. 2.1 Effect of beam intensity on the measured heat transfer efficiency for CO<sub>2</sub> laser welding of 1018 steel, 304 stainless steel, and tin [13].

### 2.1.2 Melting Efficiency

Melting efficiency, which is defined as the ratio of heat necessary to just melt the base metal to the heat absorbed by the workpiece, is another important parameter in evaluating energy absorption in welding processes. Fuerschbach [13] found that the melting efficiency,  $\eta_m$ , in CO<sub>2</sub> laser welding of 1018 steel, 304 stainless steel, and tin could be correlated with a modified Rykalin number,  $Ry$ :

$$\eta_m = 0.48 - 0.29 \exp(-Ry/6.8) - 0.17 \exp(-Ry/59) \quad (2.3)$$

where  $Ry = q_{in}v/(\alpha^2\Delta H_m)$ , where  $q_{in}$  is the net power absorbed by the workpiece,  $v$  is welding speed,  $\alpha$  is the thermal diffusivity of the workpiece at the liquidus temperature, and  $\Delta H_m$  is the enthalpy of melting. Fig. 2.2 shows that although there is considerable scatter in the data, the proposed correlation provides a useful framework for understanding melting efficiency of different alloys. Eqn. (2.3) indicates that the melting efficiency is determined by the welding parameters  $q_{in}$  and  $v$ , and the thermal properties of the workpiece  $\alpha$  and  $\Delta H_m$ . Aluminum has much higher thermal diffusivity than other common metals. Therefore, under the same welding conditions, the dimensionless number,  $Ry$ , for aluminum is much lower than other alloys, resulting in a lower melting efficiency. In order to obtain satisfactory melting efficiency, high values of  $q_{in}$  and  $v$  are required. Since the value of  $q_{in}$  is determined by the laser output power and the absorptivity of the laser energy by the workpiece, operating at the maximum laser output power and maintaining the keyhole mode of welding are desirable to achieve high melting efficiency. On the other hand, increasing welding speed also increases melting efficiency. However, Fuerschbach [13] also found that extremely high welding speeds may decrease melting efficiency if the welding mode is shifted from keyhole mode to conduction mode. Therefore, the use of high laser power and high welding speed while maintaining keyhole mode of welding is helpful in obtaining desired melting efficiency in continuous fusion welding.



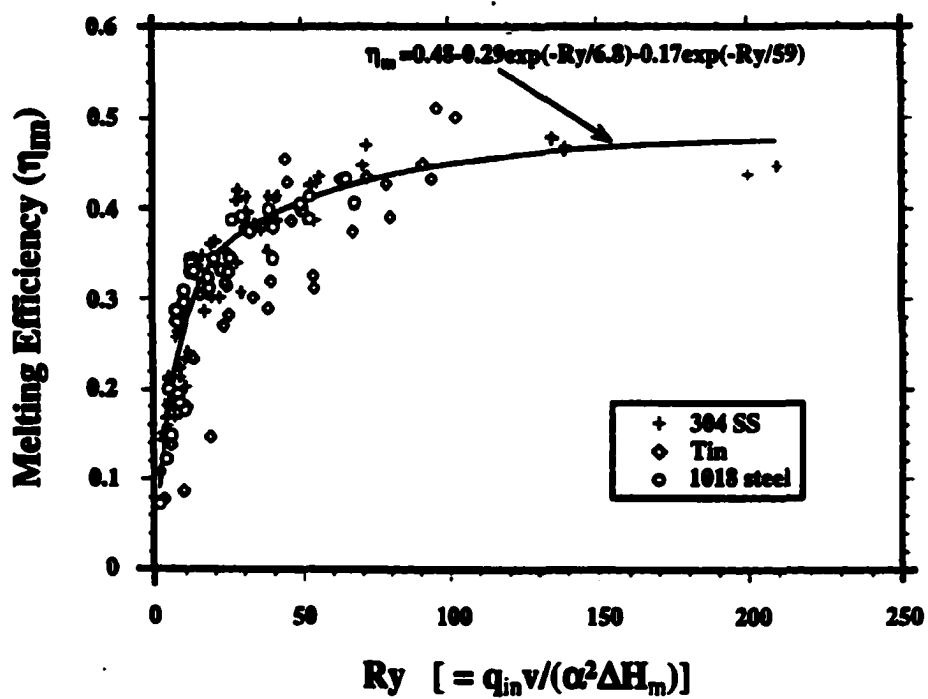


Fig. 2.2 Dependence of laser melting efficiency on the dimensionless number,  $Ry$ , for  $CO_2$  laser welding of 1018 steel, 304 stainless steel, and tin [13].

## **2.2 Heat Transfer and Fluid Flow**

### **2.2.1 Background**

The variation of temperature with time, often referred to as the thermal cycle, affects the microstructure, residual stress, and distortion produced in a welded structure. At the weld pool surface, the temperature distribution affects the vaporization of volatile alloying elements such as magnesium and zinc, the absorption and desorption of hydrogen and other gases, and thus, the weldment composition. In the interior of the weld pool, depending on the local temperature and composition, inclusions grow or dissolve. Thus, control of temperature profiles and cooling rates is important to ensure sound welds with desired fusion zone geometry, chemical composition, microstructure, and low residual stress. Therefore, understanding of heat and fluid flow in the weld pool is a prerequisite for understanding the geometry, composition, structure, and properties of the weld metal.

During laser welding, the interaction between the base metal and the heat source leads to rapid heating, melting, and vigorous circulation of the molten metal. For high power density beam welding such as laser welding, significant vaporization of the weld metal may occur resulting in the formation of a keyhole within the molten pool. In the weld pool, the circulation of molten metal is driven by buoyancy, surface tension, and when welding in the keyhole mode, by the thrust of the vapors. The resulting heat transfer and fluid flow affect the transient temperature distribution in the base material, the shape and size of the weld pool, and the solidification behavior.

Knowledge of temperature profiles in the weld pool and in the adjacent solid region can provide insight about heat transfer during welding. However, the measurement of surface temperatures during fusion welding is difficult, requires specialized equipment, and no standardized procedure for measurement is currently available. Furthermore, a technique for the measurement of temperature within the molten weld pool still remains to be developed. Temperature measurement in the solid region commonly involves the placement of thermocouples in holes drilled in the plates. This practice is cumbersome

and expensive, especially for thick plates. A recourse is to use quantitative calculations in order to understand heat transfer in fusion welding.

In the weld pool, heat is transported by convection and conduction. Because of its complexity, convective heat flow cannot be calculated analytically. As a result, most heat flow calculations in the past were limited to a simplified heat conduction calculations. Because of the availability of high speed computers in recent decades, more realistic and accurate heat transfer calculations considering both conduction and convection can now be performed. These complex calculations can predict temperature and velocity fields, weld pool geometry, and cooling rates. The computed values serve as a basis for understanding weld metal composition, and in simple systems, weldment structure. The verification of the computed values is often limited by measurement difficulties and, in many cases, the calculated results remain the only source of values.

Keyhole mode of welding results in better energy coupling and higher penetration than conduction mode of welding. Therefore, keyhole mode of welding is usually preferred in industries. However, due to the complexity of the process, modeling of heat transfer, fluid flow, and mass transfer during keyhole mode of welding is less vigorous than the available models of conduction mode laser welding. Therefore, much of the following discussions are pertinent to conduction mode of welding and modeling of transport processes in the keyhole mode of welding is discussed separately.

### **2.2.2 Temperature and Velocity Fields**

Measurements of temperature and liquid metal velocity in the weld pool have not been reported for the laser welding of automotive aluminum alloys. Furthermore, techniques for non-contact measurement of temperature during welding are still evolving. However, the fluid flow and heat transfer in all fusion welding processes share certain common features. Therefore, the findings from other fusion welding processes and results of welding of other alloys can provide useful information about the laser welding of aluminum alloys.

Schauer et al. [20] measured the temperature distributions in the keyhole during electron beam welding of several aluminum alloys, three steels, and tantalum, using a narrow band infrared radiation pyrometer. Their data showed that the peak temperature was the lowest for aluminum alloy welds and the highest for tantalum welds. They also observed that the presence of volatile elements such as magnesium and zinc in aluminum alloys significantly decreased the weld pool peak temperature. As the contents of magnesium or zinc in aluminum alloys increase in the order of 1100, 5083, and 7075 alloys, the average peak temperatures for these alloys decreased from a maximum of 2173 K for 1100 alloy to 1523 K for 5083 alloy and 1353 K for 7075 alloy. These results suggest that the higher the melting and boiling points of the weld metal, the higher the peak temperature in the weld pool. Heiple and Roper [21] estimated the surface flow velocity of GTA weld pool by measuring the motion of particles by a high-speed camera. They found that the velocities were in range of 0.5 to 1.4 m/s, with an average value of 0.94 m/s. These velocities are fairly high considering the fact that a typical weld pool is only a few millimeters wide. Krause [22] obtained surface temperature profiles for GTA welding of some steels, using a non-contact laser reflectance measurement technique. The “measurement” of pool temperature involved extrapolation of temperature versus time data after the arc is totally extinguished based on the perceived transient temperature profile prior to this time period. It is fair to say that reliable techniques for real time temperature measurement are still evolving. In the absence of adequate experimental work, contemporary literature relies heavily on the available recourse of numerical calculations of convective heat flow in the weld pool.

Since the concept of modeling fluid motion in weld pools was first proposed by Shercliff [23], numerous papers had been published [24-36] dealing with various aspects of the problem. With the aid of high performance computers, calculations of fluid flow and heat transfer in the weld pool are now routinely performed through numerical solution of the equations of conservation of mass, energy, and momentum. These calculations have led to improved insight in various complex phenomena in welding processes.

Kou and Wang [32] calculated the fluid flow during CO<sub>2</sub> laser welding of 6061 aluminum alloy and obtained a maximum flow velocity of 3000 mm/s. Fig. 2.3 shows the computed velocity and temperature fields in the laser melted pool of 6063 aluminum. The maximum computed temperature in the weld pool was found to be about 2273 K. The results show radially outward flow due to negative temperature coefficient of surface tension. The maximum computed velocity is of the order of 3 m/s in a weld pool that is about 0.6 mm wide and 0.15 mm deep. The high computed velocities indicate that mixing in the weld pool is highly efficient. An important consequence of a well-mixed pool is the absence of a significant spatial gradient of concentration of volatile components in the weld pool. Experimental data show that during laser welding of 5000 series aluminum alloys, the concentration of magnesium in the weld pool is fairly uniform [37] although the concentration of this element is significantly lower than that in the base material. The large computed surface velocities are typical of surface tension driven flow in a weld pool. The fusion boundary computed from the temperature profiles agreed well with the experimentally determined wide and shallow weld pool profile.

It is known that the magnitude of the velocities for both buoyancy and electromagnetic force driven flows in the weld pool are usually much smaller than those obtained for surface tension driven flows [13]. Kou and Wang [33] showed that during stationary GTA welding of 6061 aluminum alloy the maximum velocity caused by buoyancy, electromagnetic force, and surface tension force were 9, 180, and 3000 mm/s respectively. The maximum velocity due to the combined effects of three forces was 2300 mm/s. During laser welding, the surface tension force dominates due to the absence of electromagnetic forces.

The spatial gradient of surface tension is a stress, known as the Marangoni stress, which may arise owing to variations of both temperature and composition. Frequently, the convection in the weld pool results mainly from the stress that is determined by the

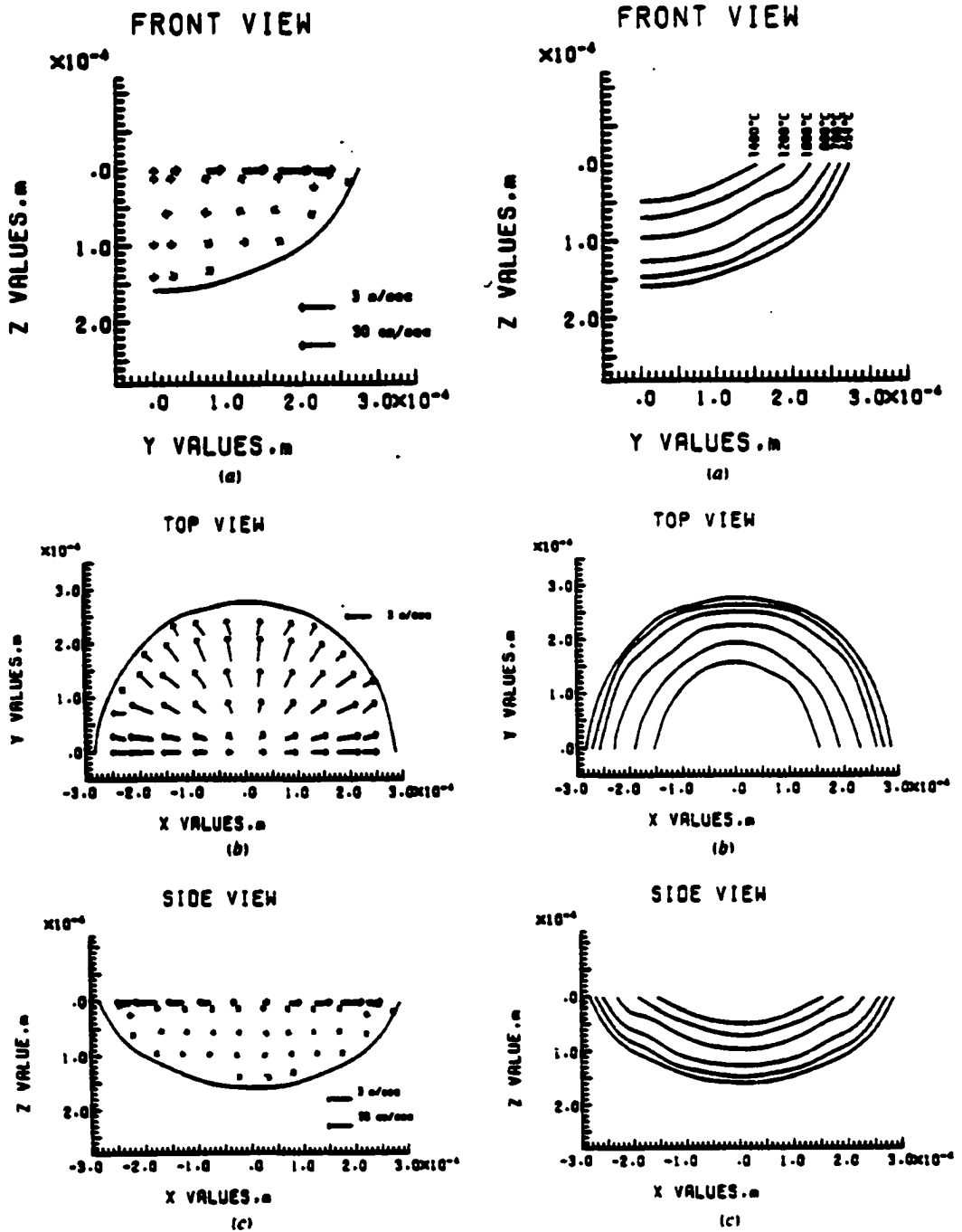


Fig. 2.3 Calculated velocity and temperature fields in a laser weld pool of 6063 aluminum alloy using a CO<sub>2</sub> laser power of 1.3 kW and welding speed of 10 IPM [32].

temperature gradient at the weld pool surface. Assuming velocity distribution in a boundary layer, the maximum velocity,  $u_m$ , can be roughly estimated [13] assuming that it occurs approximately halfway between the heat source axis and the weld pool edge:

$$u_m^{3/2} = \frac{d\gamma}{dT} \frac{dT}{dy} \frac{W^{1/2}}{0.664 \rho^{1/2} \mu^{1/2}} \quad (2.4)$$

where  $\gamma$  is the interfacial tension,  $T$  is the temperature,  $y$  is the distance along the surface from the axis of the heat source,  $\rho$  and  $\mu$  are the density and viscosity, respectively, and  $W$  is width of the weld pool. For a typical value of weld pool width of 5 mm, metal density of 2385 kg/m<sup>3</sup>, viscosity of 0.0013 kg/(m-s), temperature coefficient of surface tension,  $d\gamma/dT$ , of  $-3.5 \times 10^{-4}$  N/(m-K), and spatial gradient of temperature of  $10^5$  K/m, the maximum velocity is approximately 1.65 m/s. The maximum velocity calculated from Eqn. (2.4) can provide a rough idea of the maximum velocity of liquid metal in the weld pool. Detailed solutions of the equations of conservation of mass, momentum and heat are necessary for the calculation of temperature and velocity fields in the weld pool.

Both experiment [21] and mathematical modeling [28] showed that the maximum velocities in steel weld pools were on the order of 1 m/s. On the other hand, the calculations of Kou and Wang [32,33] obtained maximum velocities in the range of 2 to 3 m/s for welding of 6061 aluminum alloy. These high velocities in aluminum alloy weld pools may lead to turbulence in the weld pool.

### 2.2.3 Effect of Turbulence in Weld Pool

The earlier models [24-33] assumed that the fluid flows in the weld pool were laminar in nature. The validity of this assumption has yet to be verified since the critical Reynolds number for transition from laminar flow to turbulent flow in the weld pool has not been established. However, there are evidences that suggest the existence of turbulence in the weld pool. Malinowski-Brodnicka et al. [38] measured the flow velocity in AISI 310 stainless steel weld pools and found that the Reynolds number was about 3,000.

Considering the classical critical Reynolds number of 2,100 for transition from laminar to turbulent flow in pipes, they concluded that the flow in the AISI 310 weld pools was probably turbulent. In modeling, when full laminar flows were assumed [24-26], the calculated weld pool tended to be narrower but deeper than the actual welds, and the predicted peak temperature in the weld pool was higher than the actual values. One of the possible reasons for these discrepancies is that the influence of turbulence in the weld pool has been ignored in these models.

It has been established [39] that the existence of turbulence in the fluid flow greatly enhance the rates of transport and mixing of mass, momentum and energy. In many cases, magnitudes higher of transport and mixing rates are found in turbulent flows than in laminar flows. Turbulence models [40] characterize the enhanced transport and mixing of the turbulent flow in term of turbulent viscosity and turbulent thermal conductivity which are properties of the fluid flow not of the fluid and have different values at different regions depending on the structure of the flow conditions. In highly turbulent systems, these quantities can be orders of magnitude higher than the molecular values. In weld pool modeling, the enhanced viscosity and thermal conductivity due to turbulence are of great importance. Mundra et al. [27] studied the role of various thermophysical properties on weld pool. It was found that the viscosity and thermal conductivity of the liquid greatly affect the aspect ratio, the peak temperature and the peak fluid flow velocity of the weld pool.

In order to simulate the enhanced transport of mass, heat, and momentum due to the turbulence in the weld pool, some models [28-30] used effective viscosity and effective thermal conductivity, which were much higher than the molecular quantities, in the transport equations for laminar flows. The calculated weld pool shapes for GTA welding of aluminum alloy 6061 [28] and GTA and laser welding of stainless steel 304 [29,30] were in good agreement with the experimental results. However, the proper values of effective viscosity and thermal conductivity have to be chosen by trial-and error. Recently, the  $K-\epsilon$  turbulence model [40] has been adopted in modeling of stationary GTA welding



[34-36] to study the role of turbulence in the weld pool. These models can calculate the distribution of effective viscosity and thermal conductivity in the weld pool as shown in Fig. 2.4. It is observed from the figure that the values of effective viscosity of the fluid flow vary in different regions of the weld pool and can be quite different for different welding conditions. The distribution of effective thermal conductivity has the similar pattern. The calculated effective viscosity and thermal conductivity through modeling make it possible to quantitatively determine the influence of turbulence on the behavior of the fluid flow in the weld pool. As a result, these models can more precisely predict the temperature and velocity fields. A comparison of the calculated weld pool geometry using different models is shown in Fig. 2.5 [34]. It is observed that the calculated weld pool geometry has better agreement with the experimental results only when the influence of turbulence was considered in the calculations.

#### 2.2.4 Relative Importance of Conduction and Convection

The relative importance of conduction and convection in the overall transport of heat in the weld pool can be assessed from the value of the Peclet number,  $Pe$ , which is given by:

$$Pe = \frac{u\rho c_p L}{k} \quad (2.5)$$

where  $u$  is the velocity,  $\rho$  is the density,  $c_p$  is the specific heat at constant pressure,  $L$  is the characteristic length and  $k$  is the thermal conductivity of the melt. For a typical case of welding aluminum with  $\rho = 2385 \text{ kg/m}^3$ ,  $c_p = 1080 \text{ J/(kg-K)}$ ,  $L = 0.002 \text{ m}$ , and  $k = 94.03 \text{ W/(m-K)}$ , the  $Pe$  is about  $54.8u$ . In the weld pool, the average velocity is considerably lower than that of the maximum velocity, very often by more than an order of magnitude. Thus, if the average velocity is of the order of about  $0.1 \text{ m/s}$ , the value of  $Pe$  is about  $5.5$ . This value of  $Pe$  signifies that the transport of heat in the weld pool may be aided both by convection and conduction. The actual mechanism of heat transfer will depend on the value of the velocity, the size of the weld pool and other parameters. Because

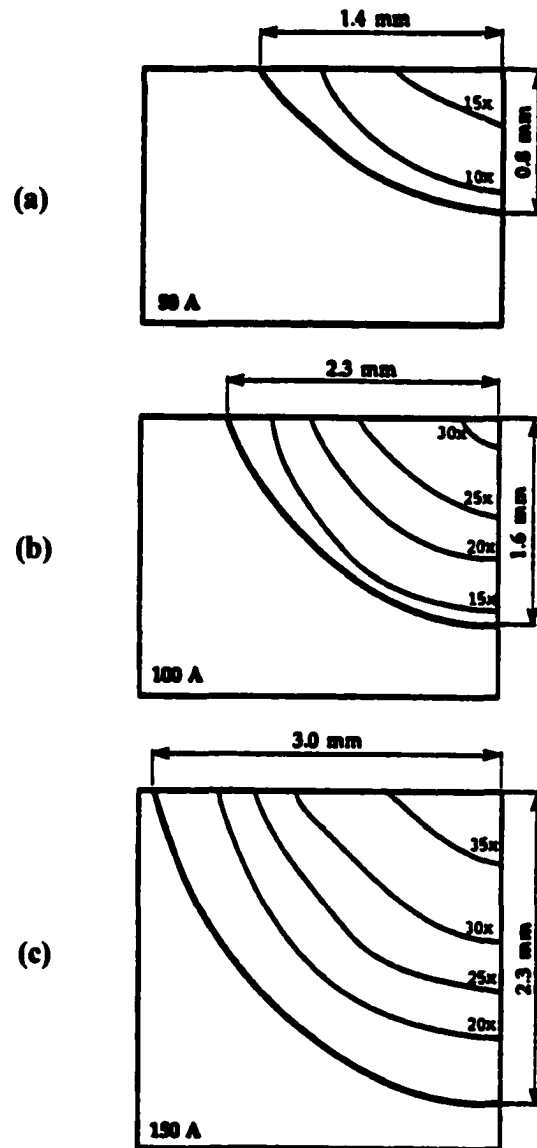


**Fig. 2.4** Contour plots of effective viscosity as calculated from the K- $\epsilon$  model for GTA stationary welding of AISI 304 stainless steel with different currents [34]: (a) 50 A; (b) 100 A; (c) 150 A. The numbers on the contour lines represent the ratios of effective viscosity to molecular viscosity.

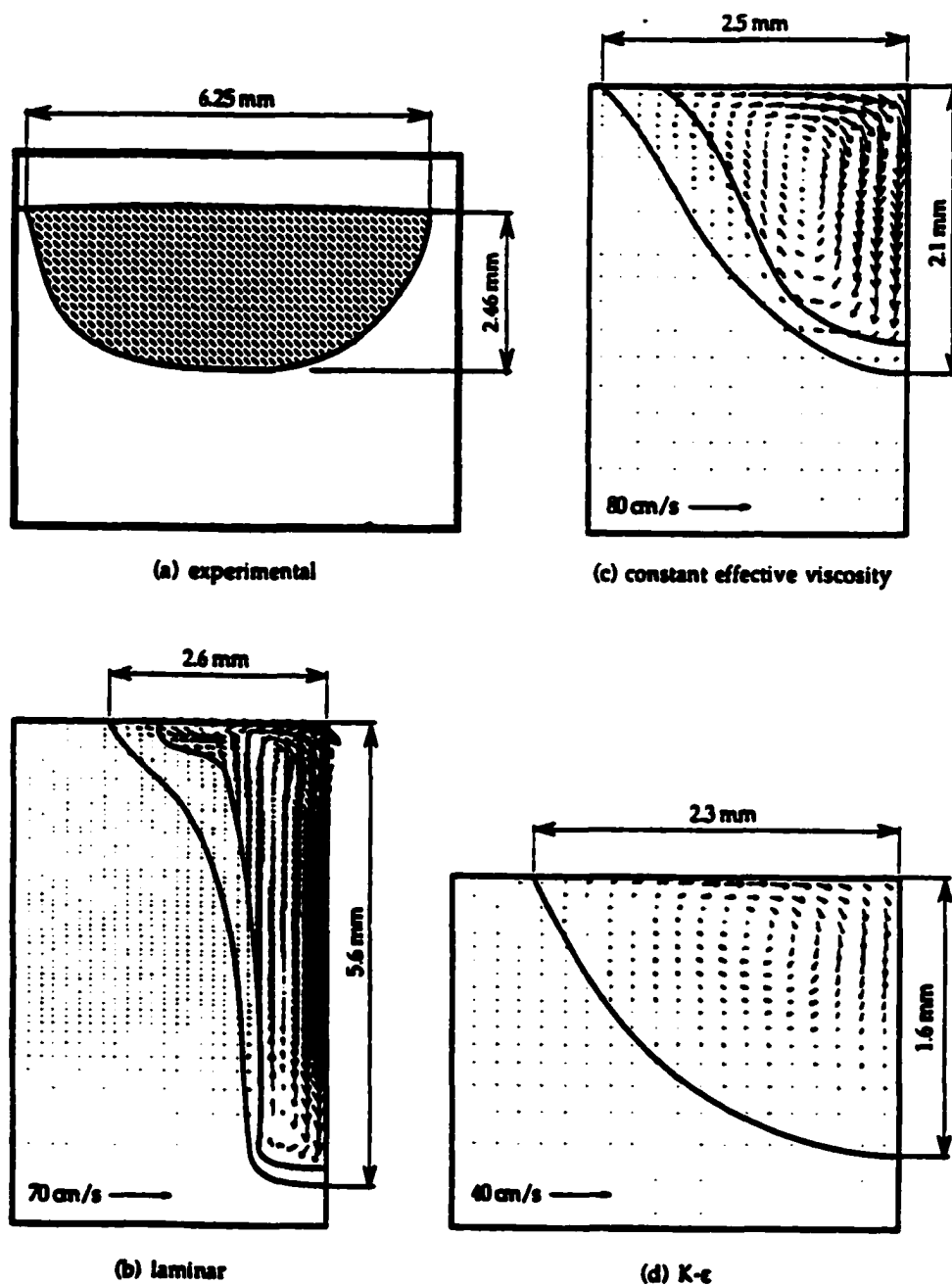


Fig. 2.5 Comparison of weld pool shapes for: (a) experimental results, (b) numerical results based on laminar properties, (c) numerical results using a constant effective viscosity and thermal conductivity which are 30 times of the molecular values, (d) numerical results based on the K- $\epsilon$  turbulence model [34].

of the high thermal conductivity of aluminum, if the velocity is low and the pool size is small, the value of  $Pe$  can be low ( $Pe \ll 1$ ), and accurate calculations of heat transfer may be done under those conditions using relatively simple heat conduction calculations.

It is often instructive to compare the welding of aluminum with that of steels. The thermophysical properties of aluminum and iron are given in Table 2.2. For a typical case of the welding of steel, if we take  $\rho = 7015 \text{ kg/m}^3$ ,  $c_p = 795 \text{ J/(kg-K)}$ ,  $L = 0.002 \text{ m}$ , and  $k = 38 \text{ W/(m-K)}$ , the  $Pe$  is about 294. Considering an average velocity of  $0.1 \text{ m/s}$ , the  $Pe$  obtained is about 29. When the Peclet number is much larger than one, heat transport occurs primarily by convection, and heat conduction in the weld pool is not important. Therefore, for the same size of the weld pool and same average velocity, the value of the  $Pe$  for the welding of steels is much higher than that for the welding of aluminum. As a result the convective heat transport is much more important for the welding of steels than for the welding of aluminum alloys. It should also be noted that the conduction of heat in the solid region is very important for the dissipation of heat away from the weld pool. Therefore, the thermal conductivity of the solid and the specimen dimensions are very important in determining the size of the molten pool.

Insight about heat transfer during welding of aluminum alloys can also be obtained by comparing properties of aluminum alloys with those of steels. First, the thermal conductivity of aluminum alloys is nearly an order of magnitude higher than that of steels. Therefore, heat transfer by conduction is more efficient for aluminum alloys than for steels. When weld pool shape and size were calculated ignoring convection, the computed values matched well with the experimental results for stationary GTA welding of 1100 aluminum alloy while significant discrepancy between the two values was observed for AISI 304 stainless steel [36]. Therefore, convective heat transfer is less important for aluminum alloys than for steels.

Table 2.2 Thermophysical properties of aluminum and iron\* [158,159]

	$\rho$ (kg/m <sup>3</sup> )	$k$ (W/m-K)	$c_p$ (J/kg-K)	$\alpha$ (m <sup>2</sup> /s)	$\mu$ (kg/m-s)	Pr	$\sigma$ (N/m)	$d\sigma/dT$ (N/m-K)
Al at melting point (933 K)	2385 [158]	94.03 [158]	1080 [158]	$3.65 \times 10^{-3}$	0.0013 [158]	0.015	0.914 [158]	$-3.5 \times 10^{-4}$ [158]
Al at 673 K	2620 [158]	238 [158]	1076 [158]	$8.44 \times 10^{-3}$	-	-	-	-
Fe at melting point (1810 K)	7015 [158]	38 [159]	795 [158]	$6.8 \times 10^{-6}$	0.0055 [158]	0.12	1.872 [158]	$-4.9 \times 10^{-4}$ [158]
Fe at 673 K	7747 [158]	48.6 [158]	611 [158]	$1.03 \times 10^{-3}$	-	-	-	-

\*  $\rho$ ,  $k$ ,  $c_p$ ,  $\alpha$ ,  $\mu$ , Pr,  $\sigma$ , and  $d\sigma/dT$  are the density, thermal conductivity, specific heat, thermal diffusivity, viscosity, Prandtl number, surface tension, and temperature coefficient of surface tension respectively.

It is also useful to examine the Prandtl numbers of aluminum alloys and steels. The physical interpretation of the Prandtl number follows from its definition as a ratio of the momentum diffusivity,  $\nu$ , to the thermal diffusivity,  $\alpha$ . The Prandtl number provides a measure of the relative effectiveness of momentum and heat transport by diffusion in the velocity and thermal boundary layers, respectively. Near the fusion boundary of the molten weld pool where the fluid flow is stagnant, transport of heat and momentum by diffusion is more important than by convection. Since the Prandtl numbers of liquid aluminum and steel are much less than one, the heat diffusion rate greatly exceeds the momentum diffusion rate near the fusion boundary. Furthermore, since the Prandtl number of liquid aluminum is about one order of magnitude lower than that of iron, heat diffusion is more efficient in liquid aluminum alloys than in liquid steels.

### **2.2.5 Effect of Power Density Distribution**

Kou and Le [41] examined the effect of power density distribution on the weld pool shape for welding of 6061 aluminum alloy. In their model, an effective thermal conductivity was used to account for the effect of convection. The calculated results showed that the nature of the heat source greatly affected the weld pool shape and size. As shown in Fig. 2.6, for the same heat source power and welding speed, a focused heat source produced a deep and large weld pool. This is consistent with the result of a recent experimental study on Nd:YAG laser welding of aluminum alloys 5182 and 5754 [37]. As shown in Fig. 2.7, changing the power density distribution by welding at different laser beam defocus values resulted in significantly different weld pool shapes. For a given total power of the heat source, the use of a higher power density heat source results in deeper penetration and enables welding of thicker plates. The experiments [37] also indicate that the beam defocusing has to be carefully controlled in order to produce reproducible weld pool geometry during laser welding of aluminum alloys.

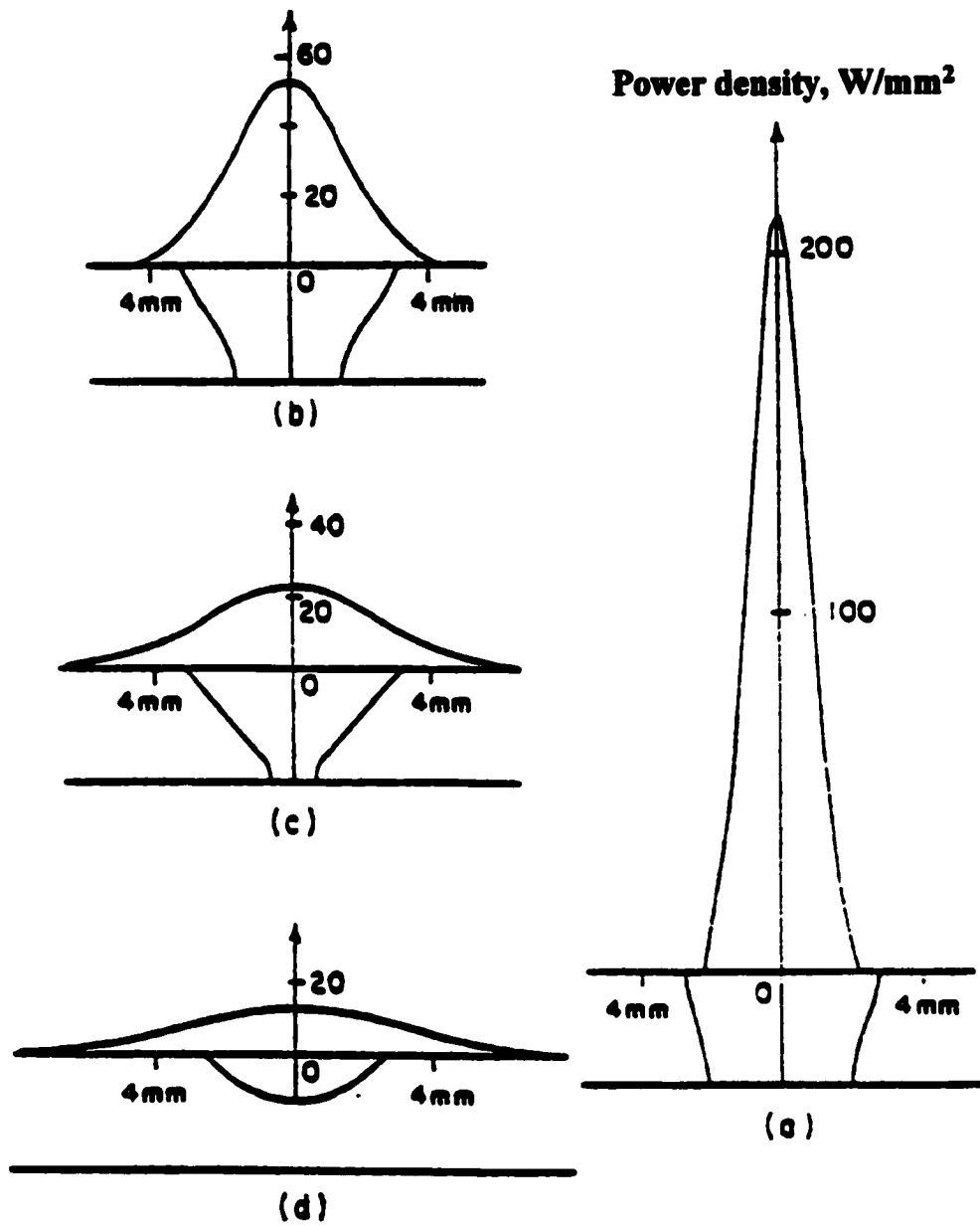
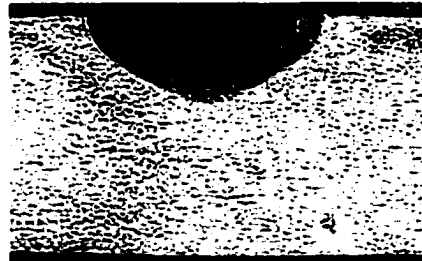
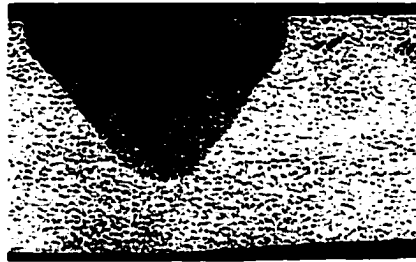


Fig. 2.6 Four different power density profiles of the heat source and their resultant welds with heat source power of 860 W and welding speed of 5.5 mm/s [41].



defocusing: 1.5 mm



defocusing: 1.0 mm



defocusing: 0.5 mm



defocusing: 0 mm

**Fig. 2.7** Cross sections of Nd:YAG laser welded 1.45 mm thick 5754 aluminum alloy for different beam defocusing values with a laser power of 3.0 kW and welding speed of 150 ipm [37].



### 2.2.6 Effect of Convection on Weld Pool Shape

It is now well known [42] that when convection is the dominant mechanism of heat transfer, small amounts of surface active elements, such as sulfur or oxygen in steels, can play an important role in enhancing weld penetration. For example, Fig. 2.8 shows that the depth of penetration was significantly affected by the concentration of sulfur in steel welds containing 20 and 150 ppm of sulfur and laser welded at a power of 5200 W. However, when convection is not the dominant mechanism of heat transfer, the pool geometries in the two steels are similar as seen from the cross sections of welds prepared at a laser power of 1900 W. Thus, the effect of sulfur on the weld geometry depended on the laser power and other welding variables. So far, the effect of surface active elements on the shape and size of aluminum weld pools has not been reported in the literature.

### 2.2.7 Surface Tension of Aluminum Alloys

The values of surface tension as a function of temperature and composition are important in determining the magnitude and direction of the Marangoni stress on the weld pool surface. In the absence of surface tension data as a function of temperature and composition, a recourse is to model the surface tension of alloys from fundamentals of thermodynamics and adsorption phenomena. Sahoo et al. [43] showed that the surface tension of many binary metal-surface active solute systems can be adequately modeled on the basis of Gibbs and Langmuir adsorption isotherms and consideration of the surface segregation of the solutes. The dependence of the surface tension of a metal on both temperature and activity of a component is expressed by:

$$\sigma = \sigma^0 - A(T - T^0) - 8314T\Gamma_s \ln[1 + \kappa a_s e^{-\Delta H^0/8314T}] \quad (2.6)$$

where  $\sigma^0$  is the surface tension of the pure metal at a reference temperature  $T^0$ ,  $A$  is a constant which expresses the variation of surface tension of the pure metal at temperatures above the melting point,  $\Gamma_s$  is the surface excess in saturation,  $\kappa$  is the entropy factor,  $a_s$  is the activity of the surface active element in the alloy, and  $\Delta H^0$  is the enthalpy of

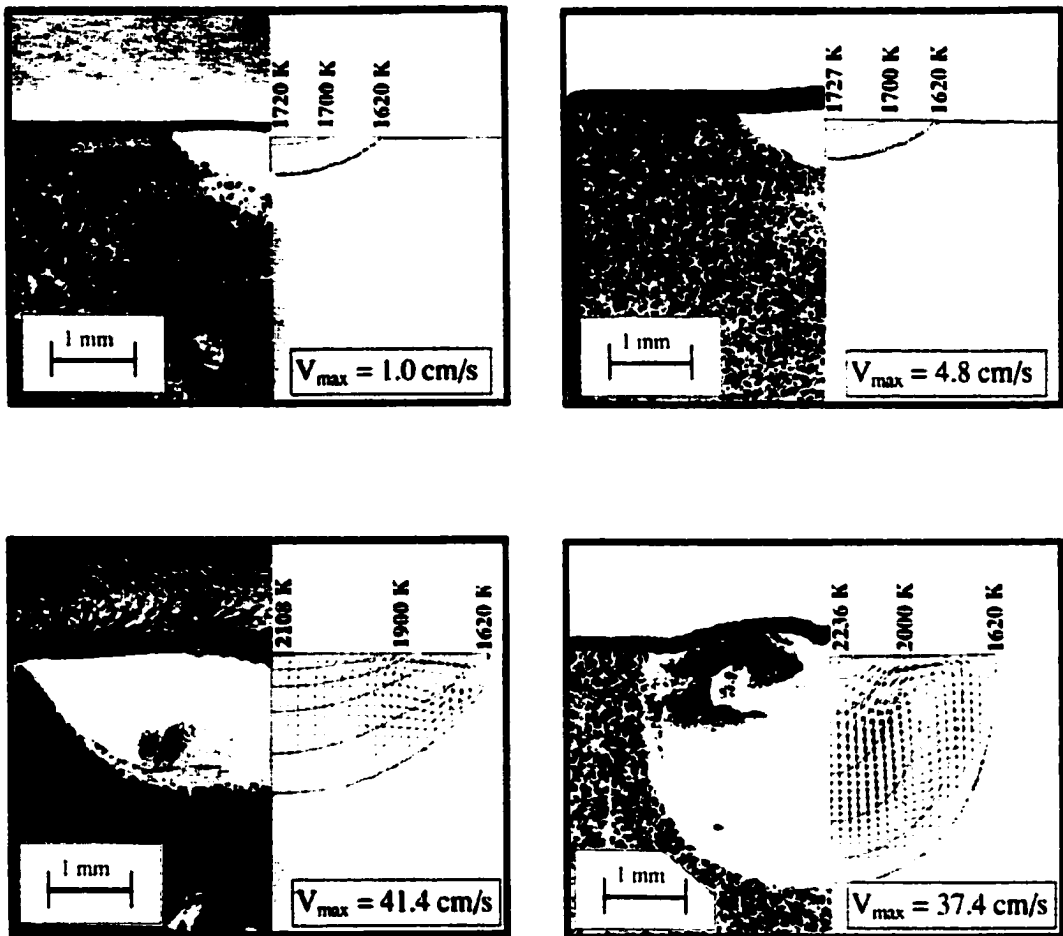


**Fig. 2.8** Spot weld pool geometries of Böhler S705 high-speed steel using  $\text{CO}_2$  laser with a power of 1900 W for the heats containing (a) 20 ppm and (b) 150 ppm of sulfur; and with a power of 5200 W for the heats containing (c) 20 ppm and (d) 150 ppm of sulfur. Plate thickness: 15 mm, irradiation time: 5 s, and shielding gas: 20 L/min of argon [42].

segregation. These models have been successfully used in predicting the surface tensions of ferrous alloys [44].

The surface tension of pure aluminum decreases with increasing temperature [45]. Therefore, the temperature coefficient of the surface tension is negative. However, the true surface tension of molten aluminum is difficult to measure due to the formation of a thin layer of oxide on its surface, even under carefully controlled conditions involving the use of high vacuum or an inert atmosphere [45]. Therefore, it is not surprising that wide discrepancies exist in the results obtained by various investigators. The effects of alloying elements on the surface tension [46] are shown in Fig. 2.9. It is observed that Li, Bi, Pb, Mg, Sb, Ca, Sn and, to a lesser extent, Si, reduce the surface tension of aluminum whereas Ge, Zn, Ag, Fe, Mn, and Cu have little effect on the surface tension of aluminum. Though much work has been done on surface tension of binary alloys containing aluminum, very little data are available for commercial and ternary alloys. Goicoechea et al. [47] measured the surface tension of two ternary aluminum alloys Al-Si-Mg and Al-Zn-Mg. They showed that the surface tension of these alloys could be obtained from the data of the binaries and pure aluminum:

$$X_{\text{Al-A-B}} = X_{\text{Al}} + \Delta X_{\text{Al-A}} + \Delta X_{\text{Al-B}} \quad (2.7)$$

where A is Si or Zn, B is Mg,  $X_{\text{Al-A-B}}$  and  $X_{\text{Al}}$  are the surface tension of the ternary alloy and pure aluminum, respectively,  $\Delta X_{\text{Al-A,B}}$  are the increments of the surface tension induced by A or B additions in binary alloys, respectively. This result indicates that the interactions between the constituent elements have little effect on the surface tension of the investigated alloy systems. An appropriate model for the calculation of the surface tension of the aluminum alloys as a function of temperature and composition is not yet available. Such a model is important for accurate calculation of heat transfer and fluid flow in laser welding of aluminum alloys.

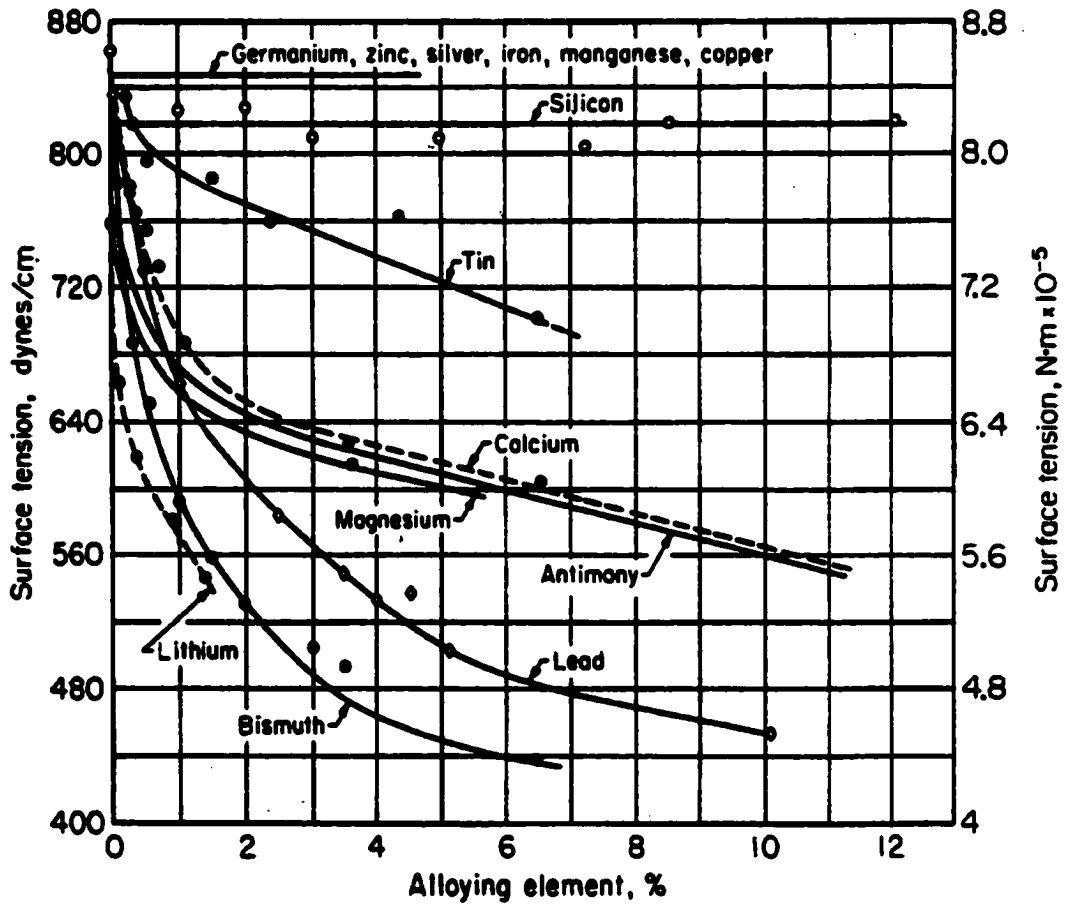


Fig. 2.9 Effect of added elements on the surface tension of 99.99% aluminum at 973 to 1013 K in argon [46].

### 2.2.8 Fluid Flow and Heat Transfer in Keyhole Mode of Welding

Keyhole mode of welding enables the laser beam to penetrate deep into the work-piece, thus achieving deep weld penetration at high welding speed with low heat input. Because of its good seam quality, low distortion and high productivity, it has found increasing applications in the automotive industry. Much of our current knowledge in the heat and fluid flow in keyhole mode of welding was derived from investigations on both laser and electron beam processing of aluminum and other alloys.

In 1973, Swift-Hook and Gick [48] formulated a model of keyhole mode of laser welding. They treated the laser beam as a moving line source and obtained a relationship between seam width, absorbed laser power, and welding speed based on heat conduction theory. The penetration depth that is usually of significant technical concern could not be calculated since full penetration for all welding conditions was assumed in this model.

Andrews and Atthey [49] and Klemens [50] proposed models that considered the conditions for the formation of a keyhole. Andrews and Atthey [49] obtained the keyhole profile based on the energy balance on the keyhole wall. They showed that the dimensions of the keyhole could be determined from two dimensionless numbers: dimensionless power density  $Q = q/(g\rho\rho_g h^2 a)^{1/2}$  and dimensionless surface tension  $\tau = T/\rho g a^2$ , where  $q$  is the power density of the beam,  $a$  is the beam radius,  $\rho$  and  $\rho_g$  are the densities of the liquid and vapor respectively,  $h$  is the heat of vaporization, and  $T$  is the surface tension coefficient. Their calculations showed that the depth of penetration was typically reduced by a factor of about three because of the surface tension force. However, the model assumed that all the laser energy was absorbed and used for the vaporization of the metal. Furthermore, heat loss by conduction into the material was neglected. Since these assumptions are not valid in most cases, the model predictions are open to question.

Klemens [50] assumed a circular keyhole with vertical walls that was kept open by a balance between vapor pressure within the keyhole, surface tension, and hydrodynamic pressure in the melt surrounding the keyhole. Absorption of radiation was assumed

to take place only by the vapor phase in the keyhole. The temperature distribution was determined from the solution of the heat conduction equation. This model [50] was able to calculate the shape of the vapor cavity and of the molten zone and, for this reason, it later served as a basis for the development of several subsequent models.

Mazumder and Steen [51] developed a heat transfer model for laser assisted materials processing with a moving Gaussian heat source using finite difference technique. The model assumed complete absorption of energy at all locations on the surface where the temperature exceeded the boiling point. The model predictions of weld pool geometry were found to be comparable with the experimental results.

The foregoing models [48-51] treated only heating of the workpiece. The fluid flow in the molten pool and the convective heat transport were not considered. Dowden et al. [52-55] treated the viscous flow in the weld pool during keyhole mode welding. They [52,53] assumed a slim cylindrical keyhole of known radius in a molten pool that was almost cylindrical but not concentric to the keyhole due to the movement of the beam. Furthermore, the temperature on the keyhole wall was assumed to be the boiling point. The size of the molten pool was determined from the computed temperature profiles. Only two-dimensional flow with horizontal components was considered. The velocities were obtained by solving Navier-Stokes equations. In their subsequent work, they [54,55] assumed that all the laser energy was absorbed by the vapor in the keyhole and the keyhole was kept open by equilibrium between vapor pressure and surface tension force. A non-viscous vertical flux of vapor in the keyhole and a viscous vertical flow of molten metal around the keyhole were assumed. With these assumptions, they developed a more comprehensive model that accounted for the vertical variations of keyhole geometry and flow conditions around the keyhole. The model involved the solutions of the Navier-Stokes equations, and the equations of conservation of mass and energy.

Kar and Mazumder [56] and Mohanty and Mazumder [57] developed models to predict the weld pool velocities, temperatures, weld pool shape, keyhole depth, and di-

ameter. The model [56,57] involves the calculations of thermocapillary convection in the weld pool due to the surface tension gradient and the energy balance at the liquid-vapor and solid-liquid interfaces. The calculations showed that the melt velocity in the weld pool could be higher at higher scanning speed for a given laser power if the laser-vapor interaction became significant. The calculated weld pool geometry was found to compare fairly well with the experimental data. Mohanty and Mazumder [57] integrated the model into an interactive software tool that can analyze laser welding for a given set of process conditions.

It is well known that the vertical cross section of deep penetration weld has a characteristic a "nail head" shape. Steen et al. [58] combined a moving point source and a moving line source to describe the laser beam absorption in the keyhole. The temperature distribution obtained from this model yielded a weld pool shape that agreed very well with that found from experimental investigations.

The models described so far did not consider any detailed energy absorption mechanism. Herziger et al. [59] presented a detailed theoretical study of the energy absorption processes by the plasma in the keyhole considering inverse Bremsstrahlung. They showed that the penetration increases with laser intensity up to a certain power density. When this power density is exceeded, the weld penetration depth does not increase significantly. They attributed this phenomenon to the shielding effect of the plasma. The theory provided guidance in choosing proper laser intensities to achieve deep penetration welds effectively. Another important absorption mechanism during keyhole mode welding is multiple Fresnel absorption due to reflections of the beam inside the keyhole [60-62]. Kar et al. [60] studied the effects of multiple reflections inside the keyhole wall. It was found that multiple reflections led to the formation of deeper and more cylindrical cavities than when multiple reflections were absent. Beck et al. [61] and Kaplan [62] considered both absorption by plasma and by the Fresnel mechanism due to multiple reflections. Kaplan [62] found that Fresnel absorption was much higher than plasma absorption during laser welding of iron with laser powers of 4 kW and 10 kW. It was shown [62]

that the number of multiple reflections was a function of the mean keyhole wall angle. With decreasing penetration depth the keyhole opening angle increased, reducing the average number of multiple reflections and the overall energy absorption.

Many of the existing models assumed a rotational keyhole symmetry and therefore, are restricted to low welding speeds. Kaplan [62] developed a model to calculate the keyhole profile at high welding speeds, using a point-by-point determination of the energy balance at the keyhole wall. A formula for heat conduction was derived considering a moving line heat source. It was assumed that the laser power absorbed by the keyhole wall balanced the heat loss by conduction into the metal. The different heat conduction conditions at the front wall and at the back wall resulted in an asymmetric profile. The calculated weld pool depth agreed well with the experimental data.

All the above models assumed a keyhole wall temperature to be equal to the boiling point of the alloy. However, the force balance on the keyhole wall requires that the temperature of the keyhole wall to be higher than the boiling point of the metal [63,64]. Kroos et al. [63] developed a model in which non-equilibrium evaporation from the keyhole surface, surface tension, hydrostatic and hydrodynamic pressures in the melt as well as heat conduction into the workpiece were considered. The temperature at the keyhole wall and the radius of the keyhole were adjustable parameters in the model. It was found that the temperature at the keyhole wall exceeded the boiling point by approximately 100 K and the keyhole radius was at least 1.7 times the laser radius.

All the models discussed so far assumed the existence of a stable keyhole geometry. However, experimental observations [65,66] showed the keyhole to be highly unstable during welding. The instability of the keyhole was directly related to the formation of weld defects such as spiking and porosity [66]. Some models [67-69] have been developed to study the dynamic behavior of the keyhole. Kroos et al. [67] showed that the characteristic collapse time of the keyhole due to sudden laser shutdown is governed by



the time constant  $(r_0^3 \rho / \gamma)^{1/2}$ , where  $r_0$  is the initial keyhole radius,  $\rho$  is the density of the melt, and  $\gamma$  is the surface tension. These results are very important for pulsed laser welding. Klein et al. [68] studied the free oscillations of the keyhole in penetration laser welding. They showed that a keyhole could oscillate in radial, axial, and azimuthal directions. Instabilities could occur for oscillations with finite amplitudes. Such instabilities could cause weld defects such as spiking or ripple formation. If the absorbed laser power exceeded a threshold value, the oscillations were stable at infinitesimally small amplitudes and the keyhole was more stable under such conditions.

Matsunawa and Semak [69] developed a model for keyhole propagation during high-speed laser welding. A numerical code for the simulation of the front keyhole wall behavior was developed assuming that only the front part of the keyhole wall was exposed to the laser beam; and the recoil pressure exceeded surface tension. The propagation of the keyhole wall inside the sample was assumed to take place by melt expulsion similar to that in laser drilling. The calculations showed that, depending on the processing conditions, the keyhole wall velocity component parallel to the translation velocity vector could be different from the beam translation speed. When this velocity component was higher than the beam translation speed, the formation of the humps on the keyhole wall was observed numerically. They found that the calculated velocity of the melt ejected from the front part of the keyhole into the weld pool could exceed 100 cm/s at high laser powers.

Reliable models must take into account all the important physical phenomena to be able to explain important features of the process. Because of the complexities of the physical processes during keyhole mode laser welding, development of a unified, comprehensive, mathematical model of temperature and velocity fields in the weld pool is a major task. Efforts are currently underway in several research groups to develop realistic models of keyhole behavior.

## 2.3 Vaporization at the Weld Pool Surface

Pronounced vaporization of alloying elements takes place in both keyhole mode and conduction mode of welding [37,70,71]. Since volatile alloying elements such as lithium, magnesium, and zinc, have much higher equilibrium vapor pressure than aluminum, they are selectively vaporized during laser welding of aluminum alloys. The 5xxx series alloys usually contain 0.8 to 5.5% of magnesium and are primarily strengthened by solid solution of magnesium in the aluminum matrix. Magnesium is also an important constituent of the strengthening precipitates in some precipitation-strengthened automotive aluminum alloys. The 6xxx series alloys are primarily precipitation-strengthened by  $\beta'$  ( $\text{Mg}_2\text{Si}$ ) phase. Many 2xxx series alloys containing magnesium are strengthened by the formation of  $\text{CuMgAl}_2$  precipitate. The correlation [72] between the tensile yield, elongation, and magnesium content for some 5xxx series alloys is given in Fig. 2.10. It is observed that the tensile strengths of these alloys increase linearly with magnesium content. Due to its high vapor pressure and low boiling point, magnesium can be easily vaporized during laser welding, leading to reduction in the tensile strength of the weldments.

Moon and Metzbower [73] found depletion of magnesium in the fusion zone of laser beam welded 5456 aluminum alloy. In their experiment, a reduction of Mg content from 5% in the base metal to 4% in the fusion zone was observed. This 20% reduction in the magnesium concentration was considered to be the main reason for the reduced tensile strength of the weldment. Therefore, a reduction in the vaporization rates of alloying elements during laser welding of aluminum alloys would be desirable.

### 2.3.1 Factors Affecting Vaporization

#### 2.3.1.1 Temperature and Composition

A simple model to calculate the vaporization rate of a pure metal in vacuum is given by Langmuir equation:

$$J = P_0 / \sqrt{2\pi MRT} \quad (2.8)$$

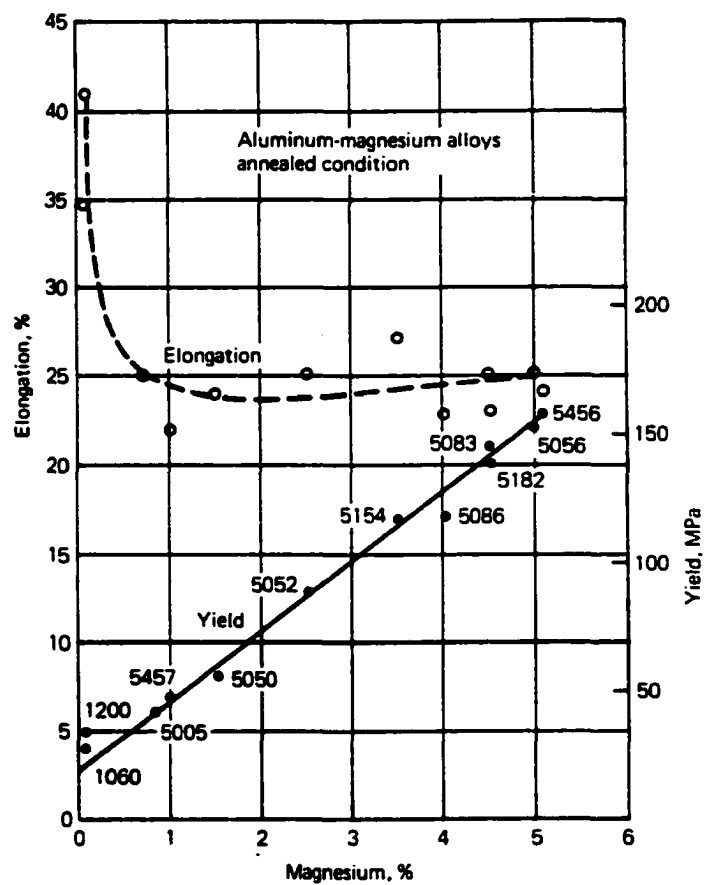


Fig. 2.10 Correlation between tensile yield, elongation, and magnesium content for some commercial alloys [72].

where  $J$  is the vaporization flux,  $P_0$  is the equilibrium vapor pressure of the vaporizing species over the liquid,  $M$  is the molecular weight of the vaporizing species,  $R$  is the gas constant, and  $T$  is the temperature. This equation shows that the vaporization rate is proportional to the equilibrium vapor pressure of the vaporizing element. For an alloy, the vaporization rate of each alloying element can be calculated separately. The overall vaporization rate of the alloy is the sum of the vaporization rates of all alloying elements.

Temperature is the most important factor in determining the vaporization rate because the vapor pressure of a metal is a strong function of temperature. The experimental data [74] for equilibrium vapor pressures of various elements as a function of temperature are given in Fig. 2.11. It is observed from this figure that at a temperature of 1000 K, magnesium has a vapor pressure of 0.002 atm. However, the vapor pressure of magnesium increases by about three orders of magnitude to 2.5 atm when the temperature is increased to 1500 K. Consequently, the vaporization rate of magnesium, calculated from Langmuir equation, increases by three orders of magnitude in this temperature range.

The overall vaporization rate of aluminum alloys is significantly increased when volatile alloying elements are present. It is observed from Fig. 2.11 that many important alloying elements in aluminum alloys such as magnesium in 5xxx and 6xxx series alloys and zinc in 7xxx series alloys have much higher vapor pressures than that of aluminum. For example, at a temperature of 1500 K, the vapor pressures of pure magnesium, zinc, and aluminum are 2.5, 10, and  $2 \times 10^{-5}$  atm respectively. Therefore, even very small additions of magnesium or zinc will significantly increase the overall vaporization rate of elements from the weld pool.

Block-Bolten and Eagar [75] studied vaporization of alloying elements during GTA welding of aluminum alloys. They classified aluminum alloys into the following four groups depending on the composition of vapors over the weld pool:

- I. Zn vapor dominates in 7xxx series alloys;
- II. Mg vapor dominates in 5xxx series alloys;

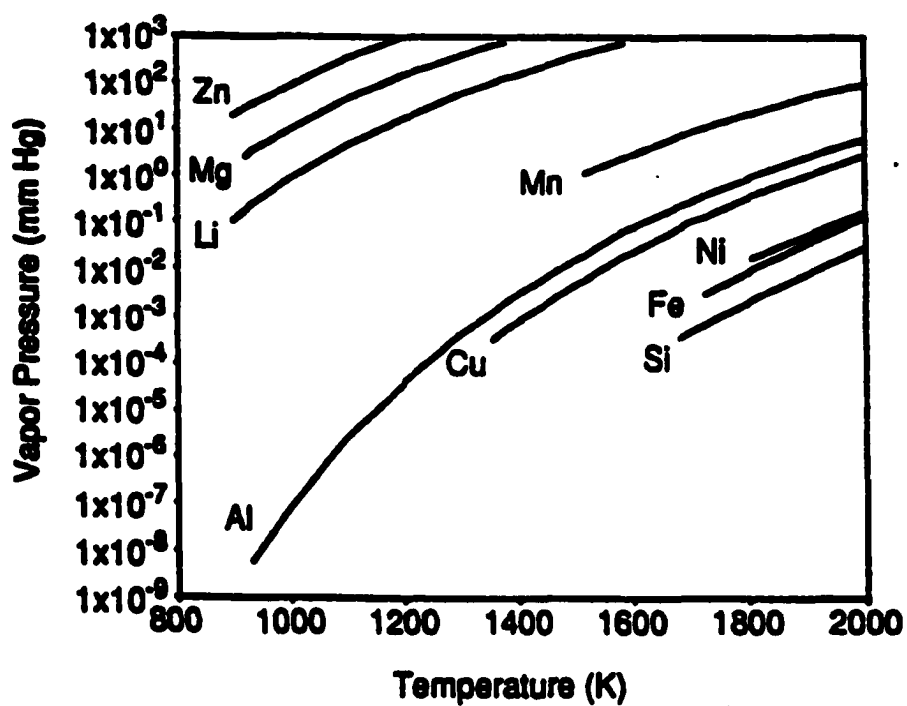


Fig. 2.11 Equilibrium vapor pressure as a function of temperature for various elements [74].

III. Nearly equivalent Zn and Mg vapor pressure exist in 2xxx and 6xxx series alloys;

IV. Al vapor dominates in 1xxx series alloys.

Block-Bolten and Eagar [75] calculated vaporization rates of the alloying elements using the Langmuir equation. The calculations correctly predicted the dominant metal vapors on weld pools. However, the Langmuir equation over estimates the vaporization rate at one atmosphere pressure because the equation was derived for vaporization in vacuum where recondensation of the vaporized elements is insignificant. Welding operations are usually carried out in one atmosphere pressure where significant amounts of the vaporized elements are recondensed on the workpiece. The recondensation rate must be taken into account in order to obtain realistic predictions of the vaporization rate. Furthermore, the vapor pressure of aluminum alloys is a strong function of temperature. Therefore, it is essential to estimate weld pool surface temperature accurately, especially its value near the beam axis where the vaporization rate is the highest.

### **2.3.1.2 Role of Plasma**

The presence of a plasma may have a significant effect on the vaporization rate of the weld metal. Collur et al. [76] and Sahoo et al. [77] studied the effect of plasma on vaporization rates of iron and copper from isothermal vaporization experiments. The experiments [76,77] revealed that the presence of a plasma reduced the vaporization rate by about 10% to 50% for iron and about 60% to 80% for copper. The reduction in the vaporization rates was considered to be consistent with the enhanced condensation of metal vapor due to a space charge effect [77]. In view of the high mobility of the electrons among the various species in the plasma, the surface of the metal becomes negatively charged since the electrons strike the metal surface at a faster rate than the ions. The attraction between the positively charged ions and the negatively charged surface leads to high condensation rates and consequently, low vaporization rates in the presence of the plasma [77]. Experimental data on the effect of plasma on vaporization of aluminum are not available.

### **2.3.1.3 Role of Surface Active Elements**

Surface active elements play a mixed role in vaporization. It is possible that these elements block a portion of the liquid metal surface and reduce the vaporization rate [76]. However, Sahoo et al. [77] found that the presence of surface active elements such as oxygen and sulfur in iron and copper resulted in increased vaporization rates of the metals in their isothermal vaporization experiments. Sahoo et al. [77] proposed that one of the possible opposing effects could be the effect of interfacial turbulence [78] caused by the movements of surface active elements from inside to the surface of the liquid. The local movements of the interface increase surface area and therefore, increase the rate of vaporization.

In aluminum alloys, additions of elements such as Li, Bi, Pb, Mg, Sb, Ca, and Sn, reduce the surface tension of aluminum [46] as shown in Fig. 2.9. Therefore, these elements are surface active in aluminum melts. The effects of these elements on vaporization rate during laser welding of aluminum alloys have not yet been explored.

### **2.3.2 Mechanism of Vaporization**

Collur et al. [76] studied the mechanism of alloying element vaporization during conduction mode laser welding. They subdivided the vaporization process into three steps. The first step involves transport of the alloying elements from the bulk to the surface of the liquid weld pool. Second, vaporization of the elements takes place at the liquid-vapor interface and finally, the transport of the vaporized species into the bulk of surrounding gas phase. It was found that the intrinsic vaporization of alloying elements at the weld pool surface controlled the overall vaporization rates.

During laser welding, the vigorous circulation of the molten metal driven by the surface tension force greatly enhances the transport of alloying elements in the weld pool. Calculations showed that the weld pool surface could be renewed about 200 times in the time period required for the laser beam to scan a distance equal to the weld pool width [76] during laser welding of pure iron. Since the maximum flow velocity in the weld pool

is generally higher during laser welding of aluminum alloys than that of iron [32], the surface renewal can be assumed to be faster in the aluminum weld pool. In studying alloying element loss during laser welding of 5754 aluminum alloy, Pastor et al. [37,79] measured the concentration profiles of magnesium along the width and depth of the transverse section of the weld pool. They found that the loss of magnesium was quite pronounced in the fusion zone. There was no concentration variation within the weld pool in macro-scale, indicating a vigorous convective mixing in the molten weld metal during welding. Therefore, the transport of alloying elements in the liquid phase does not inhibit the vaporization. Once an alloying element is transported to the weld pool surface, its vaporization rate is determined by several variables. These include the surface temperature distribution, local concentrations of the alloying elements, the extent of surface coverage by surface-active elements, and other factors such as surface agitation and the modification of the nature of the interface due to the presence of a plasma in the vicinity of the weld pool. The rate of vaporization at the surface controls the overall loss of elements [76]. After the elements are vaporized, their transport from the weld pool surface to the bulk of the gas phase does not slow down the overall vaporization process [76].

The formation of a keyhole during laser welding greatly affects the vaporization rate and composition change in the weld metal. As the welding changes from conduction mode to keyhole mode, both the volume of the molten weld pool and the vaporization rate increase [37,70,71]. However, the increase in the volume of the molten weld pool was more pronounced than the increase in vaporization rate. Therefore, the vaporized elements were drawn from a much larger volume of weld pool, resulting in less pronounced composition change in the weld pool during keyhole mode of welding [37,71].

Miyamoto and Maruo [70] found that the aspect ratio of the keyhole significantly affected the vaporization rate during laser welding. The venting of vapor was more difficult and the condensation rate was higher in a slim and long keyhole than in a thick and short keyhole. Therefore, the former resulted in lower vaporization rate. They claimed that the evaporation flux in conduction mode of welding was roughly equal to that in the



keyhole mode. Although the recoil force was not measured, they indicated that the recoil force in conduction mode welding was at least as high as that of keyhole welding. More work is needed to understand vaporization of elements during keyhole mode welding.

### **2.3.3 Calculation of Vaporization Rate and Composition Change**

The Langmuir equation can be used to calculate vaporization rates at very low pressures, where condensation of the vapor is negligible. Experimental data [76,77] show that at atmospheric pressure, the vaporization rate under most fusion welding conditions is five to ten times lower than the rate predicted by the Langmuir equation. Nevertheless, the equation is useful in calculating the relative vaporization rates of alloying elements.

DebRoy and co-workers [80-82] developed a comprehensive mathematical model to understand the vaporization of pure metals and the loss of alloying elements from stainless steel weld pools. The calculations involved numerical solution of the equations of conservation of mass, momentum, and translational kinetic energy of the vapor near the weld pool surface. The fluid flow and heat transfer within the molten pool were simulated by the solution of the Navier-Stokes equations, and the equation of conservation of energy was used to determine the temperature distribution at the weld pool surface. Heat transfer to the shielding gas and heat loss due to vaporization of the alloying elements were taken into account in the calculations. The computed weld pool temperature distribution was used for the vaporization rate calculations.

A key feature of the calculations is the consideration of the pressure-gradient-driven mass transfer. In laser processing of metals and alloys, the peak temperature at the surface often exceeds the boiling point of the irradiated material. Chan and Mazumder [83] have reported computed temperatures greater than the boiling points during laser irradiation of aluminum, titanium and a superalloy. At temperatures higher than the boiling point, the vapor pressure in the vicinity of the weld pool is greater than the ambient pressure. This excess pressure provides a driving force for the vapor to move away from the surface. To include this effect, the velocity distribution functions of the vapor molecules

escaping from the weld pool surface at various locations were used in the equations of conservation of mass, momentum, and translational kinetic energy in the gas phase to determine the rates of vaporization from and the rates of condensation on the weld pool surface [80-83]. In addition, mass transfer rates due to concentration gradients can be determined using correlation between various dimensionless numbers. The calculated vaporization rates were in good agreement with the experimentally determined values.

The main lesson to be learned from such agreement is not merely that the predicted vaporization rates are more accurate than the values obtained from Langmuir equation. In many instances, when an engineer is in search of a theory, simple models such as the Langmuir equation can be attractive. The approach adapted in the calculations [80-83] was just the opposite; higher accuracy in the calculated vaporization rate was achieved by including a more realistic and detailed description of the physical process in welding. However, more work is needed in modeling of vaporization during laser welding, especially, keyhole mode of welding, which is more attractive than conduction mode of welding for automotive industry.

## **2.4 Weldment Structure and Properties**

### **2.4.1 Microstructural Features**

Laser welded joints are characterized by narrow heat affected zones and fine-grained weld zone microstructures. These features result from low heat input and high cooling rates experienced in laser welds which are typically made at high travel speeds. The weld zone in fusion welded aluminum is defined [84] as consisting of the fusion zone, the partially melted zone, and the heat affected zone. While the partially melted zone and the heat affected zone are generally narrower and less distinct than those in processes such as GTAW with higher heat input [84], the above definition is used in this review to describe the findings of microstructural characterization studies in laser beam welding of automotive aluminum alloys. The automotive aluminum alloys for which published information is available on microstructures of laser welds include: 5083, 5086,

5251, 5456, 5754, 6013, 6061, 6063, 6082, and 6111 [73,84-93]. The effects of both CO<sub>2</sub> and Nd:YAG laser welding have been investigated.

#### **2.4.1.1 Fusion Zone**

The fusion zone of both 5xxx and 6xxx series laser welded alloys consists primarily of fine columnar-dendrites originating from the fusion line and equiaxed grains existing in the center of the fusion zone [84-90]. Fig. 2.12 shows the typical microstructures in the fusion zone of laser welded 5754-O alloy [88]. Weld defects such as solidification cracking and porosity may occur in the fusion zone. Modification of the weld metal composition through use of filler metal and proper selection of welding parameters are essential to avoid cracking and porosity.

##### **A. Laser welded 5xxx alloys**

In one of the earlier studies of the laser welding of aluminum alloys, Moon and Metzbower [73] investigated laser welding of 1/2 inch thick 5456 alloy. Although material of this thickness is of little interest in automotive applications, their observations about microstructure are consistent with work by others on thinner sections. A fine grained structure in the fusion zone was observed. In addition, depletion of magnesium and removal of precipitates such as Mg<sub>2</sub>Si and (Fe,Mn)Al<sub>6</sub>, were noted. While the depletion of magnesium is harmful to the mechanical properties of the welds, the refined structure after the removal of the precipitates was considered [73] to contribute to the increased toughness of the welds. In an investigation of laser welding of aluminum alloys for automotive application, Ramasamy and Albright [88] compared welding of 1.6 mm thick 5754-O alloy with CO<sub>2</sub> and Nd:YAG lasers using power of 5 and 3 kW respectively. They found the weld metal microstructure in both cases to be fine cellular-dendritic, with equiaxed grains in the middle of the weld. The volume of equiaxed grains increased with increasing travel speed. Venkat et al. [89] investigated CO<sub>2</sub> laser welding of 1.6 mm thick 5754-O alloy using a power of 3 kW and travel speeds of up to 400 IPM. A fine cellular-dendritic structure was commonly observed in the fusion zone. Only

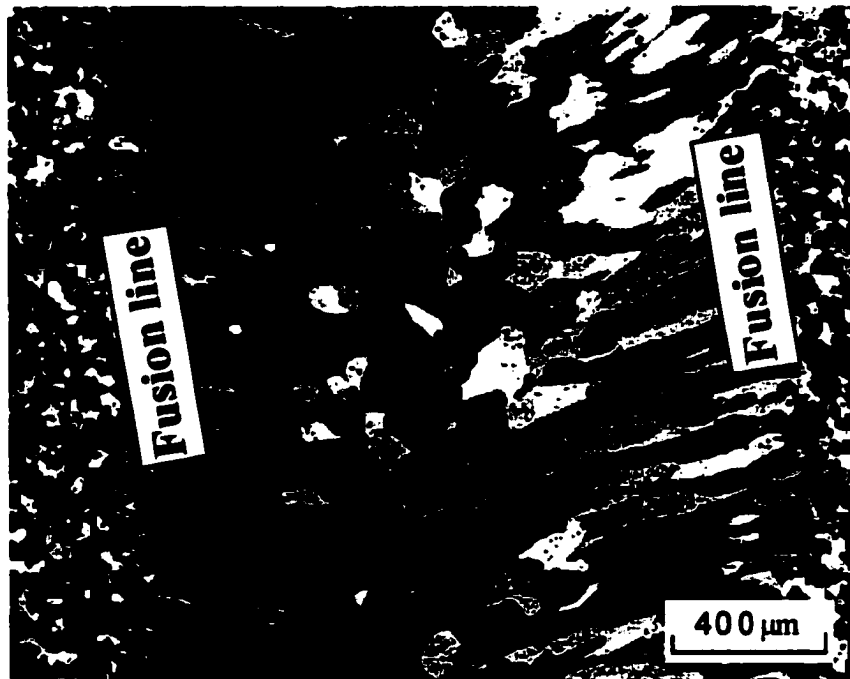


**Fig. 2.12 Typical microstructure of laser weld in aluminum alloys 5754-O using a 3 kW CW Nd:YAG laser at welding speed of 200 ipm [88].**

occasionally were the equiaxed grains observed near the weld centerline at high welding speeds.

Solidification cracking was not reported in continuous wave laser welding of 5xxx series alloys [73,85,88-91]. However, Cieslak and Fuerschbach [91] observed solidification cracking during pulsed Nd:YAG laser welding of 5456 alloy and suggested that the rapidly developing thermal strains due to the high cooling rates were responsible for the cracking.

#### **B. Laser welded 6xxx alloys**

Laser welded 6xxx series alloys [84-87,89,90,93] demonstrated fine cellular-dendrite structures that originated from the fusion line and extended to the center of the fusion zone. For these alloys equiaxed grains were consistently observed by various investigators [84-87,89,90,93] under diverse welding conditions. Both CO<sub>2</sub> and Nd:YAG lasers were used to weld plates of thickness in the range of 1 to 10 mm, with laser power from 2 to 7 kW and welding speed between 8 to 168 mm/s. Fig. 2.13 is an example of equiaxed grain structure along the center of fusion zone of laser welded 6061 alloy [93].

Solidification cracking has been observed [86,87,89] during autogenous laser welding of 6xxx alloys. Fig. 2.14 shows solidification cracking in the fusion zone of laser welded 6111-T4 alloy [87]. The cracking was more pronounced at high welding speeds due to the high cooling rates [86,87]. The mechanism and control of solidification cracking will be discussed in a later section.

#### **2.4.1.2 Partially Melted Zone**

The partially melted zone has temperatures between the liquidus and eutectic temperature of the alloy. Therefore, the low-melting-point eutectic phases which commonly exist at the grain boundaries of the recrystallized grains remelt during laser welding. Liquation cracking may occur along these weakened grain boundaries. The partially melted zone in laser welded aluminum alloys is generally narrow and is only one or two

grains wide [84,87,89]. Guiterrez et al. [84] observed that even when the grain size of the base metal was very large and high laser power was used in welding of 6013 aluminum alloy extrusions, only a small amount of liquid was formed near the fusion line as shown in Fig. 2.15. Therefore, liquation cracking is not a major concern in the laser welding of automotive aluminum alloys.

#### **2.4.1.3 Heat Affected Zone**

The heat affected zone has a maximum temperature below the eutectic temperature of the alloy and no melting occurs in this region. However, many solid phase reactions such as grain growth and precipitate coarsening occur in this region and affect the weldment properties. For welding of automotive aluminum alloys, softening is a prime concern in the heat affected zone. Softening occurs due to grain growth or loss of strain-hardened structure for non heat treatable aluminum alloys such as the 5xxx series [73]. For heat treatable aluminum alloys such as 6xxx series alloys, the dissolution of the strengthening  $\beta''$  phase (semi-coherent rods of  $Mg_2Si$ ) and formation and growth of non-strengthening  $\beta'$  precipitates (semi-coherent needles of  $Mg_2Si$ ) cause softening in the heat affected zone [84]. The high power density and high speed in laser welding cause steep temperature gradient and high cooling rate in the weld metal. Consequently, the heat affected zones in laser welds are narrower than in other fusion welding processes with lower power densities such as GTAW and GMAW [84]. Therefore, the softened region in laser welded aluminum alloys is smaller than those of the GTA or GMA welds.

#### **2.4.1.4 Role of Filler Metals**

Many automotive aluminum alloys such as 6xxx series alloys, are susceptible to solidification cracking. The cracking susceptibility is directly related to the compositions of the alloys. The use of filler materials can modify the composition of the fusion zone so that the compositions that are susceptible to solidification cracking can be avoided in the welding of these alloys. An appropriate filler metal may also compensate for the loss of volatile alloying elements.

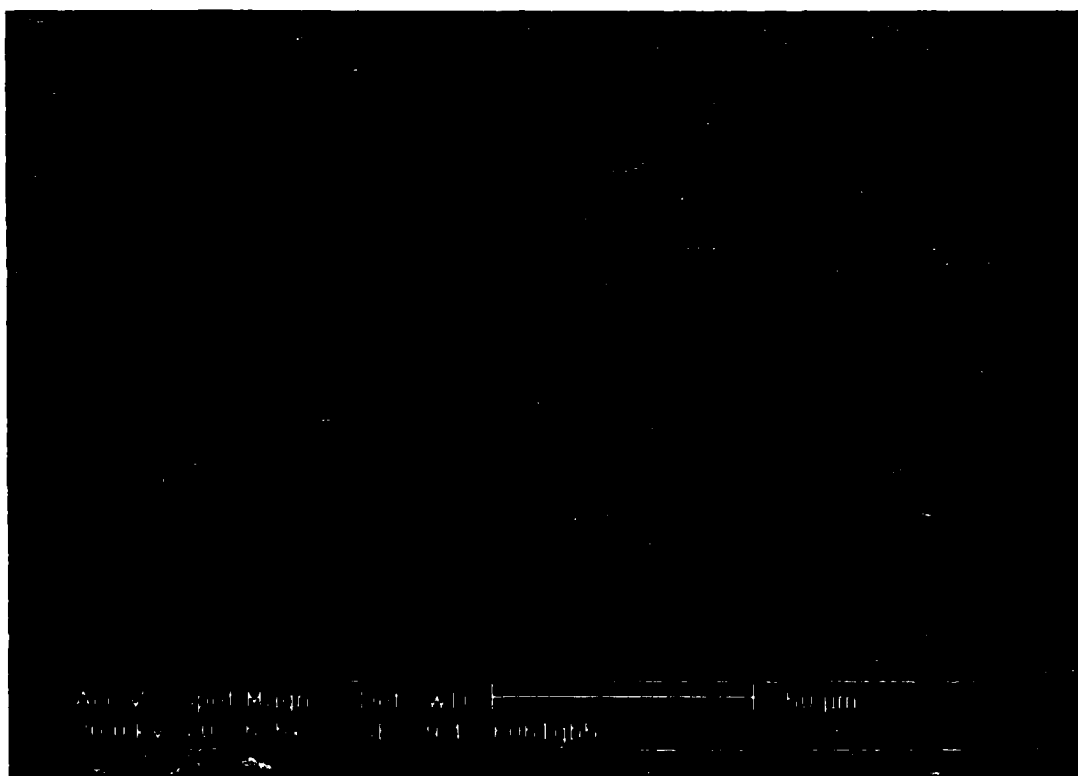


**Fig. 2.13 Microstructure showing equiaxed grain structure along the weld center of 6061 laser weld [93].**

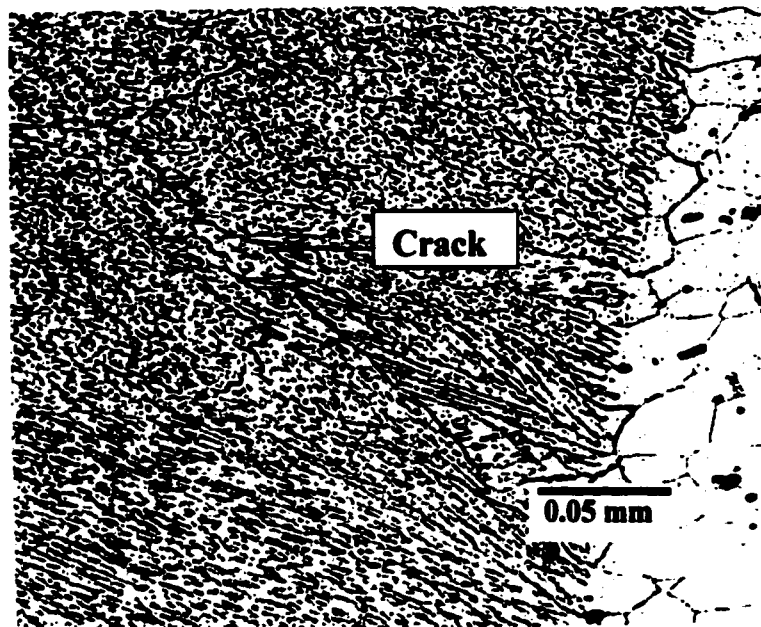


**Fig. 2.14 Solidification cracking along the cellular dendritic grain boundary of 6111-T4 aluminum alloy welded using a 3 kW CO<sub>2</sub> laser at a speed of 400 ipm [87].**



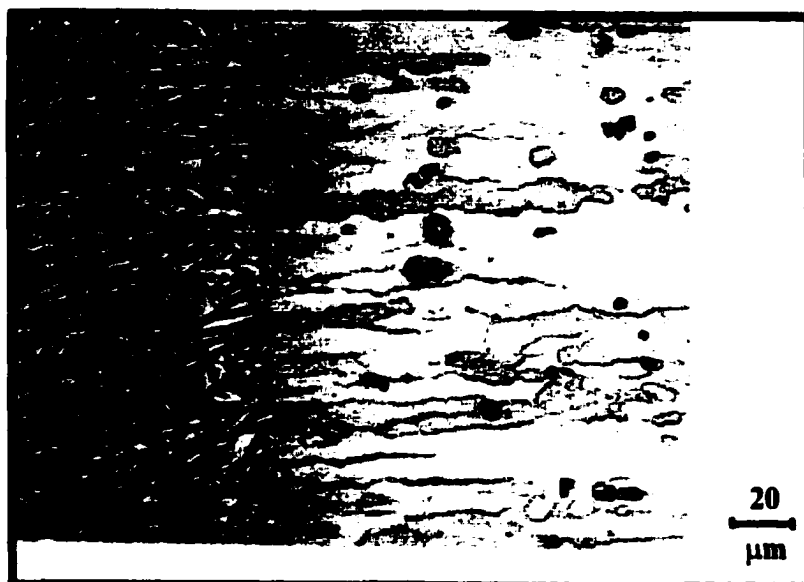


**Fig. 2.15** Photomicrograph showing evidence of liquation at the grain boundaries during welding of 6013-T6 aluminum alloy using a 7 kW CO<sub>2</sub> laser at 100 mm/s travel speed [84].

Kutsuna et al. [90] studied the addition of 4043-WY and 4047-WY filler wires during CO<sub>2</sub> laser welding of 4 mm thick 6063 plates at a power of 4 kW and speed of 3 m/min. Similar to autogenous welds, the microstructure of the weld zone was mainly cellular-dendrite with a small number of equiaxed grains at the top of the fusion zone center line. The use of 4043 filler metal at a feed rate of 50 mm/min was found to reduce the degree of solidification cracking, but microcracks were still observed at the bottom of the weld. Using electron probe microanalysis (EPMA), the concentration of silicon in the welds was found to be inhomogeneous in macro scale and it decreased from about 2% at the top of the welds to about 1% at the bottom. The inhomogeneity of the silicon distribution was attributed to the rapid solidification which prevented sufficient mixing of the filler metal and the base metal at the bottom of the weld pool [90]. Increasing the wire feed rate to 100 mm/min and using 4047 filler metal containing higher silicon content resulted in a silicon concentration of 3% at the bottom of the welds and prevented crack formation. Therefore, maintaining the concentration of silicon in 6xxx series alloys above a certain critical level is essential to avoid solidification cracking. The relationship between the solidification cracking susceptibility and the compositions of different aluminum alloys will be discussed in a later section.

Starzer et al. [94] also studied the use of filler materials in the laser welding of 6xxx series alloys. They added filler wire and powders during CO<sub>2</sub> laser welding of 4 mm thick 6060 and 6080 alloys. In their work, silicon and Al-12%Si powders with particle sizes of 40 and 150 μm, respectively were fed into the interaction zone of beam and workpiece during welding of 6060-T6 alloy. Although the powder additions were found to reduce crack susceptibility by increasing the silicon content of the fusion zone, inhomogeneous mixing at travel speeds above 0.5 m/min, high porosity, and low powder efficiency were identified as problems requiring further investigation. The effects of feeding 4043 and 4047 wires were examined during welding of 6060-T4 and 6082-T6 alloys. Filler wire additions were also found to increase weld zone silicon contents and reduce fusion zone crack susceptibility. Homogeneous mixing could be obtained at weld speeds

of up to 1.3 m/min. Starzer et al. [94] concluded that the filler wires are potentially useful for production applications.

#### **2.4.1.5 Fractography**

Fractography studies reveal information of fracture mechanisms and show the ductility of a material from the morphology of its fractured surface. Several investigators have examined the fracture surfaces of laser welded aluminum alloy tensile [84,87-89] and impact specimens [73]. Ramasamy and Albright [87] and Venkat et al. [89] observed two distinct fracture modes in different regions of the tensile specimens of CO<sub>2</sub> and Nd:YAG laser welds of 6111-T4 alloy tested in the longitudinal direction, as shown in Fig. 2.16. The base metal and the center of the fusion zone displayed a ductile type of failure, with the width of the dimple rupture zone in the center of the weld decreasing as the travel speed increased [87]. The fractured surface of the fusion zone adjacent to the fusion boundary had a different appearance, with large faceted surfaces, possibly associated with the large columnar grains of the fusion zone. However, Guitierrez et al. [84] observed ductile fracture structure in the fusion zone of laser welded 6013-T6 alloy as shown in Fig. 2.17.

The fracture surface of laser welded 5754-O alloy indicated a failure caused by dimple rupture [88] or microvoid coalescence [89] in the entire weld zone. These types of rupture are commonly observed in the ductile rupture of materials. Moon and Metzbower [73] conducted dynamic tear testing and also observed ductile fracture in laser welded alloy 5456.

Detailed microstructural studies using optical microscopy, SEM, STEM/EDS, and TEM have been done on pulsed Nd:YAG laser welded RS/PM Al-8Fe-2Mo alloy [92]. Such studies provided significant insight in the evolution of microstructure in the weld and its relation with the weld properties. However, much of the microstructural investigations on laser welded automotive aluminum alloys have been limited to optical micros-

copy and SEM fractography. More detailed microstructural analyses are needed to address the issues related to hot cracking susceptibility and joining of dissimilar alloys.

#### **2.4.2 Effect of Welding on Mechanical Properties**

Configuration of the joint such as the lap and butt joints and the presence of undercuts, humping, cracking, porosity, and other defects affect the mechanical properties of the joints. During laser welding of automotive aluminum alloys, the ultimate strength of the weld is often reduced due to poor root quality and/or undercutting [95-97]. The use of Al-4047 filler alloy was necessary for 2xxx and 6xxx series alloys to eliminate solidification cracking and undercutting [95-97]. While autogenous welding of 5xxx series alloys could be performed without producing solidification cracking, the use of Al-5554 filler alloy eliminated undercutting and increased the tensile strength and elongation of the welds [95-98]. However, the yield strength was decreased by the use of the filler material in the welding of 5xxx series alloys [95-98].

Important changes occur in different regions of the weld. The fusion zone structure is generally very different from that of the base metal. Selective vaporization of volatile constituents from the fusion zone changes the composition of the alloy and may degrade the mechanical properties of the weld metal [73,92,99]. In the partially melted zone and heat affected zone, the thermal cycles affect the original structure and mechanical properties of the alloy. Particularly, over-aging of heat treatable alloys causes loss of precipitation hardening and annealing of non heat treatable alloys causes loss of work hardening. While the loss of strengthening in non heat treatable alloys is irreversible, post weld aging of the 6xxx alloys slightly increased the tensile strength of the joints and significantly reduced elongation [95-97].

#### **2.4.3 Mechanical Characterization**

Mechanical properties of several laser welded automotive aluminum alloys have been reported in the literature [73,95-100]. These include: 2008, 2010, 5083, 5182, 5251,



**Fig. 2.16** A fractograph showing two distinct fracture modes in different regions of a tensile specimen of CO<sub>2</sub> laser welded 6111-T4 aluminum alloy tested in the longitudinal direction [89].

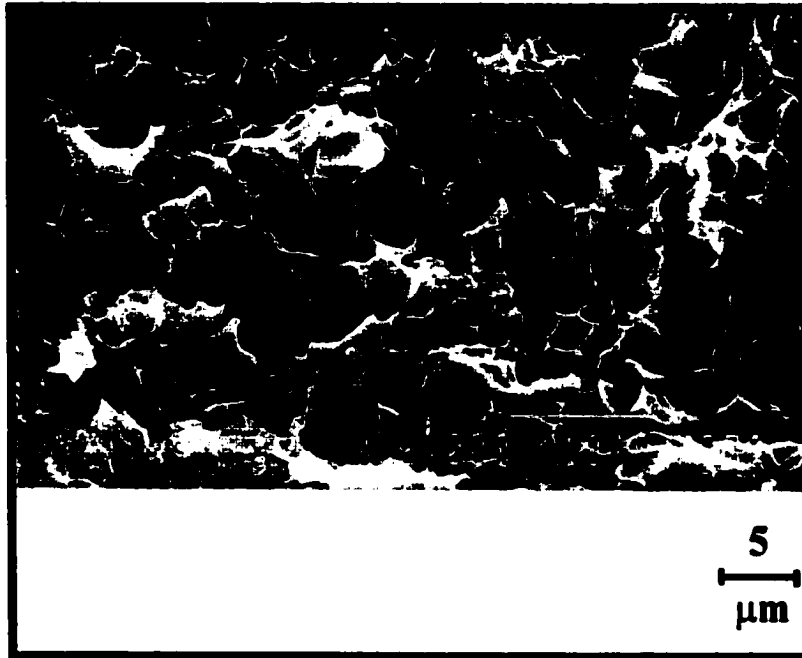


**Fig. 2.17 SEM micrograph of a fracture surface of laser welded 6013-T6 aluminum alloy tensile specimen that fractured in the fusion zone [84].**

5454, 5754, 6009, 6060, 6061, 6082, and 6111. The thickness of the material ranged from 1.0 mm to 2.5 mm. Carbon dioxide lasers with powers in the range of 4 kW to 6.8 kW [95-97,99,100] and Nd:YAG lasers with powers in the range of 2 kW to 3 kW [98-100] were used. The welding speeds varied from 0.9 m/min to 7.0 m/min, depending on the thickness of the material and the laser power. Both butt and lap welds were evaluated. In many cases, welds of the heat treatable alloys Al-2xxx and Al-6xxx were produced with Al-4047 filler alloy additions to avoid cracking [95-97]. Welds of Al-5xxx alloys were produced both autogenously [95-100] and with Al-5554 filler alloy additions [95-97,100] to compensate for magnesium loss during welding. The mechanical property tests carried out included tensile tests [95-100], guided bend tests [95-97], limiting dome height tests [95-99], and dynamic tear tests [73] for butt welds; tensile tests, tension shear tests and peel tests for lap welds [95-97]; and axial fatigue tests for both butt and lap welds [95-97]. The results are discussed in the following sections.

#### **2.4.3.1 Tensile Properties**

Tensile tests for autogenous butt welding of 5xxx series alloys failed in the fusion zone [95-99]. The tensile strengths of the welds were about 90% of those in the base metals [98,99] with higher strength being associated with higher magnesium content [99]. Butt welding of 5xxx series alloys with 5554 filler alloy additions [95-97] eliminated undercutting in the welds and increased the tensile strength and elongation of the welds. In some cases, failure occurred in the base metal.

For autogenous butt welding of 6xxx series alloys [99], tensile specimens failed in the heat affected zone. The tensile strengths of the welds were about 60% of those in the base metals. Addition of 4047 filler alloy during butt welding of 6xxx and 2xxx series alloys produced welds with strengths comparable to the lowest values in the range of the base metal strength values [95-97]. Post weld aging treatment on these welds significantly increased the hardness of the heat affected zone due to the recovery of the GP zone. However, the hardness of the fusion zone did not change significantly. The compo-

sition of this region was very different from that of the base metal due to the addition of the filler alloy. As a result, a moderate increase in tensile strength and a significant reduction in elongation were observed when the welds were examined in post weld aged conditions [95-97]. Lap joints generally resulted in lower joint efficiencies than butt joints [99]. The tensile strengths of the lap joints were in the range of 34% to 70% of the base metal values.

#### **2.4.3.2 Formability and Fracture Toughness**

Limiting dome height (or bulge height) tests showed that laser welding decreased the formability of all alloys [95-99] due to stress concentrations arising from the inhomogeneous strength across the weld [95-97] or the imperfect fusion zone geometry [98]. For laser welds with filler alloy additions [95-97], the 5xxx series alloys had a higher ratio of average dome height of welds to that of the base metal than the 2xxx or 6xxx series alloys. The laser welded 5754-O alloy with 5554 filler alloy additions exhibited formability of about 90% of the base metal. Fractures during limiting dome height tests in the 2xxx and 6xxx series alloys were initiated within the fusion zone where the hardness was the lowest. In contrast, the 5xxx series alloys developed slightly higher strength in the fusion zone than in the heat affected zone. The gradual change in strength of the 5xxx series alloys, indicated from the hardness profiles across the welds, resulted in more uniform straining and better formability. For autogenous laser welds [98,99], a formability of 70% of the base metal value was obtained in autogenous laser welded 5754-O alloy [98]. Bulge heights of 25 to 30 mm and 10 to 15 mm were achieved in the 5xxx and 6xxx series alloys, respectively [99].

Dynamic tear tests [73] in autogenous welds of 5456 alloy showed that the toughness was greater for the weld bead than for the base metal and fracture took place by microvoid coalescence. The increased toughness of the weld bead was considered to be due to the reduction of precipitates such as  $Mg_2Si$  and  $(Fe,Mn)Al_6$ , during laser welding [73].



### **2.4.3.3 Other Properties**

Other important mechanical properties of laser welded automotive alloys include fatigue strength and peel strength. Joint configuration and fusion zone geometry greatly affect the weld fatigue strength. Butt welds are found to have better fatigue performance than lap welds owing to higher stress concentration in the lap welds [95-97]. In a production application, however, consideration would have to be given to the greater difficulties involved in achieving uniformly high quality in butt welds, and the possible effects on the uniformity of mechanical properties in a large number of joints. Peel tests were used to determine the strength of lap welds under peel conditions. The non-heat treatable 5xxx series alloys exhibited nearly 2.5 times higher peel strength than the heat treatable materials [95]. The large difference in peel strength among heat treatable and non-heat treatable alloys is not well understood [95]. Since peel strength is a key parameter used by the automotive industry, this issue should be investigated further.

Rapp et al. [100] showed that the static strength of laser welded aluminum alloy butt joints was higher than that of similar joints welded using GTAW or GMAW. The higher strength was attributed to the relatively low heat input of the laser welding. They demonstrated the feasibility of producing tailored blanks with different sheet thickness and dissimilar automotive aluminum alloys using laser butt welding. The static strength of butt welded sheets of different materials (6009-T4 to 5182-O) showed values at least as good as the weaker of the two materials. Furthermore, the dynamic strengths of the dissimilar alloy tailored blanks in welded condition were also similar to the values for sheets welded with the same materials [100]. Therefore, expanded use of lasers for the welding of automotive aluminum alloys appears promising in this application.

## **2.5 Hot Cracking**

The restrained contraction of a weld during cooling sets up tensile stresses in the joint and may cause cracking, one of the most serious weld defects. There are two kinds of hot cracking: Cracking that occurs in the weld fusion zone during solidification of the weld metal is known as the solidification cracking, while cracking that takes place in the

partially melted zone due to liquation of low-melting point components is known as liquation cracking. Aluminum alloys may be susceptible to both solidification cracking and liquation cracking during fusion welding. In laser welding of aluminum alloys, solidification cracking has been reported [91,101-103], while liquation cracking was rarely observed [85] due to the low heat input and small heat affected zone of the laser welds. Therefore, the following discussion focuses on the mechanism of solidification cracking, susceptibility of various alloys to cracking, and the available remedies.

### **2.5.1 Mechanism of Solidification Cracking**

Certain special features are commonly observed when solidification cracking occurs: (1) Fractured surface is always dendritic in nature. (2) Fracture usually occurs at the grain boundaries. (3) Crack tip is dull. (4) Fractured surface is usually covered with oxides if the crack reaches the specimen surface where it can be exposed to oxygen, otherwise it has a silvery color characteristic of unoxidized metal.

Most alloys pass through a brittle temperature range (BTR) during solidification as shown in Fig. 2.18 [104]. Weld solidification cracking susceptibility is related to the extent of the BTR of the alloy. Solidification cracking occurs when the thermal tensile strains induced by internal contraction and external displacement exceed the ductility of the weld metal within the BTR. Many theories have been proposed regarding the mechanism of solidification cracking [105-109]. Automotive aluminum alloys such as 2xxx (Al-Cu), 5xxx (Al-Mg), and 6xxx (Al-Mg<sub>2</sub>Si) usually form low-melting point eutectics during solidification. Solidification cracking of these alloys is mainly associated with the alloying elements rather than, as in the case of steel, with the presence of low-melting impurities. The generalized theory proposed by Borland [109] explained the solidification behavior and the crack susceptibility of alloys that form low-melting eutectics. The solidification process was divided into four stages as shown in Fig. 2.19 with the corresponding cracking susceptibility curve:

**Stage 1:** As a liquid alloy is cooled below its liquidus temperature, solid crystals nucleate and grow until at a certain temperature (coherent temperature) they join together and form a coherent mass. Although not completely solidified, the alloy first acquires

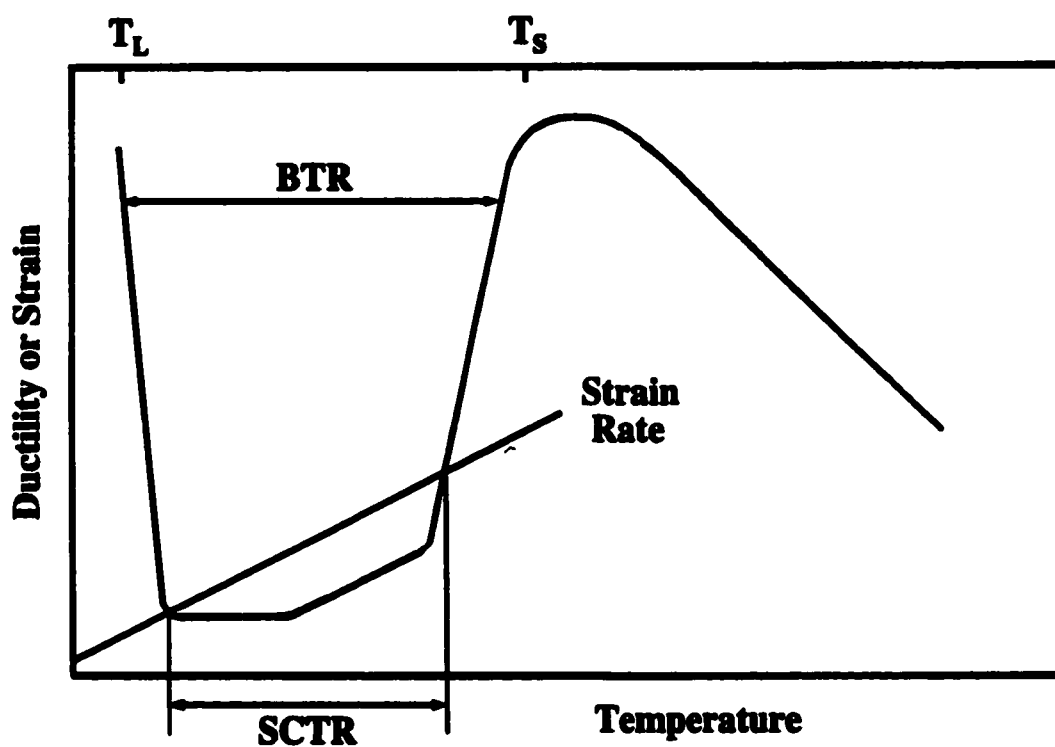


Fig. 2.18 Weld metal ductility during and following solidification [104].

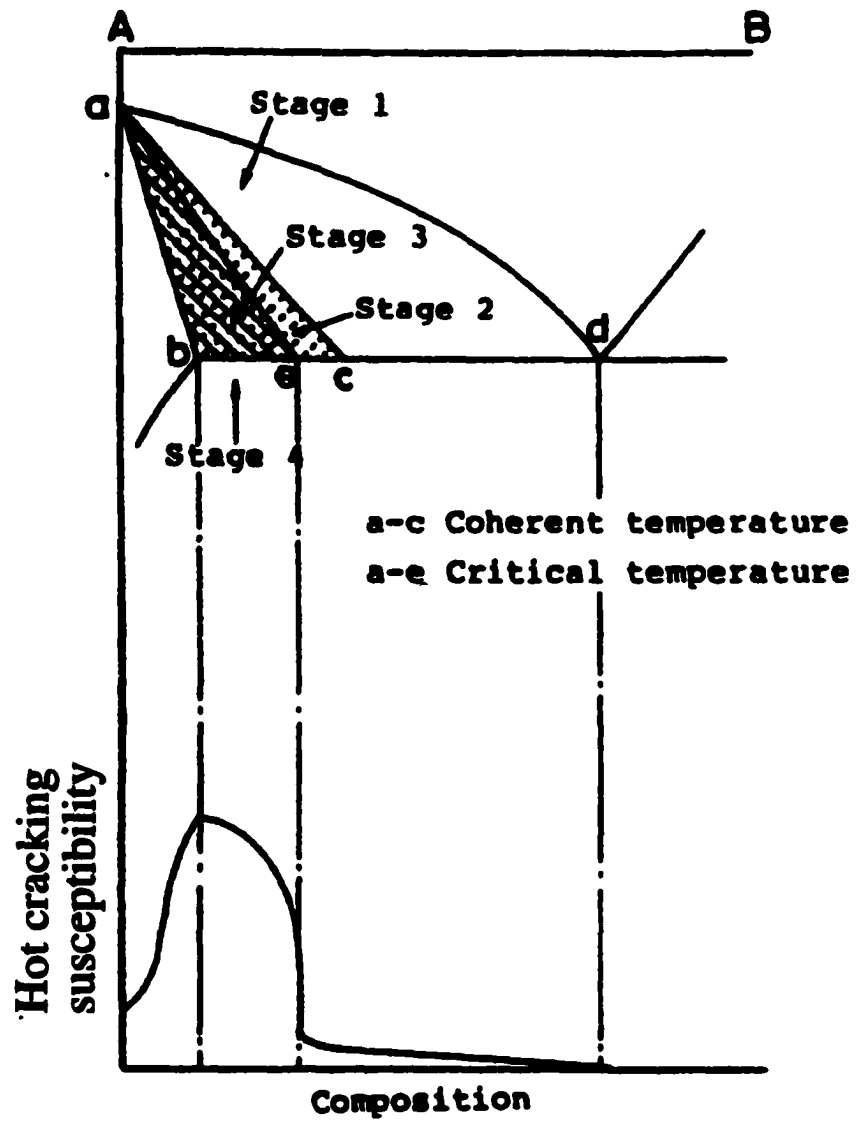


Fig. 2.19 Effect of constitutional features on cracking susceptibility in binary systems [109].

mechanical strength at this temperature. No cracking occurs at this stage due to the presence of a large quantity of residual liquid.

**Stage 2:** Interlocking of dendrites starts. The residual liquid is still capable of moving between the interlocking dendrites to refill and heal any initiated crack. Therefore, no crack is formed at this stage.

**Stage 3:** This is the so-called critical solidification range. The residual liquid is disconnected by a semi-continuous network of solid. No refilling or healing is possible once cracks are initiated due to thermal strains.

**Stage 4:** The alloy is completely solidified. No crack develops at this stage due to the high strength of the solid.

Matsuda et al. [110] reported that the temperature ranges in the above stages 1 and 2 were much narrower during welding than other slow cooling processes. Furthermore, stage 3 could be subdivided into two stages, 3(h) at higher temperature and 3(l) at lower temperature. Almost all the cracks were initiated at stage 3(h) because the residual liquid between grain boundaries was in the form of a continuous film. During stage 3(l) the joint was susceptible to crack propagation but not to crack initiation because the residual liquid was in the form of droplets.

### **2.5.2 Solidification Cracking Susceptibility**

According to the generalized theory [109], the magnitude of the critical solidification range is proportional to the difference between the nominal liquidus and solidus temperatures. An alloy has the highest solidification crack susceptibility if its critical temperature range is the widest as shown in composition b in Fig. 2.19. However, due to the highly nonequilibrium solidification during laser welding, the actual solidus temperature of the alloy is depressed, resulting in a wider critical solidification temperature range and, therefore, higher solidification crack susceptibility. Moreover, the composition which has the highest solidification crack susceptibility is shifted from b in Fig. 2.19 to a more solvent-rich composition [111]. The effect of chemical composition of weld metal

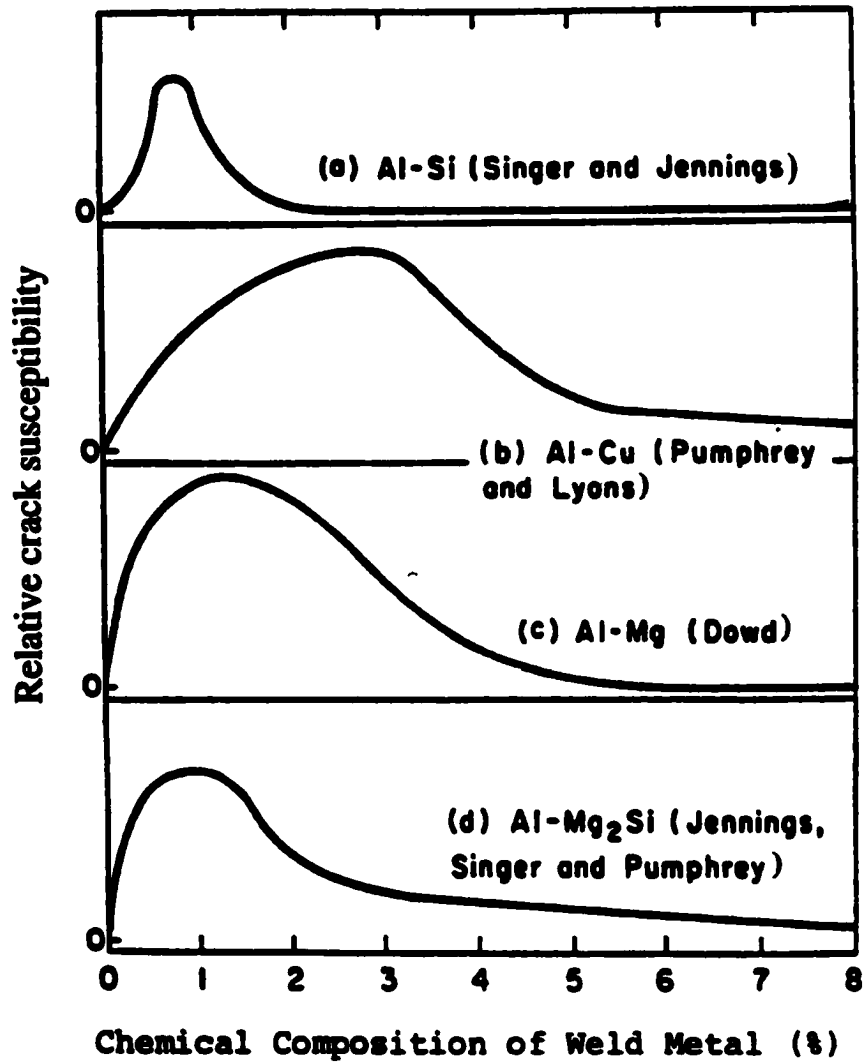


Fig. 2.20 Effect of chemical composition of weld metal on crack susceptibility in various aluminum binary alloys [111].

on crack susceptibility in various aluminum binary alloys is given [111] in Fig. 2.20. It is observed that aluminum alloys have the highest solidification crack susceptibility when the compositions are 0.6 wt.% Si in Al-Si alloys, 1-3 wt.% Cu in Al-Cu alloys, 1-1.5 wt.% Mg in Al-Mg alloys and 1.0 wt.% Mg<sub>2</sub>Si in Al-Mg-Si alloys.

The solidification cracking susceptibility of aluminum alloys is also process sensitive. It was recently reported [91,101-103] that pulsed laser welding of aluminum alloys has much higher solidification crack susceptibility than continuous laser welding. Patterson and Milewski [112] reported a similar observation comparing pulsed and continuous GTAW of alloy 625 to alloy 304L. These observations are contrary to the early views [113,114] that pulsed current welding may decrease weld cracking susceptibility due to the reduced heat input and compositional segregation.

Increased crack susceptibility during pulsed welding can be attributed to the increased cooling rate which causes a high thermal strain rate [91,92], increased stress gradient [112], and lack of refilling of the developing cracks [103]. It is likely that crack initiation by strain evolution competes with crack healing through refilling by the residual liquid. While the crack initiation rate increases with thermal strains, the refilling and healing movement of the residual liquid is controlled by the fluidity of the liquid. High cooling rates cause rapidly developing thermal shrinkage strains that result in a high crack initiation rate. Meanwhile, high cooling rates also reduce the time for the residual liquid to refill and heal the initiated cracks. Therefore, a higher cooling rate is responsible for the increased solidification crack susceptibility in pulsed laser welding of aluminum alloys.

### **2.5.3 Prevention of Solidification Cracking**

The occurrence of solidification cracking in laser welding of aluminum alloys is closely related to the chemical composition and microstructure of the alloys and the magnitude and rate of the thermal strains during welding. Therefore, the following measures can be taken to prevent solidification cracking:

### **A. Improve welding materials**

The composition of the weld metal should be controlled to avoid the high solidification cracking susceptibility range as shown in Fig. 2.20. Al-5xxx alloys used in the automotive industry are usually not susceptible to solidification cracking due to high Mg concentration in these alloys. Al-2xxx and Al-6xxx alloys, on the other hand, have higher solidification crack susceptibility [98-100]. Therefore, in case of continuous laser welding, the Al-5xxx alloys can be welded autogenously without solidification cracking, while Al-2xxx and Al-6xxx alloys require use of filler metals such as 4043 and 4047 to modify the composition and avoid solidification cracking. For example, a low crack susceptibility is achieved when silicon contents in Al-6xxx alloys are 2% or more [90,115-117].

### **B. Refine solidification structure**

The solidification structure of the weld metal can be modified to increase solidification crack resistance. Trace elements such as titanium and zirconium, can significantly refine the solidification structure of the aluminum weld metal [118]. Therefore, small additions of these elements can improve the solidification cracking resistance of aluminum alloys. Other grain refining techniques such as magnetic stirring [119], beam oscillation [120], and surface cooling [121] can also be used if necessary.

### **C. Optimize pulsed laser welding**

Pulsed laser welding has the beneficial effect of grain refining. It also offers higher process control flexibility. However, the pulsing of the laser power increases the likelihood of solidification cracking due to the high cooling rates and rapid solidification [91,92]. Therefore, optimization of pulsing is required to avoid hot cracking. It has been shown that proper pulse shape and sequence of the laser beam can reduce strain rate and promote crack refilling [66,103].



#### **D. Reduce thermal strains**

Thermal strains in welding are influenced by the welding process, heat input, joint configuration and rigidity, and the thermal properties of the welded metals. Thermal tensile strains or displacement can be minimized by designing proper welding fixture and joint configuration, controlling weld bead shape to obtain a lower aspect ratio ( $H/W$ ), and maintaining an elliptical-shaped puddle instead of a teardrop-shaped puddle [122] by using high heat input and low welding speed [123].

#### **2.6 Porosity**

Porosity is a common problem in laser welded aluminum and magnesium alloys. The detrimental effect of porosity on mechanical properties of aluminum welds has been documented in the literature [124,125]. Ashton et al. [124] studied the effects of weld porosity on the tensile and bend test performances of alloy 5086-H116 welded with 5356 electrodes. Their results are given in Fig. 2.21. They found that weld porosity is detrimental to the static tensile properties and bend ductility of the welds. The elongation can be reduced by 50% from its highest level as the porosity level is increased to 4 VPP (volume percent porosity). The yield strength is only slightly reduced by porosity levels up to about 4 VPP. The tensile strength is unaffected by a small amount of porosity, and it drops below 35 ksi when the porosity is higher than 3.6 VPP. It is also noted that when the porosity level is higher than 2.5 VPP, the reduction in tensile strength is more severe, which may exceed the effect caused by reduction in cross sectional area due to porosity.

Katoh [125] tested the tensile strength of Al-5083-O specimens with two holes drilled transverse to the direction of load to simulate porosity. It was found that when the distance between neighboring holes was greater than the hole diameter, the tensile strength decreased linearly with the increase in the hole diameter, irrespective of the hole interval. On the other hand, when the hole interval was smaller than the hole diameter, the tensile strength was further reduced. Katoh [125] proposed that when the pores were near each other, the zone between them hardly carried any load, resulting in further re-

duction in effective loading cross section area of the specimen. This may explain the accelerated reduction in tensile strength at high porosity levels, where both the porosity and the intervals between the pores contribute to reducing the effective loading area.

There are at least two possible causes for porosity formation [126]. One is based on the absorption and subsequent entrapment of the ambient gases during the welding process. For example, all aluminum alloys are prone to hydrogen induced weld metal porosity. Another is based on the entrapment of gas bubbles due to imperfect collapse of the keyhole generated by the high intensity laser beam.

### **2.6.1 Porosity due to Absorption and Entrapment of Gases**

Depending on the composition of the gases near the weld pool, the molten metals in the weld pool may absorb different amounts of ambient gases such as oxygen, nitrogen, and hydrogen. In principle, these gases may be released during subsequent cooling because of their reduced solubility at lower temperatures. If the released gases fail to escape from the weld pool before solidification, they may be entrapped in the fusion zone resulting in porosity. This type of porosity arises due to the large decrease in solubility of the gases in solid aluminum and magnesium alloys. The role of these gases in the formation of porosity in aluminum welds is examined in the following section.

#### **2.6.1.1 Solubility of Oxygen**

The oxides of aluminum, magnesium, manganese, and silicon are highly stable at the temperatures prevailing in the weld pool and the solubility of oxygen in aluminum alloys at these temperatures is very small and difficult to measure. Since the oxides formed in aluminum alloys are stable, molecular oxygen is unlikely to be formed by decomposition of these oxides during laser beam welding. Therefore oxygen is highly unlikely to be the cause of porosity in laser beam welding of aluminum alloys.

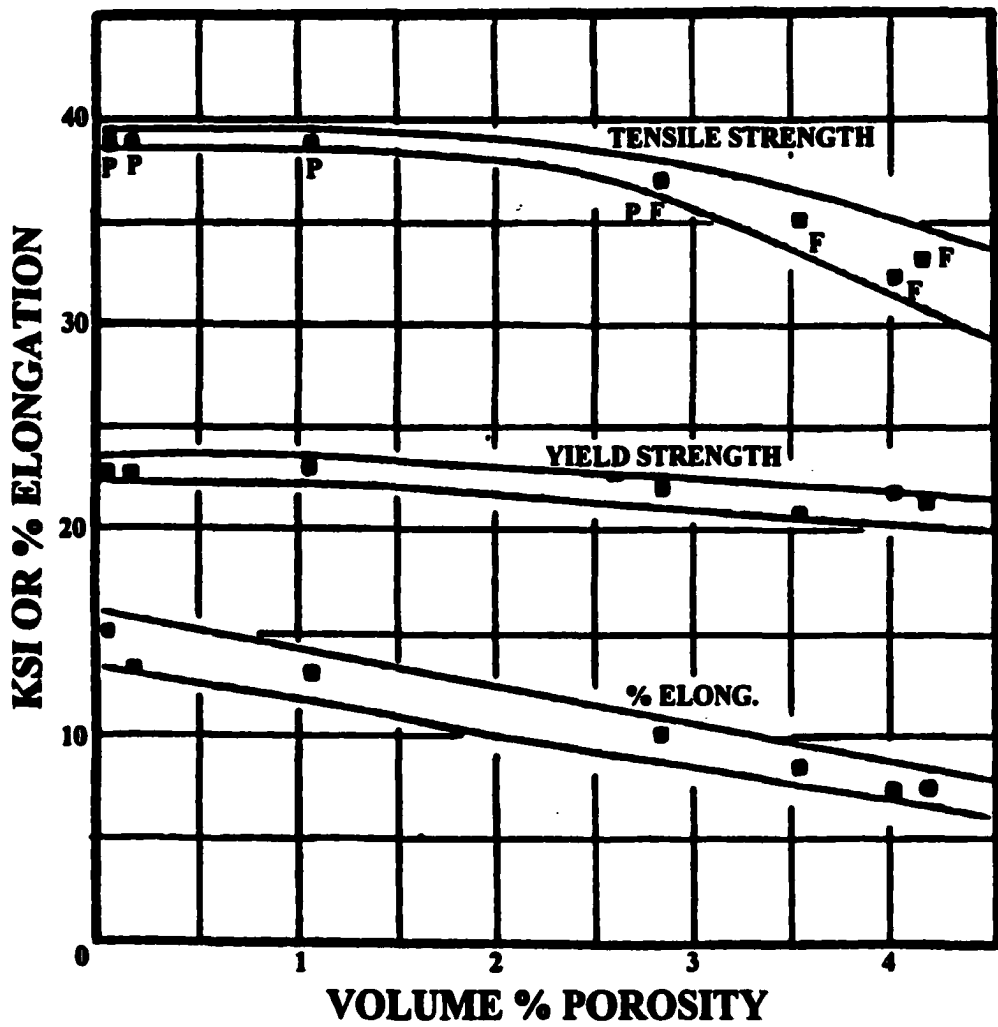
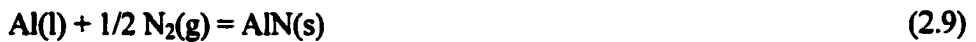


Fig. 2.21 Effect of weld porosity on tension test performance (P = passed bend test, F = failed bend test) [124].

### 2.6.1.2 Solubility of Nitrogen

The solubility [124] of nitrogen in aluminum is less than  $1 \times 10^{-11}$  atom % at about 933K. During laser beam welding, nitrogen is absorbed in the molten aluminum alloy by the reaction:



$$\Delta G_1^0 = -78170 + 27.61T \text{ calories per mole [128]} \quad (2.10)$$

In the presence of plasma over the weld pool, the possible reactions are:



$$\Delta G_3^0 = 865960 - 15.659T \text{ calories per mole [129]} \quad (2.12)$$



$$\Delta G_5^0 = \Delta G_1^0 - \Delta G_3^0 \quad (2.14)$$

The equilibrium partial pressures of  $\text{N}_2$  and  $\text{N(g)}$  according to equations (2.9) and (2.14) indicate that very low partial pressures of these gases are required to form AlN and reflect the tendency for AlN formation. From the standard free energies for the formation of AlN, the partial pressures of  $\text{N}_2$  and  $\text{N(g)}$  in equilibrium with AlN at the temperatures of interest in welding aluminum alloys can be calculated. The calculated values are plotted in Fig. 2.22 and they show that AlN can be formed at very low  $\text{N}_2$  or  $\text{N(g)}$  partial pressures. It is also seen that the equilibrium partial pressure of  $\text{N(g)}$  is much lower than that of  $\text{N}_2$  at any temperature indicating that AlN can be more readily formed in the presence of atomic nitrogen gas. The increasing values of the partial pressures of both  $\text{N(g)}$  and  $\text{N}_2$  show the greater stability of AlN at lower temperatures. Since nitrogen is absorbed by the molten pool mainly by the formation of AlN which is more stable at lower temperatures, nitrogen as the cause of porosity during laser beam welding of aluminum alloys can be ruled out. Katayama [130] reported that porosity was reduced in laser welding of aluminum alloys when nitrogen was used as the shielding gas. He proposed that the formation of nitrides on the molten pool surface inhibited the absorption of hydrogen

by the molten pool [130]. A comprehensive study of the role of nitrides on hydrogen absorption in molten aluminum during welding still remains to be undertaken.

### 2.6.1.3 Solubility of Hydrogen

Hydrogen has significant solubility in aluminum and is generally considered to be the primary cause of porosity during the welding of aluminum alloys. The measured values of hydrogen solubility in pure aluminum vary according to the data furnished by different investigators [131-139]. Among the data considered reliable are those by Ransley and Neufeld [131] who found that the solubility of hydrogen in liquid aluminum can be expressed by the following equation:

$$\log S = -2760/T + 1/2 \log P + 1.356 \quad (2.15)$$

and that in solid aluminum by:

$$\log S = -2080/T + 1/2 \log P - 0.652 \quad (2.16)$$

where S is the solubility of hydrogen in cm<sup>3</sup> measured at 273K and 760 Torr per hundred grams of aluminum, T is the temperature in K, and P is the partial pressure of hydrogen in Torr. The calculated hydrogen solubility in solid and liquid aluminum at three different H<sub>2</sub> partial pressures is given in Fig. 2.23. The plot shows that the solubility of hydrogen in aluminum decreases with decreasing temperature and that its solubility in liquid aluminum is about 20 times higher than that in solid aluminum at the melting point of 933 K. This explains why aluminum and its alloys are highly susceptible to hydrogen porosity during welding.

An additional factor to be considered in laser beam welding is that a plasma phase containing the atomic gaseous species can be formed over the weld pool. In the presence of atomic hydrogen the solubility of hydrogen in liquid aluminum can be greatly

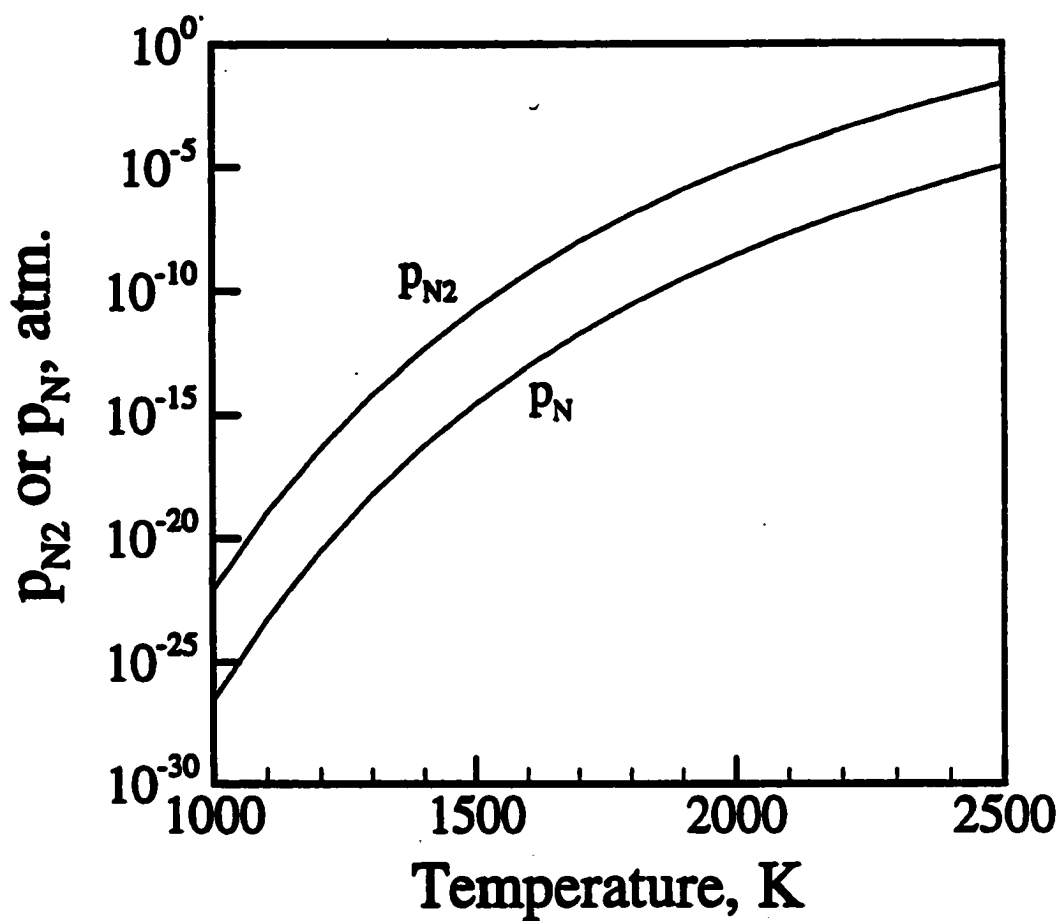


Fig. 2.22 The calculated equilibrium partial pressure of diatomic nitrogen and monatomic nitrogen in forming aluminum nitride, as a function of temperature.

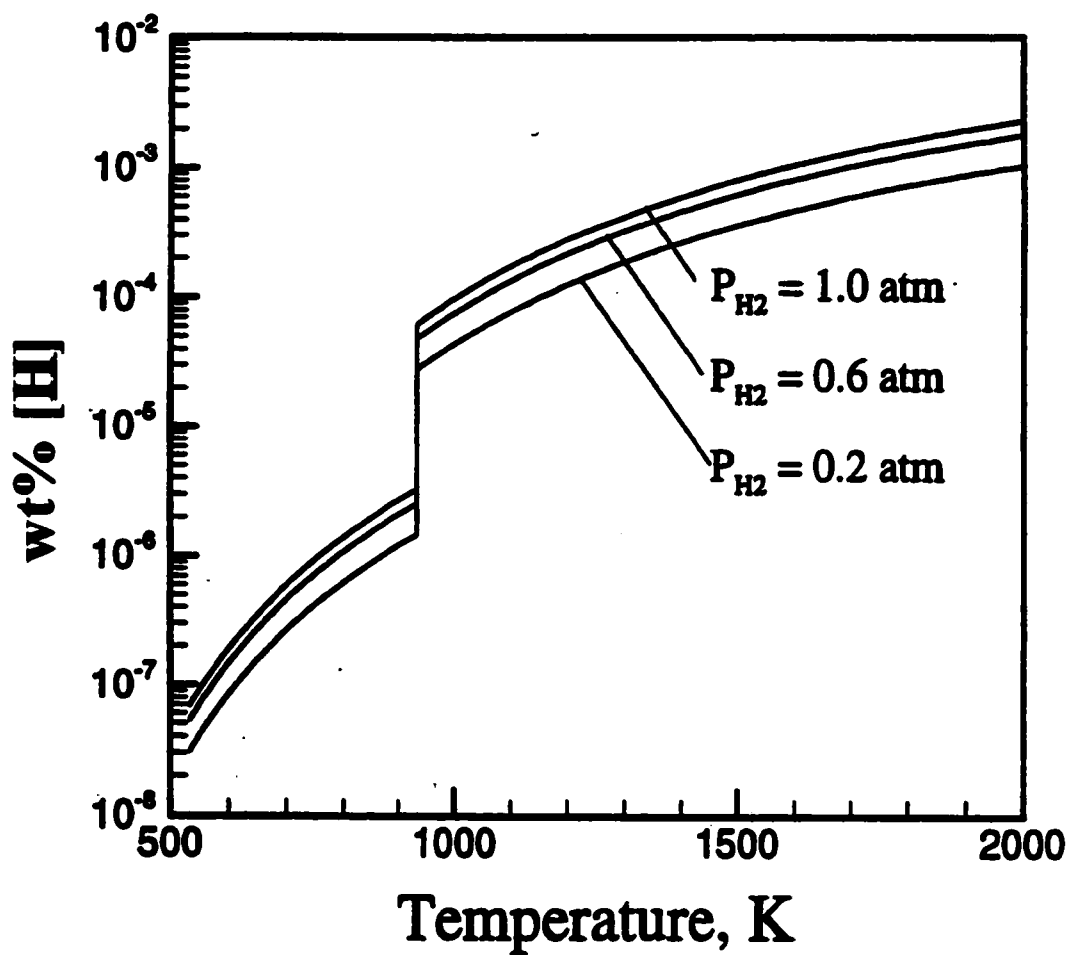


Fig. 2.23 The calculated hydrogen solubility in aluminum based on the results of Ransley and Neufeld [131].

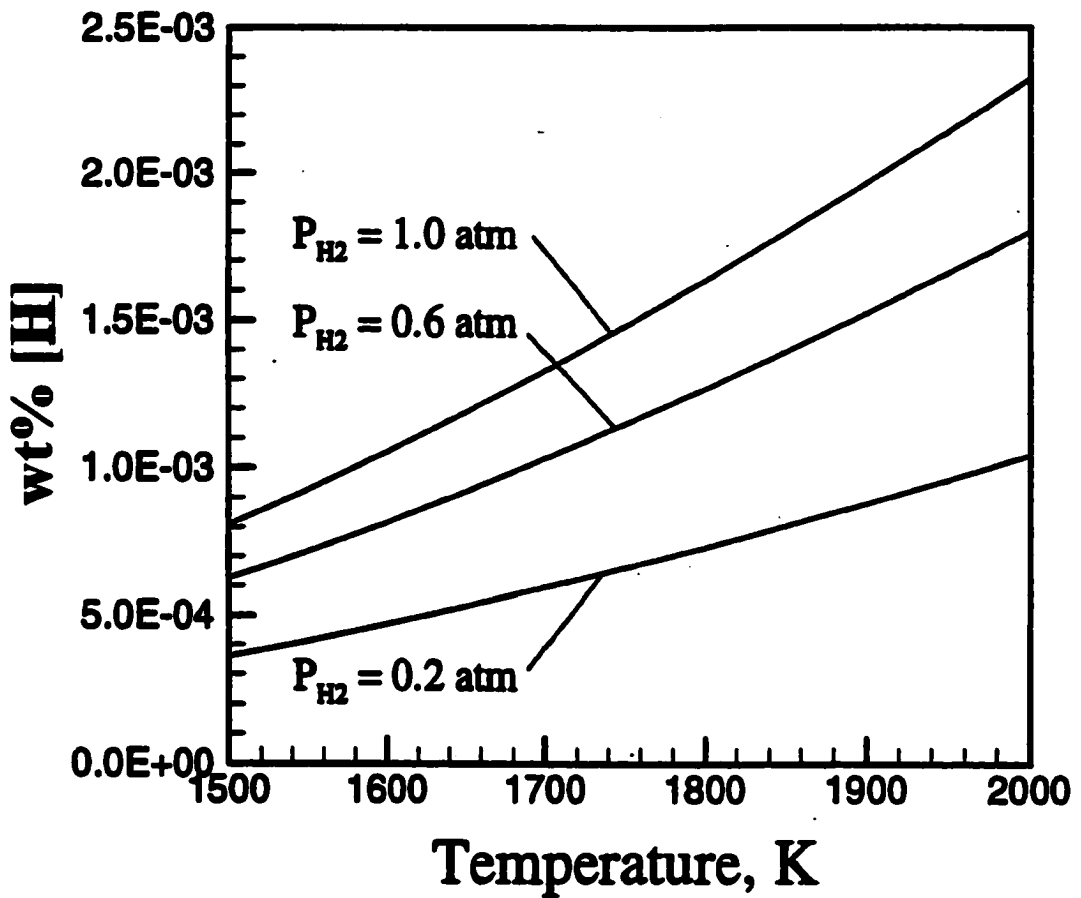


Fig. 2.24(a) The calculated hydrogen solubility in aluminum in the environment of diatomic hydrogen based on data from [131].



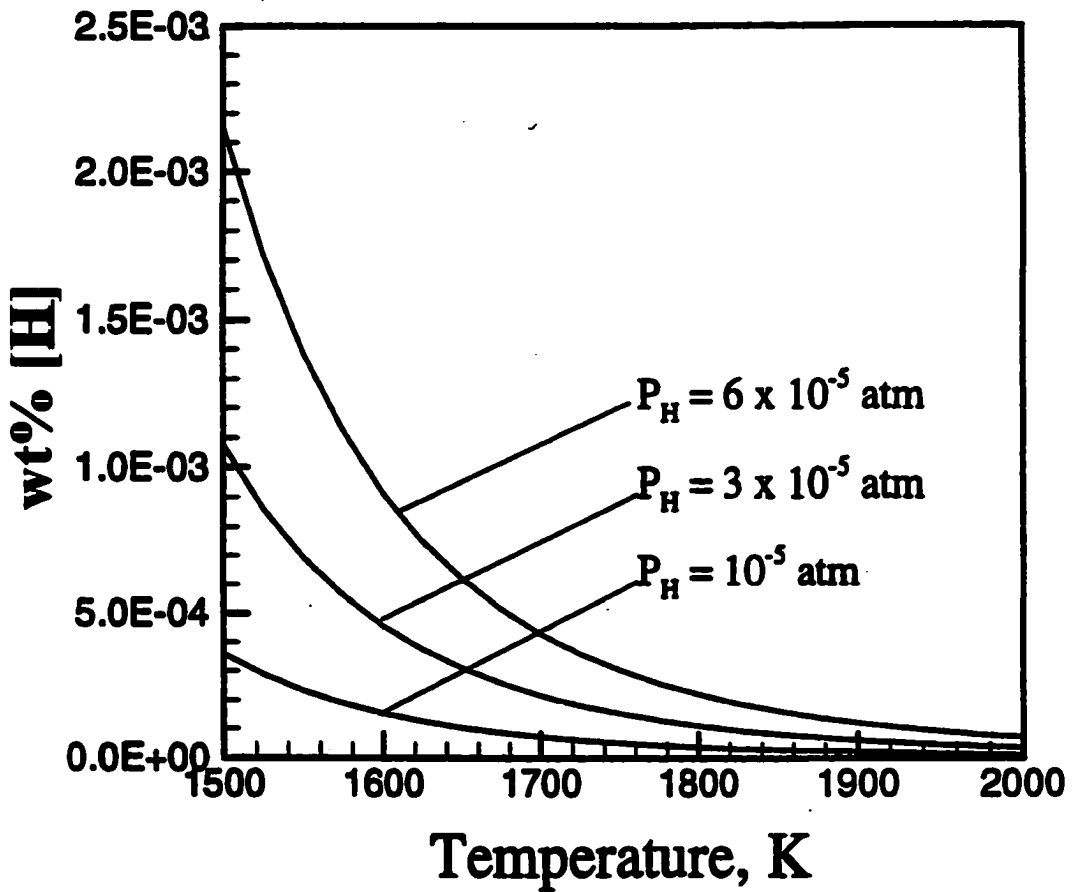


Fig. 2.24(b) The calculated hydrogen solubility in aluminum in the environment of monatomic hydrogen based on data from [131] and [140].

enhanced. Using the data [131] in Eqn. (2.15) and the standard free energy of formation [140] of atomic hydrogen gas in Eqn. (2.18), the solubility of hydrogen in liquid aluminum in environments of molecular and atomic hydrogen can be calculated.



$$\Delta G_9^0 = 53550 - 14.4T \text{ calories per mole [140]} \quad (2.18)$$

The calculated results are plotted in Fig. 2.24. It is seen that the solubility of hydrogen in aluminum at 1500 K is about 0.0008 wt.% in one atmosphere diatomic hydrogen environment and the solubility is increased to about 0.0011 wt.% in only 0.00003 atmosphere partial pressure of monatomic hydrogen.

#### **2.6.1.4 Effect of Alloying Elements on the Solubility of Hydrogen in Aluminum**

Anyalebechi [141] has reviewed the effect of alloying elements on hydrogen solubility in liquid aluminum and the results are shown in Fig. 2.25. The presence of lithium, magnesium, and titanium increases the solubility of hydrogen in liquid aluminum whereas zinc, silicon, copper, and iron reduce it. This behavior can be attributed to the strong attractive interactions between hydrogen and lithium, magnesium, and titanium on the one hand and the strong bonding of aluminum atoms to zinc, silicon, copper, and iron on the other.

#### **2.6.1.5 Nucleation and Growth of Hydrogen Bubbles in Weld Metal**

As noted previously, the solubility of hydrogen in liquid aluminum decreases with temperature and it is about 20 times higher in liquid aluminum than in the solid near the melting point. Therefore, the molten aluminum weld pool becomes highly supersaturated with absorbed hydrogen in the subsequent cooling process. To reduce the supersaturation, hydrogen bubbles form by a process of nucleation and growth. However, the high surface tension of liquid aluminum does not favor nucleation of hydrogen bubbles. Homogeneous nucleation of hydrogen bubbles in liquid aluminum is impractical. Therefore heterogeneous nucleation in the presence of imperfections or minute inclusions in the metal is the

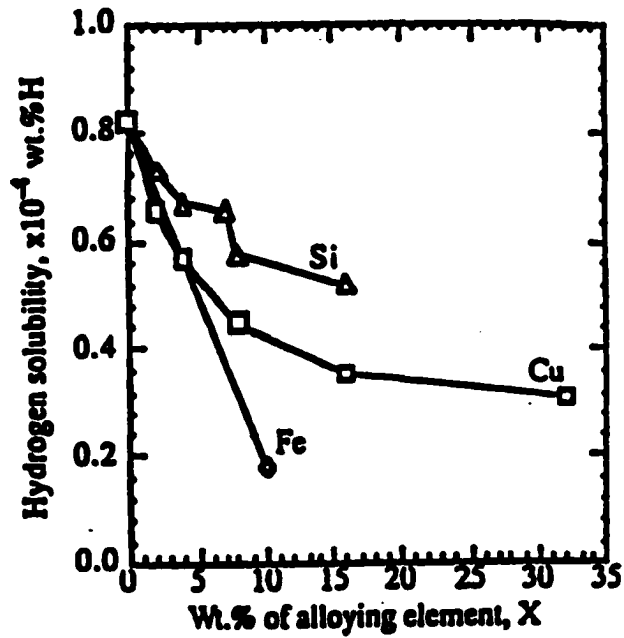
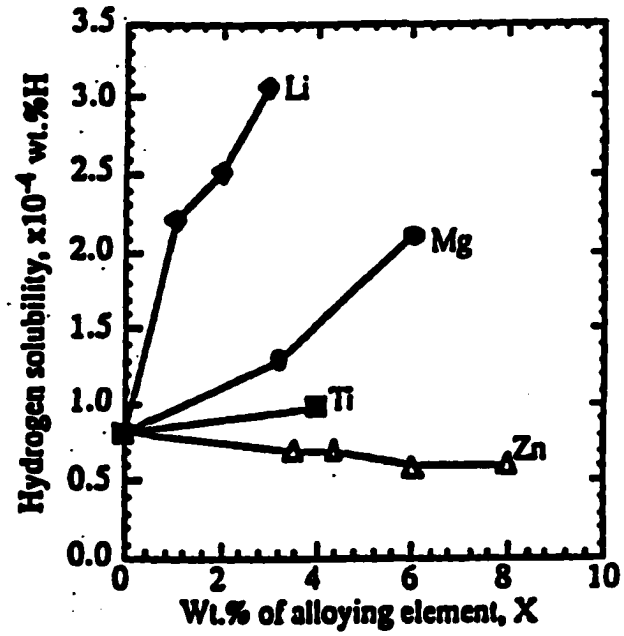


Fig. 2.25 Effect of alloying elements on the solubility of hydrogen in liquid aluminum at 973 K and 1 atm partial pressure of hydrogen [141].

primary mechanism of bubble formation. The growth of pores after nucleation is a diffusion controlled process. The possibility of hydrogen bubble entrapment during laser beam welding is governed by the viscosity and cooling rate of the molten weld pool. According to Stokes law, the rising speed,  $u$ , of a spherical gas bubble in a viscous liquid is given by:

$$u = \frac{2r^2 \Delta \rho g}{9\mu} \quad (2.19)$$

where  $r$  is the radius of the bubble,  $\Delta \rho$  is the density difference between the liquid and the gas bubble, and  $\mu$  is the viscosity of the liquid. The chances of porosity formation by entrapment of a hydrogen bubble in the weld pool increase with increase in liquid viscosity and decrease in bubble radius.

The cooling rate of the molten weld pool controls the growth and escape of hydrogen bubbles. At high cooling rates, the time available for bubble growth and escape is reduced. Therefore, high cooling rates lead to the formation small pores. In the case of castings of Al-4.7% Mg alloys, Fang et al. [142] have shown that the average size of hydrogen porosity decreased with increasing cooling rates. Higher cooling rates give less time for hydrogen to diffuse causing reduction in pore volume [142] as shown in Fig. 2.26. Many other investigations [143-145] have also shown that the volume fraction of hydrogen porosity is reduced as the cooling rate increases. In the case of laser beam welding, the cooling rates are much faster than in casting and a much smaller hydrogen pore size is to be expected.

The effect of alloying elements on hydrogen porosity formation is not well understood. Their effect on hydrogen porosity formation can be considered by examining the way in which they affect the hydrogen solubility in aluminum, the viscosity of molten aluminum, and the interfacial energy by acting as surfactants. An alteration in hydrogen

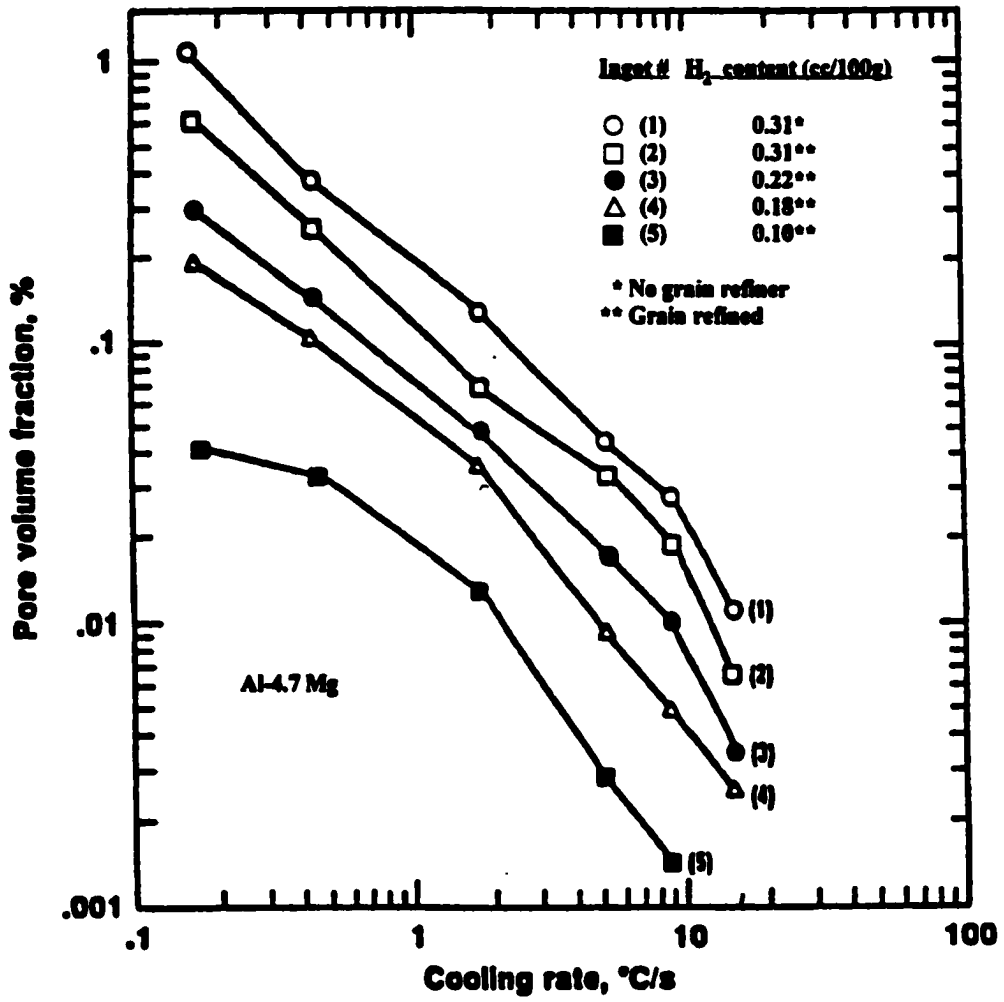


Fig. 2.26 Pore volume fraction as a function of the cooling rate in Al-4.7 Mg alloy [142].

solubility in the presence of alloying elements affects the threshold hydrogen concentration for porosity formation. The effect of alloying elements on the viscosity of molten aluminum is shown [46] in Fig. 2.27. Some surface active elements like lithium, magnesium, bismuth and lead can reduce the interfacial energy and aid the nucleation of hydrogen bubbles. The overall effect of alloying elements on the tendency for hydrogen porosity formation may depend on a combination of all the three factors. However, because of the high cooling rate associated with laser beam welding, the presence of hydrogen may lead to micro-pores. The macro-pores cannot be attributed to hydrogen solubility.

In conventional welding processes, the primary sources of hydrogen in the weld metal are the filler metal, the shielding gas, and the base metal. Eliminating hydrogen from these sources can effectively control porosity formation. However, in laser welding this is not achieved. Marsico [5] reported that severe porosity in the weld metal was consistently observed during autogenous laser welding of aluminum alloys, even when hydrogen was eliminated from all possible sources, indicating that the main source of macro porosity may not be hydrogen. An alternative mechanism has to be considered as the cause of macro porosity formation in laser beam welding.

### **2.6.2 Porosity due to Collapse of the Keyhole**

The entrapment of gaseous species including vaporized alloying elements and the shielding gas due to the instability and collapse of the keyhole can be considered as a possible cause of porosity in laser welding of aluminum alloys. During keyhole mode welding, as the keyhole moves forward, the liquid metal on the rear wall moves in to fill the space vacated by the front wall of the keyhole. If the keyhole wall is unstable, the metal may fail to fill the cavity smoothly behind the fast moving laser beam as shown schematically in Fig. 2.28 [146]. As a result, the metal vapors and gases are entrapped at the root of the weld. Therefore, establishing a stable keyhole is very importance for obtaining a good quality weld.

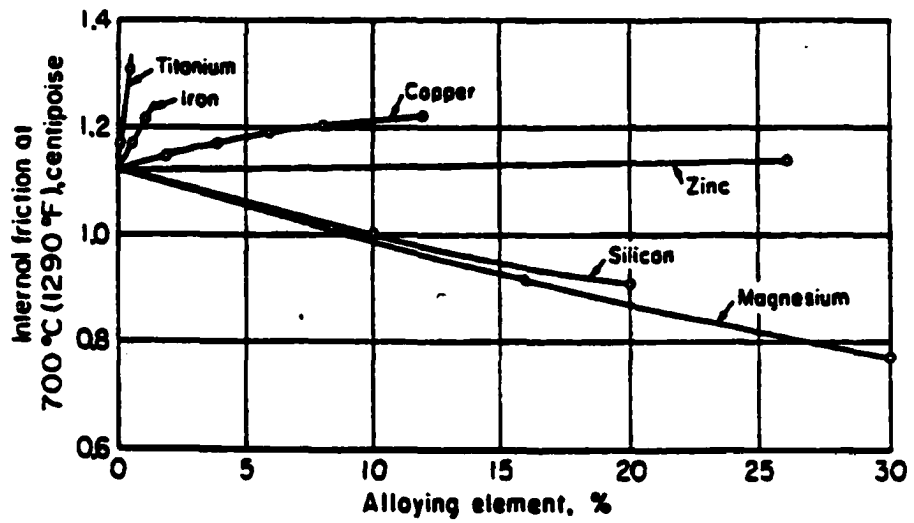


Fig. 2.27 Addition of alloying elements on viscosity of aluminum [46].

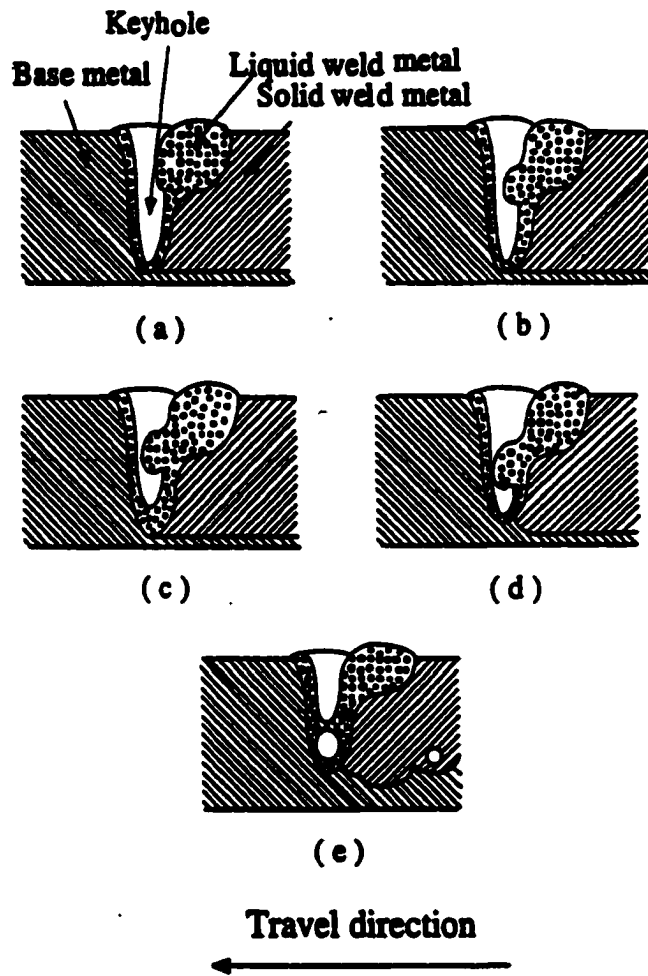


Fig. 2.28 A schematic diagram showing the formation of void at the weld root due to imperfect collapse of the keyhole [146].



The collapse of a moving keyhole has yet to be formulated theoretically although the behavior of a stationary keyhole has been modeled [147-150]. In early studies, Rayleigh [147] and Bachelor [148] established a theoretical foundation for the collapse of a spherical bubble. Later, Kroos et al. [149] formulated the problem in a cylindrical geometry to simulate the collapse of a keyhole in laser welding. The pressure on the keyhole wall was considered to be balanced mainly between the ablation pressures and the surface tension forces. The dynamic pressure due to fluid flow and the hydrostatic pressure were considered to be negligible. Their predicted keyhole radius was at least 1.7 times the laser beam radius. They also calculated the collapse time of the cylindrical keyhole due to a sudden laser beam shut-down. The typical calculated closing time of the keyhole for Al, Fe, and Cu was of the order of 0.1 ms. This result implies that if the interval between two successive pulses during pulsed laser welding exceeds 0.1 ms, the resulting weld will not be continuous. More recently, Ducharme et al. [150] included the axial variation of the keyhole geometry in their calculations. They calculated the collapse time of a keyhole following the extinction of a CO<sub>2</sub> laser beam during laser welding of iron and aluminum. The initial radius of the keyhole was first calculated using an integrated keyhole and weld pool model [151]. It was assumed that the pressure in the keyhole drops to the ambient atmospheric pressure in a period much shorter than the time necessary for the collapse of the keyhole. The keyhole was considered to collapse because of the surface tension forces acting on the keyhole wall. The calculations involved the equation of continuity and Navier-Stokes equations. The keyhole wall was treated as a moving boundary. The keyhole geometry in aluminum sheet at various collapse times is shown in Fig. 2.29. It is interesting to note that the keyhole collapses faster in the middle of the keyhole wall, which may result in entrapment of gas bubbles at the bottom of the keyhole. Matsunawa et al. [66,152] found this type of porosity near the bottom of the fusion zone in pulsed laser welding of aluminum alloys. They showed that such porosity could be prevented by improving the shape of the laser pulse.

Schauer and Giedt [153] studied keyhole stability in electron beam (EB) welding. The problem is pertinent to laser welding because the conditions for maintaining a stable

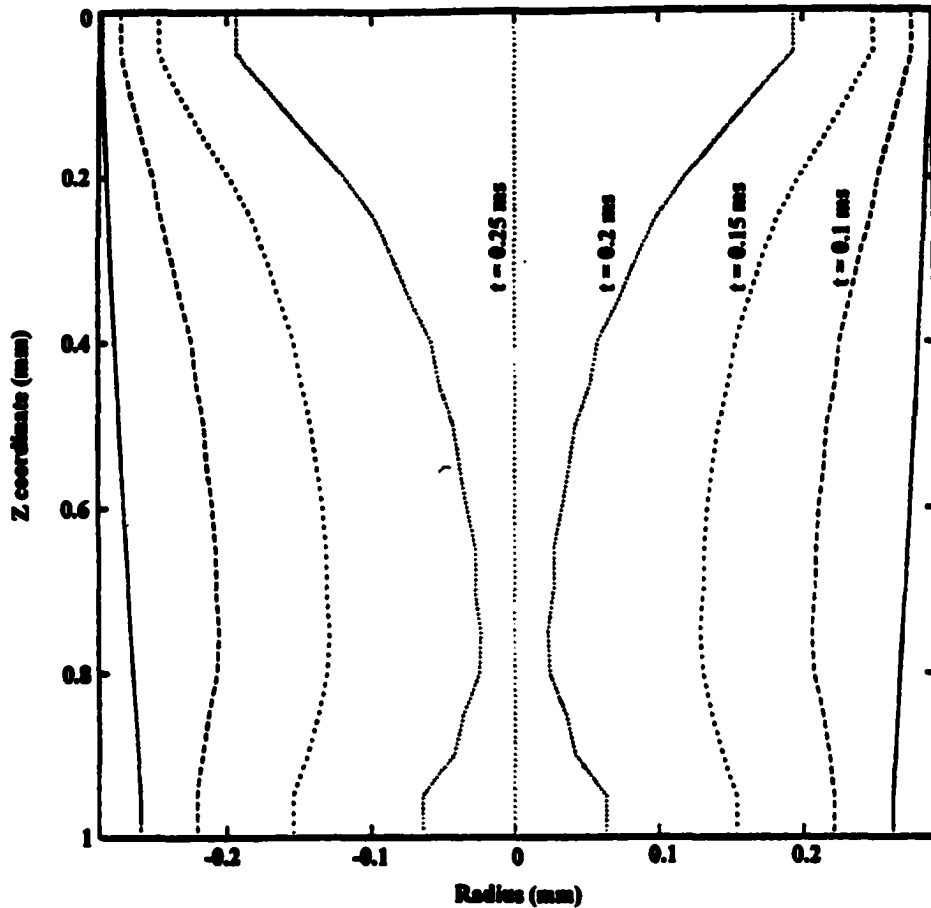


Fig. 2.29 The keyhole wall profiles during CO<sub>2</sub> laser welding of 1.0 mm thick aluminum sheet with a power of 2 kW and welding speed of 10 mm/s at time  $t = 0.1$  ms, 0.15 ms, 0.2 ms, and 0.25 ms following the extinction of the laser beam [150].

keyhole are the same in these two processes. Forces on the keyhole wall were considered to be balanced mainly between the vapor pressure and the surface tension force. Based on the measured temperature profile as a function of position on the keyhole wall, they calculated the vapor pressure force and the surface tension profile along the keyhole wall. The typical calculated profiles of surface tension pressure and vapor pressure along the keyhole depth during EB welding of 1100 aluminum are given in Fig. 2.30. It is observed from this figure that the surface tension force is greater than the vapor pressure force in the upper region of the keyhole, and lower in the lower region. A projection is likely to form in the upper region of the keyhole due to the high surface tension force as shown in Fig. 2.31. The liquid in this projection has been preheated when it moves to the bottom of the keyhole. The electron beam can easily bore through this superheated liquid causing a sudden increase in keyhole depth. The process may happen periodically which results in spiking [153]. Voids tend to form in the lower portions of the spikes because molten metal does not fill the region completely as the keyhole collapses [153].

Schauer and Giedt [153] found that the tendency to spike formation could be evaluated by a stability parameter  $S = H/h$  where  $H$  is the height between the keyhole bottom and where the liquid projection forms and  $h$  is the penetration depth of the keyhole as shown in Fig. 2.31. Based on their experimental data, they proposed that spiking would not be a problem for welds having a value of  $S$  less than 0.5. However, when  $S$  was greater than 0.5, the weld might be expected to exhibit unacceptable spiking. The narrow-deep-shaped keyhole geometry tends to have higher value of  $S$ , therefore, spiking is frequently found during deep penetration keyhole mode welding. On the other hand, the surface tension and the equilibrium vapor pressure of the welded material are two important parameters in determining the stability of the keyhole.

Many automotive aluminum alloys have lower surface tensions than Al-1100 due to the presence of surface active elements such as Mg. At the same time, they have higher vapor pressures due to the presence of volatile elements such as Mg, Mn, and Zn. Therefore, the surface tension pressure curve in Fig. 2.30 will be lower and the vapor pressure

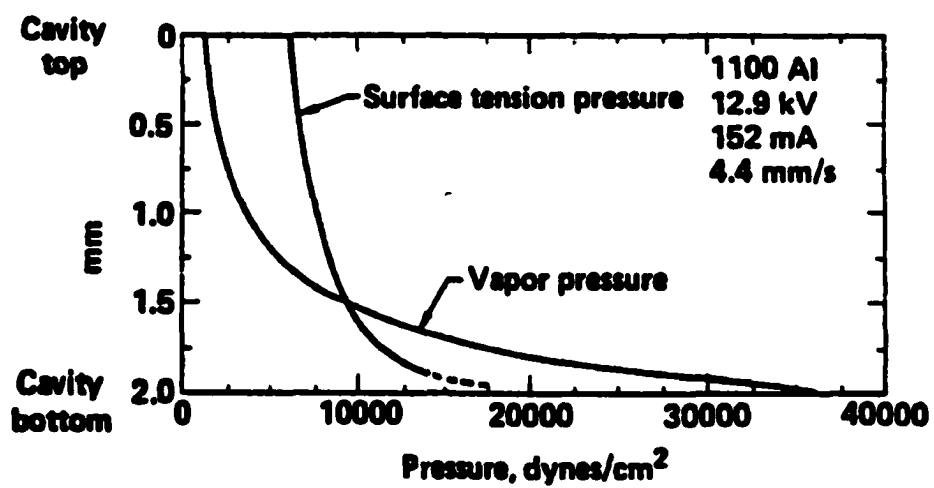


Fig. 2.30 Calculated values for surface tension pressure and vapor pressure in an 1100 aluminum EB welding cavity as a function of cavity depth [153].

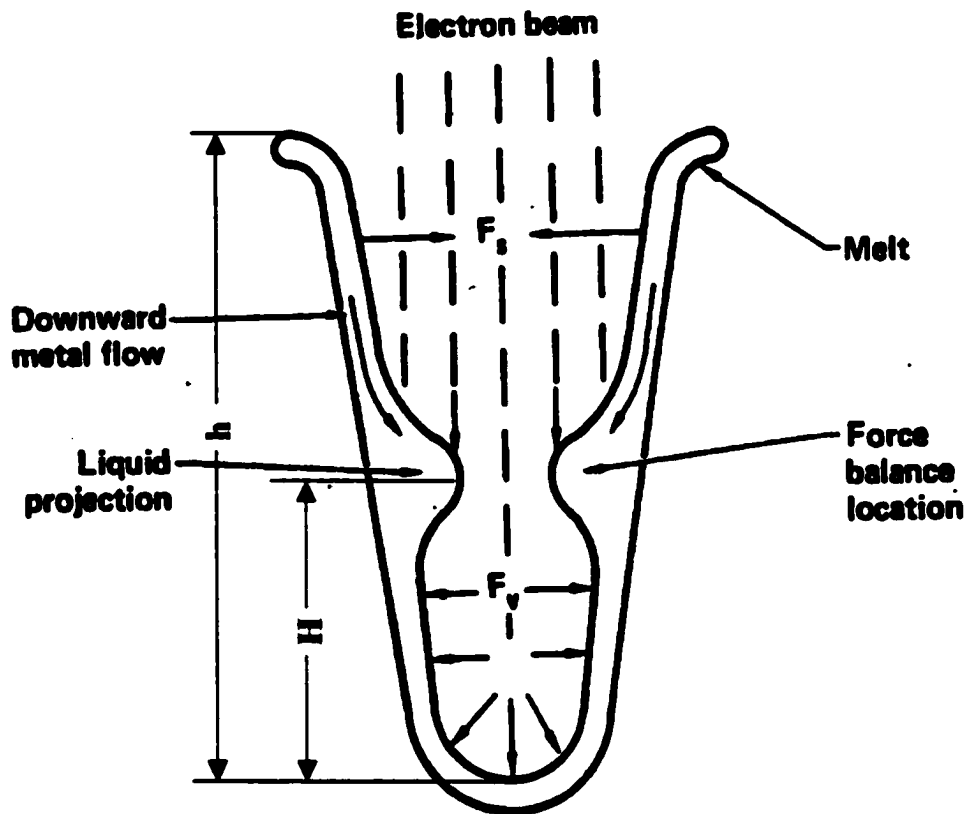


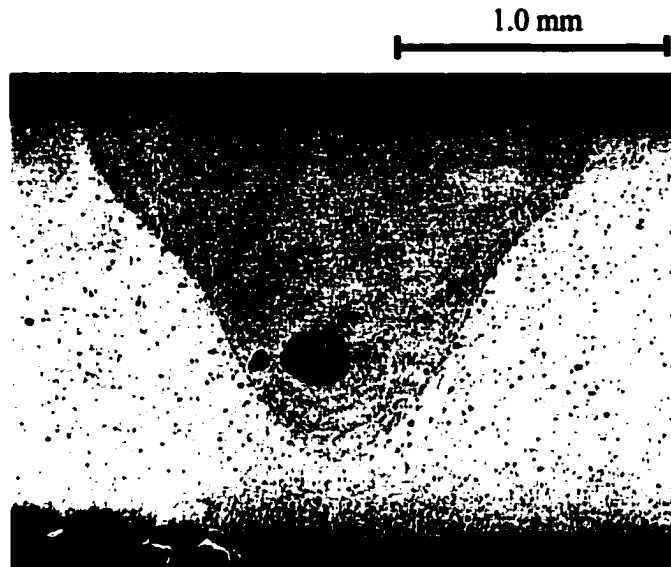
Fig. 2.31 Liquid projection formation at location where surface tension force is nearly in balance with vapor pressure force [153].

curve in the figure will be higher for welding of automotive aluminum alloys. As a result, the stability parameter,  $S$ , is high for the welding of these alloys if the penetration depth,  $h$ , and other conditions are the same. Therefore, laser welding of automotive aluminum alloys tends to have poor keyhole stability and is more susceptible to formation of porosity due to the instability of the keyhole.

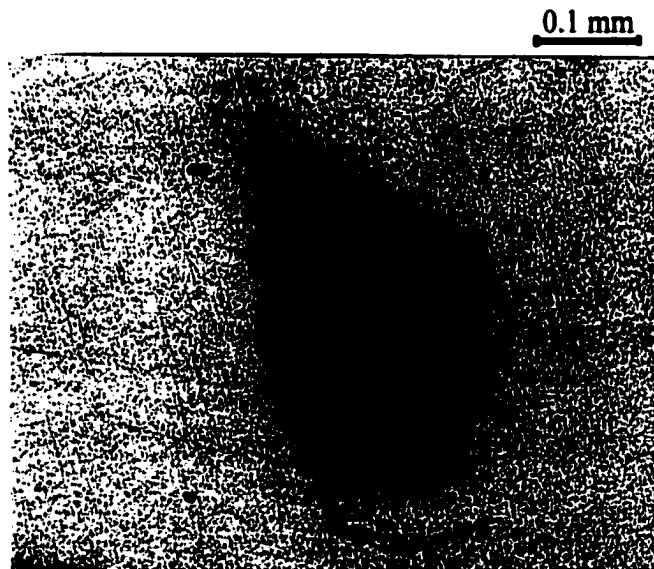
Recent investigations [37,79,146] on pore formation during continuous wave Nd:YAG laser welding of 5182 and 5754 aluminum alloys have confirmed the importance of keyhole stability in the formation of porosity. Macro-pores which are 0.2 mm or larger in size dominated the porosity distribution as shown in Fig. 2.32. The amount of macro porosity produced at several beam defocus values during laser welding of alloy 5754 is presented in Fig. 2.33. The data show that when the welding was conducted in the transition region between the keyhole and the conduction modes, macro porosity was consistently observed. Since hydrogen is generally considered to be the main cause of porosity in aluminum alloys, the role of hydrogen in pore generation was examined by using both wet and dry helium as the shielding gas during laser welding. It was found that the presence of moisture in the shielding gas did not increase the amount of macro porosity in the weld though small amounts of micro-pores were observed in some rare cases [37,146]. These studies [37,79,146] also showed that when welding parameters were properly chosen to avoid the transition region where the keyhole is unstable, porosity could be minimized.

### **2.6.3 Summary**

Hydrogen rejection and keyhole instability are the two possible causes of pore formation during laser welding of aluminum alloys with the later to be more dominant. In order to obtain porosity free aluminum welds, the weld parameters should be carefully chosen to avoid unstable keyhole. A model that predicts the stability of the keyhole for different welding conditions will be developed in this study. This model can help establish the operating parameter window to obtain welds free of porosity.



(a)



(b)

**Fig. 2.32 Typical porosity observed during Nd:YAG laser welding of 5754 aluminum alloy: (a) spherical porosity near the bottom of the weld pool, (b) irregular-shaped porosity at the fusion boundary [37].**

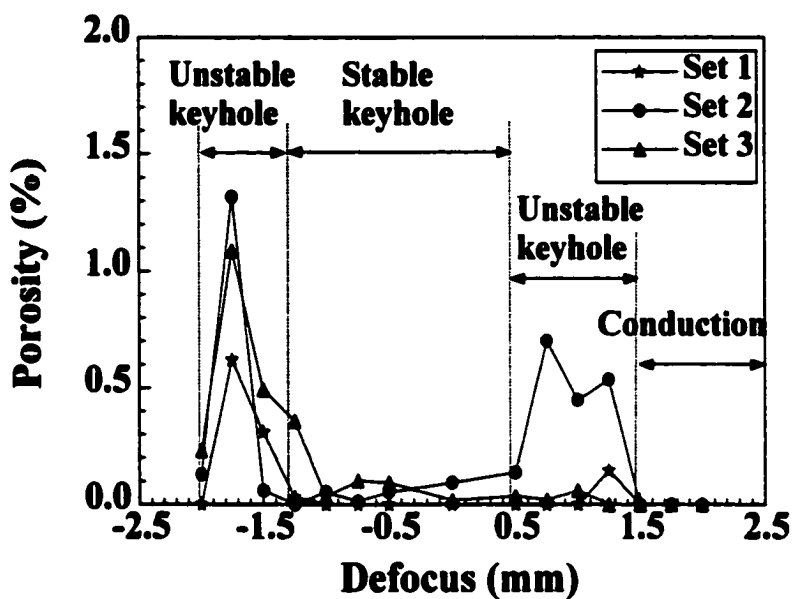


Fig. 2.33 Porosity produced at several beam defocusing values during Nd:YAG laser welding of 1.45 mm thick 5754 aluminum alloy with a power of 3.0 kW, welding speed of 150 ipm, and shielding gas of pure helium at a flow rate of 200 ft<sup>3</sup>/h [37].



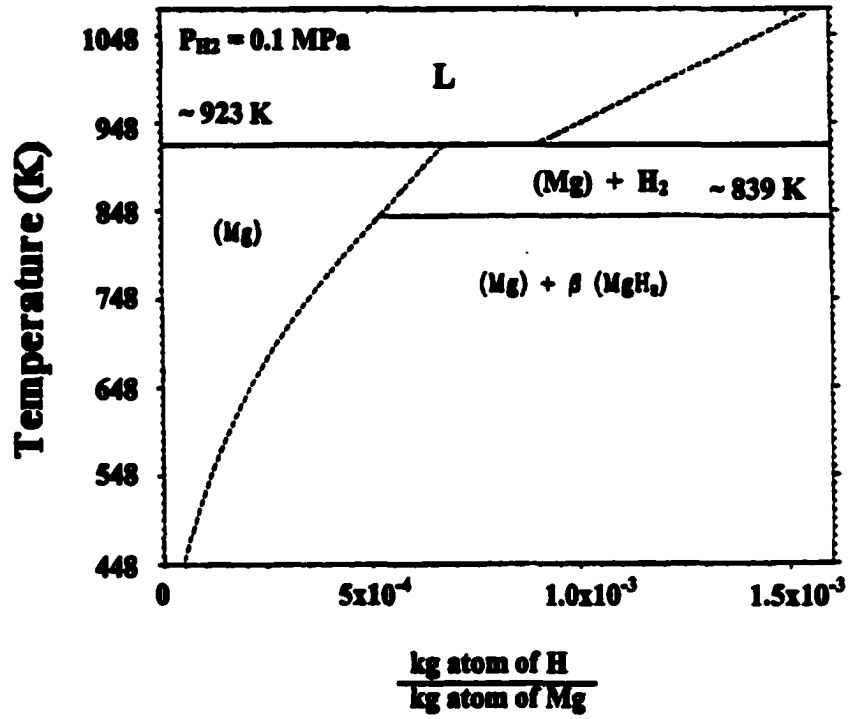


Fig. 2.34 Solubility of hydrogen in magnesium [154].

Very little study has been done in understanding porosity formation in laser welding of magnesium alloys. However, there are some similarities between the welding of these two types of alloys. Both aluminum and magnesium have significantly higher hydrogen solubility in liquid than in solid. For magnesium, this difference in the hydrogen solubility can be observed from Fig. 2.34 [154]. Mikucki and Shearouse [155] found that the amount of porosity in the solidified magnesium alloy AZ91 was proportional to the dissolved hydrogen in the alloy. They also found that the rejection of hydrogen from the  $Mg_{17}Al_{12}$  intermetallic compound assisted in the nucleation and/or growth of microporosity during the last stages of solidification of alloy AZ91 [156]. The difference in the solubility between the solid and the liquid phases and the results of previous solidification studies [155,156] indicate that hydrogen rejection needs to be considered as a possible cause of porosity formation during solidification of magnesium alloys [155,156].

Haferkamp et al. [157] observed more porosity in the fusion zone of non-vacuum die-cast alloy AM60B than vacuum die-cast alloy AZ91D that had less gas inclusions in the base metal. They found that for the same porosity level in welds, large pores are more detrimental to strength than small pores. The presence of gas inclusions in the base metal was thought to be an important factor in contributing to the formation of large pores during Nd:YAG laser welding of magnesium alloys [157].

Better understanding of pore formation in AM60B fusion zone during laser welding and alleviation of the porosity problem are needed for wider application of this alloy in the automotive industry. This research also seeks to achieve these two important goals.

## **2.7 A Selection of Important Unanswered Questions**

Although laser beam welding is widely used in the industry, several scientific and technological problems have not been satisfactorily solved. A selection of these important problems to be addressed in this study is presented below:

### **A. Control of alloying elements loss**

The loss of volatile alloying elements by vaporization during laser welding of automotive aluminum alloys is a severe problem that causes degradation of the mechani-

cal properties of the welds. It is known that the rate of vaporization in laser welding is determined by many factors such as temperature distribution on the weld pool surface, local concentrations of the alloying elements, and possibly by other factors. However, a quantitative understanding of vaporization is needed in order to control of alloying element based on scientific principles. In this study, a comprehensive model will be developed to understand the vaporization of alloying elements and welding composition change in laser welding of automotive aluminum alloys.

#### **B. Control of porosity formation**

Avoiding porosity formation remains an important goal in laser welding of automotive aluminum and magnesium alloys. Macro porosity caused by the imperfect collapse of the keyhole is a major concern in laser welding of automotive aluminum alloys. In this study, a model will be developed to seek better understanding and prevention of macro porosity formation for laser welding of automotive aluminum alloys. On the other hand, porosity formation in laser welding of magnesium alloys is not very well understood. Therefore, a thorough study will be conducted to understand the mechanism of pore formation and seek science based remedies.

#### **C. Control of weld pool geometry**

Achieving reproducible, defect-free, full penetration welds is an important goal of laser welding of automotive aluminum alloys. Acceptable combinations of welding variables are currently obtained by trial and error. However, in many cases, adjustment of welding variables by conducting a large number of experiments is time consuming and expensive. Development of numerical models based on comprehensive phenomenological understanding of the process and material has provided an effective way to calculate the weld pool geometry. The prediction of weld pool geometry for laser welding of automotive aluminum alloys is also an important undertaking in this study.

## 2.8 References

1. E. Hagen and H. Rubens: *Annln. Phys.*, 1902, 4, 8, pp. 1-21.
2. M. A. Bramson: '*Infrared Radiation: A Handbook for Applications*', 1968, Plenum Press, New York.
3. W. W. Duley: '*Laser Processing and Analysis of Materials*', 1983, p. 71, Plenum Press, New York.
4. C. A. Huntington and T. W. Eagar: *Welding Journal*, 1982, 62, 4, pp. 105s-107s.
5. T. Marsico: M. S. Thesis, 1988, The Pennsylvania State University, PA.
6. Y. Arata and I. Miyamoto: *Technocrat*, May 1978, 11, 5, pp. 33-42.
7. K. Behler, E. Beyer, and R. Schafer: *Laser Materials Processing*, November 1988, pp. 249-258, Santa Clara, California, Laser Institute of America.
8. R. C. Crafer: in *Proceedings of 4th International Conference on Advances in Welding Processes*, 1978, Cambridge, England, pp. 267-278.
9. Kaiser Aluminum Company: '*Welding Kaiser Aluminum*', 2nd edition, 1978, Oakland, California.
10. R. Jan, P. R. Howell, and R. P. Martukanitz: in *Proceedings of the 4th International Conference on Trends in Welding Research*, edited by H. B. Smartt et al., June 1995, Gatlinburg, Tennessee, pp. 329-334.
11. H. Sakamoto, K. Shibata, and F. Dausinger: *ICALEO'92, Laser Materials Processing*, edited by D. Farson, W. Steen, and I. Miyamoto, October 1992, pp. 523-528, Orlando, Florida, Laser Institute of America.
12. S. Katayama: *Journal of Light Metal Welding and Construction*, 1996, 34, 4, pp. 23-30.
13. P. W. Fuerschbach: *Welding Journal*, 1996, 75, 1, pp. 24s-34s.
14. T. DebRoy and S. A. David: *Reviews of Modern Physics*, 1995, 67, 1, pp. 85-112.
15. A. Matsunawa, H. Yoshida, and S. Katayama: *ICALEO'84*, Vol. 44, 1984, pp. 35-42, Toledo, Ohio, Laser Institute of America.
16. C. M. Banas: *The Industrial Laser Annual Handbook*, 1986, pp. 69-86, PennWell Books, Tulsa, Oklahoma.

17. D. R. Keefer: *Laser-Induced Plasmas and Applications*, 1989, pp.169-206, edited by L. J. Radziemski and D. A. Cremers, New York: Mercel Dekker Inc.
18. T. D. Rockstroh and J. Mazumder: *Journal of Applied Physics*, 1987, 61, 2, pp. 917-923.
19. R. Miller and T. DebRoy: *Journal of Applied Physics*, 1990, 68, 5, pp. 2045-2050.
20. D. A. Schauer, W. H. Giedt, and S. M. Shintaku: *Welding Journal*, 1978, 57, 5, pp. 127s-133s.
21. C. R. Heiple and J. R. Roper: in '*Trends in Welding Research in the United States*', 1982, pp. 489-520, edited by S. A. David, ASM, Metals Park, Ohio.
22. H. G. Kraus: *Welding Journal*, 1989, 68, pp. 269s-279s.
23. J. A. Shercliff: *J. Fluid Mech.*, 1970, 40, pp. 241-250.
24. G. M. Oreper, T. W. Eagar, and J. Szekely: *Welding Journal*, 1983, 62, pp. 307s-312s.
25. G. M. Oreper and J. Szekely: *Metallurgical Transactions*, 1987, 18A, pp. 1325-1332.
26. A. Paul and T. DebRoy: *Metallurgical Transactions*, 1988, 19B, pp. 851-858.
27. K. Mundra, T. DebRoy, T. Zacharia, and S. A. David: *Welding Journal*, 1992, 64, pp. 313s-320s.
28. T. Zacharia, A. H. Eraslan, and D. K. Aidun: *Welding Journal*, 1988, 67, pp. 53s-62s.
29. T. Zacharia, A. H. Eraslan, D. Aidun, and S. A. David: *Metallurgical Transactions*, 1989, 20B, pp. 645-659.
30. T. Zacharia, S. A. David, J. M. Vitek, and T. DebRoy: *Welding Journal*, 1989, 68, pp. 499s-509s.
31. T. Zacharia, S. A. David, J. M. Vitek, and T. DebRoy: *Welding Journal*, 1989, 68, pp. 510s-519s.
32. S. Kou and Y. H. Wang: *Metallurgical Transactions*, 1986, 17A, pp. 2265-2270.
33. S. Kou and Y. H. Wang: *Welding Journal*, 1986, 65, 3, pp. 63s-70s.
34. R. T. C. Choo and J. Szekely: *Welding Journal*, 1994, 73, 2, pp. 25s-31s.
35. K. Hong, D. C. Weckman, and A. B. Strong: *Trends in Welding research, Proceedings of the 4th International Conference*, edited by H. B. Smartt, J. A. Johnson, and S. A. David, 1995, pp. 399-404.

36. K. Hong: Ph.D. Thesis, 1996, University of Waterloo, Waterloo, Ontario, Canada.
37. M. Pastor, H. Zhao, R. P. Martukanitz, and T. DebRoy: *Welding Journal*, 1999, 78, 6, pp. 207s-216s.
38. M. Malinowski-Brodnicka, W. J. P. Vink, and G. den Ouden: *Welding Journal*, 1990, 62, 2, pp. 52s-59s.
39. H. Tennekes and J. L. Lumley: *A First Course in Turbulence*, 1974, The MIT Press. Cambridge, Massachusetts.
40. B. E. Launder and D. B. Spalding: *Mathematical Models of Turbulence*, 1972, Academic Press, New York, NY.
41. S. Kou and Y. Le: *Metallurgical Transactions*, 1983, 14A, pp. 2245-2253.
42. W. Pitscheneder, R. Ebner, T. DebRoy, and K. Mundra: *Welding Journal*, 1996, 75, 3, pp. 71s-80s.
43. P. Sahoo, T. DebRoy, and M. J. McNallan: *Metallurgical Transactions*, 1988, 19B, pp. 483-491.
44. P. R. Scheller, R. F. Brooks, and K. C. Mills: *Welding Journal*, 1995, 74, 2, pp. 69s-75s.
45. L. Goumiri, J. C. Joud, P. Desre, and J. M. Hicter: *Surface Science*, 1979, 83, 2, pp. 471-486.
46. J. E. Hatch: *Aluminum: Properties and Physical Metallurgy*, 1984, ASM, Metal Park, Ohio.
47. J. Goicoechea, C. Garcia-Cordovilla, E. Louis, and A. Pamies: *Journal of Materials Science*, 1992, 27, 19, pp. 5247-5252.
48. D. E. Swift-Hook and A. E. F. Gick: *Welding Journal*, 1973, 52, 11, pp. 492s-499s.
49. J. G. Andrews and D. R. Atthey: *Journal of Physics D: Applied Physics*, 1976, 9, pp. 2181-2194.
50. P. G. Klemens: *Journal of Applied Physics*, 1976, 47, 5, pp. 2165-2174.
51. J. Mazumder and W. M. Steen: *Journal of Applied Physics*, 1980, 51, 2, pp. 941-947.
52. J. Dowden, M. Davis, and P. Kapadia: *Journal of Fluid Mechanics*, 1983, 126, pp. 123-146.
53. M. Davis, P. Kapadia, and J. Dowden: *Welding Journal*, 1986, 65, 7, pp. 167s-174s.

54. J. Dowden, N. Postacioglu, M. Davis, and P. Kapadia: *Journal of physics D: Applied Physics*, 1987, 20, pp. 36-44.
55. N. Postacioglu, P. Kapadia, M. Davis, and J. Dowden: *Journal of Physics D: Applied Physics*, 1987, 20, pp. 340-345.
56. A. Kar and J. Mazumder: *ICALEO'94*, 1994, pp. 490-498.
57. P. S. Mohanty and J. Mazumder: *Science and Technology of Welding and Joining*, 1997, 2, 3, pp. 133-138.
58. W. M. Steen, J. Dowden, M. Davis, and P. Kapadia: *Journal of Physics D: Applied Physics*, 1988, 21, pp. 1255-1260.
59. G. Herziger et al.: in '*Laser Materials Processing*', Plenum Press, NY, 1984, p. 55.
60. A. Kar, T. Rockstroh, and J. Mazumder: *Journal of Applied Physics*, 1992, 71, pp. 2560-2569.
61. M. Beck, P. Berger, H. Hugel: in '*Laser Treatment of Materials*', Proceedings of ECLAT'92 conference, Gottingen, Germany, edited by B. L. Mordike, 1992, pp.693-698.
62. A. Kaplan: *Journal of Physics D: Applied Physics*, 1994, 27, pp. 1805-1814.
63. J. Kross, U. Gratzke, and G. Simon: *Journal of Physics D: Applied Physics*, 1993, 26, pp. 474-480.
64. E. A. Metzbower: *Metallurgical Transactions*, 1993, 24B, pp. 875-880.
65. A. Cybulski and Z. Mucha: *Welding International*, 1997, 11, 3, pp. 212-220.
66. A. Matsunawa, J. D. Kim, N. Seto, M. Mizutani, and S. Katayama: *Journal of Laser Applications*, 1998, 10, 6, pp. 247-254.
67. J. Kroos, U. Gratzke, M. Vicaneck, and G. Simon: *Journal of Physics D: Applied Physics*, 1993, 26, pp. 481-486.
68. T. Klein, M. Vicaneck, J. Kroos, I. Decker, and G. Simon: *Journal of Physics D: Applied Physics*, 1994, 27, pp. 2023-2030.
69. A. Matsunawa and V. Semak: *Journal of Physics D: Applied Physics*, 1997, 30, pp. 798-809.
70. I. Miyamoto and H. Maruo: *Welding International*, 1996, 10, 6, pp. 448-453.
71. P. A. A. Khan, T. DebRoy, and S. A. David: *Welding Journal*, 1988, 67, 1, pp. 1s-7s.

72. L. R. Morris et al.: in '*Aluminum Transformation Technology and Applications*', 1982, p. 549-582, edited by C. A. Pampillo et al., American Society for Metals.
73. D. W. Moon and E. A. Metzbower: *Welding Journal*, 1983, 62, 2, pp. 53s-58s.
74. T. Lida and R. I. L. Guthrie: '*The Physical Properties of Liquid Metals*', 1993, p. 88, Oxford, Clarendon Press.
75. A. Block-Bolten and T. W. Eagar: *Metallurgical Transactions*, 1984, 15B, pp. 461-469.
76. M. M. Collur, A. Paul, and T. DebRoy: *Metallurgical Transactions*, 1987, 18B, pp. 733-739.
77. P. Sahoo, M. M. Collur, and T. DebRoy: *Metallurgical Transactions*, 1988, 19B, pp. 967-972.
78. F. D. Richardson: '*Physical Chemistry of Melts in Metallurgy*', 1974, Vol. 2, pp. 452-253, Academic Press.
79. M. Pastor, H. Zhao, and T. DebRoy: *Indian National Welding Seminar*, 1997, pp. 31-46.
80. T. DebRoy, S. Basu, and K. Mundra: *Journal of Applied Physics*, 1991, 70, pp. 1313-1319.
81. K. Mundra and T. DebRoy: *Metallurgical Transactions*, 1993, 24B, pp. 145-155.
82. K. Mundra and T. DebRoy: *Welding Journal*, 1993, 72, 1, pp. 1s-9s.
83. C. L. Chan and J. Mazumder: *Journal of Applied Physics*, 1987, 62, pp. 4579-4586.
84. L.A. Guitierrez, G. Neye, and E. Zschech: *Welding Journal*, 1996, 75, 4, pp. 115s-121s.
85. S. Katayama, C. D. Lundin, and J. C. Danko: '*Recent Trends in Welding Science and Technology*', 1990, pp. 687-691, edited by S. A. David and J.M. Vitek, ASM International.
86. I. Jones, S. Riches, J.W. Yoon, and E.R. Wallach: in *Proceedings of LAMP '92*, Nagasaki, Japan, June 1992.
87. C. Ramasamy and C. E. Albright: "*CO<sub>2</sub> and Nd:YAG Laser Beam Welding of Aluminum Alloy 6111-T4*", Edison Welding Institute MR-Report, 1998.



88. C. Ramasamy and C. E. Albright: "*CO<sub>2</sub> and Nd:YAG Laser Beam Welding of Aluminum Alloy 5754-O*", Edison Welding Institute MR-Report, 1998.
89. S. Venkat, C. E. Albright, S. Ramasamy, and J.P. Hurley: *Welding Journal*, 1997, 76, 7, pp. 275s-282s.
90. M. Kutsuna, J. Suzuki, S. Kimura, S. Sugiyama, M. Yuhki, and H. Yamaoka: *Welding in the World/Le Soudage dans le Monde*, 1993, 31, 2, pp. 126-135.
91. M. J. Cieslak and P. W. Fuerschbach: *Metallurgical Transactions*, 1988, 19B, pp. 319-329.
92. S. Krishnaswamy and W. Baeslack: *Materials Characterization*, 1990, 24, pp. 331-353.
93. J. Mazumder and S. Bhandari: "*Laser Welding of Aluminum Alloys*", Report to Ford Motor Company, July 1999.
94. T. Starzer, R. Ebner, W. Glatz, F. Ellermann, and W. Kuehlein: in *Proceedings of the 26th International Symposium on Automotive Technology and Automation, Laser Applications in the Automotive Industries*, September 1993, pp. 131-138, Aachen, Germany.
95. R. P. Martukanitz, F. G. Armao, B. Altshuller, and E. R. Pickering: in *Proceedings of Developments in Aluminum Use for Vehicle Design*, Detroit, Michigan, USA, 26-29 Feb. 1996, Society of Automotive Engineers (USA), pp. 69-78.
96. R. P. Martukanitz and D. J. Smith: in *Proceedings of the Sixth International Conference on Aluminum Weldments*, 1995, pp. 309-323, AWS, Cleveland, OH.
97. D. J. Smith: M.S. Thesis, 1994, The Pennsylvania State University, PA.
98. R. P. Martukanitz and B. Altshuller: *ICALEO'96, Proceedings of Lasers and Electro-Optics for Automotive Manufacturing*, Vol. 82, p. 39, October 14-16, 1996, Detroit, Michigan.
99. P. A. Hilton: *Optical and Quantum Electronics*, 1995, 27, pp. 1127-1147.
100. J. Rapp, C. Glumann, F. Dausinger, and H. Hugel: *Optical and Quantum Electronics*, 1995, 27, pp. 1203-1211.
101. R. F. Ashton, R. P. Wesley, and C. R. Dixon: *Welding Journal*, 1975, 54, 3, pp. 95s-98s.

102. M. Katoh: *Journal of Light Metal Welding and Construction*, 1996, 34, 4, pp. 42-48.
103. K. P. Abraham and T. DebRoy: *Aluminum India*, 1998, 15, 2, pp. 13-18.
104. T. B. Massalski: *'Binary Alloy Phase Diagrams'*, 1990, Vol. 1, Materials Park, Ohio, ASM International.
105. E. T. Turkdogan: *'Physical Chemistry of High Temperature Technology'*, 1980, p.5, Academic Press, Inc., New York.
106. J. F. Elliott and M. Gleiser: *'Thermochemistry for Steelmaking (I)'*, 1963, p. 75, Addison-Wesley Publishing Co., Reading, MA.
107. S. Katayama: *Journal of Light Metal Welding and Construction*, 1996, 34, 4, pp. 31-41.
108. C. E. Ransley and H. Neufeld: *Journal of Institute of Metals*, 1948, 74, pp. 599-604.
109. W. R. Opie and N. J. Grant: *Transactions of AIME*, 1950, 188, pp. 1237-1242.
110. W. Baukloh and Z. Oesterlen: *Z. Metallkunde*, 1938, 30, pp. 386-390.
111. C. E. Ransley and D. E. J. Talbot: *Z. Metallkunde*, 1955, 46, pp. 328-332.
112. D. Stephenson: Ph. D. Thesis, 1978, Brunel University, Middlesex, England.
113. H. Shahani: Ph. D. Thesis, 1984, The Royal Institute of Technology, Stockholm, Sweden.
114. J. Kocur, K. Tomasek, and L. Rabatin: *Hutnicke Listy*, 1989, 44, 4, pp. 269-275.
115. D. E. J. Talbot and P. N. Anyalebechi: *Journal of Materials Science and Technology*, 1988, 4, 1, pp. 1-4.
116. H. Liu, L. Zhiang, and B. Bouchard: in *'Recent Developments in Light Metals'*, edited by M. Gilbert, P. Tremblay, and E. Ozberk, 1994, p. 257, Canadian Institute of Metallurgists.
117. S. A. Gedeon and T. W. Eagar: *Welding Journal*, 1990, 69, 7, pp. 264s-271.
118. P. N. Anyalebechi: *Scripta Metallurgica et Materialia*, 1995, 33, 8, pp. 1209-1216.
119. Q.T. Fang, P.N. Anyalebechi, and D. A. Granger: in *Proceedings of TMS Annual Meeting of Light Metals*, 1988, pp. 477-486.
120. P. M. Thomas and J. E. Gruzleski: *Metallurgical Transactions*, 1978, 9B, pp. 139-141.
121. J. H. Vaccari: *American Machinist*, 1991, 135, 2, pp. 50-52.

122. G. E. Metcalfe: *Journal of Institute of Metals*, 1945, 71, p. 618.
123. M. Pastor: M. S. Thesis, 1998, The Pennsylvania State University, PA.
124. L. Rayleigh: *Philosophical Magazine*, 1917, 34, 6, p. 94.
125. G. K. Batchelor: '*An Introduction to Fluid Dynamics*', 1967, p. 490, Cambridge University Press, Cambridge.
126. J. Kroos, U. Gratzke, and G. Simon: *Journal of Physics D: Applied Physics*, 1993, 26, pp. 474-480.
127. R. Ducharme, P. Kapadia, and J. Dowden: *ICALEO'93*, Laser Materials Processing, edited by P. Denney et al., October 1993, pp. 177-183, Orlando, Florida, Laser Institute of America.
128. R. Ducharme et al.: *ICALEO'92*, Laser Materials Proceeding, edited by D. Farson, W. Steen, and I. Miyamoto, October 1992, pp. 176-186, Orlando, Florida, Laser Institute of America.
129. A. Matsunawa, J. D. Kim, and S. Katayama: *ICALEO'97*, Laser Materials Processing, San Diego, CA, November 1997, pp. 73-82, Laser Institute of America.
130. D. A. Schauer and W. H. Giedt: *Welding Journal*, 1978, 57, 7, pp. 189s-195s.
131. M. Avedesian and H. Baker: *Magnesium and Magnesium Alloys*, 1999, ASM International, Materials Park, OH.
132. B. A. Mikucki and J. D. III. Shearouse: in *Proceedings of Magnesium Properties and Applications for Automobiles Conference*, Detroit, MI, 1-5 March 1993, pp. 107-115, Society of Automotive Engineers, Inc. (USA).
133. J. D. III. Shearouse and B. A. Mikucki: *SAE Transactions: Journal of Materials & Manufacturing (USA)*, 1994, 103, pp. 542-552.
134. H. Haferkamp, Fr.-W. Bach, I. Burmester, K. Kreutzburg, and M. Niemeyer: in *Proceedings of the Third International Magnesium Conference*, 1996, pp. 89-98, edited by G. W. Lorimer, the Institute of Materials, London, UK.
135. S. Katayama and C. D. Lundin: *Journal of Light Metal Welding and Construction*, 1991, 29, 9, pp. 1-13.
136. M. Kutsuna: in *Proceedings of the 27th International Symposium on Automotive Technology and Automation*, Oct 31-Nov 4 1994, p. 427, Aachen, Germany.

137. J. O. Milewski, G. K. Lewis, and J. E. Wittig: *Welding Journal*, 1993, 72, pp. 341s-346s.
138. J. C. Lippold: in *Proceedings of Taiwan International Welding Conference on Technology Advancements and New Industrial Applications in Welding*, September 1998, pp. 35-46.
139. J. C. Borland and R. N. Younger: *British Welding Journal*, 1960, 7, pp. 22-59.
140. J. C. Borland: *British Welding Journal*, 1961, 8, 11, pp. 526-540.
141. D. Van Der Torre and N. M. J. Romijn: *IIW Doc.*, IX-526-67, 1967.
142. J. A. Williams and A. R. E. Singer: *Journal of Australian Institute of Metals*, 1966, 11, 1, pp. 2-9.
143. J. C. Borland: *British Welding Journal*, 1960, 7, pp. 508-512.
144. F. Matsuda, H. Nakagawa, and K. Sonoda: *Trans. JWRI*, 1982, 11, 2, pp. 67-77.
145. J. H. Dudas and F. R. Collins: *Welding Journal*, 1966, pp. 241s-249s.
146. R. A. Patterson and J. O. Milewski: *Welding Journal*, 1985, 64, pp. 227s-231s.
147. G. M. Ecar and H. D. Brody: in *'Trends in Welding Research in the United States'*, 1982, pp. 399-417, edited by S. A. David, ASM, Metals Park, Ohio.
148. U. I. Birman and A. V. Petrov: *SVAR Proiz*, 1971, 6, pp. 14-17.
149. L. Guitierrez, G. Neye, and E. Zschech: *Welding Journal*, 1996, 75, 4, pp. 115s-121s.
150. I. Stol: *Welding Journal*, 1994, 73, pp. 57-65.
151. T. Watanabe, Y. Yoshida, and T. Arai: in *Proceedings of the International Conference on Laser Advanced Materials Processing*, 1992, pp. 505-510, Nagaoka, Japan.
152. H. Yunjia, R. H. Frost, D. L. Olson, and G. R. Edwards: *Welding Journal*, 1989, pp. 280s-289s.
153. F. Matsuda, H. Nakagawa, K. Nakata, and R. Ayani: *Trans. JWRI*, 1978, 7, 1, pp. 111-127.
154. S. Venkataraman, J. H. Devletian, W. E. Wood, and D. G. Atteridge: in *'Grain Refinement in Castings and Welds'*, 1983, p. 275, edited by G. J. Abbaschian and S. A. David, The Metallurgical Society, Warrendale, PA.
155. M. E. Wells and W. Z. Lukens: *Welding Journal*, 1986, 65, 12, pp. 314s-320s.

156. F. Matsuda: in *'Recent Trends in Welding Science and Technology'*, 1989, pp. 127-136, edited by S. A. David and J. M. Vitek, ASM International, Materials Park, Ohio.
157. S. Kou: in *'Recent Trends in Welding Science and Technology'*, 1989, pp. 137-146, edited by S. A. David and J. M. Vitek, ASM International, Materials Park, Ohio.
158. E. A. Brandes: *'Smithells Metals Reference Book'*, 6th ed., 1983, in association with Flumer Research Institutes Ltd.
159. Y. S. Touloukian: *'Thermophysical Properties of High Temperature Solid Materials'*, v. 1, 1967, New York, Macmillan.

## **Chapter 3**

### **WELD METAL COMPOSITION CHANGE DURING CONDUCTION MODE LASER WELDING OF ALUMINUM ALLOY 5182**

#### **3.1 Background**

During laser welding of automotive aluminum alloys, weld metal composition change caused by selective vaporization of volatile alloying elements may affect the mechanical properties, corrosion resistance, and hot cracking susceptibility of weldments [1-3]. Experimental and theoretical investigations have been conducted to understand the vaporization of various species from the weld pool during fusion welding of several important engineering alloys and pure metals [4-13]. The weld metal composition change depends on the vaporization flux and the melting rate, the latter often being more important in determining the composition change [13]. These understandings are qualitative in nature. In order to achieve quantitative understanding and accurate prediction of vaporization rates and weld metal composition change, a comprehensive model needs to be developed.

Accurate determination of weld pool temperature field is a prerequisite for the calculation of weld metal composition change since temperature is the most important factor in determining the vaporization rates of alloying elements. Due to the small size of the weld pool, experimental study of the nature of the fluid flow and measurement of temperature in the weld pool are difficult. However, through simulation of the fluid flow and heat transfer in the weld pool, comprehensive mathematical models [14-23] can help address some of these difficulties and provide a reliable means of determining the temperature and velocity fields in the weld pool. With the aid of high performance computers, calculations of fluid flow and heat transfer in the weld pool are now routinely performed through numerical solution of the equations of conservation of mass, heat, and momentum.

The earlier models [14-17] assumed that the fluid flow in the weld pool was laminar in nature. However, there are evidences [24] that suggest the existence of turbulence in the weld pool. It is known that the existence of turbulence in the fluid flow greatly enhances the rates of transport and mixing of mass, momentum, and energy [25]. Some models [18-21] treat the fluid flows in the weld pool the same way as with laminar flows. But the enhanced mixing and transport rates by the presence of turbulence are taken into account by using constant effective viscosity and effective thermal conductivity which are much higher than their respective molecular values. The calculated weld pool shapes have better agreement with the experiment data than laminar models. However, the effective viscosity and effective thermal conductivity should vary with the structure and condition of the flow. More rigorous calculations [22,23] incorporated turbulence models such as K- $\epsilon$  model [26] to calculate the spatial distributions of turbulence viscosity and turbulence thermal conductivity. The present study will adopt this approach.

Mathematical modeling has been used to understand complex physical phenomena related to welding. Several of these phenomena include the prediction of microstructures in C-Mn steels [27,28] and titanium [29], the growth and dissolution of oxide inclusions during the submerged metal arc welding of low alloy steels [30], the role of sulfur in affecting weld pool size and shape during the laser spot welding of tool steels [31,32], and concentrations of dissolved gases in GTA welds [33,34].

Vaporization of alloying elements and consequently, weld metal composition change involve complex physical phenomena. In early studies, the Langmuir equation [35] was widely used for the estimation of vaporization rates during welding. This simple model is useful in predicting the relative vaporization rates of various alloying elements. However, since it was derived for vaporization in vacuum, where no significant condensation of the vaporized species occurs, the Langmuir equation significantly overestimates the vaporization rate under commonly used welding conditions [7]. Therefore, a realistic

model for the calculation of vaporization rate has to take into account the condensation rate in the ambient pressure.

Anisimov and Rakhmatulina [36] and Knight [37] derived equations for the calculation of vaporization and condensation rates for pure metals by solving the equations of conservation of mass, momentum and energy in a thin layer adjacent to the liquid-vapor interface, known as the Knudsen layer. Their results have been incorporated into several recent models [10-12] to calculate laser-induced vaporization rates and the resulting composition changes in welding of pure metals and alloys. Higher accuracy in the calculated vaporization rates was achieved due to the consideration of more details of the physical processes involved. However, these models are applicable only to spot welding [10] or welding at low speeds [11,12]. A more realistic three-dimensional model is needed for applications in high speed laser welding.

The comprehensive model developed in the present study includes the calculations of the turbulent fluid flow and heat transfer in three-dimensional weld pool, the vaporization rates of alloying elements, and the resulting weld metal composition change for conduction mode laser welding. The calculation of fluid flow and heat transfer involves numerical solutions of the equations of conservation of mass, momentum, and energy. The effect of turbulence on fluid flow and heat transfer in the weld pool has been taken into account by incorporating the K- $\epsilon$  turbulence model [26] into the laminar model previously developed in Penn State [38]. The vaporization rates of alloying elements are calculated by considering vapor flux due to total pressure and concentration gradients. The condensation rates have been taking into account in the calculations. The validity of this model has been tested by comparing the modeling results with the experimental results.



### **3.2 Experimental Procedure**

**Bead-on-plate autogenous welds of aluminum alloy 5182 plates of 1.0 mm thickness were produced using a continuous wave Nd:YAG laser. The composition of the alloy is given in Table 3.1. In the table, the concentrations of magnesium and zinc were determined by a spectrochemical technique from actual test samples while the concentrations of other elements are nominal specified values. The welding parameters used in this investigation are given in Table 3.2. A defocused laser beam was used in order to obtain a conduction mode welding. A nomenclature of positive defocusing to represent the focal point to be above the top surface of the workpiece and negative defocusing to represent the focal point to be below the top surface will be used throughout this thesis. The laser beam was delivered, using a 600  $\mu\text{m}$  diameter fiber of fused silica to an f2 focus optic manipulated by a micro-positioning stage mounted on a linear translation device. An ancillary copper nozzle having an 8.0 mm inner diameter was utilized to provide helium shielding gas at a flow rate of 1.6 l/s.**

**After welding, the weld pool cross sectional area, depth and width were measured by standard metallography and computer image analysis. The elemental composition in the weld pool was determined by electron microprobe analysis. The concentrations of magnesium and aluminum in the weld metal were obtained from the average of at least 15 data points at different locations within the fusion zone. Since other alloying elements constitute less than 1 wt%, they were not measured. In order to avoid erroneous data caused by localized interdendritic segregation, each elemental measurement was obtained over an area of 100 x 100  $\mu\text{m}$ .**

**Table 3.1 Composition of aluminum alloy 5182.**

<b>Alloying element</b>	<b>Mg</b>	<b>Si</b>	<b>Mn</b>	<b>Cr</b>	<b>Cu</b>	<b>Zn</b>	<b>Ti</b>	<b>Al</b>
<b>wt. %</b>	<b>4.20</b>	<b>0.20</b>	<b>0.35</b>	<b>0.10</b>	<b>0.15</b>	<b>0.07</b>	<b>0.10</b>	<b>balance</b>

**Table 3.2 Welding parameters used in the study.**

<b>Laser power</b>	<b>1.5 to 3.0 kW</b>
<b>Welding speed</b>	<b>95.3 to 116.4 mm/s</b>
<b>Beam defocusing</b>	<b>+/-1.5, +/-1.75, +/-2.0 mm</b>

### **3.3 Mathematical Modeling**

#### **3.3.1 Turbulent Fluid Flow and Heat Transfer in the Weld Pool**

During typical laser welding operations, the heat source moves at a constant velocity. When a Lagrangian or fixed coordinate system is used, the welding problem becomes unsteady and the solution of the equations of conservation of mass, energy, and momentum requires a large number of grids to accurately represent the moving heat source and the spatial variation of the heat flux. A small time step is also necessary to ensure accuracy and stability of the solution, making computation time very large and the solution procedure rather burdensome. On the other hand, these problems can be avoided by the use of an Eulerian coordinate system which moves with the heat source as schematically shown in Fig. 3.1. In this case, the governing equations for the conservation of mass, energy, and momentum are formulated for a coordinate system that is attached to the moving heat source, and the material enters and leaves the computational domain at the welding velocity. Under these conditions, the welding problem becomes steady state in a short period of time after the start of welding, thus making the solution much easier by decreasing computation time and the number of grids required significantly.

##### **3.3.1.1 Governing equations**

The present model uses an Eulerian coordinate system as shown in Fig. 3.1 to formulate the equations of conservation of mass, momentum, and energy. In order to treat the convective velocity as the primary unknown in the governing equations in the Eulerian coordinate system, the net velocity,  $V'$ , is subdivided into two components, i.e., the convective velocity,  $V$ , and the velocity of the moving heat source,  $U$ , as the following relationship:

$$V' = V + U \quad (3.1)$$

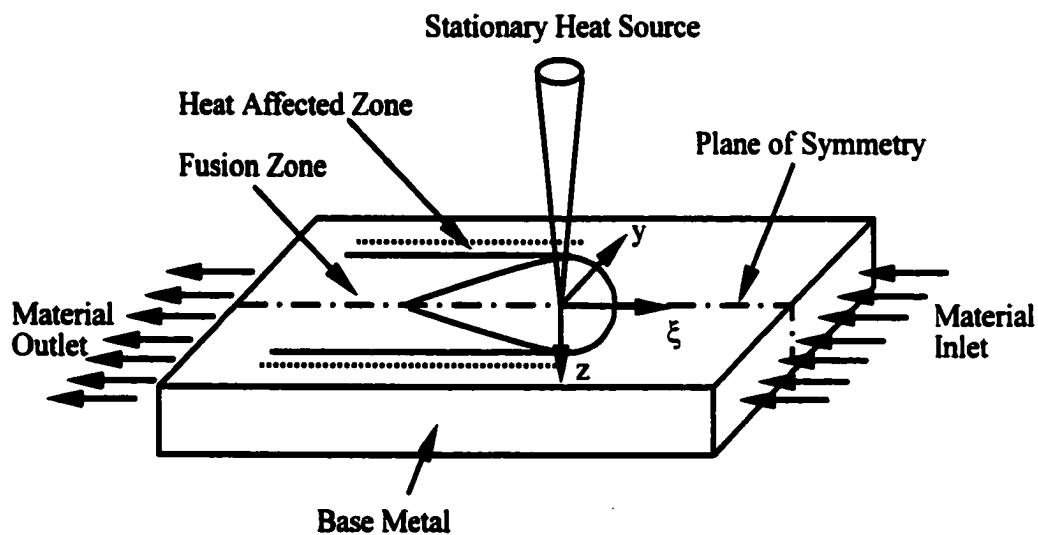


Fig. 3.1 Schematic diagram of coordinate system used in the 3D heat transfer and fluid flow model.

Using Eqn. (3.1), the steady state versions of the modified governing equations can be derived with  $\mathbf{V}$  as the primary unknown velocity. The equations of conservation of mass, momentum, and energy are formulated as

$$\nabla \cdot (\rho \mathbf{V}) = 0 \quad (3.2)$$

$$\nabla \cdot (\rho \mathbf{V} \mathbf{V}) = -\nabla P + \nabla \cdot (\mu_{\text{eff}} \nabla \mathbf{V}) + (S_v - \nabla \cdot (\rho \mathbf{U} \mathbf{V})) \quad (3.3)$$

$$\nabla \cdot (\rho \mathbf{V} h) = \nabla \cdot \left( \frac{k_{\text{eff}}}{C_p} \nabla h \right) + S_h + S_l - \nabla \cdot (\rho \mathbf{U} h) \quad (3.4)$$

where  $\rho$  is the density,  $P$  is the pressure,  $\mu_{\text{eff}}$  is the effective viscosity,  $S_v$  is the source term that takes into account the combined effect of buoyancy force and Marangoni force,  $h$  is the enthalpy,  $k_{\text{eff}}$  is the effective thermal conductivity,  $C_p$  is the specific heat,  $S_h$  is the source term that takes into account the heat input from the welding heat source and the heat losses due to convection, radiation, and evaporation,  $S_l$  is the source term that accounts for the latent heat of melting and convective transport of latent heat, and  $U$ ,  $V$ , and  $V'$  are velocity components described above.

The effective viscosity and thermal conductivity are used in the equations of conservation of momentum and energy to take into account the effects of turbulence on the fluid flow and heat transfer. The effective viscosity and thermal conductivity is given by

$$\mu_{\text{eff}} = \mu + \mu_t \quad (3.5)$$

$$k_{\text{eff}} = k + k_t \quad (3.6)$$

where  $\mu$  and  $\mu_t$  are the molecular and turbulent viscosity respectively,  $k$  and  $k_t$  are the molecular and turbulent thermal conductivity respectively. Here  $\mu$  and  $k$  are physical properties of the fluid, while  $\mu_t$  and  $k_t$  are properties of both the fluid and the flow system. The turbulent viscosity is calculated by

$$\mu_t = C_\mu \rho \frac{K^2}{\varepsilon} \quad (3.7)$$

where  $C_\mu$  is an empirical constant equal to 0.09,  $K$  is the time-averaged turbulent kinetic energy, and  $\varepsilon$  is the dissipation rate of turbulent kinetic energy. The two variables in this equation,  $K$  and  $\varepsilon$ , are obtained from the solution of their respective conservation equations [26] given by

$$\rho \left( V_x \frac{\partial K}{\partial x} + V_y \frac{\partial K}{\partial y} + V_z \frac{\partial K}{\partial z} \right) = \frac{1}{\sigma_k} \left[ \frac{\partial}{\partial x} \left( \mu_t \frac{\partial K}{\partial x} \right) + \frac{\partial}{\partial y} \left( \mu_t \frac{\partial K}{\partial y} \right) + \frac{\partial}{\partial z} \left( \mu_t \frac{\partial K}{\partial z} \right) \right] + \mu_t G_k - \varepsilon \quad (3.8)$$

$$\rho \left( V_x \frac{\partial \varepsilon}{\partial x} + V_y \frac{\partial \varepsilon}{\partial y} + V_z \frac{\partial \varepsilon}{\partial z} \right) = \frac{1}{\sigma_\varepsilon} \left[ \frac{\partial}{\partial x} \left( \mu_t \frac{\partial \varepsilon}{\partial x} \right) + \frac{\partial}{\partial y} \left( \mu_t \frac{\partial \varepsilon}{\partial y} \right) + \frac{\partial}{\partial z} \left( \mu_t \frac{\partial \varepsilon}{\partial z} \right) \right] + \frac{\varepsilon}{K} (C_1 G_k - C_2 \rho \varepsilon) \quad (3.9)$$

where  $V_x$ ,  $V_y$ , and  $V_z$  are the components of the convective velocity  $\mathbf{V}$  in the  $x$ ,  $y$ , and  $z$  directions in Cartesian system, the empirical constants  $\sigma_k$ ,  $\sigma_\varepsilon$ ,  $c_1$ , and  $c_2$ , are 1.0, 1.3, 1.45, and 1.92, respectively,  $\mu_t G_k$  is the turbulent counterpart to the viscous dissipation, and  $G_k$  is calculated by

$$G_k = 2 \left[ \left( \frac{\partial V_x}{\partial x} \right)^2 + \left( \frac{\partial V_y}{\partial y} \right)^2 + \left( \frac{\partial V_z}{\partial z} \right)^2 \right] + \left[ \left( \frac{\partial V_x}{\partial y} + \frac{\partial V_y}{\partial x} \right)^2 + \left( \frac{\partial V_x}{\partial z} + \frac{\partial V_z}{\partial x} \right)^2 + \left( \frac{\partial V_y}{\partial z} + \frac{\partial V_z}{\partial y} \right)^2 \right] \quad (3.10)$$

The turbulent thermal conductivity is obtained from its relationship with turbulent Prandtl number,  $Pr_t$ , and the turbulent viscosity as follows:

$$Pr_t = \frac{C_p \mu_t}{k_t} \quad (3.11)$$

For most of the well developed turbulent flows, the turbulent Prandtl number is usually 0.9. In this way, the spatial distributions of viscosity and thermal conductivity in the liquid weld pool can be calculated.

### 3.3.1.2 Boundary Conditions

Since the weld pool is symmetrical along the vertical plane that passes through the axis of the heat source and the welding direction, only half of the workpiece is considered. The boundary conditions for the solution of the equations of conservation of mass, momentum, and energy are defined primarily along the plane of symmetry and the top surface.

#### A. Boundary conditions for mass and momentum equations

In the solid region of the weldment, velocity is set equal to zero. On the vertical plane of symmetry ( $y = 0$  plane), the velocity components are defined by

$$\frac{\partial V_x}{\partial y} = 0 \quad (3.12)$$

$$V_y = 0 \quad (3.13)$$

$$\frac{\partial V_z}{\partial y} = 0 \quad (3.14)$$

On the top surface, the velocity component in z direction is set to zero and the velocity components in x and y directions are considered to be driven by the Marangoni stress and are defined by

$$-\mu_{\text{eff}} \frac{\partial V_x}{\partial z} = f_1 \frac{\partial \gamma}{\partial T} \frac{\partial T}{\partial x} \quad (3.15)$$

$$-\mu_{\text{eff}} \frac{\partial V_y}{\partial z} = f_1 \frac{\partial \gamma}{\partial T} \frac{\partial T}{\partial y} \quad (3.16)$$

where  $\partial \gamma / \partial T$  is the temperature coefficient of surface tension and  $f_1$  is the fraction of liquid, which is assumed to vary linearly with temperature in the mushy zone.

### B. Boundary conditions for energy equation

On the top surface ( $z=0$  plane), the heat flux, including the energy flux absorbed from the heat source and the energy fluxes lost to the surrounding due to radiation, convection, and evaporation is given by

$$J(\xi, y, z)_{z=0} = \frac{2\eta Q}{\pi r_b^2} e^{-\frac{2(\xi^2 + y^2)}{r_b^2}} - \epsilon_1 \sigma [T_1^4 - T_a^4] - h_c [T_1 - T_a] - \sum_{i=1}^n (\Delta H_i - \Delta H_i') J_i \quad (3.17)$$

where  $\eta$  is the heat absorption coefficient,  $Q$  is the laser power,  $r_b$  is the laser beam radius at the top surface of the workpiece,  $\epsilon_1$  is the emissivity,  $\sigma$  is the Stefan-Boltzmann constant,  $T_1$  is the local temperature on the top surface,  $T_a$  is the ambient temperature,  $h_c$  is the heat transfer coefficient,  $\Delta H_i$  is the heat of evaporation of alloying element  $i$ ,  $\Delta H_i'$  is the partial heat of mixing for alloying element  $i$  in the alloy, and  $J_i$  is the evaporation mass flux of alloying element  $i$ . On the right side of Eqn. (3.17), the first term represents the absorbed heat flux from the heat source that has a Gaussian distribution. The other



three terms represent the heat fluxes that are lost to the surrounding due to radiation, convection, and evaporation, respectively.

The laser beam profile and its relative position with the workpiece are schematically shown in Fig. 3.2. The laser beam radius at the top surface of the workpiece is given by [39]

$$r_b = r_0 \left[ 1 + \left( \lambda z_0 M^2 / (\pi r_0^2) \right)^2 \right]^{1/2} \quad (3.18)$$

where  $r_0$  is the beam radius at the focal point,  $\lambda$  is the beam wavelength,  $z_0$  is the beam defocusing, i.e. the distance from the focal point to the top surface of the weldment, and  $M^2$  is a dimensionless beam quality figure of merit that is given by [39]

$$M^2 = \pi r_0 \beta / \lambda \quad (3.19)$$

where  $\beta$  is the half angle of beam divergence. For a given laser, the value of  $M^2$  usually varies with increasing laser power due to the intrinsic distortions of the laser beam [39]. For a Nd:YAG laser, intrinsic distortion is caused by the temperature gradient across the laser rod. As a result, the beam size often increases with increasing laser power. This effect is taken into account in the calculations.

At the plane of symmetry ( $y = 0$  plane), the gradient of the enthalpy in  $y$  direction is set to be zero, i.e.:

$$\frac{\partial h}{\partial y} = 0 \quad (3.20)$$

At other surfaces of the system, the enthalpy is defined by setting the temperature to be ambient temperature.

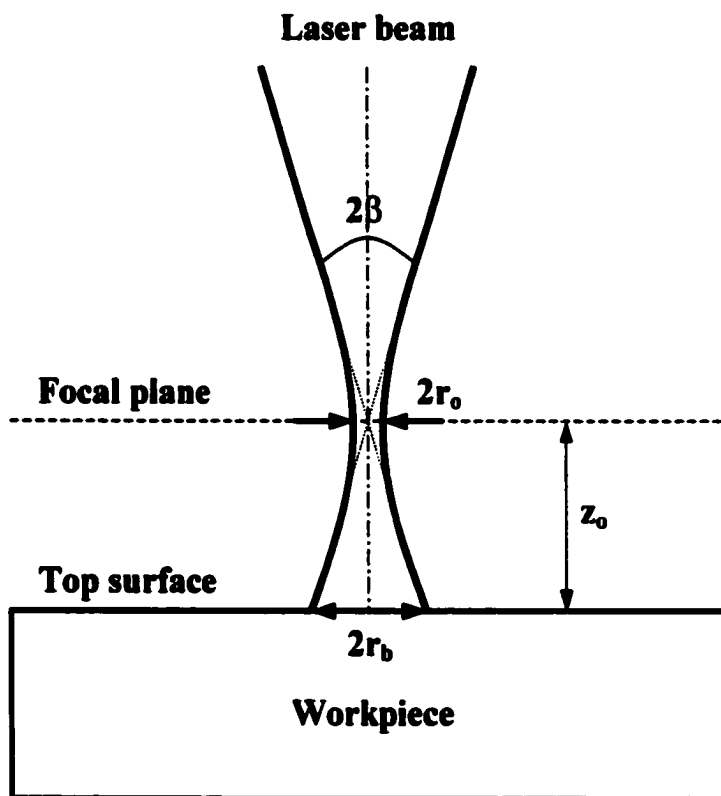


Fig. 3.2 Schematic diagram of laser beam profile and its position relative to the work-piece.

### C. Boundary conditions for K and $\varepsilon$

At the vertical plane of symmetry ( $y = 0$  plane), the boundary conditions for the turbulent kinetic energy, K, and its dissipation rate,  $\varepsilon$ , are defined as

$$\frac{\partial K}{\partial y} = 0 \quad (3.21)$$

$$\frac{\partial \varepsilon}{\partial y} = 0 \quad (3.22)$$

Similarly, at the top surface ( $z = 0$  plane), the boundary conditions for these two variables are defined as

$$\frac{\partial K}{\partial z} = 0 \quad (3.23)$$

$$\frac{\partial \varepsilon}{\partial z} = 0 \quad (3.24)$$

At the solid-liquid interface, the values of K and  $\varepsilon$  are set to be zero.

#### 3.3.1.3 Solution Procedure

A control-volume-based computational method developed by Patankar [40] has been used here to solve the governing equations defined above. In the solution scheme, these governing equations are represented in a finite difference form and solved iteratively on a line-by-line basis utilizing a Tri-Diagonal Matrix Algorithm (TDMA). The Semi-Implicit Method for Pressure-Linked Equations (SIMPLE) algorithm has been employed for the discretization of the equations. COMPACT-3D [41], a general-purpose Computational Fluid Dynamic (CFD) software package, developed by Innovative Research, Inc., has been used to solve these governing equations. In order to solve for each of the different variables, the program utilizes the solution of a general equation shown below [41]:

$$\frac{\partial}{\partial t}(\rho\phi) + \frac{\partial}{\partial x_i}(\rho u_i \phi) = \frac{\partial}{\partial x_i} \left( \Gamma \frac{\partial \phi}{\partial x_i} \right) + S \quad (3.25)$$

where  $\rho$  is the density,  $\phi$  is the dependent variable to be solved,  $\Gamma$  is the equivalent of diffusion coefficient, and  $S$  is the source term. The four terms in the above equation are the unsteady term, the convection term, the diffusion term, and the source term. For a steady state system, the unsteady term is set to zero by assigning a very large time step. The dependent variable can stand for a variety of physical quantities, and the choice of  $\phi$  gives appropriate meaning to both  $\Gamma$  and  $S$ . The value of  $\Gamma$  can be defined for conservation of momentum, energy, kinetic energy and its dissipation rate, respectively, using the following equations:

$$\Gamma = \mu_{\text{eff}} \quad \text{for transport of momentum} \quad (3.26)$$

$$\Gamma = \frac{k_{\text{eff}}}{C_p} \quad \text{for transport of energy} \quad (3.27)$$

$$\Gamma = \frac{\mu_t}{\sigma_k} \quad \text{for transport of kinetic energy} \quad (3.38)$$

$$\Gamma = \frac{\mu_t}{\sigma_\epsilon} \quad \text{for transport of kinetic energy dissipation rate} \quad (3.29)$$

where all the symbols in the above equations are as defined previously.

All of the governing equations are coupled and are solved iteratively. In the present study, the iterative procedure was made until the following criterion was satisfied:

$$\frac{\sum_p |\Phi - \Phi^{\text{old}}|}{\sum_p |\Phi|} < 0.001 \quad (3.30)$$

where  $\sum_p$  denotes summation over all the grid point P,  $\Phi$  is the variable to be solved, and  $\Phi^{\text{old}}$  is its value in the previous iteration step. In addition, two other quantities, SMAX and RSMAX, can be used to monitor the progress towards convergence. The quantity SMAX is the largest absolute value of the coefficients of the pressure-correction equation used in COMPACT-3D. The quantity RSMAX is a dimensionless form of SMAX and is obtained by dividing SMAX by the largest mass flow rate across any control volume face. These quantities are a measure of the lack of satisfaction of the continuity equation. Therefore, their values should be small when a converged solution is made. In the present study, the convergence is considered to be achieved only when these two quantities are on the order of  $10^{-3}$ .

In the course of calculation, the values of the calculated quantities may oscillate or even drift continuously. In order to avoid such divergence of the variables, several measures have been taken to promote convergence. First the following scheme, called “underrelaxation”, is employed:

$$a_p \Phi_p = \sum a_{nb} \Phi_{nb} + b \quad (3.31)$$

$$\text{as } (a_p + I) \Phi_p = \sum a_{nb} \Phi_{nb} + b + I \Phi_p^{\circ} \quad (3.32)$$

where  $a_p$  is the discretization coefficient at grid point p,  $\Phi_p$  is the unknown variable to be solved,  $a_{nb}$  are the discretization coefficients of neighbor grid points,  $\Phi_{nb}$  are the values of the unknown variable at the neighbor grid points, b is a constant term in discretization equation,  $\Phi_p^{\circ}$  is the value of  $\Phi_p$  in the previous iteration step, and I is the so-called inertia, defined as

$$I = \frac{(1-\alpha)}{\alpha} a_p \quad (3.33)$$

where  $\alpha$  is the relaxation factor and its value can be chosen in range between zero and unity. When  $\alpha$  equals to unity, no underrelaxation is introduced. As  $\alpha$  is close to zero, strong underrelaxation takes place and the changes in  $\phi$  from iteration to iteration are greatly reduced. Such underrelaxation serves to temporarily weaken the links between different variables so that the changes in one variable will not strongly affect the other ones and therefore, promote convergence. To promote faster convergence, another measure is to subdivide the calculation into several steps. Initially, the calculation is run in laminar model where the turbulent kinetic energy and its dissipation rate are not solved. After getting converged results from the laminar model, the K- $\epsilon$  model is incorporated starting from using very low values of relaxation factors for K and  $\epsilon$ . In later steps, the values of relaxation factors increase progressively until converged results are obtained.

### 3.3.2 Vaporization Rate and Composition Change in the Weld Metal

The present model is developed for studying vaporization and composition change in laser welding of 5000 series aluminum alloys. Several assumptions were made to simplify the calculations:

1) The 5000 series aluminum alloys are taken as Al-Mg binary alloys.

2) The activity of magnesium in the molten pool was calculated assuming Henry's law. At temperature of 1073K, the activity of magnesium is  $a_{Mg} = \gamma_{Mg}X_{Mg} = 0.88X_{Mg}$  [42], where  $X_{Mg}$  is the mole fraction of magnesium in the alloy. The activities of magnesium at other temperatures are calculated by assuming that the partial excess free energy of mixing ( $\Delta G^{xs} = RT \ln \gamma_{Mg}$ ) is constant. The activity of aluminum at any temperature is obtained from Raoult's law, i.e.,  $a_{Al} = X_{Al}$ , where  $X_{Al}$  is the mole fraction of aluminum in the alloy.

3) The concentrations of aluminum and magnesium in the weld pool are uniform but are different from those in the base metal. This was shown to be true in an experimen-

tal study [9] and is consistent with the existence of a strong recirculating flow of liquid metal in the weld pool.

Two driving forces for vaporization are considered in the model. One is the diffusion driven flux caused by the concentration gradient. Another one is the flux due to pressure gradient resulting from the high pressure at the center of the weld pool surface.

### 3.3.2.1 Vaporization Flux due to Concentration Gradient

The concentrations of metal vapors are higher near the weld pool surface than in the bulk shielding gas. The vapor flux of element  $i$ ,  $J_{c,i}$ , due to such a concentration gradient is defined as

$$J_{c,i} = K_{g,i} \left( M_i \frac{a_i P_i^\circ}{RT_i} - C_i^b \right) \quad (3.34)$$

where  $a_i$  is the activity of element  $i$  in the liquid metal,  $P_i^\circ$  is the equilibrium vapor pressure of element  $i$  over pure liquid,  $M_i$  is the molecular weight of element  $i$ ,  $R$  is the gas constant,  $T_i$  is the temperature at the weld pool surface,  $K_{g,i}$  is the mass transfer coefficient of element  $i$ , and  $C_i^b$  is the concentration of element  $i$  in the shielding gas. Since the concentration of element  $i$  in the shielding gas,  $C_i^b$ , is significantly lower than that at the weld pool surface, it can be neglected. The mass transfer coefficient between the weld pool surface and the exit of the shielding gas nozzle is calculated from the graphical results of Schlunder and Gnielinski for a jet impinging on a flat surface [43] and is given by

$$K_{g,i} = \frac{2Sc_i^{0.42} Re^{0.5} D_i}{d} \left( 1 + \frac{Re^{0.55}}{200} \right)^{0.5} \left[ 0.483 - 0.108 \frac{r}{d} + 7.71 \times 10^{-3} \left( \frac{r}{d} \right)^2 \right] \quad (3.35)$$

where  $d$  is the diameter of the nozzle in meters,  $r$  is the radial distance on the pool surface in meters,  $D_i$  is the average diffusivity of element  $i$  in the shielding gas,  $Re$  is the Reynolds number at the nozzle exit, and  $Sc_i$  is the average Schmidt number.

### 3.3.2.2 Vapor Flux due to Pressure Gradient

During laser welding, the peak temperature on the weld pool surface can exceed the boiling point of the alloy and, consequently, the vapor pressure at the weld pool surface can be higher than one atmosphere. For example, von Allmen [44] determined molten pool temperatures in excess of the boiling point for the laser treatment of copper. Batanov et al. [45] also indicated that temperatures on the surface of a laser irradiated material can be higher than the boiling point. Chan and Mazumder [10] have also reported computed temperatures greater than the boiling point during laser irradiation of aluminum, titanium and a superalloy. Theoretical calculations of the vaporization rates by Anisimov [36] and Knight [37] are based on the premise that the liquid pool surface temperatures are higher than the boiling point. Therefore, the convective flux of the vaporized elements, driven by the excess pressure, is an important contributor to the overall vaporization flux.

The velocity distribution functions,  $f_1$ ,  $f_2$ , and  $f_3$ , of the vapor molecules, escaping from the weld pool surface at various locations are shown schematically in Fig. 3.3. On the weld pool surface, the velocity distribution,  $f_1$ , is half-Maxwellian because the vapor molecules only move away from the pool surface, i.e. the velocity varies from 0 to  $+\infty$ . There exists a space of several mean free paths length near the weld pool surface, known as the Knudsen layer, at the outer edge of which the velocity distribution,  $f_3$ , just reaches Maxwellian distribution. Here, the velocity can vary from  $-\infty$  to  $+\infty$  as shown in Fig. 3.3. A portion of the vaporized material condenses on the liquid surface. The velocity



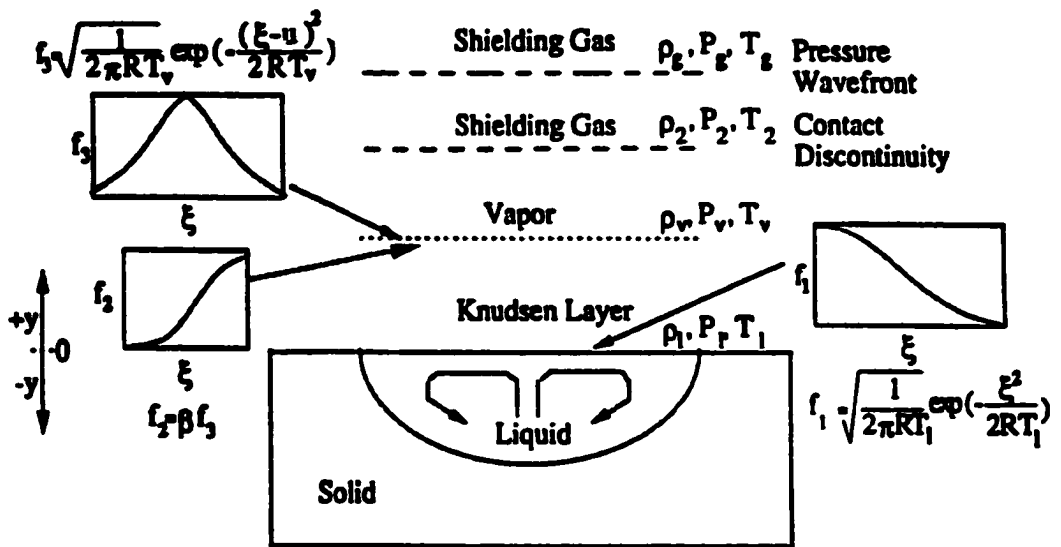


Fig. 3.3 Velocity distribution functions of vapor molecules at various locations.

distribution here,  $f_2$ , is half Maxwellian, i.e. the velocity varies from  $-\infty$  to 0. This rate of condensation was taken into account in the model.

The temperature  $T_v$ , density  $\rho_v$ , pressure  $P_v$ , and the mean velocity  $u$  of the vapor at the edge of the Knudsen layer can be related to temperature  $T_l$ , density  $\rho_l$ , and pressure  $P_l$ , of the vapor at the liquid surface by treating the Knudsen layer as a gas dynamic discontinuity. Anisimov [36] and Knight [37] derived expressions for the jump conditions in the vapor temperature, density, velocity, and the extent of condensation across the Knudsen layer by solving the equations of conservation of mass, momentum and translational kinetic energy, using the velocity distribution functions presented in Fig. 3.3. The derived jump conditions across the Knudsen layer are given by

$$\frac{T_v}{T_l} = \left[ \sqrt{1 + \pi \left( \frac{\gamma_v - 1}{\gamma_v + 1} \frac{m}{2} \right)^2} - \sqrt{\pi} \frac{\gamma_v - 1}{\gamma_v + 1} \frac{m}{2} \right]^2 \quad (3.36)$$

$$\frac{\rho_v}{\rho_l} = \sqrt{\frac{T_l}{T_v}} \left[ \left( m^2 + \frac{1}{2} \right) e^{m^2} \operatorname{erfc}(m) - \frac{m}{\sqrt{\pi}} \right] + \frac{1}{2} \frac{T_l}{T_v} \left[ 1 - \sqrt{\pi} m e^{m^2} \operatorname{erfc}(m) \right] \quad (3.37)$$

$$\beta = \left[ \left( 2m^2 + 1 \right) - m \sqrt{\pi \frac{T_l}{T_v}} \right] e^{m^2} \frac{\rho_l}{\rho_v} \sqrt{\frac{T_l}{T_v}} \quad (3.38)$$

where  $m = u / \sqrt{2R_v T_v}$ ,  $R_v = R/M_v$ ,  $R$  is the gas constant,  $\gamma_v$  is the ratio of specific heats of the vapor which is treated as a monatomic gas, and  $\beta$  is the condensation factor. The equilibrium vapor pressure,  $P_l$ , at the pool surface is obtained from the equilibrium vapor pressure-temperature relationships of the various alloying elements:

$$P_l = \sum_{i=1}^n a_i P_i^\circ \quad (3.39)$$

and  $M_v$ , the average molecular weight of the vapor is given by

$$M_v = \sum_{i=1}^n M_i \frac{a_i P_i^\circ}{P_l} \quad (3.40)$$

where  $a_i$  is the activity of element  $i$  in the weld pool,  $P_i^\circ$  is the equilibrium vapor pressure of pure element  $i$  at temperature  $T_i$ , and  $M_i$  is the molecular weight of element  $i$ .

There are four unknowns in equations (3.36) through (3.38), namely,  $T_v$ ,  $\rho_v$ ,  $\beta$ , and  $m$ . Therefore, another independent equation is required to obtain unique values of these variables. The necessary equation is obtained by applying the Rankine-Hugoniot relation [46] to relate the pressure at the edge of the Knudsen layer to the ambient conditions by

$$\frac{P_l}{P_g} \frac{P_2}{P_l} = 1 + \gamma_g M \Gamma \left[ \frac{\gamma_g + 1}{4} M \Gamma + \sqrt{1 + \left( \frac{\gamma_g + 1}{4} M \Gamma \right)^2} \right] \quad (3.41)$$

where  $P_g$  and  $P_2$  are the pressures in front of and behind the wavefront, respectively,  $P_2 = P_v$ ,  $\gamma_g$  is the ratio of specific heats for shielding gas, and  $\Gamma = \sqrt{\gamma_v R_v T_v} / \sqrt{\gamma_g R_g T_g}$ ,  $M$  is the Mach number which is related to  $m$  by the following relation:

$$m = M \sqrt{\frac{\gamma_v}{2}} \quad (3.42)$$

The Mach number  $M$  and the density  $\rho_v$ , obtained by solving equations (3.36) through (3.42), can be used to calculate the vaporization flux due to pressure gradient at the weld pool surface corresponding to a local surface temperature  $T_l$  from

$$J_p = \rho_v M S \quad (3.43)$$

where  $S$  is the speed of sound in vapor at temperature  $T_v$ . The vaporization flux of an alloying element  $i$ ,  $J_{p,i}$ , is given by the product of the total vapor flux and the mole fraction of  $i$  in the gas:

$$J_{p,i} = a_i \frac{P_i^\circ}{P_1} \frac{M_i}{M_v} J_p \quad (3.44)$$

From the results of equations (3.34) and (3.44), the total vaporization flux for element  $i$  can be obtained from

$$J_i = J_{c,i} + J_{p,i} \quad (3.45)$$

### 3.3.3 Vaporization Rate and Composition Change

The vaporization rate of element  $i$ ,  $G_i$ , is obtained by integrating the vapor flux over the entire weld pool surface, and the total vaporization rate of all the elements,  $G$ , is given by

$$G = \sum_{i=1}^n G_i = \sum_{i=1}^n \iint_s J_i dx dy \quad (3.46)$$

where  $J_i$  is the vapor flux of element  $i$  and  $s$  indicates the weld pool surface. The final composition in the weld pool is calculated by an iterative scheme with the initial values chosen to be those of the base metal. The concentration of element  $i$  in the weld pool,  $C_i$ , is given by

$$C_i = \frac{v A \rho C_{i,b} - G_i}{v A \rho - G} \quad (3.47)$$

where  $C_i$  and  $C_{i,b}$  are the concentration of element  $i$  in the weld pool and in the base metal, respectively,  $v$  is the welding speed,  $A$  is the across section area of the weld, and  $\rho$  is the density of the weld metal. After each iteration, the activities of the alloying elements in the weld pool are recalculated based on the calculated composition in the weld pool. Using the new values of activities of alloying elements, all calculations are repeated until the calculated composition in the weld pool converges.

The calculation of turbulent fluid flow and heat transfer and that of weld metal composition change are coupled. As seen in the schematic flow chart of the model in Fig. 3.4, vaporization rates of alloying elements are calculated based on the weld pool surface temperature. On the other hand, the evaporative heat loss is taken into account in the calculation of turbulent fluid flow and heat transfer.

#### **3.3.4 Data Used for the Calculations**

The temperature and velocity fields in the weld pool were calculated using the data presented in Table 3.3 [1,47-49]. The surface condition and addition of alloying elements greatly affects the absorption of laser radiation by aluminum. The reported values of absorption coefficient of Nd:YAG laser radiation by aluminum alloys vary from about 0.05 for very clean aluminum [50,51] to about 0.45 for chemically etched alloy AA1050 [52]. Due to the high sensitivity of the absorption coefficient to the surface conditions, small variations in absorption coefficient are expected. In the present model, the absorption coefficient was adjusted in the range of 0.22 to 0.25 to fit the experimentally determined weld pool size. The laser beam radius and absorption coefficient for various welding conditions are presented in Table 3.4. The nominal laser powers, which are different from the measured laser powers, are used to identify the welding conditions throughout this paper.

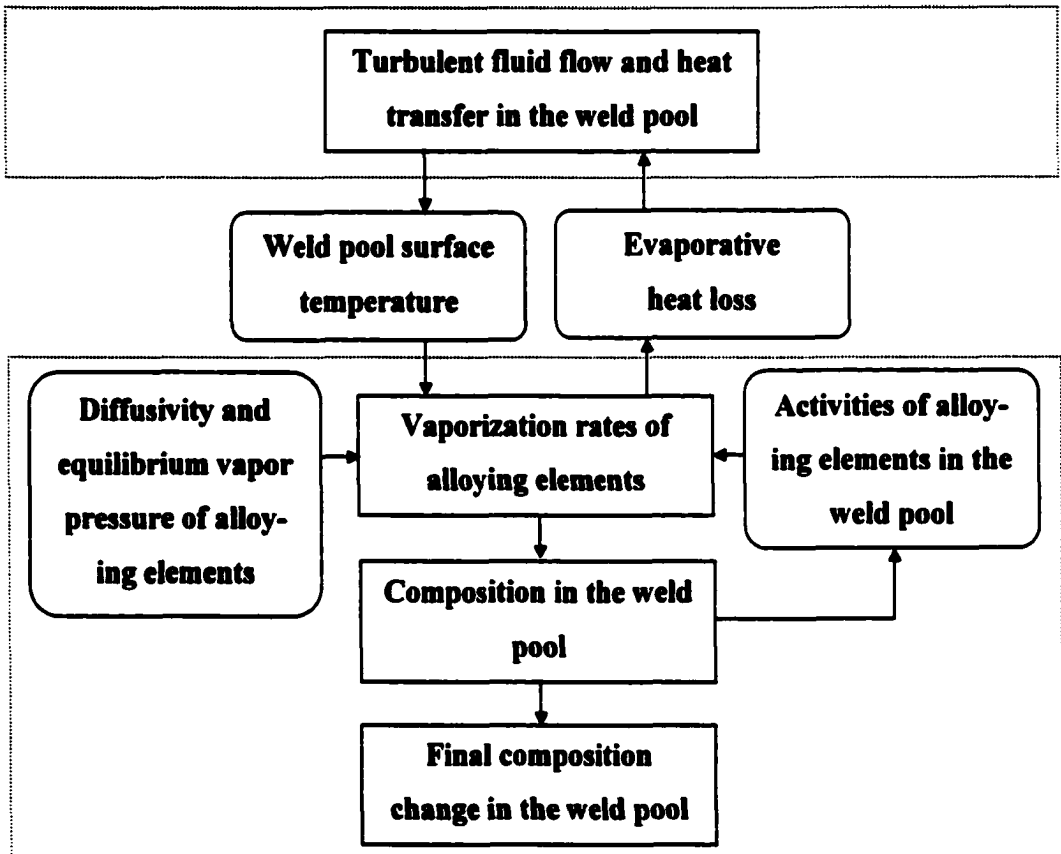


Fig. 3.4 Flow chart of the comprehensive model.

The data used for the calculation of vapor fluxes are presented as a function of temperature,  $T$ , and/or pressure,  $P$ , as shown in Table 3.5 [48, 53-55]. The procedure for the calculation of shielding gas viscosity and binary gaseous diffusivity is given below.

The viscosity of a gas,  $\mu_g$ , at absolute temperature  $T$ , is given by [53]

$$\mu_g = \frac{2.6693 \times 10^{-5}}{\sigma^2 \Omega_\mu} \sqrt{M_g T} \quad (3.48)$$

where  $\mu_g$  is in  $\text{gm cm}^{-1} \text{s}^{-1}$ ,  $\sigma$  is the collision diameter in  $\text{\AA}$ ,  $M_g$  is the molecular weight of gas in  $\text{gm/gm-mole}$ , and  $\Omega_\mu$  is a slowly varying function of the dimensionless parameter  $k_B T / \epsilon$ , where  $k_B$  is the Boltzmann constant in  $\text{erg/molecule-K}$  and  $\epsilon$  is the maximum energy of attraction between a pair of molecules in the Lennard-Jones potential energy function. The values of  $\Omega_\mu$  are tabulated as a function of  $k_B T / \epsilon$  [54]. The values of  $\sigma$  and  $\epsilon$  are known for many gases. When they are not readily available, they can be estimated from their empirical relations with the properties of the fluid at critical point, melting point or boiling point and molar volume [55]. In the present study the following relations are used to estimate the values of  $\sigma$  and  $\epsilon/k$  [55]:

$$\sigma = 1.22 V_m^{1/3} \quad (\text{\AA}) \quad (3.49)$$

$$\epsilon/k = 1.92 T_m \quad (\text{K}) \quad (3.50)$$

where  $V_m$  is the molar volume and  $T_m$  is the melting point.

The binary molecular diffusivity,  $D_{A/B}$ , of a gas pair A and B, at absolute temperature  $T$  is given by [53]

$$D_{A/B} = \frac{1.8583 \times 10^{-3}}{P \sigma_{A/B}^2 \Omega_D} \sqrt{\left(\frac{1}{M_A} + \frac{1}{M_B}\right) T^3} \quad (3.51)$$

where  $D_{A/B}$  is in  $\text{cm}^2\text{s}^{-1}$ ,  $P$  is pressure in atm,  $M_i$  is the molecular weight of the element  $i$ ,  $\sigma_{A/B} = (\sigma_A + \sigma_B)/2$ , the values of  $\Omega_D$  are also tabulated [54] as a function of  $k_B T/\epsilon_{A/B}$ , where  $\epsilon_{A/B} = \sqrt{\epsilon_A \epsilon_B}$ .

The viscosity of helium and the diffusivity of binary gas systems (Al-He and Mg-He) are calculated at temperatures in the range of 1000 to 3000K and pressure of 1 atm. Then the viscosity and diffusivity as a function of temperature,  $T$  and/or pressure,  $P$  in atm, are obtained from the calculated data by polynomial regression. These relations are given in Table 3.5.



Table 3.3 Data used for the calculations of weld pool temperature and velocity fields [1,47-49].

Property (unit)	Value	Reference
Liquidus temperature (K)	911	47
Solidus temperature (K)	850	47
Density of liquid metal (kg/m <sup>3</sup> )	2300	1
Enthalpy of solid at melting point (J/g)	721	1
Enthalpy of liquid at melting point (J/g)	1116	1
Specific heat of solid (J/g-K)	0.9	1
Specific heat of liquid (J/g-K)	1.2	1
Thermal conductivity of solid (J/m-s-K)	168	1
Thermal conductivity of liquid (J/m-s-K)	108	1
Viscosity of liquid (g/m-s)	1.1	1
Temperature coefficient of surface tension (N/m-K)	$-3.5 \times 10^{-4}$	48
Heat of vaporization for Mg (J/g)	5253	48
Heat of vaporization for Al (J/g)	10780	48
Partial heat of mixing for Mg in alloy 5182 (J/g)	556	49
Partial heat of mixing for Al in alloy 5182 (J/g)	0	49

**Table 3.4 Welding conditions and the corresponding beam radius and absorption coefficient used for the calculations.**

Nominal power (W)	Measured power (W)	Beam de-focusing (mm)	Welding speed (mm/s)	Absorption coefficient	Beam radius (mm)
1500	1600	1.50	105.8	0.23	0.32
2000	1700	1.50	105.8	0.25	0.35
2500	2040	1.50	105.8	0.23	0.38
3000	2510	1.50	105.8	0.22	0.41
3000	2510	1.75	95.3	0.22	0.42
3000	2510	1.75	105.8	0.22	0.42
3000	2510	1.75	116.4	0.22	0.42
3000	2510	2.00	95.3	0.23	0.43
3000	2510	2.00	105.8	0.23	0.43
3000	2510	2.00	116.4	0.23	0.43

Table 3.5 Data used for the calculations of vaporization rates [48,53-55].

Parameter	Formula	Reference
Viscosity of He (g/m-s)	$2.20 \times 10^{-2} + 2.22 \times 10^{-3} \times T$	[53-55]
Diffusivity of Al in He (mm <sup>2</sup> /s)	$(-1.20 \times 10^2 + 0.39 \times T + 2.09 \times 10^{-3} \times T^2) / P$	[53-55]
Diffusivity of Mg in He (mm <sup>2</sup> /s)	$(-1.10 \times 10^2 + 0.36 \times T + 1.96 \times 10^{-3} \times T^2) / P$	[53-55]
Al vapor pressure over pure liquid Al, P (atm)	$\log P = 12.36 - 1.65 \times 10^4 / T - 1.02 \times \log T - \log 760$	[48]
Mg vapor pressure over pure liquid Mg, P (atm)	$\log P = 12.79 - 7.55 \times 10^3 / T - 1.41 \times \log T - \log 760$	[48]

### 3.4 Results and Discussion

#### 3.4.1 Temperature and Velocity Fields in the Weld Pool

The calculated temperature and velocity fields in weld pool cross sections and the experimentally obtained weld pools for laser powers of 1.5 kW to 3.0 kW are shown in Fig. 3.5. The general features of the calculated temperature and velocity fields are consistent with calculated results reported in the literature [22,23,29]. It is observed that the calculated weld pool geometry and dimensions agree well with the experimental results. The peak temperatures near the center of the weld pool were about 2150 K, and these decreased progressively towards the periphery. For all cases, there is a recirculating flow in the weld pool driven mainly by surface tension (Marangoni) force. Since the temperature coefficient of surface tension is negative for this alloy, the molten metal on the surface flows from the center to the periphery of the pool as shown in the figures. The maximum flow velocities on the weld pool surface are on order of 1 m/s.

The high velocity flows occurring in weld pools resulted in rapid mixing and caused turbulence, which enhanced the rates of transport of energy and momentum. In the present model, turbulence was simulated by the use of effective viscosity,  $\mu_{\text{eff}} = \mu + \mu_t$ , and effective thermal conductivity,  $k_{\text{eff}} = k + k_t$ , in the equations of conservation of energy and momentum. Here,  $\mu$  and  $k$  are the molecular values of viscosity and thermal conductivity of the liquid, respectively. The turbulent viscosity,  $\mu_t$  and turbulent thermal conductivity,  $k_t$ , in the weld pool were calculated by solving the equations of conservation of turbulent kinetic energy,  $K$ , and its dissipation rate,  $\epsilon$ , from the  $K$ - $\epsilon$  model.

The distributions of the ratio of effective to molecular viscosity,  $\mu_{\text{eff}}/\mu$ , and the ratio of effective to molecular thermal conductivity,  $k_{\text{eff}}/k$ , in the cross section of a weld pool are shown in Fig. 3.6. The ratio of turbulent to molecular viscosity,  $\mu_t/\mu$ , reflects the degree of turbulence and is also defined as turbulence Reynolds number. The flow is considered fully turbulent when the value of  $\mu_t/\mu$  is higher than 100 [23]. Fig. 3.6 (a)

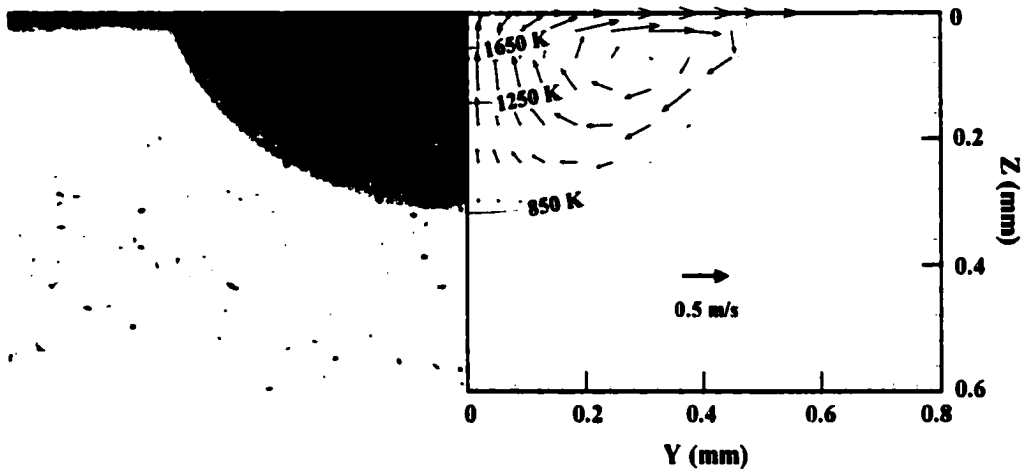


Fig. 3.5(a)

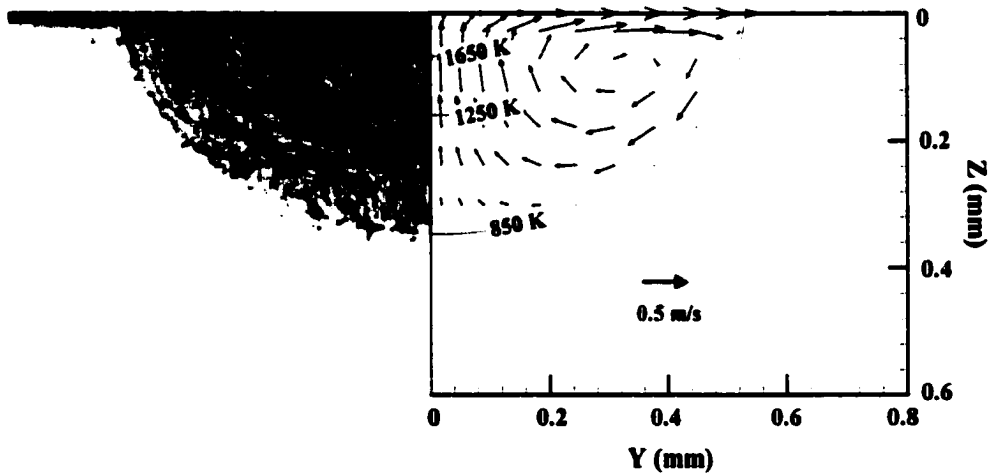


Fig. 3.5(b)

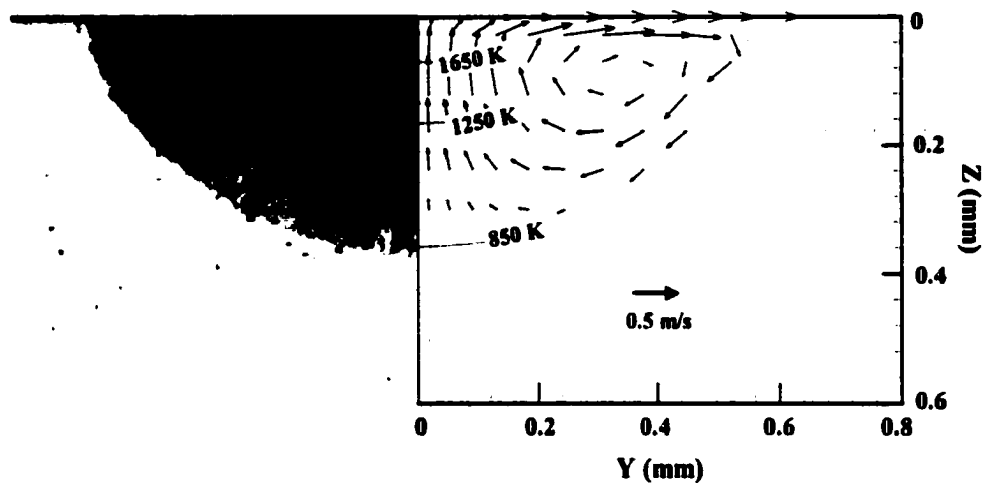


Fig. 3.5(c)

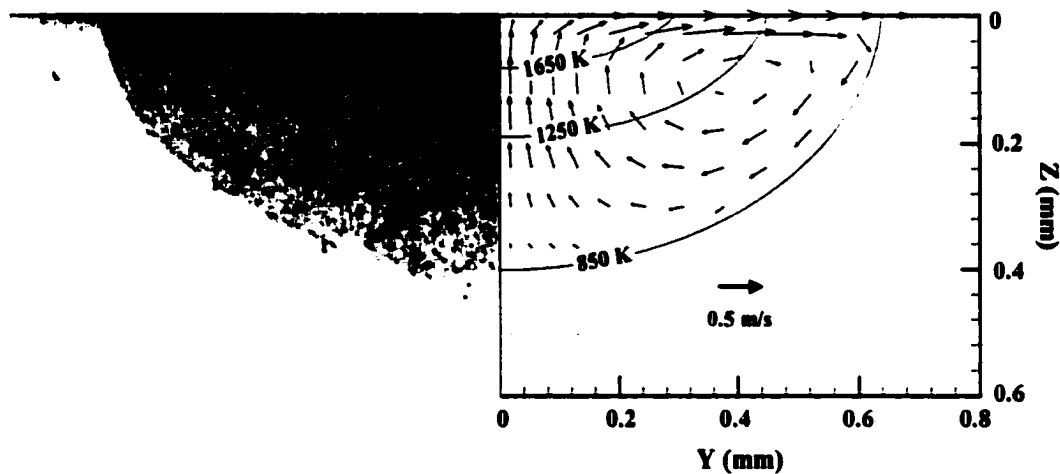


Fig. 3.5(d)

Fig. 3.5 Experimental and calculated weld pool cross sections for laser power of (a) 1.5 kW, (b) 2.0 kW, (c) 2.5 kW, and (d) 3.0 kW. Welding speed 105.8 mm/s, beam defocusing +1.5 mm, and other parameters are listed in Table 3.4.

shows that the maximum value of  $\mu_t/\mu$  is more than 110 near the weld pool surface, indicating a fully turbulent flow there. The maximum value of  $\mu_t/\mu$  is almost the same as that obtained for GTA welding of aluminum alloy 6061 [23]. The distribution of the ratio of effective to molecular thermal conductivity,  $k_{eff}/k$ , shown in Fig. 3.6(b) has the same pattern as that of  $\mu_{eff}/\mu$ . The maximum value of  $k_{eff}/k$  is about 2.5. It is observed that the maximum values of  $\mu_t/\mu$  and  $k_t/k$  occur at locations where the velocity gradient is the highest. The values and distribution patterns of  $\mu_{eff}/\mu$  and  $k_{eff}/k$  shown in Fig. 3.6 are comparable with the calculated results in the literature [23].

### 3.4.2 Vaporization and Composition Change

The distributions of temperature and various vapor fluxes on the weld pool surface are shown in Fig. 3.7. The total vapor flux is the sum of fluxes in parts (b) and (c) or alternatively, the sum of fluxes in parts (d) and (e). It is observed that the distribution patterns of vapor fluxes are similar to the patterns of the surface temperature, indicating the vapor fluxes are predominantly determined by temperature. Most of the vaporization occurs from a small region near the center of the beam-workpiece interaction zone where the weld pool surface temperatures exceed the boiling point of the alloy (about 1930 K). The vaporization flux here is primarily driven by the pressure gradient. The radius of this active region is approximately 0.15 mm, which is smaller than the laser beam radius of 0.41 mm. The vaporization flux outside of this active region is very low and is driven by diffusion. Figure 3.7 also shows that magnesium vapor flux is about two orders of magnitude greater than aluminum vapor flux, resulting in a lowering of the magnesium concentration in the weld metal.

The vaporization rates of alloying elements were calculated by integrating the vapor fluxes over the weld pool surface in the model. The vaporization rates can also be obtained from the experimental data of magnesium loss from the weld pool,  $\Delta C_{Mg}$ , the weld pool cross section area,  $A$ , and the welding speed,  $v$ . Assuming the vaporization

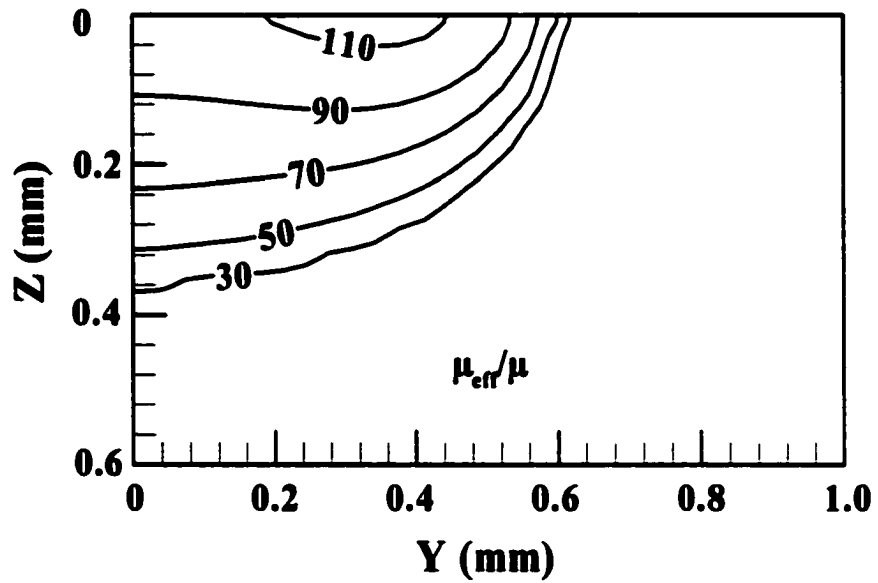


Fig. 3.6(a) Distributions of ratio of effective to molecular viscosity in weld pool cross section. Laser power 3.0 kW, welding speed 105.8 mm/s, beam defocusing  $\pm 1.5$  mm, and other parameters are listed in Table 3.4.



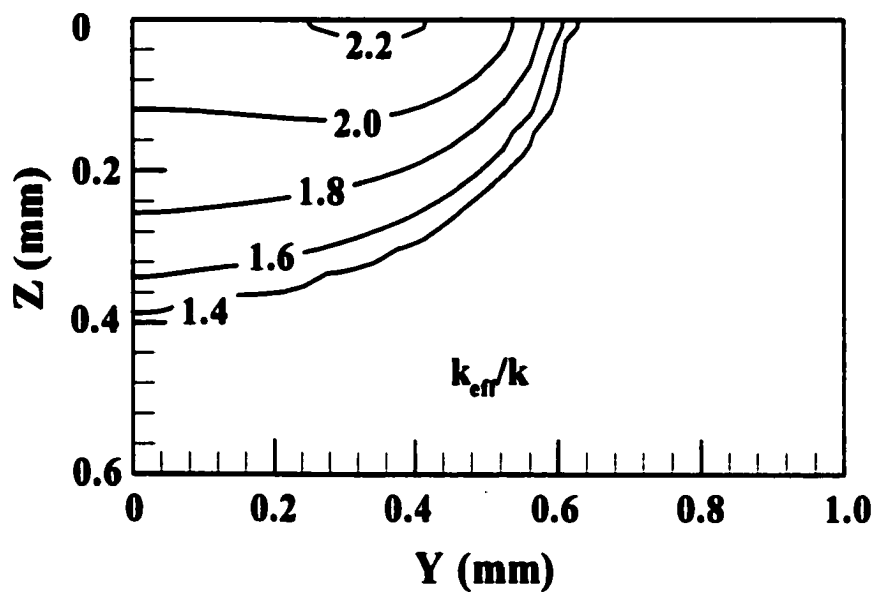


Fig. 3.6(b) Distribution of ratio of effective to molecular thermal conductivity in weld pool cross section. Laser power 3.0 kW, welding speed 105.8 mm/s, beam defocusing  $\pm$  1.5 mm, and other parameters are listed in Table 3.4.

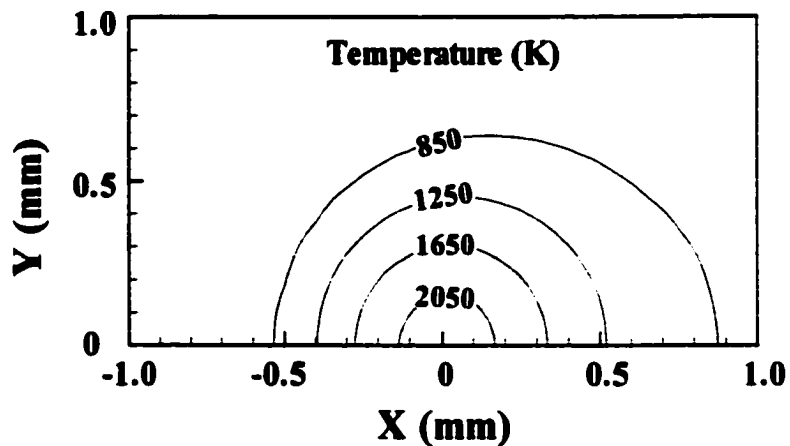


Fig. 3.7(a)

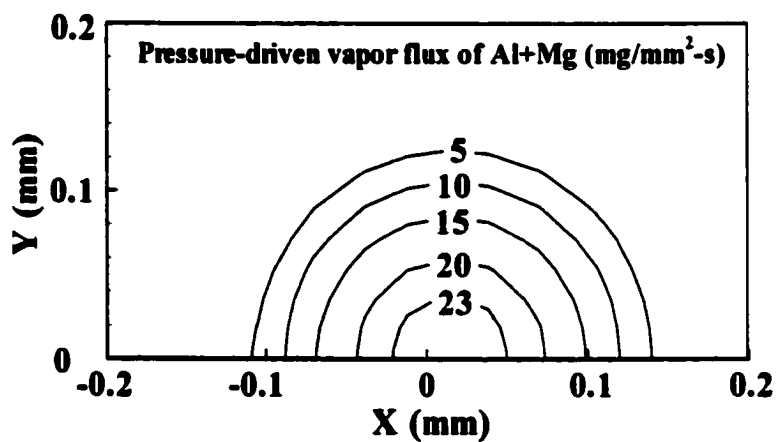


Fig. 3.7(b)

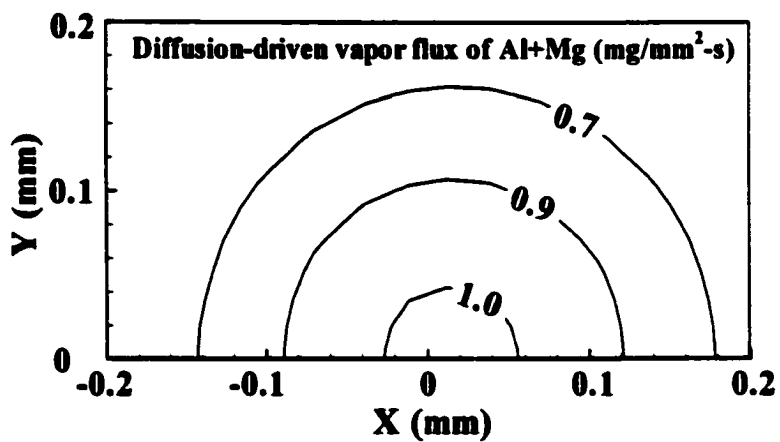


Fig. 3.7(c)

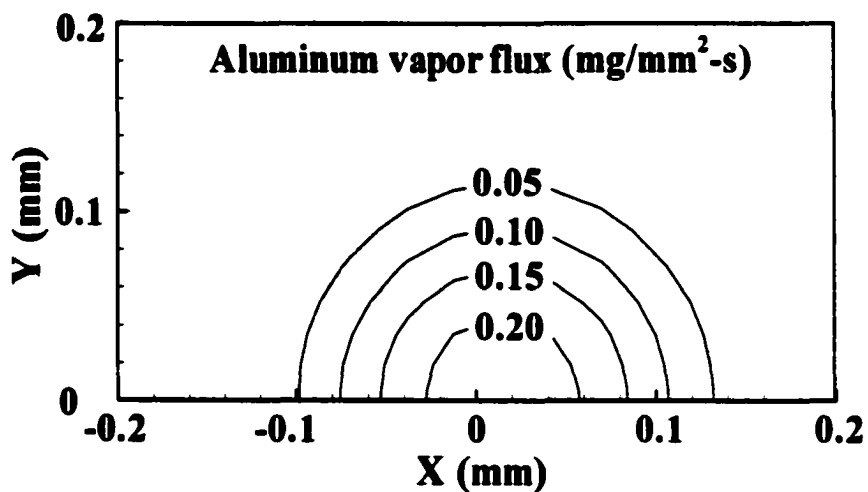


Fig. 3.7(d)

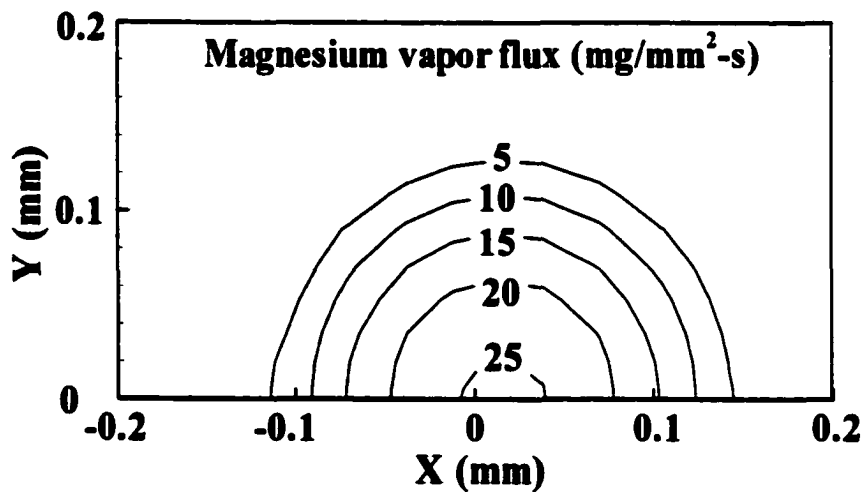


Fig. 3.7(e)

**Fig. 3.7** Distributions of temperature and various vapor fluxes on the weld pool surface. Laser power 3.0 kW, welding speed 105.8 mm/s, beam defocusing +/-1.5 mm, and other parameters are listed in Table 3.4.

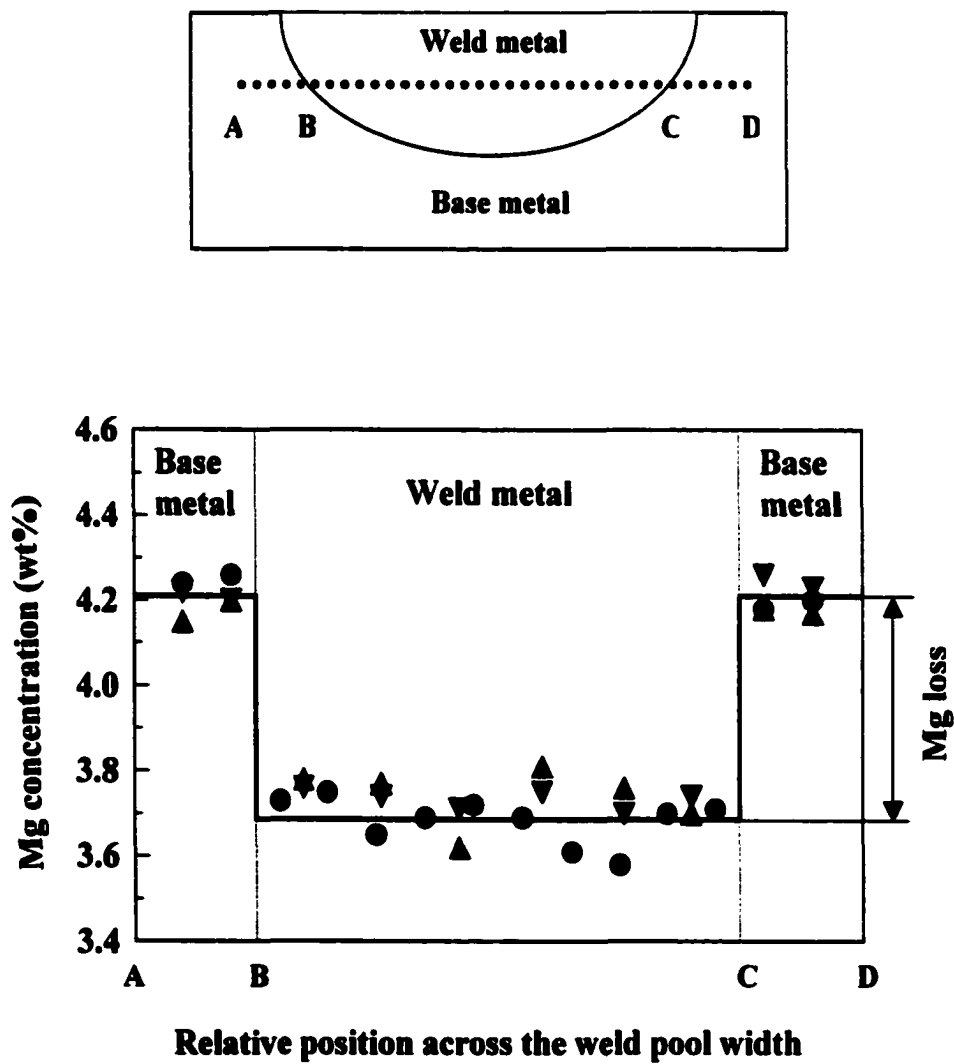


Fig. 3.8 Typical magnesium concentration profile across the weld pool width. The data were taken on three weld pool cross sections made using the same welding conditions: laser power 3.0 kW, welding speed 105.8 mm/s, and beam defocusing +1.5 mm.

rate of aluminum to be negligible, a mass balance of magnesium results in the following expression for magnesium vaporization rate,  $G_{Mg}$ :

$$G_{Mg} = \Delta C_{Mg} \rho v A \quad (3.52)$$

where  $\rho$  is the density of the alloy. The experimental data of magnesium loss in the weld pool,  $\Delta C_{Mg}$ , were obtained from the concentration profiles across the weld pool as shown in Fig. 3.8.

The computed vaporization rates are compared with the corresponding experimental values in Table 3.6. The data show that the calculated rates agree well with the experimental results for various welding conditions. Therefore, the comprehensive modeling presented here can serve as a basis for the quantitative understanding of the influences of various welding parameters on weld pool geometry, vaporization rate and composition change during conduction mode laser welding of aluminum alloys.

### 3.4.3 Influence of Laser Power

According to Eqn. (3.52), the composition change from evaporation during welding is proportional to the ratio of vaporization rate and melting rate given by  $\rho v A$ . At a constant welding speed, the melting rate is proportional to the cross sectional area,  $A$ . The influences of laser power on weld pool cross sectional area, vaporization rate, and composition change in the weld pool are presented in Fig. 3.9. Data in Fig. 3.9(a) show that both the vaporization rate and the cross sectional area increased roughly equally with the increase in the power, keeping their ratio almost constant. Since this ratio was not sensitive to laser power, the difference in the concentrations of magnesium between the base metal and the weld metal was not affected by the laser power. This behavior is observed in Fig. 3.9(b).

It is instructive to compare the observed effect of power on the compositional change in the aluminum alloy with that reported for loss of manganese from stainless

**Table 3.6(a) Calculated and experimental weld pool geometry, vaporization rate and loss of magnesium in the weld pool for different laser powers at welding speed of 105.8 mm/s and beam defocusing of +/-1.5 mm.**

Laser power (W)	1500		2000	
Calculated or experimental	Calculated	Experiment	Calculated	Experiment
Depth (mm)	0.32	0.31	0.35	0.35
Width (mm)	0.96	0.98	1.06	1.04
Cross section area (mm <sup>2</sup> )	0.24	0.23	0.29	0.29
Vaporization rate (mg/s)	0.32	0.32	0.45	0.44
$\Delta$ wt% Mg loss	0.47	0.49	0.54	0.55
Laser power (W)	2500		3000	
Calculated or experimental	Calculated	Experiment	Calculated	Experiment
Depth (mm)	0.36	0.37	0.40	0.42
Width (mm)	1.12	1.11	1.26	1.32
Cross section area (mm <sup>2</sup> )	0.32	0.31	0.39	0.40
Vaporization rate (mg/s)	0.53	0.49	0.59	0.58
$\Delta$ wt% Mg loss	0.56	0.57	0.53	0.52

**Table 3.6(b) Calculated and experimental weld pool geometry, vaporization rate and loss of magnesium in the weld pool for different welding speed and beam defocusing at laser power of 3.0 kW.**

<b>Beam defocusing (mm)</b>	+/-1.75					
<b>Welding speed (mm/s)</b>	95.3		105.8		116.4	
	Calculated	Experiment	Calculated	Experiment	Calculated	Experiment
<b>Depth (mm)</b>	0.41	0.41	0.40	0.41	0.39	0.37
<b>Width (mm)</b>	1.27	1.26	1.26	1.27	1.20	1.20
<b>Cross section area (mm<sup>2</sup>)</b>	0.40	0.39	0.39	0.39	0.35	0.34
<b>Vaporization rate (mg/s)</b>	0.69	0.64	0.72	0.60	0.68	0.59
<b><math>\Delta</math>wt% Mg loss</b>	0.66	0.65	0.64	0.55	0.61	0.56
<b>Beam defocusing (mm)</b>	+/-2.00					
<b>Welding speed (mm/s)</b>	95.3		105.8		116.4	
	Calculated	Experiment	Calculated	Experiment	Calculated	Experiment
<b>Depth (mm)</b>	0.42	0.44	0.42	0.42	0.40	0.40
<b>Width (mm)</b>	1.33	1.35	1.30	1.29	1.25	1.26
<b>Cross section area (mm<sup>2</sup>)</b>	0.43	0.46	0.41	0.41	0.39	0.38
<b>Vaporization rate (mg/s)</b>	0.68	0.68	0.69	0.76	0.69	0.70
<b><math>\Delta</math>wt% Mg loss</b>	0.60	0.59	0.57	0.66	0.55	0.60

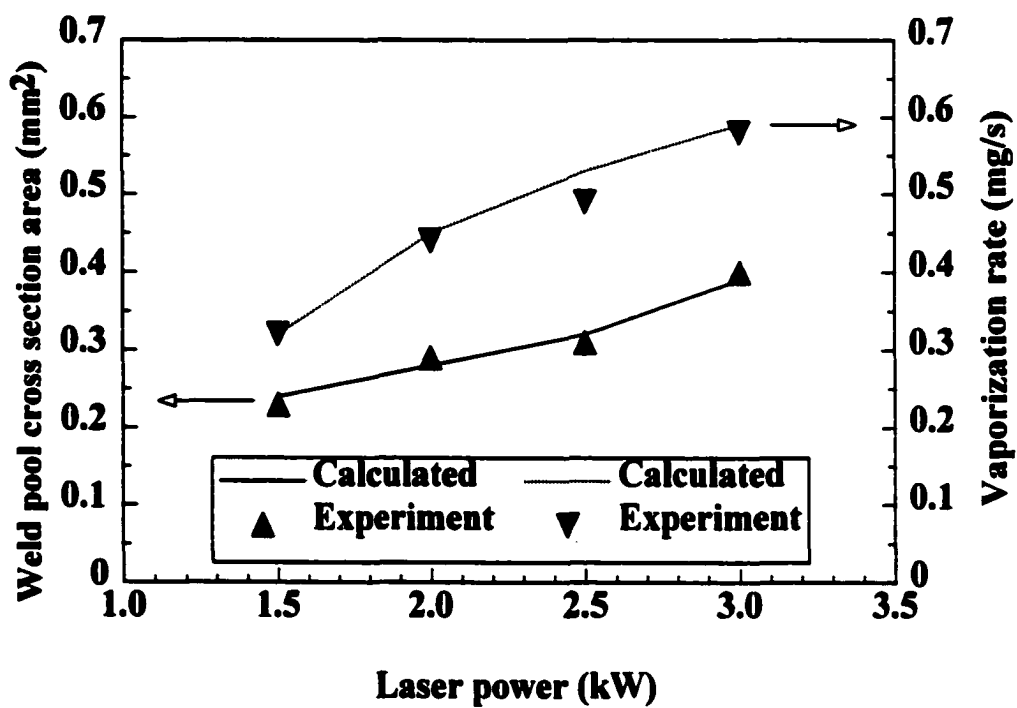


Fig. 3.9(a) Influence of laser power on weld pool size and vaporization rate. Welding speed 105.8 mm/s and beam defocusing +/-1.5 mm.



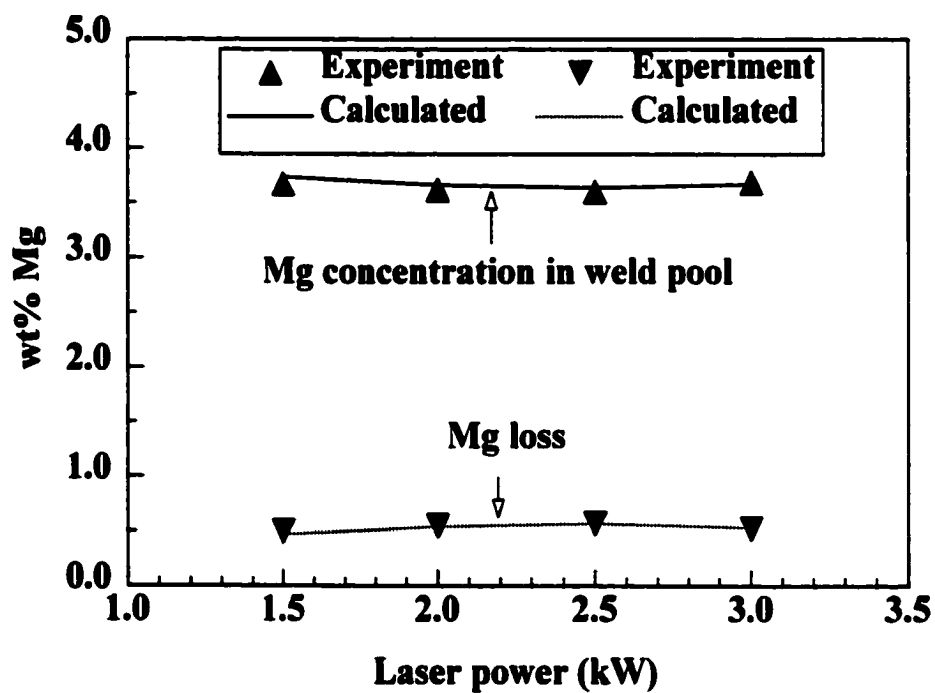


Fig. 3.9(b) Influence of laser power on weld metal composition change. Welding speed 105.8 mm/s and beam defocusing +/-1.5 mm.

steels during laser welding. During CO<sub>2</sub> laser welding of stainless steel [8], the change in the weld pool size with power was much more pronounced than that for the aluminum alloy. As a result, the change in the concentration of manganese was much more pronounced at low powers. Therefore, quantitative understanding of the influences of laser power on weld pool cross section area and vaporization rate is a key in predicting weld metal composition change for welding with different laser powers.

#### **3.4.4 Influence of Welding Speed**

The influence of welding speed on the melting rate, vaporization rate, and composition change are presented in Fig. 3.10. The decrease in weld pool cross section area was roughly compensated by the increase in welding speed and, as a result, the melting rate did not change significantly with welding speed, as shown in Fig. 3.10(a). Similarly, the vaporization rate was almost unaffected by the welding speed in the range of variables reported in this investigation. Since the ratio of vaporization rate and the melting rate was almost constant, the difference in the concentration of magnesium between the base metal and the weld metal did not vary with welding speed as shown in Fig. 3.10(b).

A similar result was also reported by Khan et al. [8] who, for a different reason, found that the composition change during CO<sub>2</sub> laser welding of stainless steels was not sensitive to welding speed. Unlike the welding of aluminum alloys using Nd:YAG laser, during CO<sub>2</sub> laser welding of stainless steels, absorption of laser beam by plasma was important and as a result, beam absorption by the workpiece was more efficient at higher welding speeds. Consequently, the vaporization rate of manganese increased somewhat with the increase in welding speed. However, this increase was compensated by the increase in the product of the weld pool cross section area and the welding speed, i.e., the volumetric melting rate. Therefore, the composition change in the welding of stainless steel and aluminum alloy 5182 was practically unaffected by the changes in the welding speed.

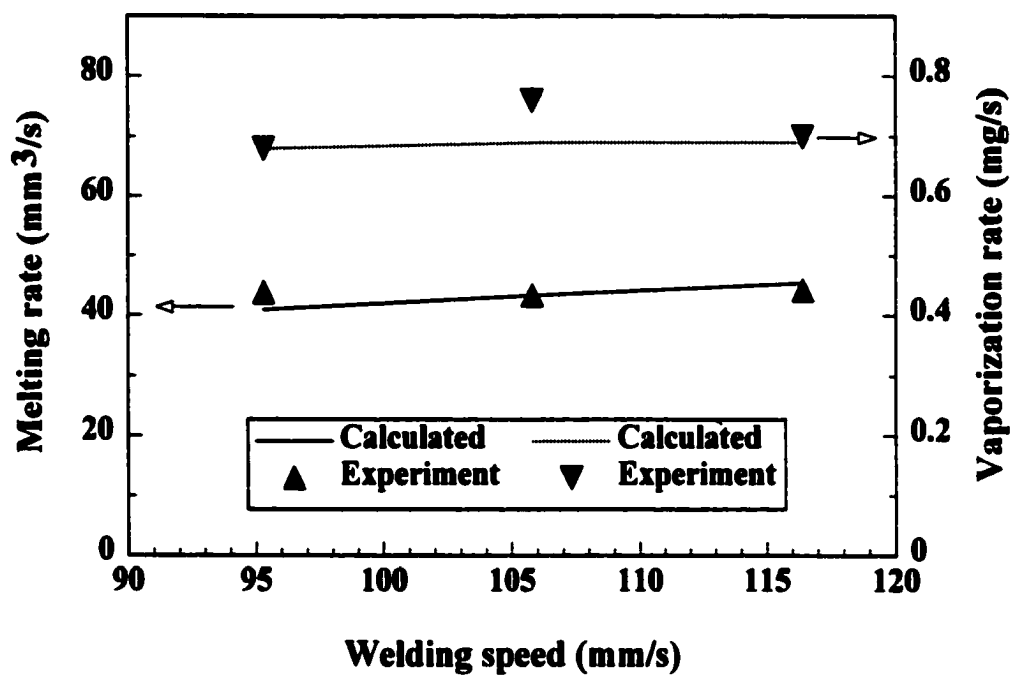


Fig. 3.10(a) Influence of welding speed on melting rate and vaporization rate. Laser power 3.0 kW and beam defocusing  $\pm 2.0$  mm.

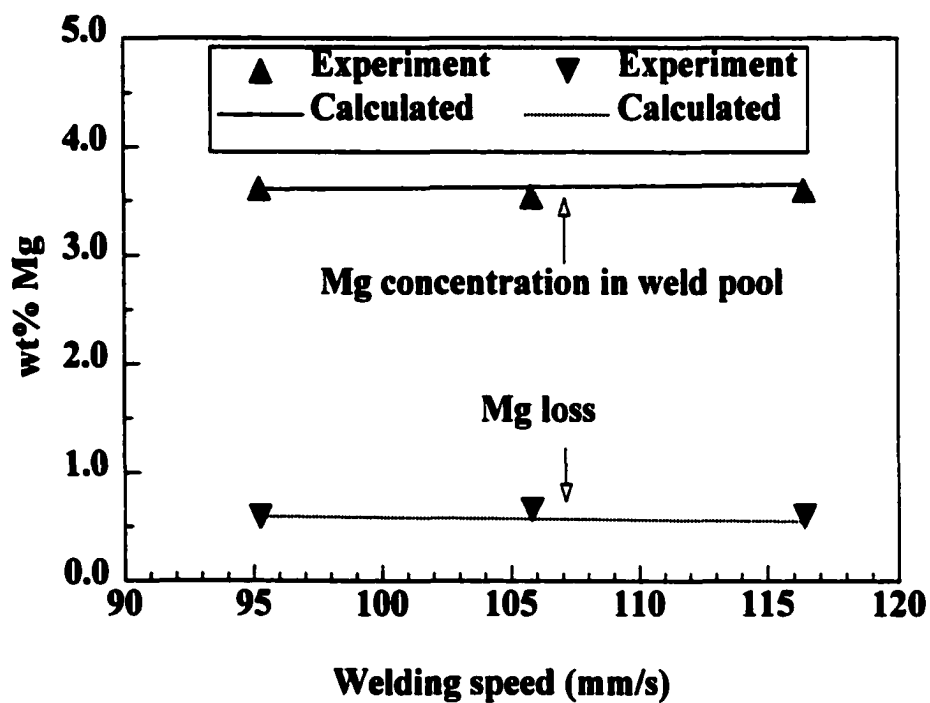


Fig. 3.10(b) Influence of welding speed on weld metal composition change. Laser power 3.0 kW and beam defocusing  $\pm 2.0$  mm.

### **3.5 Summary and Conclusions**

The weld metal composition change during conduction mode continuous wave laser beam welding of aluminum alloy 5182 was investigated through experiments and computer modeling. The major findings are as follows:

1) The vaporization rate of magnesium was about two orders of magnitude greater than that of aluminum. The significant magnesium loss from the weld pool resulted in a lower magnesium concentration in the weld metal than present in the base metal. The vaporization rate increased with an increase in laser power. However, the higher loss was compensated by an equivalent increase in the melting rate and, as a result, the concentration of magnesium in the weld metal, although lower than found in the base metal, was not affected by changes in the laser power. The weld metal composition was also unaffected by the variation of welding speed for the welding conditions investigated in this research.

2) Calculations showed that for all the welding conditions studied here, the peak temperature at the weld pool surface slightly exceeded the boiling point of the alloy. As a result, the pressure in a small region near the center of the weld pool surface was higher than one atmosphere. Vaporization was most pronounced in this active region, which had a smaller cross section area than the laser beam. The vaporization here was dominantly driven by the pressure gradient that existed between the weld pool surface and the atmosphere. The vaporization rate outside of the active region was much lower.

3) A comprehensive model for the calculation of temperature and velocity fields, vaporization rates, and weld metal composition changes during conduction mode laser welding was developed. The calculated results of weld pool geometry, vaporization rates, and composition changes agreed well with the corresponding experimental results. The good agreement between the calculated and experimental results indicates that the model can serve as a basis for the quantitative understanding of influences of various

welding parameters on fluid flow and heat transfer, vaporization of alloying elements, and weld metal composition changes during laser welding.

### 3.6 References

1. J. E. Hatch, *Aluminum: Properties and Physical Metallurgy*, American Society for Metals, Metals Park, OH, 1984.
2. M. J. Cieslak and P. W. Fuerschbach: *Metallurgical Transactions*, 1988, 19B, pp. 319-329.
3. J. H. Dudas and F. R. Collins: *Welding Journal*, 1966, 45, pp. 241s-249s.
4. A. Block-Bolten and T. W. Eagar: *Metallurgical Transactions*, 1984, 15B, pp. 461-469.
5. M. Collur, A. Paul, and T. DebRoy: *Metallurgical Transactions*, 1987, 18B, pp.733-740.
6. P. A. A. Khan and T. DebRoy: *Metallurgical Transactions*, 1984, 15B, pp. 641-644.
7. P. Sahoo, M. M. Collur, and T. DebRoy: *Metallurgical Transactions*, 1988, 19B, pp. 967-972.
8. P. A. A. Khan, T. DebRoy, and S. A. David: *Welding Journal*, 1988, 67, 1, pp. 1s-7s.
9. M. Pastor, H. Zhao, R. P. Martukanitz, and T. DebRoy: *Welding Journal*, 1999, 78, 6, pp. 207s-216s.
10. C. L. Chan and J. Mazumder: *Journal of Applied Physics*, 1987, 62, pp. 4579-4586.
11. T. DebRoy, S. Basu, and K. Mundra: *Journal of Applied Physics*, 1991, 70, pp.1313-1319.
12. K. Mundra and T. DebRoy: *Metallurgical Transactions*, 1993, 24B, pp. 145-155.
13. S. A. David and T. DebRoy: *Science*, 1992, 257, pp. 497-502.
14. G. M. Oreper, T. W. Eagar, and J. Szekely: *Welding Journal*, 1983, 62, pp. 307s-312s.
15. S. Kou and Y. H. Wang: *Welding Journal*, 1986, 65, 3, pp. 63s-70s.
16. G. M. Oreper and J. Szekely: *Metallurgical Transactions*, 1987, 18A, pp. 1325-1332.

17. M. E. Thompson and J. Szekely: *International Journal of Heat and Mass Transfer*, 1987, 32, pp. 1007-1020.
18. K. Mundra, T. DebRoy, T. Zacharia, and S. A. David: *Welding Journal*, 1992, 64, pp. 313s-320s.
19. T. Zacharia, A. H. Eraslan, D. Aidun, and S. A. David: *Metallurgical Transactions*, 1989, 20B, pp. 645-659.
20. T. Zacharia, S. A. David, J. M. Vitek, and T. DebRoy: *Welding Journal*, 1989, 68, pp. 499s-509s.
21. T. Zacharia, S. A. David, J. M. Vitek, and T. DebRoy: *Welding Journal*, 1989, 68, pp. 510s-519s.
22. R. T. C. Choo and J. Szekely: *Welding Journal*, 1994, 73, 2, pp. 25s-31s.
23. D. C. Weckman: in *Trends in Welding Research (USA)*, edited by J. M. Vitek et al., ASM International, Materials Park, OH, 1998, pp. 3-12.
24. M. Malinowski-Brodnicka, W. J. P. Vink, and G. den Ouden: *Welding Journal*, 1990, 62, 2, pp. 52s-59s.
25. H. Tennekes and J. L. Lumley: *A First Course in Turbulence*, 1974, The MIT Press. Cambridge, Massachusetts.
26. B. E. Launder and D. B. Spalding: *Mathematical Models of Turbulence*, 1972, Academic Press, New York, NY.
27. K. Mundra, T. DebRoy, S. S. Babu, and S. A. David: *Welding Journal*, 1997, 76, 4, pp. 163s-171s.
28. Z. Yang and T. DebRoy: *Science and Technology of Welding and Joining*, 1997, 2, 2, pp. 53-58.
29. Z. Yang, J. W. Elmer, J. Wong, and T. DebRoy: *Welding Journal*, 2000, 79, 4, pp. 97s-112s.
30. T. Hong, W. Pitscheneder, and T. DebRoy: *Science and Technology of Welding and Joining*, 1998, 3, 1, pp. 33-41.
31. W. Pitscheneder, T. DebRoy, K. Mundra, and R. Ebner: *Welding Journal*, 1996, 75, 3, pp. 71s-80s.

32. W. Pitscheneder, M. Gruböck, K. Mundra, T. DebRoy, and R. Ebner: in *Mathematical Modelling of Weld Phenomena 3*, edited by H. Cerjak, London, The Institute of Materials, 1997, pp. 41-63.
33. K. Mundra, J. M. Blackburn, and T. DebRoy: *Science and Technology of Welding and Joining*, 1997, 2, 4, pp. 174-184.
34. T. A. Palmer and T. DebRoy: *Science and Technology of Welding and Joining*, 1998, 3, 4, pp. 190-203.
35. S. Dushman and J. M. Lafferty: *Scientific Foundations of Vacuum Science*, 2nd ed., John Wiley, New York, NY, 1962.
36. S. I. Anisimov and A. Kh. Rakhmatulina: *Soviet Physics-JET*, 1973, 37, pp. 441-444.
37. C. J. Knight: *AIAA Journal*, 1979, 17, pp. 519-523.
38. K. Mundra, T. DebRoy, and K. Kelkar: *Numerical Heat Transfer*, Part A, 1996, 29, pp. 115-129.
39. K. D. Hachfeld: in *The Industrial Laser Handbook*, edited by D. Belforte and M. Levitt, Springer-Verlag New York Inc., New York, 1992-1993 edition, pp. 48-54.
40. S. V. Patankar: *Numerical Heat Transfer and Fluid Flow*, Hemisphere, New York, 1980.
41. Innovative Research, Inc.: *Documentation of COMPACT-3D*, Version 3.1, Minneapolis, Minnesota, 1994.
42. B. L. Tiwari: *Metallurgical Transactions*, 1987, 18A, pp. 1645-1651.
43. E. U. Schlunder and V. Gnielinski: *Chem. -Ing. -Tech*, 1967, 39, pp. 578-584.
44. M. von Allmen: *Laser-Beam Interactions with Materials*, Springer-Verlag, Berlin, 1987.
45. V. A. Batanov, F. V. Bunkin, A. M. Prokhorov, and V. B. Fedorov: *Sov. Phys.-JETP*, 1973, 36, pp. 311-322.
46. W. G. Vincenti and C. H. Kruger, Jr.: *Introduction to Physical Gas Dynamics*, Wiley, New York, NY, 1965.
47. *ASM Handbook*, v. 2, *Properties and Selection--Nonferrous Alloys and Special-purpose Materials*, 10th edition, ASM International, Materials Park, OH, 1990.



48. E. A. Brandes: *Smithells Metals Reference Book*, 6th edition, in association with Fulmer Research Institute Ltd., Butterworths, 1983.
49. R. Hultgren: *Selected values of thermodynamic properties of metals and alloys*, American Society for Metals, Metals Park, Ohio, 1973.
50. W. T. Walter, N. Solimene, K. Park, T. H. Kim, and K. Mukherjee: in *Laser in Metallurgy*, edited by K. Mukherjee and J. Mazumder, TMS-AIME, 1981, pp. 179-194.
51. W. W. Duley: in *Laser Surface Treatment of Metals*, edited by C. W. Draper and P. Mazzoldi, Kluwer Academic Publishers, 1986, pp. 3-15.
52. T. Watanabe, Y. Yoshida, and T. Arai: *LAMP'92*, Japan High Temperature Society, Nagaoka, Japan, 1992, pp. 505-510.
53. J. O. Hirschfelder, C. F. Curtiss, and R. B. Bird: *Molecular Theory of Gases and Liquids*, John Wiley and Sons, Inc., New York, NY, 1954.
54. J. O. Hirschfelder, R. B. Bird, and E. L. Spatz: *Chem. Revs.*, 1949, 44, p. 205.
55. E. T. Turkdogan: *Physical Chemistry of High Temperature Technology*, Academic Press, New York, NY, 1980.

## Chapter 4

### MATHEMATICAL MODELING OF MACROPOROSITY FORMATION DURING LASER WELDING OF ALUMINUM ALLOYS

#### 4.1 Background

Recent applications of transport phenomena in fusion welding have led to better understanding of the evolution of weld metal geometry in both stationary [1-3] and linear welds [4-7]. In addition, weld metal composition changes owing to both evaporation of alloying elements [8,9] and dissolution of gases [10,11] can now be understood from scientific principles. Applications of transport phenomena to quantitatively understand the phase composition [12,13], grain structure [13,14] and the inclusion structure [15] in welds of relatively simple alloys are now emerging. While most of these advances focused on the composition, macrostructure and microstructure of weldments, structurally sound welds of desirable weld metal composition often contain defects that make them unsuitable for service. The formation of macro porosity during fusion welding of aluminum alloys adversely affects the mechanical properties of weldments as shown in Fig. 4.1 [16]. In this chapter, new computational and experimental results are presented that demonstrate that applications of transport phenomena can lead to better understanding of the formation and prevention of macroporosity during laser welding of aluminum alloys 5182 and 5754.

Previous studies [17-21] showed that macroporosity could be formed due to imperfect collapse of the keyhole during high-energy laser or electron beam welding. A recent study [21] showed that porosity was rarely observed in either conduction mode or keyhole mode laser welding of aluminum alloys. However, when the beam power density was just above the threshold value for keyhole formation, an unstable keyhole was

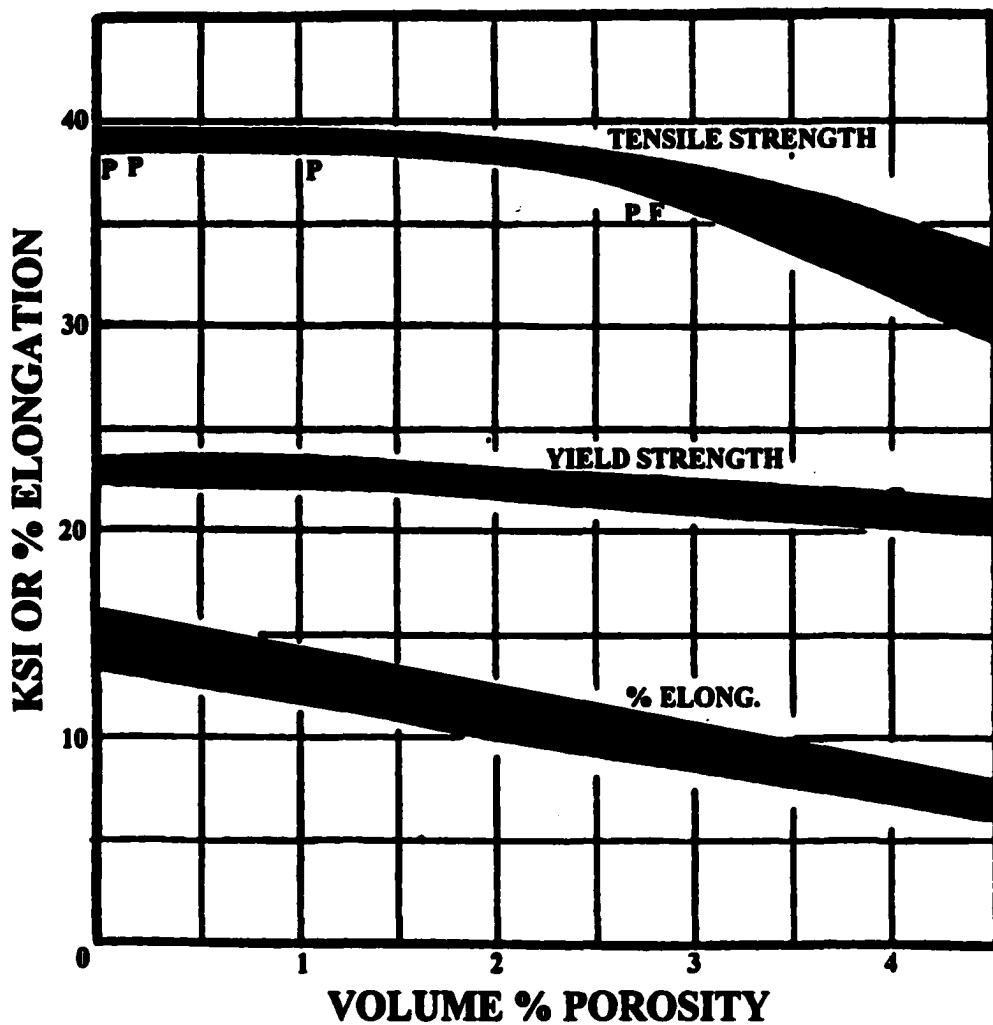


Fig. 4.1 Effect of weld porosity on tension test performance (P = passed bend test, F = failed bend test) of aluminum alloy 5086-H116 welded with 5356 electrodes [16].

formed that collapsed with any small disturbance. As a result, in various cross sections of the same welded sample, the weld pool shapes characteristic of either conduction mode or keyhole mode were observed. Macroporosity was formed primarily in this mixed mode of welding due to instability of the keyhole.

Previous studies [22-46] have led to significant advances in the understanding of the various physical processes in keyhole mode welding. Swift-Hook and Gick [22] formulated a model of keyhole mode of laser welding. They treated the laser beam as a moving line source and obtained a relationship between seam width, absorbed laser power, and welding speed based on heat conduction theory. Andrews and Atthey [23] obtained the keyhole profile based on the energy balance on the keyhole wall, assuming that all the absorbed laser energy was used for the vaporization of the metal. Klemens [24] assumed a circular keyhole with vertical walls that was kept open by a balance between vapor pressure within the keyhole, surface tension, and hydrodynamic pressure in the melt surrounding the keyhole. Mazumder and Steen [25] developed a heat transfer model for a moving Gaussian heat source using finite difference technique. The model assumed complete absorption of energy at all locations on the surface where the temperature exceeded the boiling point. The model predictions of weld pool geometry were found to be comparable with the experimental results. Dowden et al. [26-29] treated the viscous flow in the weld pool during keyhole mode welding. They assumed a slim cylindrical keyhole of known radius in a molten pool that was almost cylindrical but not concentric to the keyhole due to the movement of the beam. Kross et al. [36] developed a model in which non-equilibrium evaporation from the keyhole surface, surface tension, hydrostatic and hydrodynamic pressures in the melt as well as heat conduction into the workpiece were considered. The temperature at the keyhole wall and the radius of the keyhole were adjustable parameters in the model. Their calculations showed that the keyhole radius was at least 1.7 times the laser radius. Metzbowler [37] calculated the size and temperature of the keyhole and melt pool on the top surface of the workpiece based on the laser

power loss due to evaporation. A minimum laser power density required to form a keyhole was calculated.

Many of the existing models assumed a rotational keyhole symmetry. However, it was observed [42-45] using in situ X-ray transmission imaging system that the keyhole was not symmetrical with respect to the beam axis for high speed welding. Figures 4.2 to 4.4 [43-45] show that the keyhole bended in a direction opposite to that of the moving heat source. It is also observed from the figures that the front keyhole wall has a larger angle of inclination than the rear wall. Arata et al. [43] suggested that the bent keyhole shape was caused by inertia and “wall focusing” effect that caused the local delay of energy absorption in the lower part of the keyhole wall. Kaplan [46] has developed a model for the calculation of keyhole profile for high speed laser welding. The predicted keyhole shape was consistent with that observed experimentally. In his model, the calculated weld pool depth was equal to the depth of the keyhole. This is not true for partial penetration welding since the thermal conduction at the bottom of the keyhole will cause the molten pool to be deeper than the keyhole. Furthermore, the model did not consider the heat of evaporation in the calculation of keyhole profile. In this study, a more realistic calculation of keyhole profile and weld pool geometry is achieved by the consideration of heat conduction below the keyhole and heat of evaporation on the keyhole wall.

The objective of this study is to better understand and prevent the formation of macroporosity during laser welding of automotive aluminum alloys 5182 and 5754 through mathematical modeling. The modeling approach is based on the fact that during laser welding of thin plates of aluminum alloys, macroporosity is formed when the beam intensity is just above the threshold value for keyhole formation, where the keyhole is unstable. Macroporosity does not form during welding in either stable conduction mode or in stable keyhole model. A key feature of this model is its ability to determine geometric stability of the keyhole for a given set of welding parameters. The model can be used

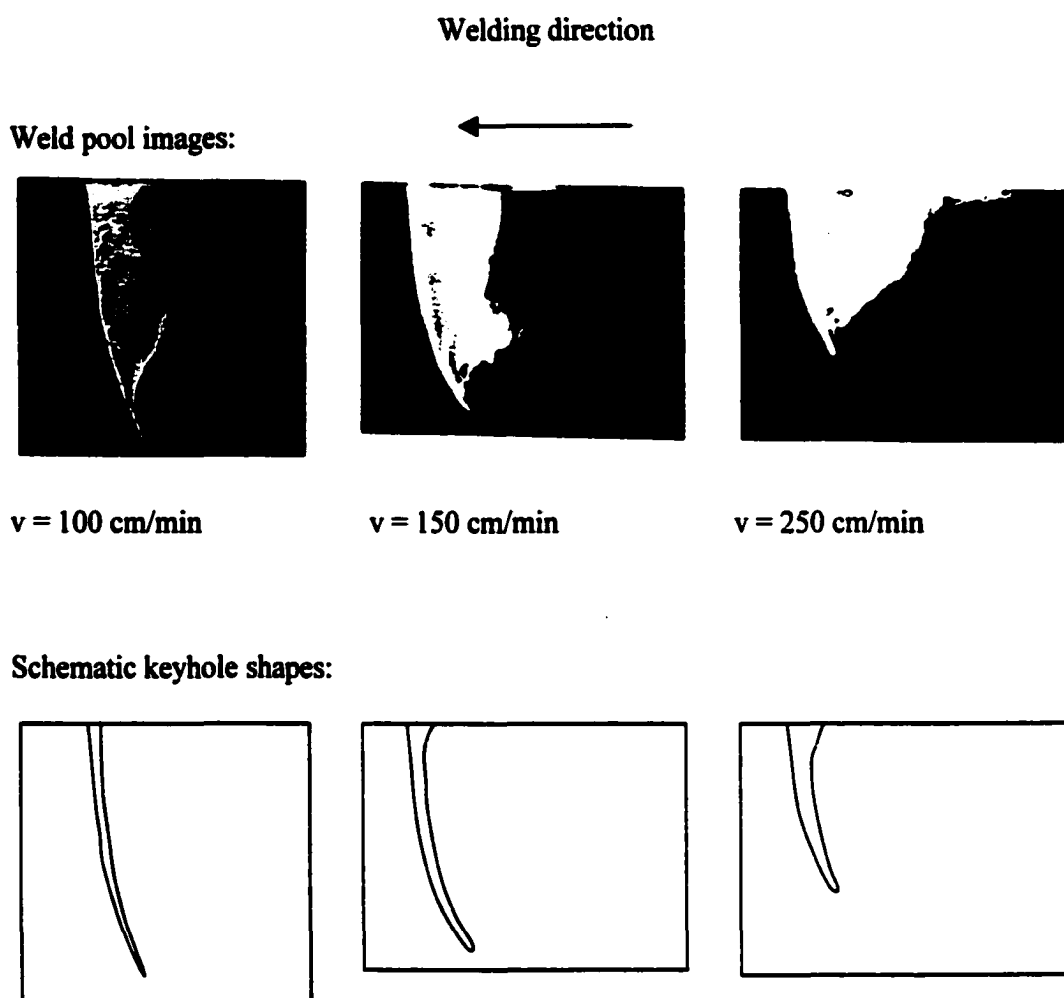


**Fig. 4.2 Typical keyhole shape for high-speed CO<sub>2</sub> laser welding of glass observed using in situ X-ray transmission imaging system [43].**

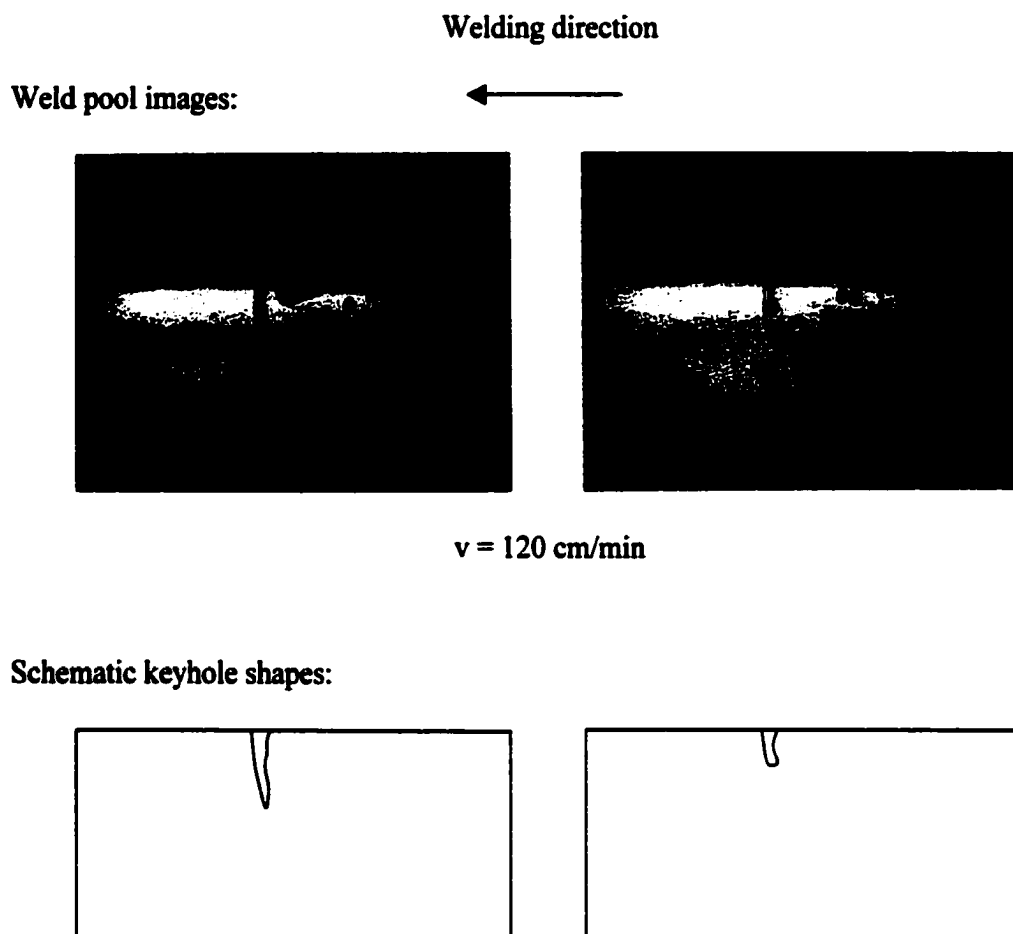


**Fig. 4.3** Typical keyhole shape for high-speed CO<sub>2</sub> laser welding of ice observed using in situ X-ray transmission imaging system [44]. Laser power: 70 W.

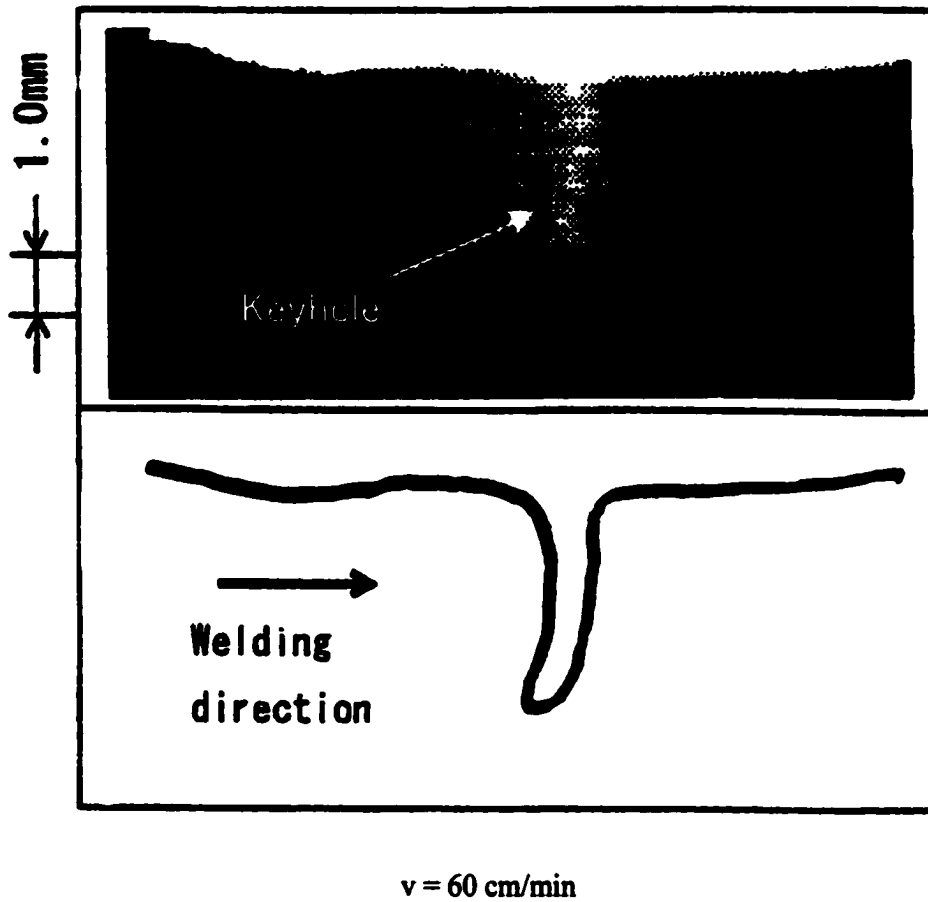


Fig. 4.4 Typical keyhole shape for high speed pulsed Nd:YAG laser welding of stainless steel 304 observed using in situ X-ray transmission imaging system [45].



to determine the operating window of welding parameters where a stable keyhole can be formed and macroporosity can be avoided. The model predictions of the stability of the keyhole and weld pool geometry were compared with the experimental data to validate the model. Formation of macroporosity was then linked to lack of stability of the keyhole.

## **4.2 Mathematical Model**

In the model, the geometrical stability of the keyhole is first determined by examining the energy balance at the beam-material interaction zone where the temperature is assumed to be equal to the boiling point of the alloy. The heat of evaporation is taken into account in the calculations. The energy loss caused by plasma absorption and the enhanced energy absorption by multiple reflections within the keyhole are also considered in the model.

If a stable keyhole can be formed, the keyhole profile is calculated based on point-by-point energy balance on the keyhole wall. The model then calculates the three-dimensional temperature field of the weld pool based on principles of thermal conduction. If a stable keyhole cannot be formed for the given welding conditions, the calculations are done considering conduction mode. For conduction mode welding, the weld pool temperature field can be calculated by the model described in Chapter 3.

There are three groups of input data for the present model, including material properties, welding parameters, and computational and geometrical parameters. The output of the model includes geometry of the keyhole when the keyhole forms and three-dimensional temperature field of the weld pool.

### **4.2.1 Energy Balance on the Keyhole Wall**

In the model, the temperature on the keyhole wall is assumed to be the boiling point of the alloy where the total equilibrium partial pressure of the alloying elements over the liquid alloy reaches one atmosphere. The laser energy is absorbed and transferred into the molten metal on the keyhole wall. As illustrated in Fig. 4.5, the local angle

of the keyhole wall is considered to be determined by the balance between heat flux transferred into the keyhole wall,  $I_c$ , the locally absorbed beam energy flux,  $I_a$ , and the heat loss due to heat of evaporation,  $I_v$ . The heat balance on the keyhole wall requires  $(I_a - I_v) \sin\theta = I_c \cos\theta$ . Therefore, we have

$$\tan(\theta) = \frac{I_c}{I_a - I_v} \quad (4.1)$$

The calculation of local keyhole angle  $\theta$  requires the determination of  $I_c$ ,  $I_a$ , and  $I_v$ . The calculation is done in two steps. In the first step, the effects of plasma absorption and multiple reflections are not considered. In the second step, these effects will be taken into account based on the keyhole geometry obtained in the first run of calculation.

The heat flux conducted into the keyhole wall is deduced from a moving line source model developed by Rosenthal [47], which gives a solution for the temperature field in an infinite plate of certain thickness by

$$T(r, \varphi) = T_a + \frac{P'}{2\pi\lambda_{th}} K_0(Pe' r) e^{-Pe' r \cos\varphi} \quad (4.2)$$

where  $r$  and  $\varphi$  are defined schematically in the coordinate system shown in Fig. 4.6,  $T_a$  is the ambient temperature,  $P'$  is the strength of the line source, i.e., power per unit depth,  $\lambda_{th}$  is the thermal conductivity,  $K_0(\ )$  is the second kind and zeroth order solution to the modified Bessel function, and  $Pe'$  is defined as  $Pe' = v/(2\kappa)$ , where  $v$  is the welding speed and  $\kappa$  is the thermal diffusivity.

Let  $T(r, \varphi)$  in Eqn. (4.2) equal  $T_v$ , the boiling point of the material. The strength of the line source  $P'$  necessary to reach the boiling point at an arbitrary point  $(r, \varphi)$  can be calculated by rearranging Eqn. (4.2):

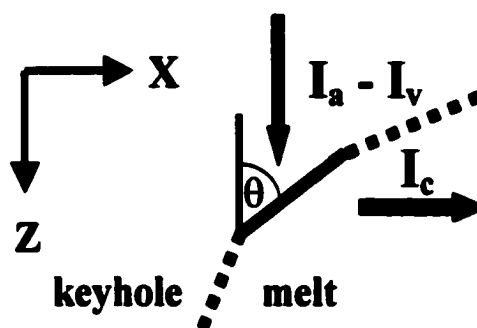


Fig. 4.5 The relationship between the locally absorbed beam energy flux,  $I_a$ , the heat loss due to heat of evaporation,  $I_v$ , and the heat flux conducted into the metal,  $I_c$ , determines the keyhole wall angle  $\theta$ .

$$P' = (T_v - T_a) 2\pi \lambda_{th} \frac{1}{K_0(Pe'r)} e^{Pe'rcos\varphi} \quad (4.3)$$

Assuming the heat flow in z direction to be negligible, Fourier's law of heat conduction determines the heat flux in radial direction to be

$$I_c(r, \varphi) = -\lambda_{th} \nabla T \approx -\lambda_{th} \frac{\partial T}{\partial r} \quad (4.4)$$

The spatial gradient of temperature with respect to r is obtained from Eqn. (4.2) as

$$\frac{\partial T}{\partial r} = \frac{P'}{2\pi \lambda_{th}} Pe' \left[ -K_0(Pe'r) \cos\varphi + K_0'(Pe'r) \right] e^{-Pe'rcos\varphi} \quad (4.5)$$

where  $K_0'(\cdot)$  is the derivation of  $K_0(\cdot)$ . Bronstein and Semendjajew [48] showed that

$$K_0'(x) = -K_1(x) \quad (4.6)$$

where  $K_1(x)$  is the second kind and first order solution to the modified Bessel function. Combining Eqns. (4.4), (4.5) and (4.6), we have

$$I_c(r, \varphi) = \frac{P'}{2\pi} Pe' \left[ K_0(Pe'r) \cos\varphi + K_1(Pe'r) \right] e^{-Pe'rcos\varphi} \quad (4.7)$$

If we consider that the boiling point  $T_v$  is reached at the keyhole wall, the heat flow at any point  $(r, \varphi)$  on the keyhole wall can be obtained by combining Eqn. (4.3) and Eqn. (4.7):

$$I_c(r, \varphi) = (T_v - T_a) \lambda_{th} Pe' \left( \cos\varphi + \frac{K_1(Pe'r)}{K_0(Pe'r)} \right) \quad (4.8)$$

At the front keyhole wall,  $\varphi = 0$ , therefore

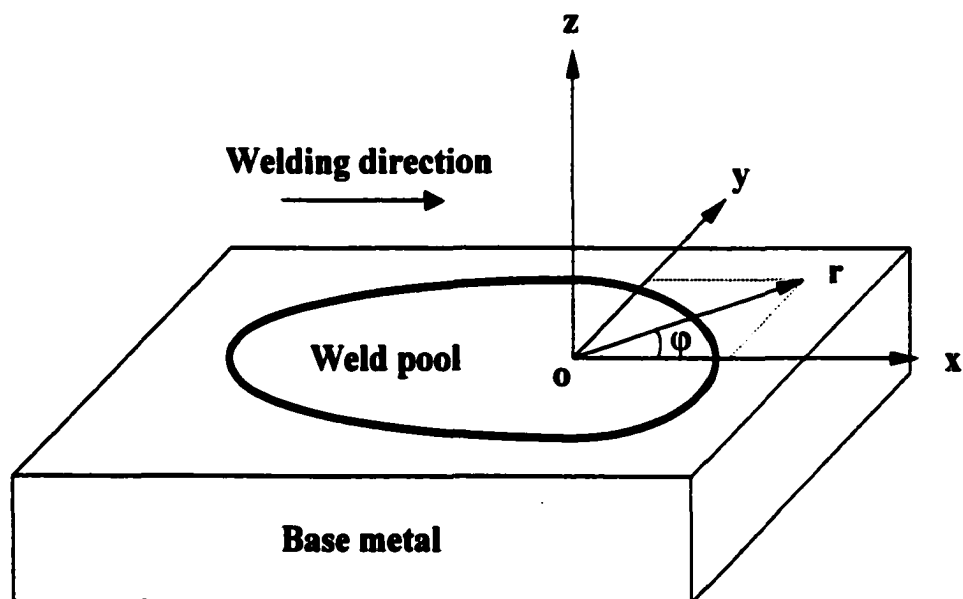


Fig. 4.6 Schematic diagram of the coordinate system used in the model.

$$I_c(x_{fs}, 0) = (T_v - T_a)\lambda_{th} Pe' \left( 1 + \frac{K_1(Pe' x_{fs})}{K_0(Pe' x_{fs})} \right) \quad (4.9)$$

At the rear keyhole wall,  $\varphi = \pi$ , therefore

$$I_c(x_{rs}, \pi) = (T_v - T_a)\lambda_{th} Pe' \left( -1 + \frac{K_1(Pe' x_{rs})}{K_0(Pe' x_{rs})} \right) \quad (4.10)$$

where  $x_{fs}$  and  $x_{rs}$  are the distances between the line source and the front and rear keyhole walls, respectively.

For the first time calculation, only Fresnel absorption on the keyhole wall is considered. Therefore, the absorbed laser beam energy flux at any point  $(r, \varphi, z)$  on the keyhole wall is given by

$$I_a(r, \varphi, z) = \alpha I_0(r, \varphi, z) \quad (4.11)$$

where  $\alpha$  is the Fresnel absorption coefficient,  $I_0(r, \varphi, z)$  is the local power intensity of the beam, and is given [49] by

$$I_0(r, \varphi, z) = I_{f0} \left( \frac{r_{f0}}{r_f} \right)^2 \exp\left( -\frac{r^2}{r_f^2} \right) \quad (4.12)$$

where  $I_{f0}$  is the peak intensity at the focal point, given by  $2P/(\pi r_{f0}^2)$ ,  $P$  is the laser power,  $r_{f0}$  is the beam radius at the focal point,  $r_f$  is the local beam radius, given [49] by

$$r_f = r_{f0} \left[ 1 + \left( \frac{z + z_0}{2r_{f0} f/d_b} \right)^2 \right] \quad (4.13)$$

where  $z_0$ ,  $f$  and  $d_b$  are the beam defocusing, beam focal length and beam diameter on the optics, respectively. The value of  $z_0$  is positive when the focal point is above the workpiece surface and is negative when the focal point is below the workpiece surface.

The evaporative heat flux,  $I_v$ , on the keyhole wall is calculated from

$$I_v = \sum_{i=1}^n J_{v,i} \Delta H_{v,i} \quad (4.14)$$

where  $n$  indicates the total number of alloying elements in the alloy,  $J_{v,i}$  is the evaporation flux of element  $i$ , and  $\Delta H_{v,i}$  is the heat of evaporation. The evaporation flux at very low pressures can be accurately calculated from the Langmuir equation [50]. However, at one atmosphere pressure the Langmuir equation significantly over predicts the vaporization rate. Based on previous studies [51-53], the calculated evaporation flux using the Langmuir equation is usually 5 to 10 times higher than the experimental results. In this study, a factor of 7.5 is used to calculate the evaporation flux from the modified Langmuir equation:

$$J_{c,i} = \frac{44.34}{7.5} a_i P_i^\circ(T_v) \sqrt{\frac{M_i}{T_v}} \quad (4.15)$$

where  $a_i$  is the activity of element  $i$  in the liquid alloy,  $P_i^\circ(T_v)$  is the equilibrium vapor pressure of element  $i$  over pure liquid at temperature  $T_v$ ,  $M_i$  is the molecular weight of element  $i$ . The calculation of activity of each alloying element is described in section 3.3.2 of Chapter 3. The values of heat of evaporation and equilibrium vapor pressure of each alloying element are listed in Tables 3.3 and 3.5.

#### 4.2.2 Keyhole Stability and Keyhole Wall Profile

Assuming that the beam axis is located at  $x = 0$  and the temperature on the keyhole wall is the boiling point of the material, the keyhole profile can be calculated point

by point starting from the top surface of the workpiece ( $z = 0$ ) by the following procedure:

(1) Assume that the positions of the front and rear keyhole walls at the top surface are at  $x = x_f$  and  $x = x_r$ , respectively. The distance between  $x_f$  and  $x_r$  should be larger than the beam diameter as shown in Fig. 4.7.

(2) According to Eqn. (4.3), a given value of line source  $P'$  results in a fixed temperature field and vice versa. Therefore, for a given distance ( $x_{fs} - x_{rs}$ ) between the front and rear keyhole walls where the temperature is  $T_v$ , the strength of the line source,  $P'$ , and its position,  $x_s$ , can be uniquely determined as shown in the above figure. Accordingly, the distances between the line source and the front and rear keyhole wall,  $x_{fs}$  and  $x_{rs}$ , can be determined by the following procedure.

From Eqn. (4.3), we obtain

$$P' = (T_v - T_a)2\pi\lambda_{th} \frac{1}{K_0(Pe'x_{fs})} e^{Pe'x_s} = (T_v - T_a)2\pi\lambda_{th} \frac{1}{K_0(Pe'x_{rs})} e^{-Pe'x_s}$$

and therefore,

$$\frac{e^{Pe'x_{fs}}}{K_0(Pe'x_{fs})} = \frac{e^{-Pe'x_{rs}}}{K_0(Pe'x_{rs})} \quad (4.16)$$

Eqn. (4.14) can be solved, considering  $x_{fs} + x_{rs} = x_f - x_r$ , to obtain  $x_{fs}$  and  $x_{rs}$ . The position of line source is then calculated from

$$x_s = x_f - x_{fs} \quad (4.17)$$

(3) The heat fluxes on the front and rear keyhole wall,  $I_c(x_{fs})$  and  $I_c(x_{rs})$ , are calculated from Eqns. (4.9) and (4.10) using the known values of  $x_{fs}$  and  $x_{rs}$ .

(4) The locally absorbed laser energy fluxes on the front and rear keyhole wall,  $I_{af}$  and  $I_{ar}$ , are calculated from Eqns. (4.11), (4.12) and (4.13).



(5) The local angles of the front and rear keyhole walls,  $\theta_f$  and  $\theta_r$ , are calculated from Eqn. (4.1).

(6) The keyhole wall positions at the next depth ( $z$ ) value can be determined from the current positions and the local angles. As shown in Fig. 4.8, for a current front keyhole wall position of  $(x_i, z_i)$  and a local angle of  $\theta_f$ , the next position  $(x_{i+1}, z_{i+1})$  at a distance  $dz$  below the current position can be obtained by

$$x_{i+1} = x_i - dz \tan(\theta_f) \quad (4.18)$$

$$z_{i+1} = z_i + dz \quad (4.19)$$

Small values of  $dz$  are used in Eqns. (4.18) and (4.19) to obtain a smooth keyhole wall profile. The positions of rear keyhole wall are calculated similarly.

At the beginning of the calculation, large values of  $x_f$  and  $x_r$  are used and consequently, the values of  $x_{fs}$  and  $x_{rs}$  are larger than the actual values. Since these positions are far away from the beam axis, the absorbed laser intensity is very small and the value of  $\tan(\theta_f)$  in Eqn. (4.1) is very large. The next keyhole wall positions, if calculated from Eqn. (4.18), would jump far away from the previous positions or even cross the beam axis as shown in Fig. 4.9, indicating the keyhole wall positions on the top surface should be nearer to the beam axis than that assumed. If the value of  $x_i - x_{i+1}$  is larger than  $dx$ , a small value that determines precision of the keyhole wall position, the position of the keyhole wall on the top surface is relocated to be nearer to the beam axis by a small distance of  $dx$  and the calculation is repeated from steps (2) through (5). As the position comes nearer to the beam axis, the value of  $\tan(\theta_f)$  becomes smaller as shown in Fig. 4.9. When the value of  $dz \tan(\theta_f)$  in Eqn. (4.18) is less than  $dx$ , the positions of front and rear keyhole wall at the top surface are obtained.

In the above process of determining the keyhole wall positions on the top surface, the distance between the front and rear the keyhole wall becomes smaller after each

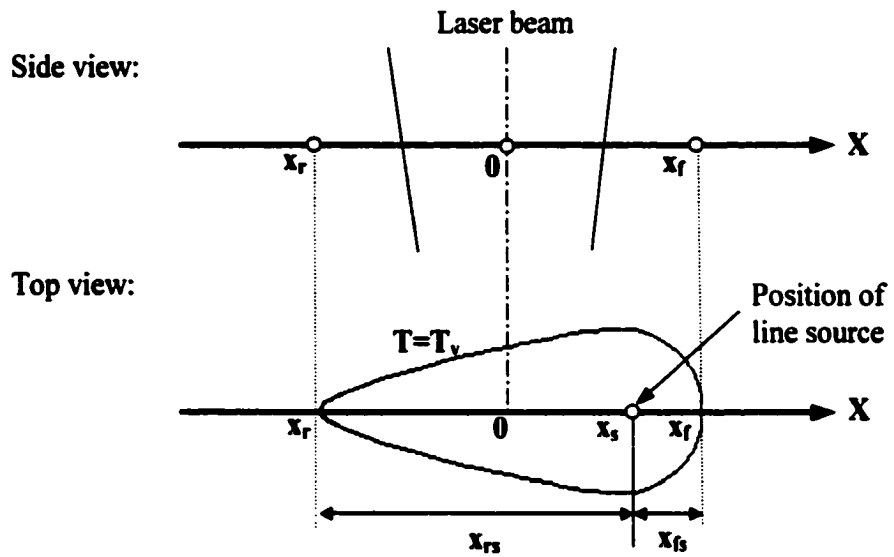
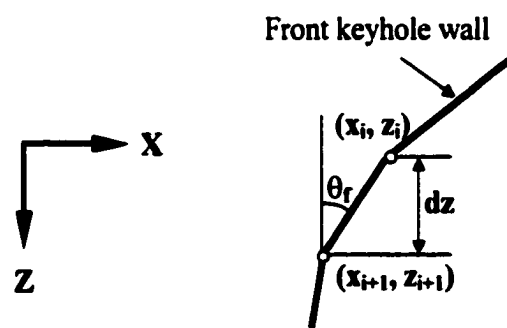


Fig. 4.7 The laser beam location and the keyhole profile on the top surface of the work-piece.



**Fig. 4.8** From the current keyhole wall position,  $(x_i, z_i)$  and the local angle,  $\theta_f$ , the next position,  $(x_{i+1}, z_{i+1})$ , at a distance,  $dz$ , below the current point can be obtained.

round of calculation. If this distance becomes zero before the keyhole wall position can be found, a stable keyhole cannot be formed under the current welding condition. The calculation in this model terminates and the temperature field is calculated considering conduction mode laser welding described in Chapter 3.

(7) If the positions of front and rear keyhole wall at the top surface are obtained, the calculation procedure from steps (2) through (6) is repeated. In each step, the current positions of the front and rear keyhole wall and the position of the line source are recorded in a file. The next keyhole wall position in x direction is calculated from Eqn. (4.18) and the keyhole wall position in z direction is obtained from Eqn. (4.19). The calculation procedure stops when the front and the rear walls intersect each other or the thickness of the plate is reached.

The above calculation considers only Fresnel absorption of the laser energy. The calculation can take into account other absorption mechanisms such as plasma absorption due to inverse Bremsstrahlung and Fresnel absorption by multiple reflections. When these absorption mechanisms are considered, Eqn. (4.1) can be modified as

$$\tan(\theta) = \frac{I_c(x)}{I'_a(x, z) + I_{mr} - I_v} \quad (4.20)$$

where  $I'_a(x, z)$  is the absorbed laser intensity by the workpiece during the first incidence considering plasma absorption and  $I_{mr}$  is the absorbed intensity by the workpiece during multiple reflections. The definitions of other variables are the same as in Eqn. (4.1). These are calculated from

$$I'_a(x, z) = (1 - \alpha_{ib})I_a(x, z) = (1 - \alpha_{ib})\alpha I_0(x, z) \quad (4.21)$$

$$I_{mr} = (1 - \alpha_{ib})(1 - \alpha)\alpha_{mr}I_0(x, z) \quad (4.22)$$

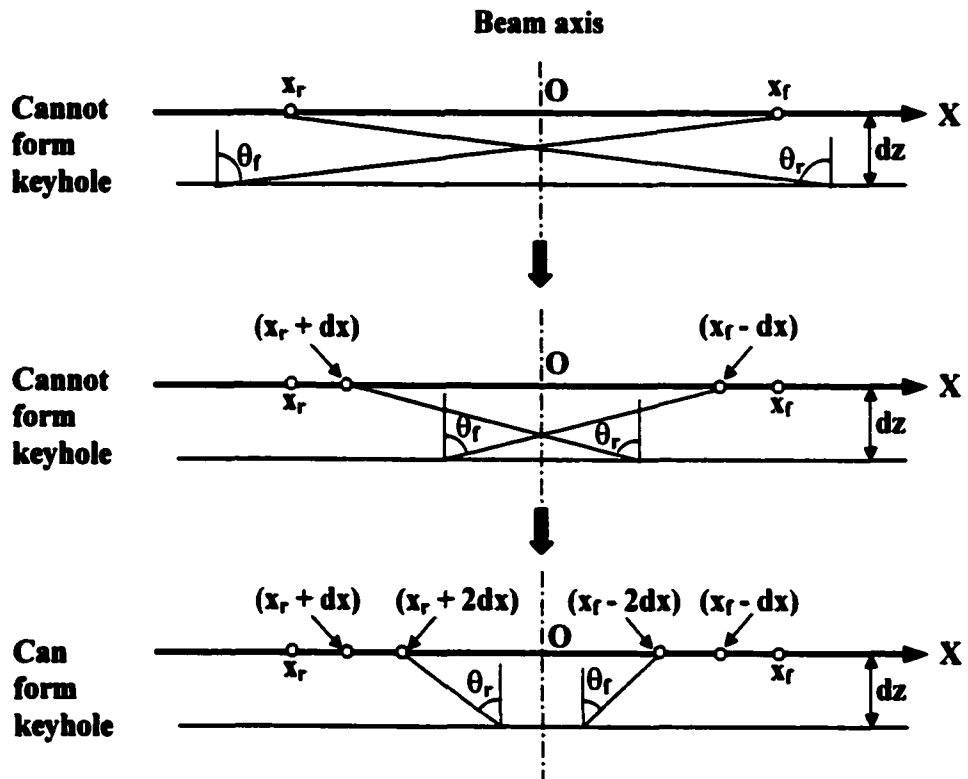


Fig. 4.9 Determination of front and rear keyhole wall positions on top surface along x-axis.

where  $\alpha_{ib}$  is the plasma absorption coefficient by the plume inside of the keyhole before the laser beam hits the keyhole wall for the first time and  $\alpha_{mr}$  is the absorption coefficient by the workpiece during multiple reflections. These are calculated from

$$\alpha_{ib} = 1 - e^{-\alpha_p d^2} \quad (4.23)$$

$$\alpha_{mr} = 1 - (1 - \alpha)^{n(4\bar{\theta})-1} \quad (4.24)$$

where  $\alpha_p$  is the inverse Bremsstrahlung absorption coefficient,  $d$  is the depth of the keyhole, and  $\bar{\theta}$  is the mean angle of the keyhole wall. The calculation procedure for the above two absorption coefficients is discussed in the Appendix in this chapter.

Second round of calculation is performed taking into account the Fresnel absorption by the workpiece during multiple reflections and inverse Bremsstrahlung absorption by plasma. Therefore, using Eqn. (4.20) instead of Eqn. (4.1), the calculations from steps (1) through (7) are repeated. From these calculations, the final front and rear keyhole wall profiles on the  $x$ - $z$  plane and the position of local line source,  $x_s$ , are obtained.

### 4.2.3 Three-dimensional Temperature Field

The preceding calculations obtain the positions of front and rear keyhole wall,  $x_{fs}$  and  $x_{rs}$ , as a function of depth,  $z$ . Using the calculated position of front or rear keyhole wall, the strength of the line source at any given depth,  $z$ , is calculated from

$$P' = (T_v - T_s) 2\pi\lambda_{th} \frac{1}{K_0(Pe' x_{fs})} e^{Pe' x_s} \quad (4.25)$$

Using the calculated strength  $P'$ , and the location,  $x_s$ , of the line source, the temperature field in  $x$ - $y$  plane at each depth,  $z$ , is calculated by

$$T(x, y) = T_a + \frac{P'}{2\pi\lambda_{th}} K_0(Pe' \sqrt{(x - x_s)^2 + y^2}) e^{\frac{-Pe'(x-x_s)}{\sqrt{(x-x_s)^2 + y^2}}} \quad (4.26)$$

If the depth of the keyhole is equal to the thickness of the workpiece, the three-dimensional temperature field can be calculated using Eqn. (4.26). However, if the depth of the keyhole is less than the plate thickness, the temperature field below the bottom of the keyhole cannot be calculated using Eqn. (4.26). To calculate the temperature field in this domain, the following heat diffusion equation is solved:

$$\frac{\partial^2 T}{\partial x^2} + \frac{\partial^2 T}{\partial y^2} + \frac{\partial^2 T}{\partial z^2} - \frac{v}{\kappa} \frac{\partial T}{\partial x} = 0 \quad (4.27)$$

The boundary conditions necessary to solve the above equation are given below. The top surface of the domain is the x-y plane at the bottom of the keyhole. The temperature on this plane is obtained from Eqn. (4.26). The boundary condition for the bottom surface is given by

$$J(x, y, z)|_{z=\max} = h[T_a - T(x, y, z)|_{z=\max}] \quad (4.28)$$

where  $J(x, y, z)$  is the heat flux,  $h$  is the heat transfer coefficient,  $T_a$  is the ambient temperature, and  $T(x, y, z)$  is the local temperature. The temperatures on other surfaces of the domain are assumed to be ambient temperature since the surfaces are far away from the heat source.

The calculation of the three-dimensional temperature field was carried out on a material dimension of 10 mm x 5 mm x 1 mm. The calculation domain was subdivided into uniform grids of 100, 50, and 20 along its length, width, and depth, respectively.

### 4.3 Results and Discussion

The model has been used to predict the welding mode, keyhole profile, and three-dimensional temperature field for Nd:YAG laser welding of aluminum alloys 5182 and 5754. The calculated results are compared with the experimental values. The material properties and process parameters are listed in Table 4.1. Since many material properties of alloys 5182 and 5754 are not available in open literature, some data used are estimated values. A nomenclature of positive beam defocusing to represent the focal point to be above the top surface of the workpiece and negative beam defocusing to represent the focal point below the top surface will be used in this paper.

#### 4.3.1 Keyhole Profile and Temperature Field

The calculated keyhole profile for welding of alloy 5182 with a laser power of 2.5 kW, welding speed of 300 ipm (127 mm/s), and zero beam defocusing is shown in Fig. 4.10. The location and profile of the beam are also shown in the figure. It is observed that the front keyhole wall has a larger angle with the beam axis than does the rear keyhole wall. This is consistent with the keyhole shape experimentally observed by in situ X-ray transmission imaging system [43-45]. The different angles were caused by the different temperature gradients and the resulting heat fluxes near the front and rear keyhole walls. The calculated three-dimensional temperature field for this welding condition is given in Fig. 4.11. During high-speed laser welding, cold material is fed into the front keyhole wall while the material that is fed into the rear wall has been heated to higher temperatures. As a result, the temperature gradient near the front keyhole wall is much larger than that near the rear wall as observed in Fig. 4.11. Consequently, the heat flux conducted into the front wall is larger than into the rear wall. Therefore, according to Eqn. (4.20), the front wall should have a larger angle since the heat flux conducted into the front wall  $J_v$  is larger for the same absorbed heat flux  $I_a$ . It is also observed from Fig. 4.10 that the beam axis intersects the front keyhole wall. This indicates that larger beam intensity is needed to maintain the front wall since the cooling effect here is stronger than the rear wall. Furthermore, it is observed that the size of the keyhole opening at the top surface of the workpiece is slightly smaller than the beam diameter.



Table 4.1 Material properties and process parameters.

Material	Aluminum alloy 5182	Aluminum alloy 5754
Ambient temperature, $T_a$	298 K	298 K
Melting point, $T_m$	850 K [54]	880 K
Boiling point, $T_v$	1930 K [9]	2035 K
Density, $\rho$	2300 kg/m <sup>3</sup> [55]	2300 kg/m <sup>3</sup>
Thermal conductivity, $\lambda_{th}$	108 W/m-K [55]	138 W/m-K
Specific heat, $C_p$	1200 J/kg-K [55]	1250 J/kg-K
Thermal diffusivity, $\kappa$	$3.9 \times 10^{-5}$ m <sup>2</sup> /s	$4.8 \times 10^{-5}$ m <sup>2</sup> /s
Heat of fusion, $\Delta H_f$	$3.95 \times 10^5$ J/kg [55]	$3.95 \times 10^5$ J/kg
Heat transfer coefficient, $h$	15 W/m <sup>2</sup> -K [56]	
Laser	Continuous wave Nd:YAG	
Laser power, $P$	2.5 kW	3.0 kW
Fresnel absorption, $\alpha$	0.1 [57]	
Inverse Bremsstrahlung absorption coefficient, $\alpha_p$	100 m <sup>-1</sup> [46]	
Welding speed, $v$	0.064 – 0.13 m/s (150 – 300 ipm)	
Beam focal length, $f$	0.078 m	
Beam diameter on optics, $d_b$	0.028 m	
Beam radius at focal point, $r_{f0}$	$3.0 \times 10^{-4}$ m	
Beam defocusing, $z_0$	-0.0025 to 0.0025 m	

\* The values of  $\rho$  and  $\Delta H_f$  are taken from those for pure aluminum considering the low concentrations of magnesium in the alloys.

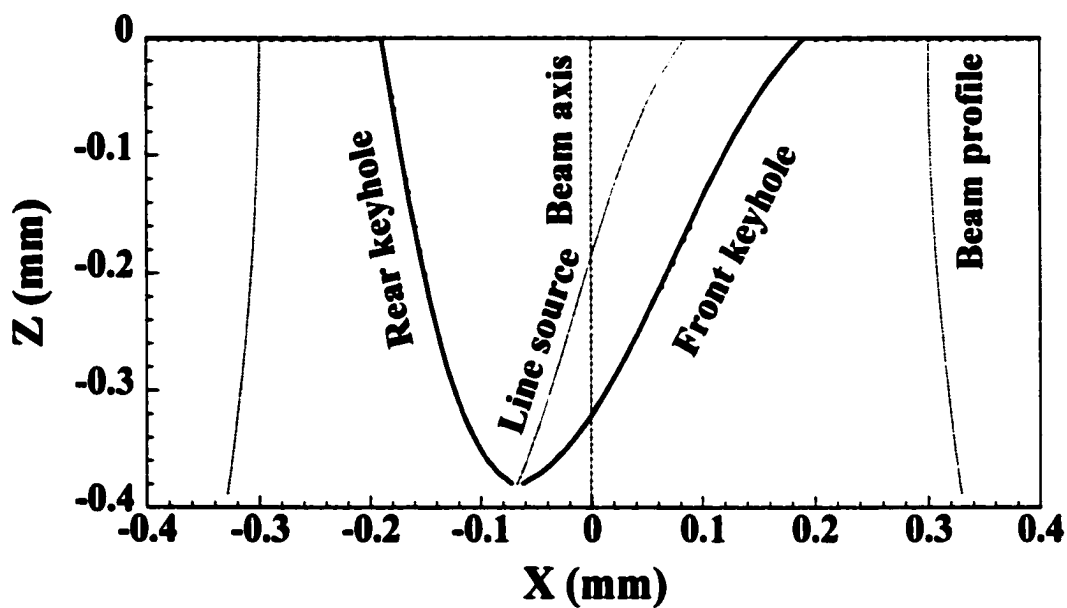


Fig. 4.10 Beam profile, line source location, and keyhole profile. Alloy: 5182, laser power: 2.5 kW, welding speed: 300 ipm (127 mm/s), and beam defocus: 0 mm.

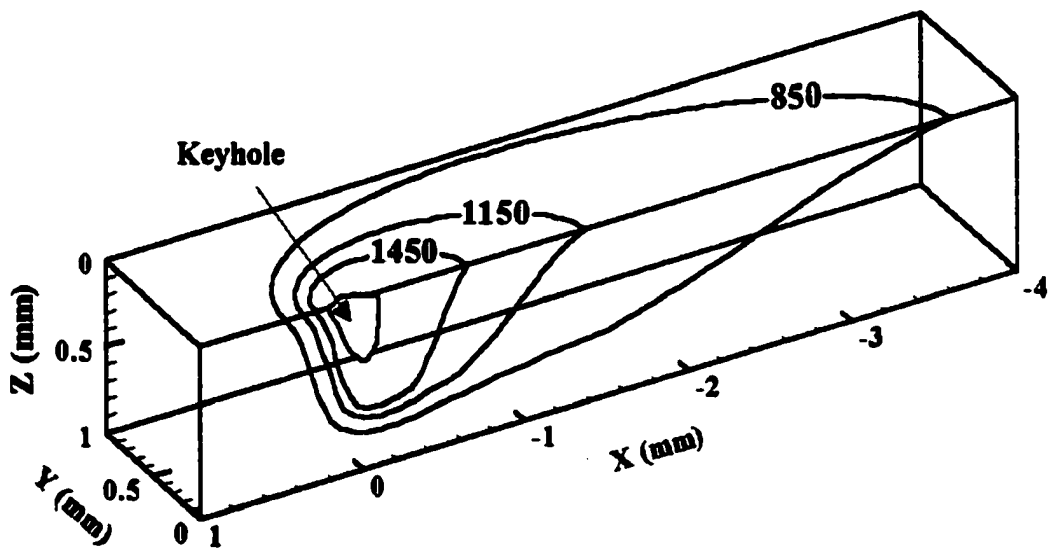


Fig. 4.11 Calculated three-dimensional temperature field in the weld pool. Temperatures are shown in K. Alloy: 5182, laser power: 2.5 kW, welding speed: 300 ipm (127 mm/s), and beam defocus: 0 mm.

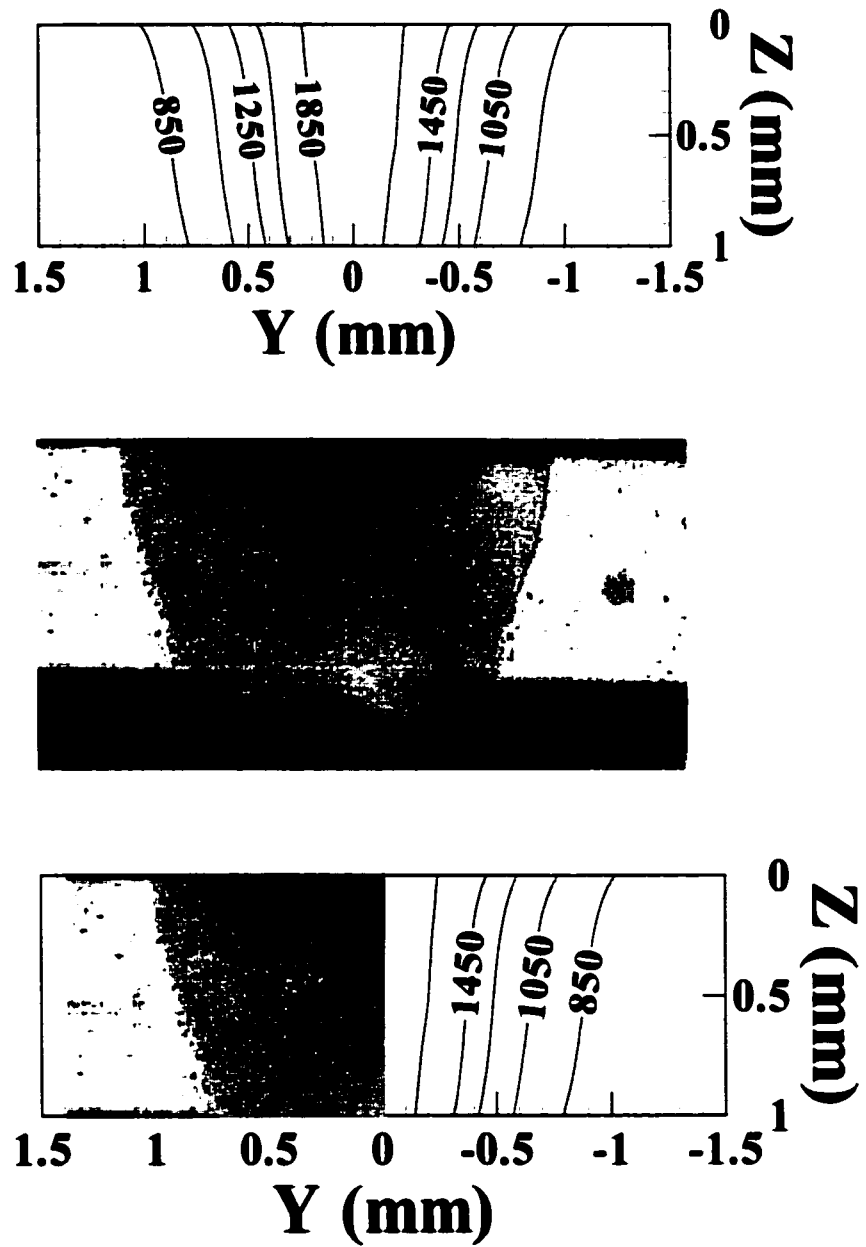


Fig. 4.12(a) Welding speed: 150 ipm

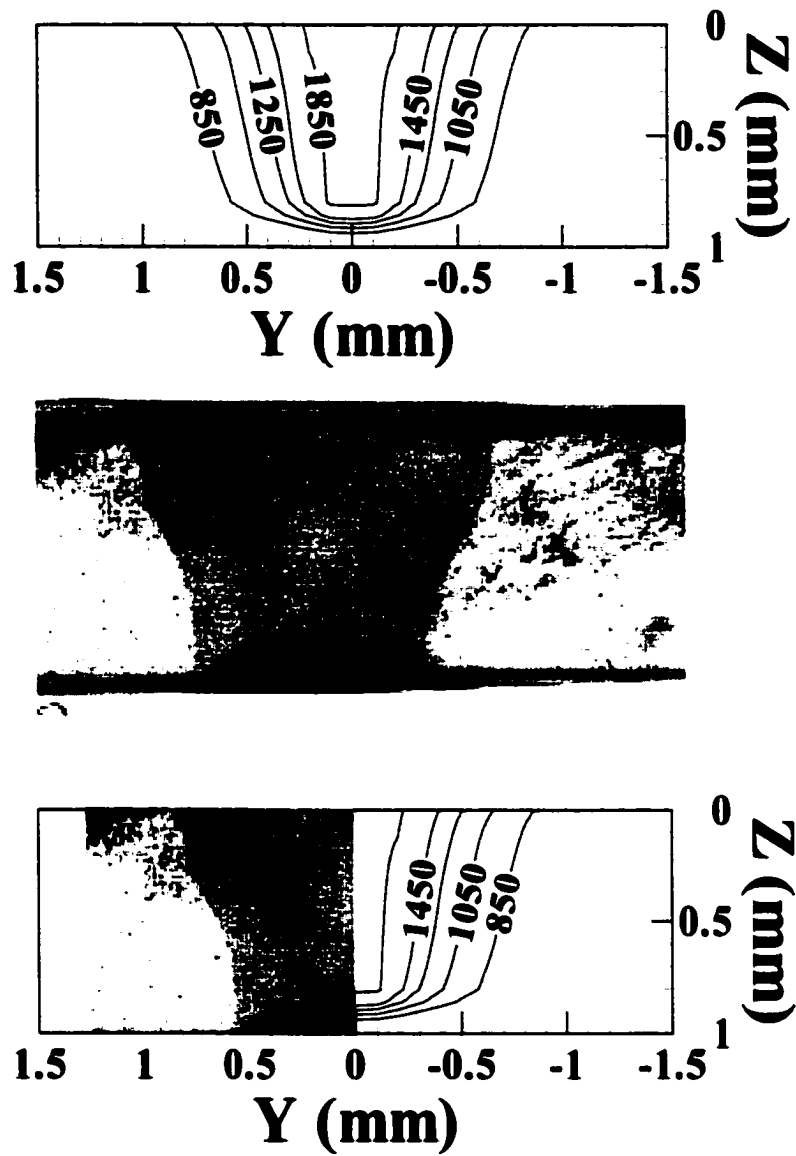


Fig. 4.12(b) Welding speed: 200 ipm

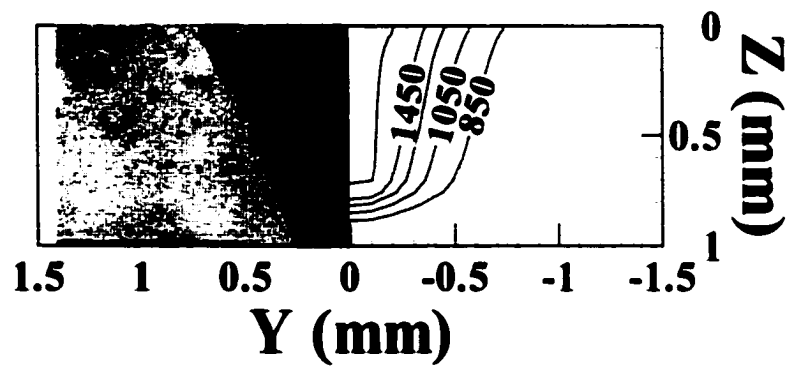
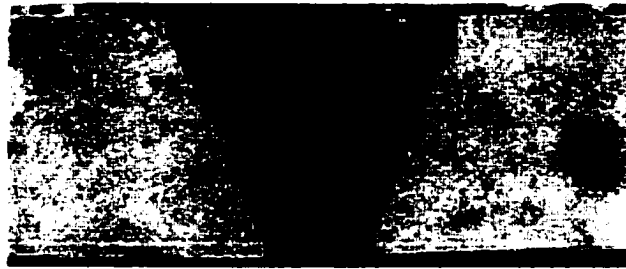
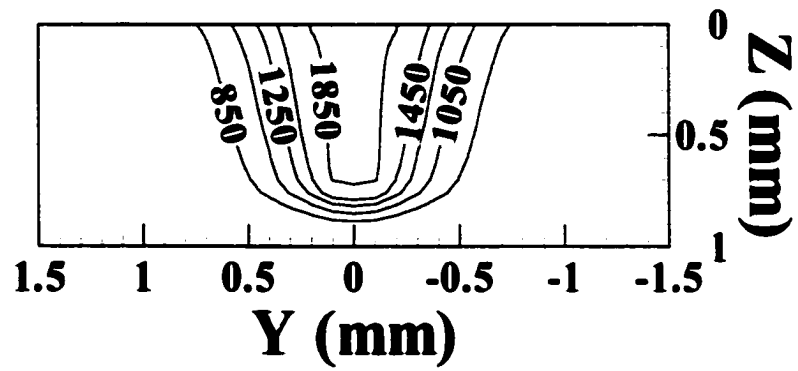


Fig. 4.12(c) Welding speed: 250 ipm

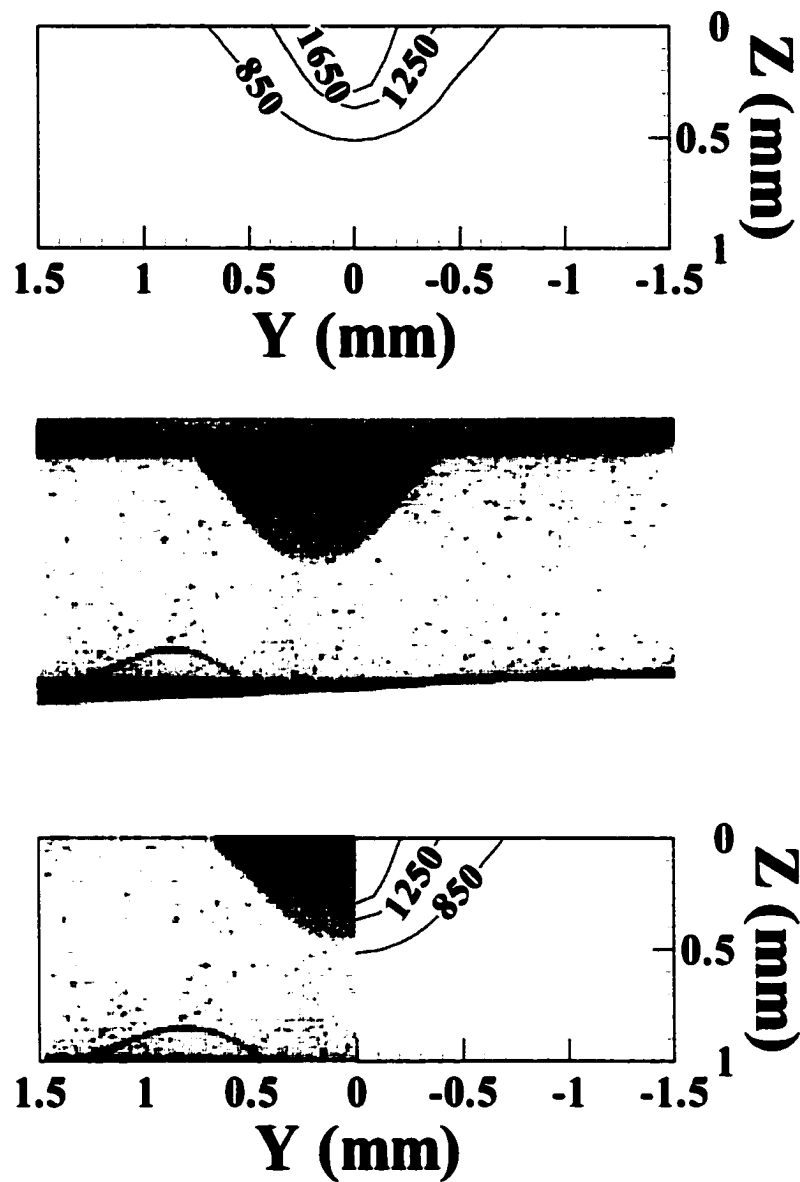


Fig. 4.12(d) Welding speed: 300 ipm

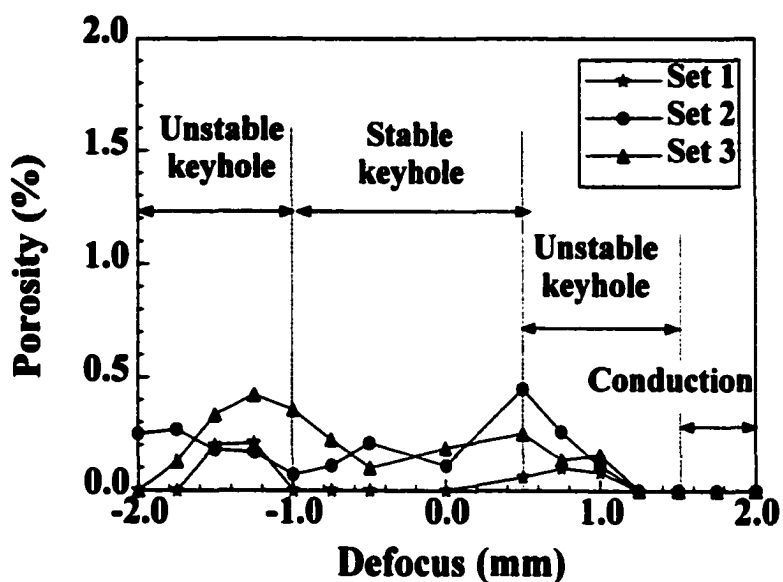
Fig. 4.12 Comparing of the experimentally obtained weld pool cross sections at several welding speeds with the calculated results. Alloy: 5182, plate thickness: 1.0 mm, laser power: 2.5 kW, beam defocus: 0 mm, and shielding gas flow rate: 200 ft<sup>3</sup>/h (5.66 m<sup>3</sup>/h) of helium. All figures have the same scale.

The experimental and calculated alloy 5182 weld pool cross sections for different welding speeds are shown in Fig. 4.12. The welding was performed using a focused beam at an output laser power of 2.5 kW and helium as the shielding gas at a flow rate of 200 ft<sup>3</sup>/h (5.66 m<sup>3</sup>/h). The isotherms for 1850K, 1450K, 1250K, 1050K, and 850K are shown in each of the calculated weld pool cross sections. The isotherm for solidus temperature 850 K gives the outline of the calculated molten pool. It is observed that the calculated weld pool geometry and the temperature distribution are consistent with the experimental results. As the welding speed increases, both the width and depth of the weld pool decrease. Furthermore, the heat conduction pattern also changes with the welding speed. At a welding speed of 150 ipm (0.064 m/s), the keyhole depth was equal to the plate thickness and a full penetration welding was obtained. All the isotherms are almost parallel to the beam axis, indicating a two-dimensional heat conduction that occurred predominantly in the direction vertical to the beam axis. At higher welding speeds, the keyhole depths were less than the plate thickness and partial penetration welds were obtained. The heat conduction in vertical direction became increasingly important as the welding speed was increased. At welding speed of 300 ipm (0.13 m/s), the keyhole depth was much less than the plate thickness and the rates of heat conduction in all directions are similar.

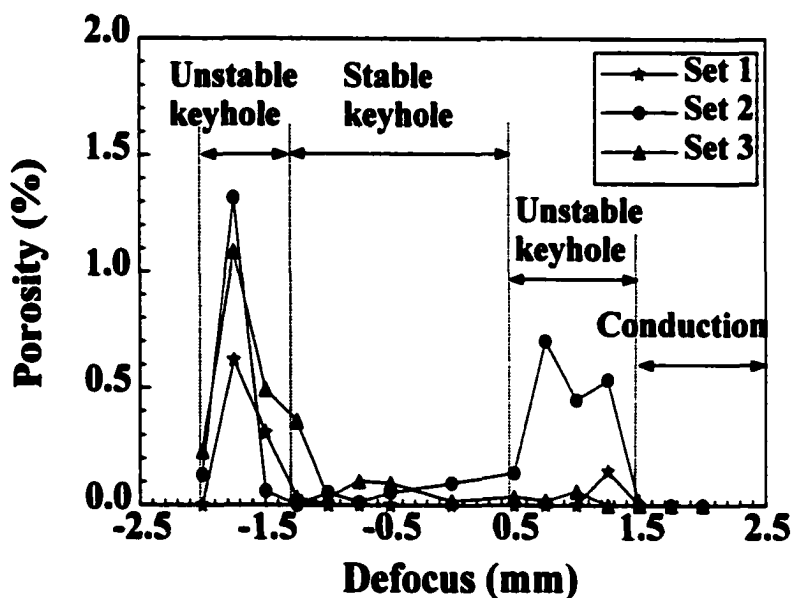
#### **4.3.2 Keyhole Stability and Macroporosity Formation**

Previous study [21] showed that the extent of laser beam defocusing greatly affected the keyhole stability, weld pool geometry, and macroporosity formation during laser welding of aluminum alloys 5182 and 5754. Fig. 4.13 [21] shows that porosity is minimum when welding is conducted in either keyhole or conduction mode. In contrast, high porosity in the weld metal is observed in the transition region where the keyhole is not stable. Therefore, the formation of macroporosity is linked to the instability of the keyhole. In this study, the stability of the keyhole and the mode of welding were predicted for different beam defocusing for these alloys and compared with the experimental results.





(a)



(b)

Fig. 4.13 Porosity produced at several defocus values in alloys (a) 5182 and (b) 5754. Nominal power: 3.0 kW, welding speeds: 250 ipm (106 mm/s) and 150 ipm (63.5 mm/s) for alloys 5182 and 5754, respectively, and shielding gas flow rate: 200 ft<sup>3</sup>/h (5.66 m<sup>3</sup>/h) of helium [21].

The calculated keyhole depth and weld pool depth for laser welded aluminum alloy 5182 for different beam defocusing values are given in Figs. 4.14(a) and 4.14(b), respectively. Three sets of experimental data for weld pool depths and the regions of welding mode based on the observation of weld pool geometry are also shown in Fig. 4.14(b). It is observed that the calculated weld pool depths agree well with the experimental data. For the welding conditions considered in this research, three distinct regions are identified based on the mode of welding depending on the beam defocusing. The three regions are stable keyhole, unstable keyhole, and conduction. When the beam is highly defocused, the beam intensity is well below the threshold value to form a keyhole, resulting in conduction mode welding characterized by shallow and wide weld pool shape. When the beam is nearly focused, the beam intensity is well above the threshold value to form a stable keyhole, resulting in deep weld pool characteristic of keyhole mode welding. The unstable keyhole regions are between the regions of conduction mode and stable keyhole mode, where the beam intensity is almost equal to the threshold value for keyhole formation. The welding mode in this intermediate region is unpredictable. Any disturbance in the system can cause the welding mode to shift between the keyhole and the conduction modes. As a result, in various cross sections of the same welded sample, the weld pool shapes characteristic of either conduction or keyhole mode were observed.

Based on the calculated keyhole depths shown in Fig. 14(a), keyhole mode welding occurred for beam defocusing values in the range of -1.0 to 1.0 mm. This prediction agrees fairly well with the experimentally obtained [21] stable keyhole region shown in Fig. 4.14(b). It is observed in Fig. 4.14(a) that for positive beam defocusing, the keyhole depth drops rapidly as the beam defocusing increases from 0.5 to 1.0 mm. This region can be considered to the transition region between stable keyhole mode to conduction mode. On the other hand, the predicted transition region for negative defocusing is more abrupt, which is a very small region near a beam defocusing value of -1.0 mm. It is also observed that the keyhole depth and consequently the weld pool depth are deeper for

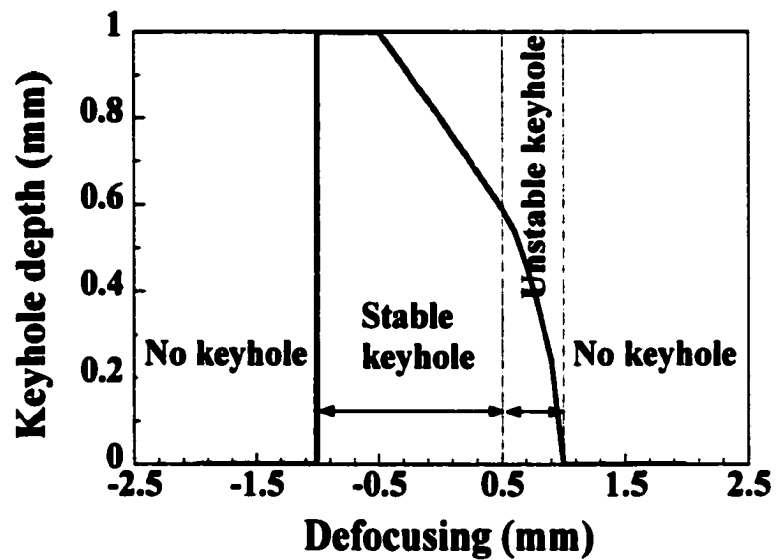


Fig. 4.14(a) Calculated keyhole depth for laser welded 1.0 mm-thick aluminum alloy 5182 plates at several beam defocus values. Laser power: 2.5 kW, welding speeds: 250 ipm (106 mm/s), and shielding gas flow rate: 200 ft<sup>3</sup>/h (5.66 m<sup>3</sup>/h) of helium.

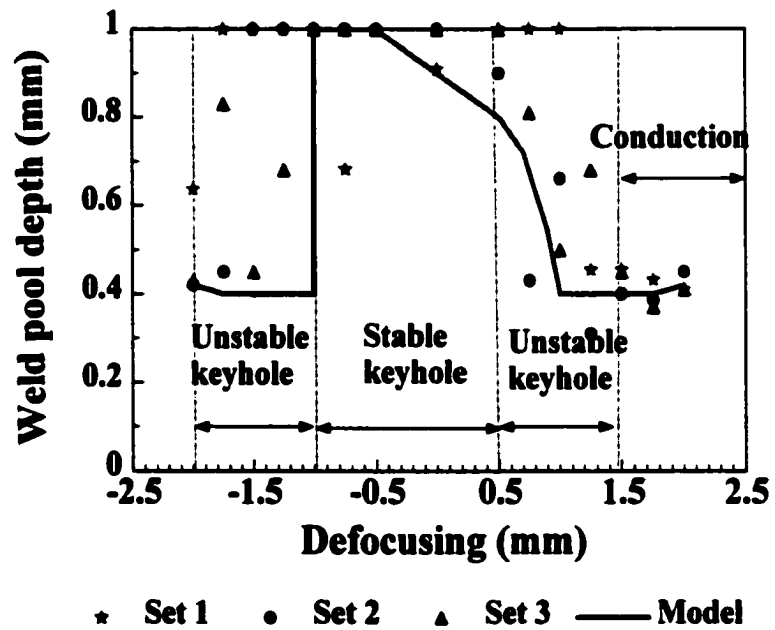


Fig. 4.14(b) Experimental [21] and calculated weld pool depths for laser welded 1.0 mm-thick aluminum alloy 5182 plates at several beam defocus values. Laser power: 2.5 kW, welding speeds: 250 ipm (106 mm/s), and shielding gas flow rate: 200 ft<sup>3</sup>/h (5.66 m<sup>3</sup>/h) of helium.

negative beam defocusing than positive defocusing. These differences in using positive and negative beam defocusing have been observed in an earlier study of laser welding of stainless steel [58] and can be explained from the interactions between the beam intensity and the keyhole. For negative beam defocusing, the beam is convergent and its intensity increases with the deepening of the keyhole, promoting the formation of a deeper keyhole. Such a positive feedback between the beam intensity and the keyhole depth also causes the keyhole depth to be either very deep or zero. Therefore, when the beam defocusing value is just lower than  $-1.0$  mm, the keyhole depth changes to zero as shown in Fig. 4.14(a). On the other hand, for positive beam defocusing, the beam is divergent and its intensity decreases with increase in keyhole depth, restricting further deepening of the keyhole. Such a negative feedback between the beam intensity and the keyhole depth causes the keyhole depth to decrease more gradually with increase in positive value of beam defocusing. Similarly, the experimental and calculated weld pool depths for laser welded aluminum alloy 5754 plates at several defocusing values are shown in Fig. 4.15. A good agreement is observed between the experimental and calculated values of weld pool depth.

Moreover, the model correctly predicted the transition from stable keyhole mode to conduction mode and therefore, the formation of macroporosity during welding. Figures 4.16(a) and 4.16(b) show the calculated weld pool depth and measured porosity in laser welded alloys 5182 and 5754, respectively. Based on the calculated weld pool depth, stable keyhole mode welding is obtained in the range of  $-1.0$  to  $0.5$  mm for alloy 5182 and  $-1.75$  to  $1.0$  mm for alloy 5754. As shown in the figures, no significant porosity is observed in the stable keyhole mode or conduction mode. However, at defocus values close to  $-1.0$  mm or  $0.5$  mm for alloy 5182 and  $-1.75$  mm or  $1.0$  mm for alloy 5754, the welding mode easily switches between conduction and keyhole modes and significant amount of porosity is formed. The results show that the model can be used as a tool to choose the appropriate welding parameters and prevent macroporosity formation.

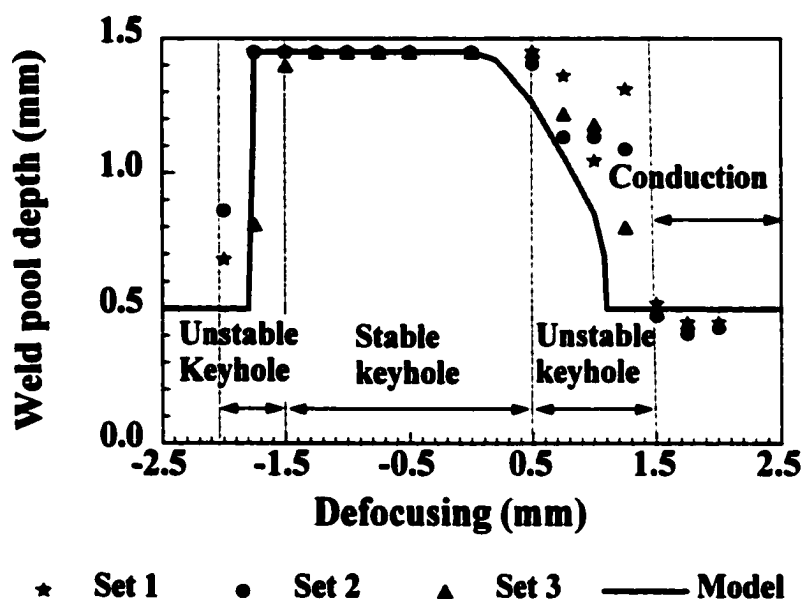


Fig. 4.15 The experimental [21] and calculated weld pool depths for laser welded 1.45 mm-thick aluminum alloy 5754 plates at several defocus values. Laser power: 3.0 kW, welding speed: 150 ipm (63.5 mm/s), and shielding gas flow rate: 200 ft<sup>3</sup>/h (5.66 m<sup>3</sup>/h) of helium. Three sets of experiments were conducted for each welding conditions.

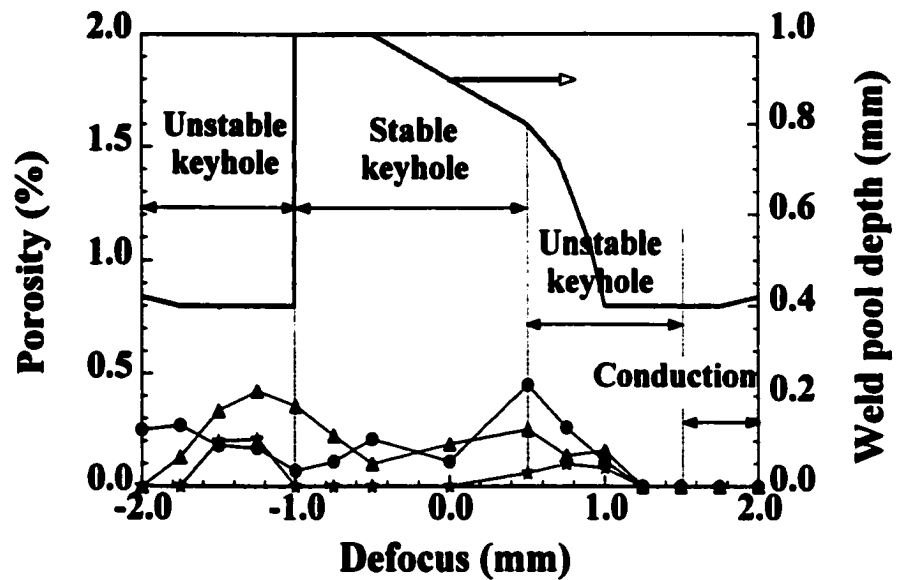


Fig. 4.16(a) The calculated weld pool depth and measured porosity [21] at several defocus values in alloy 5182. Laser power: 2.5 kW, welding speed: 250 ipm (106 mm/s), and shielding gas flow rate: 200 ft<sup>3</sup>/h (5.66 m<sup>3</sup>/h) of helium.

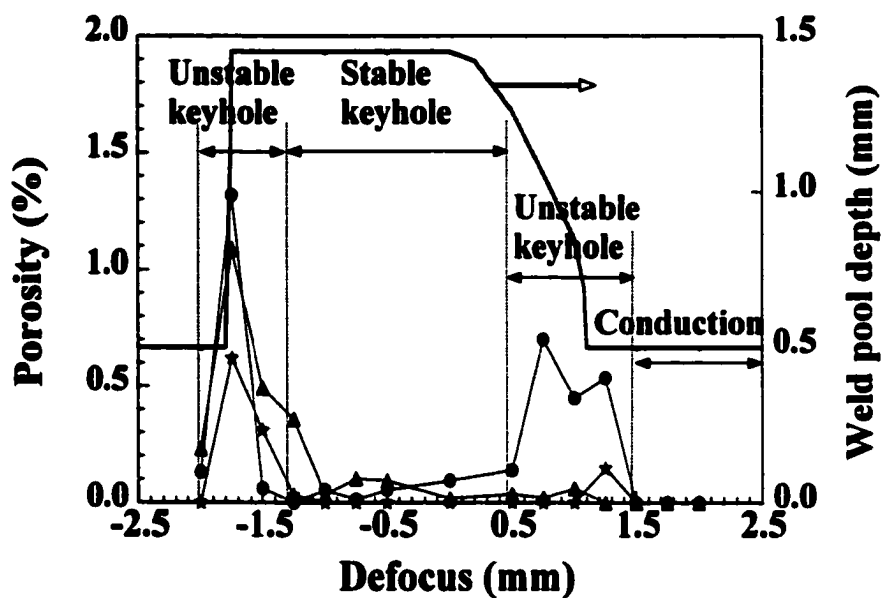


Fig. 4.16(b) The calculated weld pool depth and measured porosity [21] at several defocus values in alloy 5754. Laser power: 3.0 kW, welding speed: 150 ipm (63.5 mm/s), and shielding gas flow rate: 200 ft<sup>3</sup>/h (5.66 m<sup>3</sup>/h) of helium.



#### **4.4 Summery and Conclusions**

A model has been developed for keyhole mode laser beam welding. The keyhole profile was calculated based on point-by-point calculation of the energy balance on the keyhole wall where the temperature was assumed to be equal to the boiling point of the alloy. The three-dimensional temperature field of the weldment was calculated considering heat conduction from the computed keyhole geometry. In case of partial penetration welding, the temperature below the bottom of the keyhole was calculated by solving the heat conduction equation with appropriate boundary conditions. The model has been used to predict the mode of welding, the keyhole profile, and weld pool temperature field for high-speed laser welding of aluminum alloys 5182 and 5754. The following are the major conclusions:

1) The predicted welding mode for different beam defocusing agreed well with the experimental results. The model can be used to predict the welding mode and therefore it can determine the welding parameters that ensure stable keyhole formation and avoid macro porosity caused by the instability of the keyhole.

2) The intensity of a convergent (negative defocusing) beam increases, whereas that of a divergent (positive defocusing) beam decreases, with the deepening of the keyhole. Due to such a difference, welding with negative beam defocusing resulted in deeper keyhole than with positive beam defocusing. The transition from keyhole to conduction mode was also more abrupt for negative beam defocusing. The model is the first to be able to predict these differences between positive and negative defocusing beams.

3) The calculated keyhole profile was asymmetric with the rear wall being steeper than the front wall. This is consistent with the different heat conduction rates at the rear and front walls. The heat conduction rate at the front wall was faster since colder material was fed into the front wall during high speed laser welding. In order to balance the heat

loss, the front wall was more inclined so that more beam energy could be intercepted and absorbed. Such asymmetric features of the calculated keyhole wall profiles agree well with those experimentally observed.

4) The model can be used to predict the weld pool width, depth, and shape for different welding conditions. The predicted molten pool temperature fields were consistent with the salient features of experimentally obtained weld pool. As the welding speed increases, the welds changed from full penetration and two-dimensional cooling to partial penetration and three-dimensional cooling.

#### 4.5 References

1. G. M. Oreper, T. W. Eagar, and J. Szekely: *Welding Journal*, 1983, 62, pp. 307s-312s.
2. C. Chan, J. Mazumder, and M.M. Chen: *Metallurgical Transactions*, 1984, 15A, pp. 2175 –2184.
3. W. Pitscheneder, T. DebRoy, K. Mundra, and R. Ebner: *Welding Journal*, 1996, 75, 3, pp. 71s – 80s.
4. S. Kou and Y.H. Wang: *Metallurgical Transactions*, 1986, 17A, pp. 2271-2277.
5. A. Paul and T. DebRoy: *Metallurgical Transactions*, 1988, 19B, pp. 851-858.
6. T. Zacharia, A. H. Eraslan, and D. K. Aidun: *Welding Journal*, 1988, 67, pp. 53s-62s.
7. K. Mundra, T. DebRoy, T. Zacharia, and S. A. David: *Welding Journal*, 1992, 64, pp. 313s-320s.
8. K. Mundra and T. DebRoy: *Welding Journal*, 1993, 72, 1, pp. 1s-9s.
9. H. Zhao and T. DebRoy: *Metallurgical and Materials Transactions*, 2001, 32B, pp. 163-172.
10. K. Mundra, J. M. Blackburn, and T. DebRoy: *Science Technology of Welding and Joining*, 1997, 2, 4, pp. 174-184.
11. T. A. Palmer and T. DebRoy: *Science Technology of Welding and Joining*, 1998, 3, 4, pp. 190-203.

12. Z. Yang and T. DebRoy: *Sci. Tech. Weld. Joining*, 1997, 2, 2, pp. 53-58.
13. Z. Yang, J. W. Elmer, J. Wong, and T. DebRoy: *Welding Journal*, 2000, 79, 4, pp. 97s-112s.
14. S. Sista, Z. Yang, and T. DebRoy: *Metallurgical and Materials Transactions*, 2000, 31B, pp. 529-535.
15. T. Hong, W. Pitscheneder, and T. DebRoy: *Science Technology of Welding and Joining*, 1998, 3, 1, pp. 33-41.
16. R. F. Ashton, R. P. Wesley, and C. R. Dixon: *Welding Journal*, 1975, 54, 3, pp. 95s-98s.
17. S. Katayama: *Journal of Light Metal Welding and Construction*, 1996, 34, 4, pp. 31-41.
18. D. A. Schauer and W. H. Giedt: *Welding Journal*, 1978, 57, 7, pp. 189s-195s.
19. I. R. Whitaker, D. G. McCartney, and W. M. Steen: *ICALEO'92*, 1992, pp. 565-573.
20. R. P. Martukanitz and D. J. Smith: in *Proceedings of the Sixth International Conference on Aluminum Weldments*, AWS, Cleveland, OH, 1995, pp. 309-323.
21. M. Pastor, H. Zhao, R. P. Martukanitz, and T. DebRoy: *Welding Journal*, 1999, 78, 6, pp. 207s-216s.
22. D. E. Swift-Hook and A. E. F. Gick: *Welding Journal*, 1973, 52, 11, pp. 492s-499s.
23. J. G. Andrews and D. R. Atthey: *Journal of Physics D: Applied Physics*, 1976, 15, 9, pp. 2181-2194.
24. P. G. Klemens: *Journal of Applied Physics*, 1976, 47, 5, pp. 2165-2174.
25. J. Mazumder and W. M. Steen: *Journal of Applied Physics*, 1980, 51, 2, pp. 941-947.
26. J. Dowden, M. Davis, and P. Kapadia: *Journal of Fluid Mechanics*, 1983, 126, pp. 123-146.
27. M. Davis, P. Kapadia, and J. Dowden: *Welding Journal*, 1986, 65, 7, pp. 167s-174s.
28. J. Dowden, N. Postacioglu, M. Davis, and P. Kapadia: *Journal of physics D: Applied Physics*, 1987, 20, 1, pp. 36-44.
29. N. Postacioglu, P. Kapadia, M. Davis, and J. Dowden: *Journal of Physics D: Applied Physics*, 1987, 20, 3, pp. 340-345.
30. A. Kar and J. Mazumder: *ICALEO'94*, 1994, pp. 490-498.

31. P. S. Mohanty and J. Mazumder: *Science and Technology of Welding and Joining*, 1997, 2, 3, pp. 133-138.
32. W. M. Steen, J. Dowden, M. Davis, and P. Kapadia: *Journal of Physics D: Applied Physics*, 1988, 21, 8, pp. 1255-1260.
33. G. Herziger et al.: in '*Laser Materials Processing*', 1984, p. 55, Plenum Press, NY.
34. A. Kar, T. Rockstroh, and J. Mazumder: *Journal of Applied Physics*, 1992, 71, pp. 2560-2569.
35. M. Beck, P. Berger, H. Hugel: in '*Laser Treatment of Materials*', Proceedings of ECLAT'92 conference, Gottingen, Germany, edited by B. L. Mordike, 1992, pp.693-698.
36. J. Kross, U. Gratzke, and G. Simon: *Journal of Physics D: Applied Physics*, 1993, 26, 3, pp. 474-480.
37. E. A. Metzbower: *Metallurgical Transactions*, 1993, 24B, 5, pp. 875-880.
38. A. Cybulski and Z. Mucha: *Welding International*, 1997, 11, 3, pp. 212-220.
39. A. Matsunawa, J. D. Kim, N. Seto, M. Mizutani, and S. Katayama: *Journal of Laser Applications*, 1998, 10, 6, pp. 247-254.
40. J. Kroos, U. Gratzke, M. Vicanek, and G. Simon: *Journal of Physics D: Applied Physics*, 1993, 26, 3, pp. 481-486.
41. T. Klein, M. Vicanek, J. Kroos, I. Decker, and G. Simon: *Journal of Physics D: Applied Physics*, 1994, 27, 10, pp. 2023-2030.
42. A. Matsunawa and V. Semak: *Journal of Physics D: Applied Physics*, 1997, 30, 5, pp. 798-809.
43. Y. Arata: '*Plasma, Electron and Laser Beam Technology*', American Society for Metals, Metal Park, OH, 1986.
44. V. Semak, W. Bragg, B. Damkroger, and S. Kempka: *Journal of Physics D: Applied Physics*, 1999, 32, pp. L61-L64.
45. S. Fujinaga, H. Takenaka, T. Narikiyo, S. Katayama, and A. Matsunawa: *Journal of Physics D: Applied Physics*, 2000, 33, 5, pp. 492-497.
46. A. Kaplan: *Journal of Physics D: Applied Physics*, 1994, 27, pp. 1805-1814.
47. D. Rosenthal: *Transactions of ASME*, 1946, 48, pp. 848-866.

48. I. N. Bronstein and K. A. Semendjajew: *Taschenbuch der Mathematik*, 22nd edition, 1985, Teubner, Leipzig.
49. P. Mouroulis and J. Macdonald: '*Geometrical Optics and Optical Design*', 1997, Oxford University Press, Cambridge, U. K.
50. A. Block-Bolten and T. W. Eagar: *Metallurgical Transactions*, 1984, 15B, pp. 461-469.
51. M. M. Collur, A. Paul, and T. DebRoy: *Metallurgical Transactions*, 1987, 18B, pp. 733-739.
52. P. Sahoo, M. M. Collur, and T. DebRoy: *Metallurgical Transactions*, 1988, 19B, pp. 967-972.
53. M. M. Collur: '*Alloying Element Vaporization and Emission Spectroscopy of Plasma during Laser Welding of Stainless Steels*', Ph.D. thesis, Metal Science and Engineering, The Pennsylvania State University, University Park, PA, December, 1988.
54. *ASM Handbook*, v. 2, *Properties and Selection--Nonferrous Alloys and Special-purpose Materials*, 10th edition, 1990, ASM International, Materials Park, OH.
55. J. E. Hatch: '*Aluminum: Properties and Physical Metallurgy*', 1984, American Society for Metals, Metals Park, OH.
56. F. Incropera and D. DeWitt: '*Introduction to Heat Transfer*', 1985, Wiley, New York.
57. M. A. Bramson: '*Infrared Radiation: A Handbook for Applications*', 1968, Plenum Press, New York.
58. I. Miyamoto, H. Maruo, and Y. Arata: in '*Plasma, Electron and Laser Beam Technology*', edited by Y. Arata, 1986, pp. 492-497, American Society for Metals, Metal Park, OH.
59. D. Williams: '*Spectroscopy*', 1976, Academic Press, New York.

#### 4.6 List of Symbols

$T$	Temperature, K
$T_a$	Ambient temperature, K
$T_m$	Melting point, K
$T_v$	Boiling point, K
$\rho$	Density, $\text{kg/m}^3$
$\lambda_{th}$	Thermal conductivity, $\text{W/m-K}$
$C_p$	Specific heat, $\text{J/kg-K}$
$\kappa$	Thermal diffusivity, $\text{m}^2/\text{s}$
$\Delta H_v$	Heat of evaporation, $\text{J/kg}$
$h$	Heat transfer coefficient, $\text{W/m}^2\text{-K}$
$K_0$	Modified Bessel function of second kind and zero order
$K_0'$	Derivation of $K_0$
$K_1$	Modified Bessel function of second kind and first order
$v$	Welding speed, $\text{m/s}$
$P$	Laser power, $\text{W}$
$P'$	Strength of line source, $\text{W/m}$
$Pe'$	Modified Peclet number, $v/(2\kappa)$ , $\text{m}^{-1}$
$I_c$	Heat flux conducted into the keyhole, $\text{W/m}^2$
$I_v$	Evaporation heat flux, $\text{W/m}^2$
$J_v$	Evaporation flux, $\text{kg/m}^2\text{-s}$
$x_{fs}$	Distance between line source and front keyhole wall, $\text{m}$
$x_{rs}$	Distance between line source and rear keyhole wall, $\text{m}$
$x_f$	Location of front keyhole wall in Cartesian coordinate system, $\text{m}$
$x_r$	Location of rear keyhole wall in Cartesian coordinate system, $\text{m}$
$x_s$	Location of line source in Cartesian coordinate system, $\text{m}$
$I_0$	Beam intensity at any given point, $\text{W/m}^2$
$I_{f0}$	Peak beam intensity at the focal point, $\text{W/m}^2$
$I_a$	Absorbed beam intensity at any given point, $\text{W/m}^2$

$I'_a$	Absorbed beam intensity considering the damping effect of plasma, $W/m^2$
$I_{ib}$	Laser intensity absorbed by plasma due to inverse Bremsstrahlung, $W/m^2$
$I_{mr}$	Absorbed beam intensity during multiple reflections, $W/m^2$
$\alpha$	Fresnel absorption coefficient
$\alpha_{ib}$	Plasma absorption coefficient by the plume inside of the keyhole before the laser beam hits the keyhole wall for the first time
$\alpha_{mr}$	Absorption coefficient by the workpiece during multiple reflections
$\alpha_p$	Inverse Bremsstrahlung absorption coefficient, $m^{-1}$
$d$	Depth of the keyhole, m
$f$	Beam focal length, m
$d_b$	Beam diameter on optics, m
$r_f$	Beam radius at any given location on the beam axis, m
$r_0$	Beam radius at focal point, m
$\theta$	Angle between the keyhole wall and beam axis
$\theta_f$	Angle between the front keyhole wall and beam axis
$\theta_r$	Angle between the rear keyhole wall and beam axis
$\bar{\theta}$	Mean angle of keyhole wall
$z_0$	Beam defocusing, m

#### 4.7 Appendix: Calculation of Various Absorption Coefficients

##### a) Plasma absorption coefficient before the beam hits the keyhole wall

Plasma absorption of an incident laser beam due to inverse Bremsstrahlung can be described by Beer-Lambert's law [59]:

$$\alpha_{ib} = 1 - \frac{I_t}{I_i} = 1 - e^{-\alpha_p l} \quad (4.1A)$$

where  $I_i$  is the incident intensity,  $I_t$  is the transmitted intensity when passing through a path of length  $l$ , and  $\alpha_p$  is the absorption coefficient.

Assuming that for Nd:YAG laser welding plasma exists only within the keyhole and the mean path of the laser beam passing through the plasma is half of the keyhole depth, the fraction of beam absorbed by the plasma inside of the keyhole before the beam hits the keyhole wall for the first time is calculated by

$$\alpha_{ib} = 1 - e^{-\alpha_p d/2} \quad (4.2A)$$

where  $d$  is the keyhole depth.

##### b) Absorption coefficient by the workpiece during multiple reflections

When the beam impinges on the workpiece, part of its energy is absorbed by the workpiece and the remaining part is reflected. The absorbed energy is equal to the product of incident beam energy and the Fresnel absorption coefficient. Assuming the Fresnel absorption coefficient to be constant and equal to the value for normal incidence, the remaining fraction of the beam energy after  $n_{mr}$  reflections is given by

$$\alpha_{rf} = (1 - \alpha)^{n_{mr}} \quad (4.3A)$$

where  $\alpha$  is the Fresnel absorption coefficient.



Based on the keyhole profile calculated in the first round, the keyhole wall is approximated to be symmetrical with respect to the initial incident beam with a mean wall angle of  $\bar{\theta}$  as shown in Fig. 4.17. Based on optical geometry, the angle between the reflected beam and the initial incident beam after  $n_{mr}$  reflections is calculated to be

$$\theta' = 2n_{mr}\bar{\theta} \quad (4.4A)$$

When the angle  $\theta'$  reaches  $\pi/2$ , the reflected beam leaves the keyhole without being further absorbed. Therefore, a limiting angle of  $\pi/2$  can be defined for  $\theta'$ , above which the reflected beam leaves the keyhole. Consequently, the number of total reflections within the keyhole can be calculated from Eqn. (4.4A) as

$$n_{mr} = \frac{\theta'}{2\bar{\theta}} = \frac{\pi/2}{2\bar{\theta}} = \frac{\pi}{4\bar{\theta}} \quad (4.5A)$$

If the first reflection is separately considered, the number of multiple reflections is equal to  $n_{mr}-1$ . The remaining fraction of beam energy after multiple reflections is calculated from Eqn. (4.3A) and Eqn. (4.5A) as

$$\alpha_{rf} = (1-\alpha)^{n_{mr}-1} = (1-\alpha)^{\pi/(4\bar{\theta})-1} \quad (4.6A)$$

Accordingly, the fraction of beam energy absorbed by the workpiece on the keyhole wall during the multiple reflections is given by

$$\alpha_{mr} = 1 - \alpha_{rf} = 1 - (1-\alpha)^{\pi/(4\bar{\theta})-1} \quad (4.7A)$$

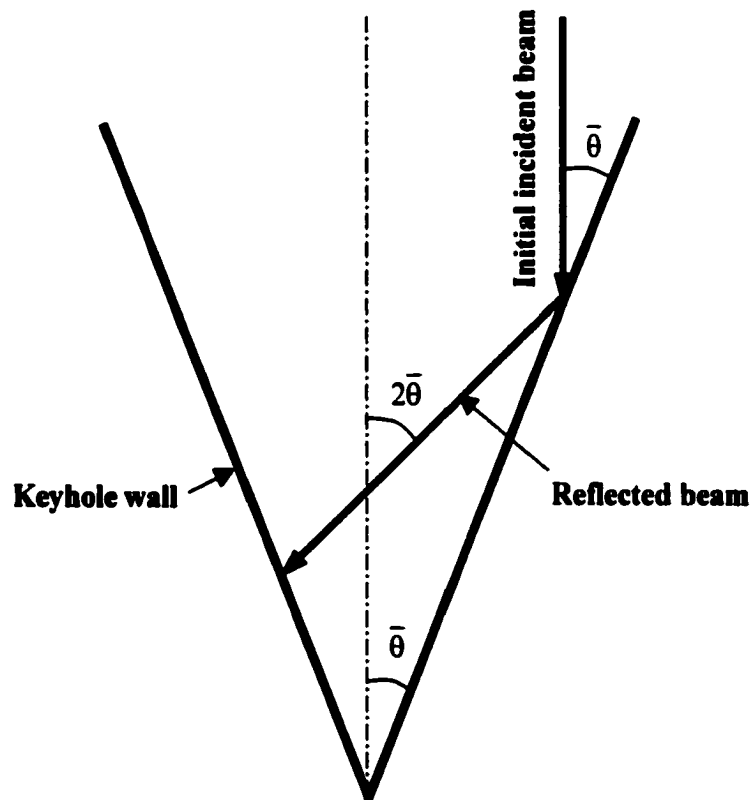


**Fig. 4.17** Schematic diagram showing the angles among the initial incident beam, the reflected beam and the keyhole wall.

**c) Typical case study**

The data for plasma absorption of Nd:YAG lasers are not available in the literature. The value for  $\alpha_p$  is estimated based on the value used for CO<sub>2</sub> laser welding [46]. Using typical values of 100 m<sup>-1</sup>, 0.8 x 10<sup>-3</sup> m,  $\pi/6$ , and 0.1 for  $\alpha_p$ ,  $d$ ,  $\bar{\theta}$ , and  $\alpha$ , respectively, the plasma absorption coefficient before the beam hits the keyhole wall and the absorption coefficient by the workpiece during multiple reflections are calculated from Eqn. (4.2A) and Eqn. (4.7A) as

$$\alpha_{ib} = 1 - e^{-\alpha_p d/2} = 1 - e^{(-100 \times 0.8 \times 10^{-3} / 2)} = 0.04$$

$$\alpha_{mr} = 1 - (1 - \alpha)^{\pi/(4\bar{\theta})-1} = 1 - (1 - 0.1)^{6\pi/(4\pi)-1} = 1 - 0.9^{0.5} = 0.05$$

From Eqn. (4.21), the fraction of absorbed laser intensity by the workpiece during the first incidence considering the damping effect of plasma is

$$(1 - \alpha_{ib})\alpha = (1 - 0.04)0.1 = 0.096$$

From Eqn. (4.22), the fraction of absorbed laser energy by the workpiece during multiple reflections is

$$(1 - \alpha_{ib})(1 - \alpha)\alpha_{mr} = (1 - 0.04)(1 - 0.1)0.05 = 0.043$$

The total fraction of laser energy absorbed by the work piece on the keyhole wall is  $0.043 + 0.096 = 0.14$ . Part of the remaining laser energy is absorbed by the plasma and part of it is reflected away from the keyhole without being absorbed.

## Chapter 5

### PORE FORMATION DURING LASER WELDING OF DIE-CAST MAGNESIUM ALLOY AM60B – MECHANISM AND REMEDY

#### 5.1 Background

Magnesium alloys are finding increasing use in the automotive industry because of their excellent specific strength and good elongation and toughness. The specific strength, i.e., the ratio of tensile strength and specific gravity, of die-cast magnesium alloy AM60B, 122 MPa, far exceeds that of low carbon steel which is 45 MPa. The use of these lightweight alloys can help automakers improve fuel economy and reduce greenhouse gas emissions. To make the most weight and cost savings in the use of automotive alloys, tailor welded blanks are widely used in the autobody. Laser welding is a preferred method in the manufacture of tailor welded blanks due to its high speed, low heat input and low weldment distortion. Increasing use of aluminum and magnesium alloys in tailor welded blanks will require improved technology to fabricate structurally sound and defect-free welds easily and reproducibly.

One of the major concerns during welding of magnesium and aluminum alloys is the presence of porosity in the weld metal. The presence of porosity in the weld metal deteriorates mechanical properties, particularly the tensile strength and elongation [1-3]. However, pore formation during welding of magnesium alloys has not been systematically studied. In contrast, the mechanism of porosity formation during welding of aluminum alloys has received considerable attention [4-12]. The pore formation has been attributed to hydrogen rejection from the solid phase during solidification [4-7] and imperfect collapse of the keyhole [7-10]. In addition, turbulent flow in the weld pool [11] has also been linked with porosity formation. However, in a recent study, Pastor et al. [12] found that keyhole stability played a major role in porosity formation during continuous-wave Nd:YAG laser welding of aluminum alloys 5182 and 5754. Furthermore,

they showed that segregation of hydrogen played an insignificant role in the formation of large pores in the welds.

Although the mechanism of pore formation during welding of aluminum alloys is better understood than magnesium alloys, there are some similarities between the welding of these two types of alloys. Both aluminum and magnesium have significantly higher hydrogen solubility in liquid than in solid. For magnesium, this difference in the hydrogen solubility can be observed from Fig. 5.1 [13]. Mikucki and Shearouse [14] found that the amount of macroporosity in the solidified magnesium alloy AZ91 was proportional to the dissolved hydrogen in the alloy. They also found that the rejection of hydrogen from the  $Mg_{17}Al_{12}$  intermetallic compound assisted in the nucleation and/or growth of microporosity during the last stages of solidification of alloy AZ91 [15]. The difference in the solubility between the solid and the liquid phases and the results of previous solidification studies [14,15] indicate that hydrogen rejection needs to be considered as a possible cause of porosity formation during solidification of magnesium alloys [14,15].

Haferkamp et al. [16] observed more porosity in the fusion zone of non-vacuum die-cast alloy AM60B than vacuum die-cast alloy AZ91D that had less gas inclusions in the base metal. They found that for the same porosity level in welds, large pores are more detrimental to strength than small pores. The presence of gas inclusions in the base metal was thought to be an important factor in contributing to the formation of large pores during Nd:YAG laser welding of magnesium alloys [16].

Better understanding of pore formation in AM60B fusion zone during laser welding and alleviation of the porosity problem are needed for wider application of this alloy in the automotive industry. This research seeks to achieve these two important goals.

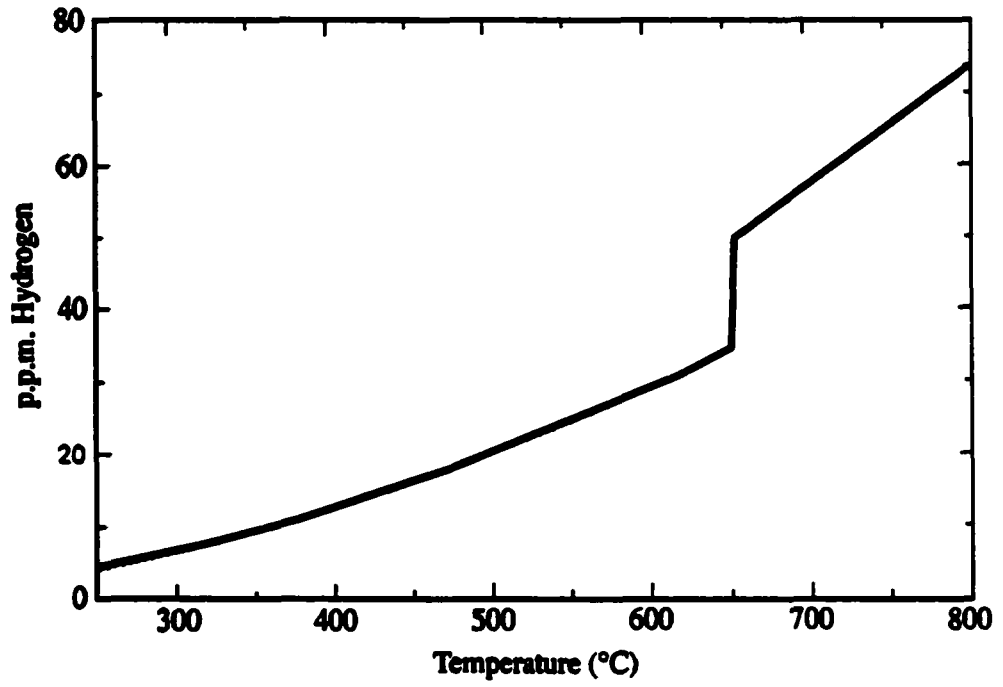


Fig. 5.1 Solubility of hydrogen in magnesium [13].

## 5.2 Experimental Procedure

Bead-on-plate autogenous welds were produced on 2 to 6 mm thick plates of die-cast magnesium alloy AM60B using a 3.0 kW continuous-wave Nd:YAG laser at Penn State. The composition of alloy AM60B sample was determined by spectrochemical characterization and the results are presented in Table 5.1.

Table 5.1 Chemical composition (wt%) of alloy AM60B

Al	Cu	Fe	Mn	Ni	Si	Zn	Mg
5.22	< 0.01	< 0.01	0.26	< 0.01	0.04	0.05	Balance

The base metal, alloy AM60B, contained 1.8 to 5 area percent porosity, depending on the plate thickness. Prior to welding, the samples were ground with 400 grit SiC paper and cleaned with acetone. The laser beam was delivered using a 600  $\mu\text{m}$  diameter fiber of fused silica to an  $f2$  focus lens. A robot was employed to manipulate the motion of the lens assembly relative to the workpiece mounted horizontally on a stage. Prior to welding, the samples were ground with 400-grit grind cloth and then cleaned with acetone. The variables used were laser power in the range of 1.0 to 3.0 kW, welding speed between 125 and 300 in./min (53 to 127 mm/s), and beam defocusing in the range of -3.5 to +3.0 mm. At a nominal laser power of 1.5 kW (actual power is 1.55 kW), the laser power density varied in the range of approximately  $9.6 \times 10^4$  to  $5.3 \times 10^5$  W/cm<sup>2</sup> depending on the beam defocusing values as shown in Table 5.2. A nomenclature of positive defocusing to indicate the focal point of the laser beam above the top surface of the workpiece and negative defocusing to represent the focal point below the top surface is used throughout this paper. A cylindrical copper nozzle having an inside diameter of 8.0 mm was utilized to provide helium as the shielding gas at a flow rate of 200 ft<sup>3</sup>/h (5.7 m<sup>3</sup>/h). Some specimens were re-welded to study the effect of re-melting on fusion zone porosity.

**Table 5.2 Power density on the specimen surface at different beam defocusing at a nominal laser power of 1.5 kW**

Beam defocusing (mm)	0	0.5	1.0	1.5	2.0	2.5	3.0	3.5
Power density (W/cm <sup>2</sup> )	$5.3 \times 10^5$	$4.9 \times 10^5$	$3.9 \times 10^5$	$2.9 \times 10^5$	$2.1 \times 10^5$	$1.6 \times 10^5$	$1.2 \times 10^5$	$9.6 \times 10^4$

Metallographic samples were prepared using cold resin mounting and consequently polished with SiC paper and progressively finer alumina powders down to 0.05  $\mu\text{m}$  in size. Some of the macrographs showing the weld pool geometry and macro pores were electronically enhanced to improve contrast. The weld pool geometry, area percent porosity, pore size distribution, and average pore radius in the base metal and fusion zone were measured by optical microscopy and computer image analysis using Image Pro® software. Based on the observed morphology and distribution of the pores in several cross-sections, it was assumed that the pores were spherical and evenly distributed. Therefore, the values of average pore radii for 3D spherical pores were calculated by multiplying the average radii measured in 2D cross sections by  $\pi/2$  based on Fullman's theory [17] for a polydispersed system of spheres. The number of pores per unit volume was calculated from the average 3D pore radius and the volume percent porosity, which is equal to the measured area percent porosity. Unless specified otherwise, all the data of pore radii hereafter are 3D pore radii. The microstructures in the weld metal were observed using optical microscopy and Vickers microhardness testing was conducted across the welds.



## **5.3 Results and Discussion**

### **5.3.1 Enhanced Porosity due to Melting of the Base Metal**

During welding of alloy AM60B it became clear that the area percent porosity in the fusion zone was often higher than that in the base metal that contained pre-existing pores. Therefore, the origin of the enhanced porosity level in the fusion zone is an important question in this study. In order to answer this question fully, it is intuitive to consider the mechanisms of porosity formation in the welding of other non-ferrous alloys. For example, during continuous wave laser welding of automotive aluminum alloys, a significant number of large pores was formed in the fusion zone [12]. The pore formation was found to result from the instability of the keyhole. Therefore, the role of keyhole instability in the formation of large pores in the welding of alloy AM60B needs to be investigated together with other possible causes of porosity enhancement resulting from the coalescence and expansion of the pre-existing pores.

Melting of the base metal can serve as a control experiment where the coalescence of the pores can be studied in the absence of any keyhole formation. The solidus and liquidus temperatures of alloy AM60B are 813 and 888 K, respectively. A few samples of the base metal were partially melted at 863 K and held for 2 hours to study coalescence of pores. In this system, the changes in the porosity can be attributed to the heating, melting and pore coalescence while reducing the escape of gases that may occur easily from a fully melted alloy. Figure 5.2 shows the extent of porosity in the base metal and solidified sample after 2 hours of heating at 863 K. Quantitative microscopy showed that the heating resulted in increase in the average pore radius from about 2 to 6  $\mu\text{m}$ , decrease in number density from about 3400 to about 1500 per  $\text{mm}^2$ , and increase in area percent porosity from about 1.8% to about 7.0%. In short, the control experiment showed that just partial melting of the alloy resulted in significant increase in pore size and, more important, higher area percent porosity than the base metal.



**Fig. 5.2(a) Micrograph showing features of porosity on an unetched sample of 2 mm-thick alloy AM60B plate base metal before heat treatment.**

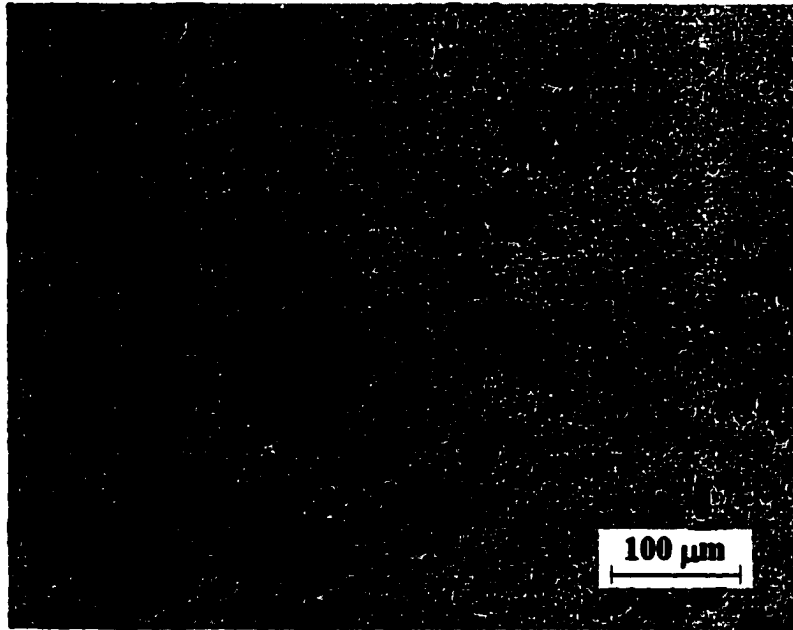


**Fig. 5.2(b) Micrograph showing features of porosity on an unetched sample of 2 mm-thick alloy AM60B plate after heat treatment at 863 K for 2 hours.**

The increase in the pore size and the decrease in the pore number density can be readily attributed to pore coalescence. However, coalescence alone cannot explain the increase in area percent porosity observed in the partially melted and solidified samples. The thermal expansion of gas in the pores also has to be considered to understand the enhanced porosity in the heated metal as discussed later in this paper.

### **5.3.2 Enhanced Porosity in Welded Metal**

It is observed from Fig. 5.3 that many large pores were formed in the fusion zone during laser welding of alloy AM60B. These pores are much larger than the pre-existing pores in the base metal shown in Fig. 5.2 (a). Fig. 5.4 shows that many large pores are connected with the pre-existing smaller pores in the base metal through one or more channels. For example, Fig. 5.4 (a) shows that a pore near the center of the picture was expanding by infusion of gas from the small pre-existing pores in the base metal. Fig. 5.4 (b) shows that a large pore was formed from the coalescence of several pre-existing pores. Similarly, Figs. 5.4 (c) and 5.4 (d) show that large pores in the fusion zone grew from the expansion and coalescence of small pre-existing pores. The elongated shapes of these pores indicate that they were expanding from the fusion boundary into the fusion zone. The proximity and the connections between the large and the small pores and the shape of the large pores in Fig. 5.4 reveal that the growth of the pores resulted from the coalescence and expansion of the pre-existing pores in the base metal near the fusion boundary.

### **5.3.3 Pore Coalescence and Expansion**

Figure 5.5 shows the typical number densities of pores of various sizes in the base metal and weld metal. It is observed that the pore radii in the fusion zone are more than one order of magnitude larger than those in the base metal, while the pore number densities in the weld metal are nearly two orders of magnitude smaller. The reduction in the number of pores per unit area of fusion zone indicates significant coalescence of the pre-existing pores during welding. The average pore radius, number density, and area percent porosity measured in the base metal and weld metal for different welding speeds are

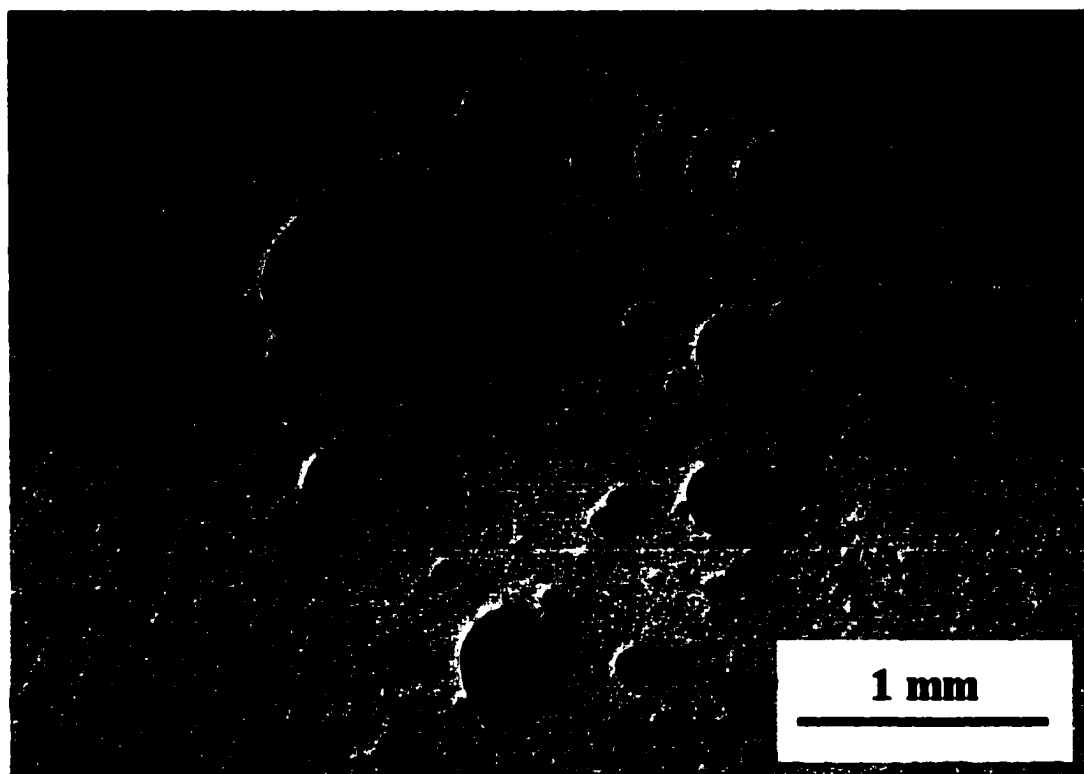


**Fig. 5.3** Typical pores observed in weld pool of laser welded alloy AM60B. Plate thickness 6 mm, laser power 1.5 kW, welding speed 250 in./min (106 mm/s), beam defocusing +1.0 mm, and shielding gas flow rate 200 ft<sup>3</sup>/h (5.7 m<sup>3</sup>/h) of helium.

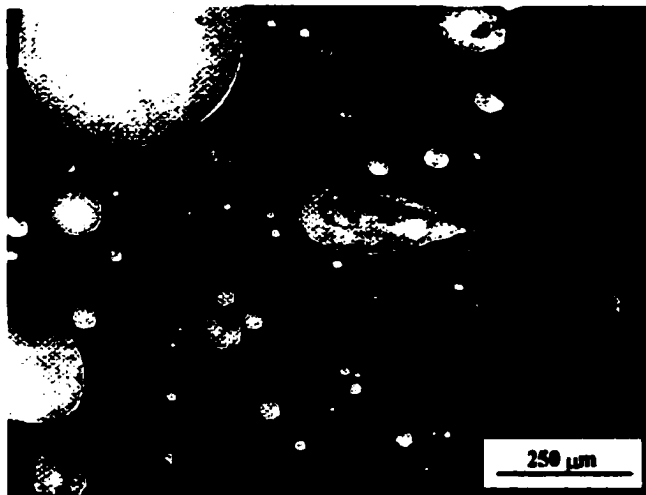
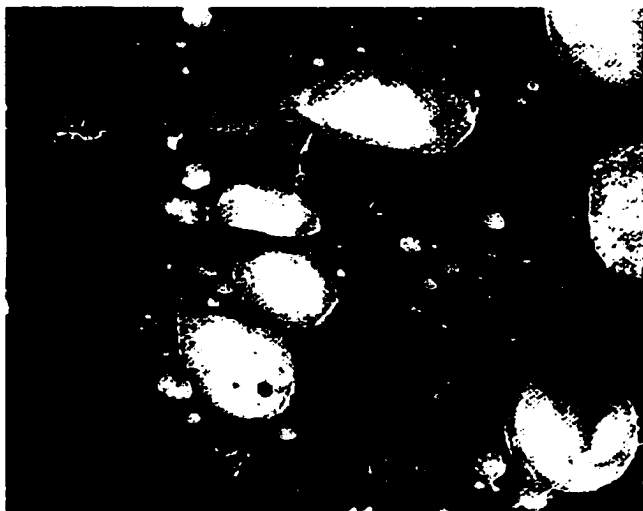


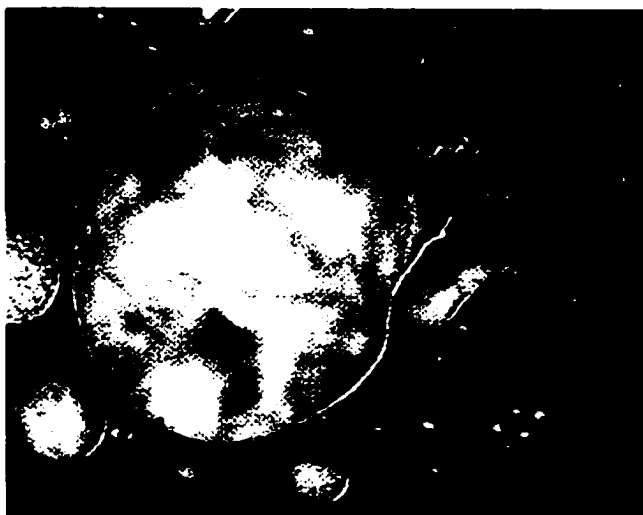
Fig. 5.4(a)



Fig. 5.4(b)



**Fig. 5.4(c)**



**Fig. 5.4(d)**

**Fig. 5.4** Formation of large pores in the fusion zone (the black background) due to the expansion and coalescence of the pre-existing pores in the base metal (the gray background) of alloy AM60B. All the figures have the same magnification as shown in (a).

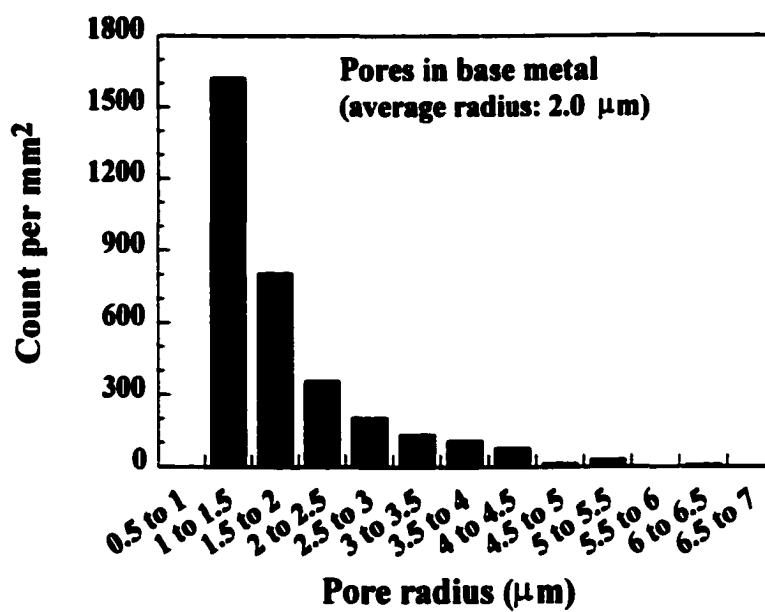


Fig. 5.5(a) Pore size distribution in 2 mm-thick alloy AM60B base metal.



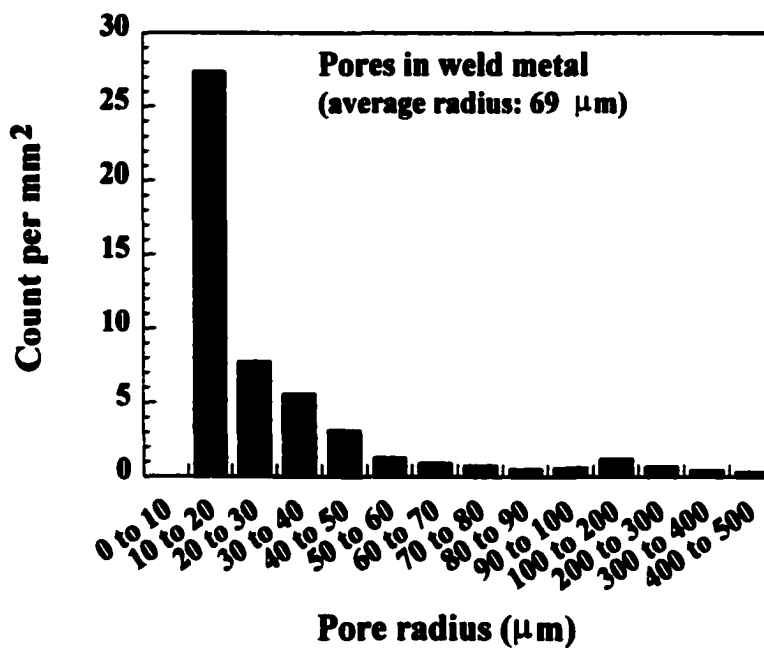


Fig. 5.5(b) Pore size distribution in the fusion zone of laser welded alloy AM60B using a focused beam. Plate thickness 2 mm, laser power 1.5 kW, welding speed 125 in./min (53 mm/s), and shielding gas flow rate 200 ft<sup>3</sup>/h (5.7 m<sup>3</sup>/h) of helium.

given in Table 5.3. It is observed that the area percent porosity in the weld metal was about 11 to 17 times that in the base metal depending on the welding speed.

In order to understand the increase in area percent porosity in the weld metal, the pore expansion due to coalescence of the pre-existing pores needs to be considered. When the base metal is melted, the pressure in the pores tends to equal the sum of the surface tension pressure and the pressure in the surrounding liquid. Since the surface tension pressure decreases with increase in pore radius and the pressure in the surrounding liquid is almost constant, the pressure inside a small pore is larger than that in a large pore. If several small pores coalesce to form a large pore, there will be a net increase in total pore volume both due to coalescence and reduction of surface tension pressure. Furthermore, pores in the alloy can expand when they are heated to higher temperatures. Therefore, the thermal expansion of pores also needs to be considered. During welding, significant pore expansion occurs due to heating. However, during solidification, the pores shrink with the reduction in the temperature of the liquid metal. The shrinking continues until the solidus temperature is reached. Any further lowering of temperature reduces the pore sizes by a relatively much smaller amount. Thus the net expansion due to the temperature change is equivalent to heating the pores from room temperature to the solidus temperature.

The average pore radius and area percent porosity in the weld metal for different welding conditions were estimated considering pore coalescence and thermal expansion. The calculation procedure is described in the Appendix I. Results in Table 5.3 show that fair agreement was achieved between the measured and estimated values of average pore radius and area percent porosity. Such an agreement indicates that the increase in porosity in the weld metal can be attributed to pore coalescence and thermal expansion during welding.

**Table 5.3 Pore number density, average pore radius, and area percent porosity in the base metal and weld metal of 2 mm-thick alloy AM60B plates. Welding conditions: laser power 1.5 kW, focused beam, shielding gas flow rate 200 ft<sup>3</sup>/h (5.7 m<sup>3</sup>/h) of helium, and various welding speeds.**

	Base metal	Weld metal					
Welding speed (mm/s)		53	64	74	85	95	106
Measured number of pores per unit area (mm <sup>-2</sup> )	3.4x10 <sup>3</sup>	51	33	52	43	43	51
Number of pores per unit volume (mm <sup>-3</sup> )	5.37x10 <sup>3</sup>	223	119	293	199	193	280
Measured average 2D pore radius (μm)	1.3	43.7	52.8	37.1	42.0	42.4	36.0
Average 3D pore radius (μm)	2.0	68.6	82.9	58.3	65.9	66.6	56.5
Estimated average 3D pore radius (μm)		66.5	82.7	60.4	69.2	69.9	61.4
Measured area percent porosity	1.8	30.7	28.6	22.7	24.0	24.3	20.6
Estimated area percent porosity		27.5	28.2	27.1	27.6	27.6	27.1

### **5.3.4 Keyhole Stability**

In order to study the influence of keyhole stability on the porosity formation, different laser beam power densities were used by changing the extent of beam defocusing during welding of alloy AM60B. The porosity in the fusion zone is plotted as a function of beam defocusing in Fig. 5.6. It is observed that the amount of porosity is not sensitive to beam defocusing. As shown later in Appendix II, the welding pool depth change gradually as the extent of beam defocusing increased. The mixed mode of welding, characterized by the presence of two types of weld pool geometry typical of both conduction and keyhole modes in various cross sections of the same welded sample, was not observed in the welding of AM60B.

In contrast with the mode of welding for AM60B, three modes of welding were identified depending on the degree of beam defocusing in the welding of aluminum alloys 5182 and 5754 [12]. At high degree of beam defocusing, the beam power density was lower than the threshold value for keyhole formation, resulting in conduction mode welding and a shallow weld pool. When the beam was nearly focused, the power density was well above the threshold value to form a keyhole and a deep weld pool characteristic of keyhole mode of welding formed. Porosity was rarely observed in either conduction or keyhole mode of welding. However, when the beam power density was just above the threshold value for keyhole formation, an unstable keyhole was formed that collapsed with any small disturbance. As a result, in various cross sections of the same welded sample, the weld pool shapes characteristic of either conduction or keyhole mode were observed. Porosity was formed primarily in this mixed mode of welding due to instability of the keyhole in these automotive aluminum alloys as shown in Fig. 4.13(b).

The absence of mixed mode of welding during welding of magnesium alloy AM60B indicates that the keyhole was more stable than that for the welding of aluminum alloys. The stability of the keyhole depends on a balance between surface tension pressure and vapor pressure. The surface tension pressure tends to close the keyhole while the vaporization tends to keep it open. Aluminum alloys have higher surface tension and

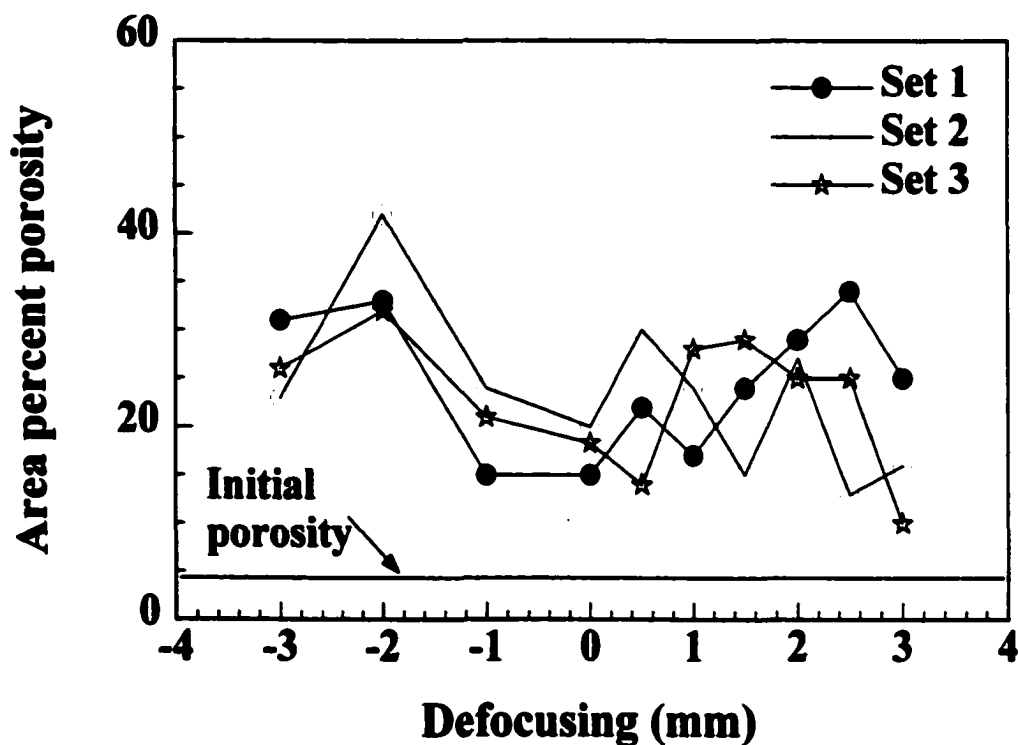


Fig. 5.6 Porosity formed in laser welds of alloy AM60B at several beam defocusing values. Plate thickness 6 mm, laser power 1.5 kW, welding speed 250 in./min (106 mm/s), and shielding gas flow rate 200 ft<sup>3</sup>/h (5.7 m<sup>3</sup>/h) of helium.

much lower vapor pressure than magnesium alloys [18]. Therefore, it is easier to maintain a keyhole for the welding of magnesium alloys than aluminum alloys. Furthermore, the vapor pressure in the keyhole during laser welding of alloys 5182 and 5754 was mainly due to magnesium in the alloys due to the very high vapor pressure of magnesium [19,20]. Because of its low concentrations in these alloys, magnesium could be depleted from the keyhole surface, resulting in vapor pressure drop and consequently, collapse of the keyhole. On the other hand, magnesium is the main constituent in alloy AM60B and vaporization of magnesium has little impact on the alloy composition. Therefore, the keyhole was more stable during laser welding of AM60B than during laser welding of aluminum alloys. The keyhole instability was not a problem in the pore formation during laser welding of alloy AM60B.

### **5.3.5 Reduction of Weld Metal Porosity**

The area percent porosity formed in the fusion zone for different welding conditions is shown in Fig. 5.7. The data show that the porosity in the fusion zone was much higher than that in the base metal for most welding conditions used. It is also observed that the porosity in the fusion zone decreased with decreasing heat input, i.e. decreasing laser power and increasing welding speed. At low heat input, it was possible to obtain welds with porosity levels similar to that in the base metal. However, as shown later, the weld pool cross section area decreased with decrease in heat input, especially with decrease in laser power. For a given plate thickness, the heat input has to be higher than a certain level to obtain full penetration welding. Therefore, besides reducing the heat input, a more practical method to alleviate the porosity problem has to be found. This issue is addressed in the following paragraph.

The transport of gas bubbles in a weld pool containing recirculating liquid metal is complex. During the welding, the gas bubbles drifted with the flow of liquid metal and at the same time had a tendency to float upward due to the difference in the densities of the bulk liquid and the bubbles. Furthermore, the vigorous flow of the weld metal promoted coalescence of bubbles. It is fair to expect that due to the rapid thermal cycle, the pores formed in the fusion zone had little time to float out of the weld pool in a single

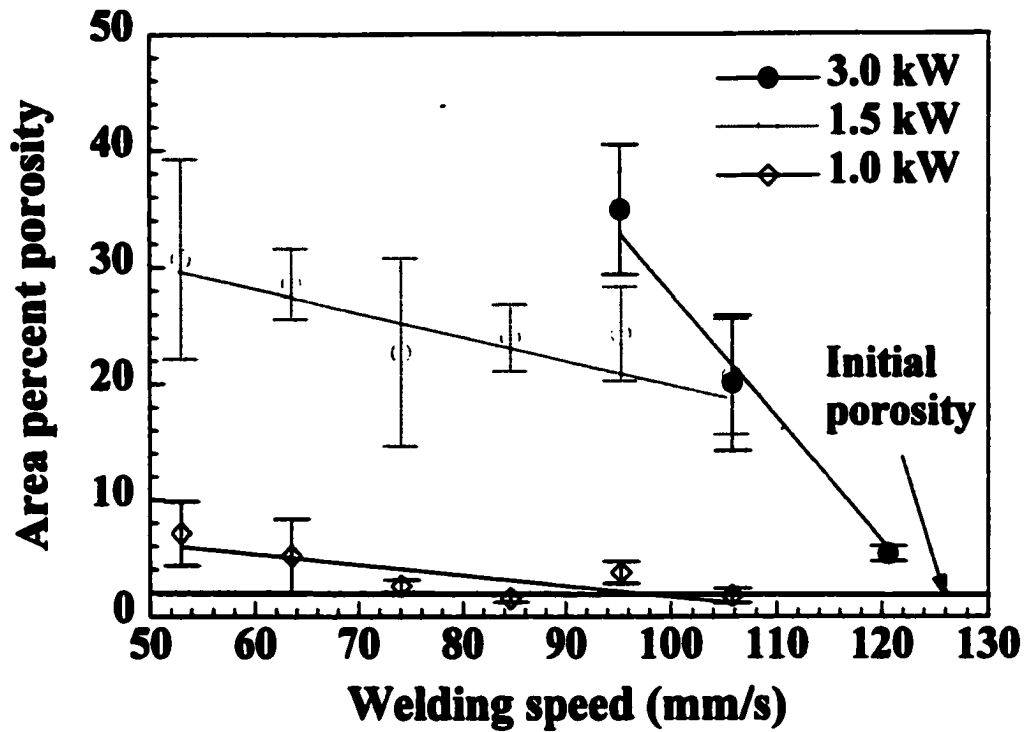


Fig. 5.7(a) Porosity formed in laser welds of 2 mm-thick alloy AM60B plates for different welding speeds and laser powers using focused beam and shielding gas flow rate 200 ft<sup>3</sup>/h (5.7 m<sup>3</sup>/h) of helium.

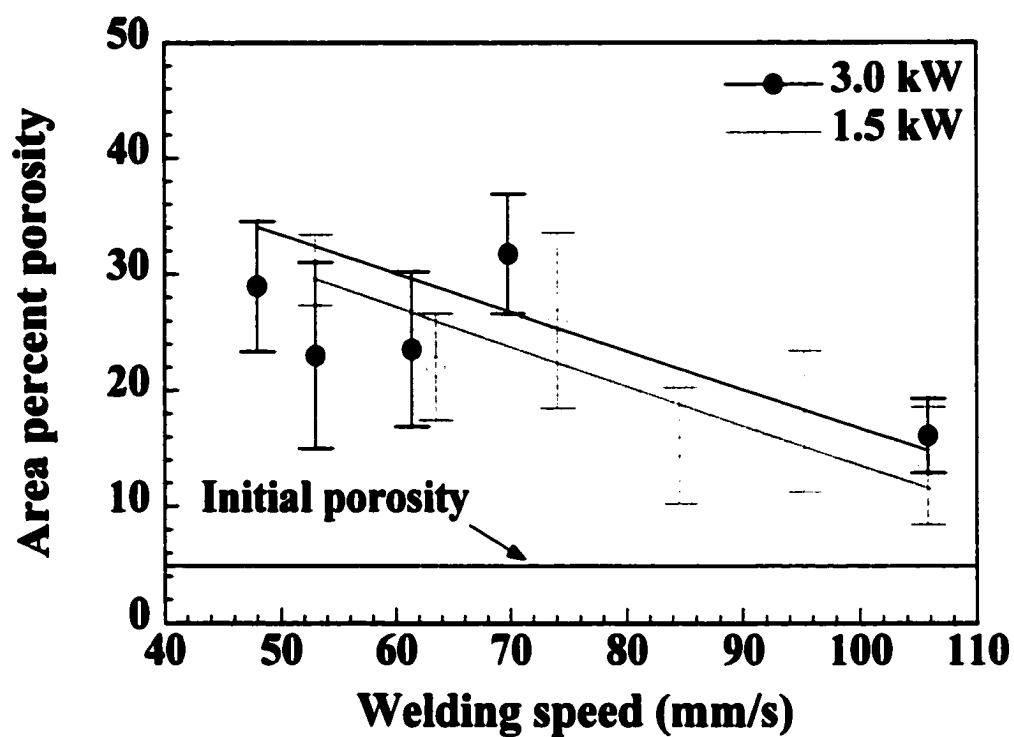


Fig. 5.7(b) Porosity formed in laser welds of 6 mm-thick alloy AM60B plates for different welding speeds and laser powers using focused beam and shielding gas flow rate 200 ft<sup>3</sup>/h (5.7 m<sup>3</sup>/h) of helium.



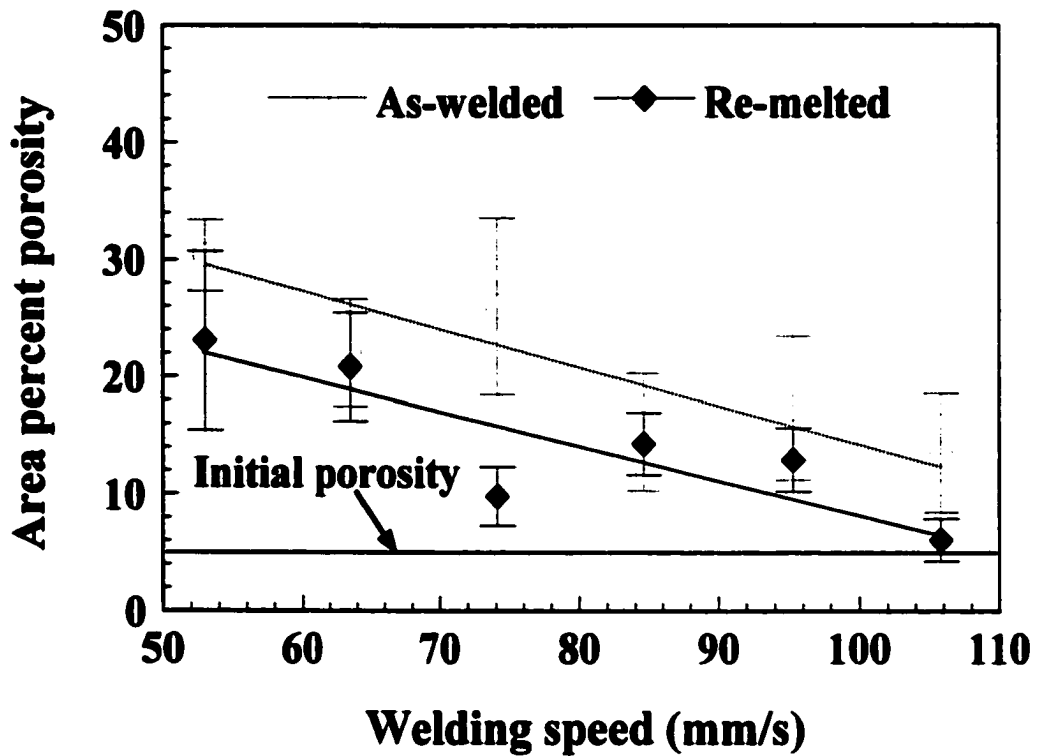


Fig. 5.8 Area percent porosity produced on as-welded (single-run) and re-melted (double-run) samples of alloy AM60B with a focused beam. Plate thickness 6 mm, laser power 1.5 kW for first run and 1.0 kW for second run and shielding gas flow rate 200 ft<sup>3</sup>/h (5.7 m<sup>3</sup>/h) of helium.

welding thermal cycle. Therefore, small pores that require long time for floatation could not be removed from the weld pool within the available time. If a second run of welding is performed, the pores in the fusion zone that are already much larger than the pre-existing pores in the base metal have a second chance to float out of the weld pool. Moreover, these pores can also coalesce to form even larger bubbles. Therefore, more significant floatation of these bubbles will take place during re-melting of the fusion zone since larger bubbles are more easily separated by gravity. Based on these considerations, a second run of welding was performed on some welded samples to examine the effect of remelting on porosity reduction. Fig. 5.8 shows the area percent porosity formed in the as-welded (single run) and re-melted (double run) samples for different welding speeds. It is observed that remelting of the fusion zone significantly reduced porosity. Therefore, well controlled remelting of the fusion zone by a second run of welding can reduce porosity by allowing some pores formed during the first run of welding to be removed. Keyhole mode of welding was obtained for both first and second run of welding. The reduction of porosity in the re-melted fusion zone also indicated that porosity due to keyhole instability during welding was not significant and the porosity formed in the fusion zone was due to the coalescence and expansion of the pre-existing pores in the base metal.

#### **5.4 Summary and Conclusions**

The mechanism of porosity formation during continuous-wave Nd:YAG laser welding of die-cast magnesium alloy AM60B has been studied. A practical method to alleviate the porosity problem was sought based on the mechanistic understanding. The major findings are as follows:

- 1) Significant increase in volume percent of porosity was observed in the fusion zone for most of the welding conditions used. The coalescence and expansion of small pre-existing pores due to heating and reduction of internal pressure contributed to the porosity increase in the fusion zone.

2) The stability of the keyhole was not a major factor in the pore formation in the fusion zone during laser welding of alloy AM60B. The keyhole formed during welding of alloy AM60B was more stable than that formed in aluminum alloys 5182 and 5754.

3) The amount of porosity in the fusion zone decreased with decrease in heat input, i.e., decrease in laser power or increase in welding speed. The porosity levels similar to that in the base metal could be obtained when the heat input was low.

4) Well controlled remelting of the fusion zone allowed some of the pores to be removed, resulting in reduced porosity in the fusion zone. The reduction in porosity also indicates that keyhole instability during laser welding of alloy AM60B was not important for pore formation.

5) Significant overfill was caused by the formation macro-porosity in autogenous deep penetration welds. The extent of overfill could be lowered by reducing heat input.

6) The power density needed for the formation of keyhole in AM60B was significantly lower than that necessary for the welding of 5000 series automotive aluminum alloys. The reduction in the threshold power density resulted from relatively higher equilibrium vapor pressure of the magnesium alloy.

## 5.5 References

1. F. V. Lawrence, Jr.: *WRC Bulletin* 181, 1973, pp. 1-23.
2. R. F. Ashton and R. P. Wesley: *Welding Journal*, 1975, 54, 3, pp. 95s-98s.
3. M. Katoh: *Welding International* (UK), 1996, 10, 10, pp.771-777.
4. R. A. Woods: *Hydrogen in Metals*, eds. I. M. Bernstein and A. W. Thompson, ASM International, Materials Park, Ohio, 1974, pp. 713-725.
5. U. Masahiro and O. Satoru: *Trans. Nat. Res. Inst. Met.*, 1974, 16, 2, pp. 67-74.
6. M. Kutsuna: *Welding in the World* IIW 31, 1993, pp. 126-135.

7. S. Katayama: *Journal of Light Metal Welding and Construction*, 1996, 34, 4, pp. 31-41.
8. D. A. Schauer and W. H. Giedt: *Welding Journal*, 1978, 57, 7, pp. 189s-195s.
9. I. R. Whitaker, D. G. McCartney, and W. M. Steen: *ICALEO'92*, 1992, pp. 565-573.
10. A. Matsunawa, J. D. Kim, N. Seto, M. Mizutani, and S. Katayama: *Journal of Laser Applications*, 1998, 10, 6, pp. 247-254.
11. J. S. Kim, T. Watanabe, and Y. Yoshida: *Journal of Laser Applications*, 1995, 7, 1, pp. 38-46.
12. M. Pastor, H. Zhao, R. P. Martukanitz, and T. DebRoy: *Welding Journal*, 1999, 78, 6, pp. 207s-216s.
13. T.A. Engh: *Principles of Metal Refining*, Oxford University Press Inc., New York, 1992.
14. B. A. Mikucki and J. D. Shearouse III: *Proceedings of Magnesium Properties and Applications for Automobiles Conference*, Detroit, MI, 1-5 March 1993. Society of Automotive Engineers, Inc. (USA), 1993, pp. 107-115.
15. J. D. Shearouse III and B. A. Mikucki: *SAE Transactions: Journal of Materials & Manufacturing (USA)*, 1994, 103, pp. 542-552.
16. H. Haferkamp, Fr.-W. Bach, I. Burmester, K. Kreutzburg, and M. Niemeyer: *Proceedings of the Third International Magnesium Conference*, edited by G. W. Lorimer, The Institute of Materials, London, UK, 1996, pp. 89-98.
17. R. L. Fullman: *Trans. AIME*, 1953, 197, pp. 447-452.
18. E. A. Brandes: *Smithells Metals Reference Book*, 6th edition, London, Boston, Butterworth, in association with Fulmer Research Institute Ltd., 1983.
19. A. Block-Bolten and T. W. Eagar: *Metallurgical Transactions*, 1984, 15B, pp. 461-469.
20. H. Zhao and T. DebRoy: *Metallurgical and Materials Transactions*, 2001, 32B, pp. 163-172.

### 5.6 Appendix I: Estimation of Pore Expansion during Welding

The pressure inside a stable bubble,  $P_i$ , is the sum of surface tension pressure,  $P_s$ , and pressure in the liquid,  $P_a$ , i.e.,

$$P_i = P_s + P_a \quad (5.1A)$$

The surface tension pressure is given by:

$$P_s = 2\sigma/r \quad (5.2A)$$

where  $\sigma$  and  $r$  are the surface tension and pore radius, respectively, and the pressure in the liquid consists of the ambient pressure and a small hydrostatic head.

Consider that  $N$  number of small spherical bubbles of radius  $r_0$  are heated from temperature  $T_0$  to temperature  $T$  and then these pores coalesce to form a single large spherical bubble of radius  $r$ . Assuming that the pores are stable before and after the heating and coalescence and considering for simplicity a constant surface tension,  $\sigma$ , the pressure inside the small bubbles is given by:

$$P_0 = 2\sigma/r_0 + P_a \quad (5.3A)$$

And the pressure inside the large bubble is given by:

$$P = 2\sigma/r + P_a \quad (5.4A)$$

According to ideal gas law, we have:

$$nRT_0 = P_0V_0 = \frac{4}{3}\pi N(2\sigma/r_0 + P_a)r_0^3 \quad (5.5A)$$

$$nRT = PV = \frac{4}{3}\pi(2\sigma/r + P_a)r^3 \quad (5.6A)$$

where  $n$  is the total number of moles of gas in the bubbles,  $R$  is the gas constant, and  $V_0$  and  $V$  are the total volumes of the bubbles before and after the heating and coalescence, respectively. Combining Eqn. (5.5A) and Eqn. (5.6A), we obtain:

$$(2\sigma/r + P_a)r^3 = \frac{T}{T_0}N(2\sigma/r_0 + P_a)r_0^3 \quad (5.7A)$$

The radius  $r$  of the large bubble can be calculated from Eqn. (5.7A) from known values of  $\sigma$ ,  $P_a$ ,  $T$ ,  $T_0$ ,  $N$ , and  $r_0$ . The ratio of volumes after and before the heating and coalescence is given by:

$$V/V_0 = r^3 / (Nr_0^3) \quad (5.8A)$$

Let us consider the coalescence of pre-existing pores in the weld metal obtained using laser power of 1.5 kW and welding speed of 53 mm/s. As shown in Table 5.3, in the base metal, the average radius of the pre-existing pores is 2.0  $\mu\text{m}$ , the pore number density is  $5.37 \times 10^5$  per  $\text{mm}^3$ , and area percent porosity is 1.8. In the weld metal, the pore number density is 223 per  $\text{mm}^3$ . Therefore, on an average, about 2408 of pre-existing pores in the base metal coalesced to form one large pore in the weld metal. During welding, the weld metal was first heated to very high temperatures and the pores in the metal expanded significantly. During the subsequent cooling process, the pores shrank with the reduction in the temperature of the liquid metal until the solidus temperature was reached. Thus the net expansion due to the temperature is equivalent to heating the pores from room temperature (298 K) to the solidus temperature, which is 813 K for alloy AM60B. Therefore, taking  $N = 2408$ ,  $r_0 = 2.0 \mu\text{m}$ ,  $T_0 = 298 \text{ K}$ ,  $T = 813 \text{ K}$ ,  $P_a = 1.013 \times 10^5 \text{ Pa}$ , and  $\sigma = 0.56 \text{ Nm}^{-1}$ , we can solve Eqn. (5.7A) and obtain the average radius of the resulting

large pores in the weld metal to be  $r = 66.5 \mu\text{m}$ . The ratio of total volume of pores in the weld metal and that in the base metal is calculated by:

$$V/V_0 = r^3/(Nr_0^3) = 66.5^3 / (2408 \times 2.0^3) \approx 15.3.$$

Since the area percent porosity is equal to volume percent porosity, the area percent porosity in the weld metal will be estimated to be  $1.8 \times 15.3 = 27.5$ . Similar calculations were done for other welding conditions to estimate the area percent porosity in the weld metal and the results are shown in Table 5.3. It is observed that the estimated values of average pore radius and area percent porosity in the weld metal fairly agree with the measured values. The good agreement indicates that the increase in porosity in the weld metal can be attributed to pore coalescence and thermal expansion during welding.

## 5.7 Appendix II: Weld Geometry, Microstructure and Microhardness

### 1) Weld Geometry

As shown in Fig. 5.9, overflow is the region of the weld metal located above the original surface of the base metal. Fig. 5.10 shows the area percent of both overflow and porosity in the fusion zone produced at several welding speeds. It is observed that both area percent overflow and area percent porosity decrease with increasing welding speed. It is also found that the area percent porosity is roughly equal to the area percent overflow. On the other hand, when a weld does not contain a large amount of porosity, the upper surface of the weld has a smooth profile and no overflow is formed. This evidence indicates that overflow was caused by the displacement of liquid metal by the pores. Therefore, any measure that decreases porosity in the weld pool will reduce overflow.

As shown in Fig. 5.9, the weld pool width, depth, and cross section area were measured without considering the area of overflow. The influences of welding speed and defocusing on the width, depth and cross-sectional area of the weld pool are shown in figures 5.11, 5.12 and 5.13, respectively. Each data point represents the average value of five measurements. As expected, the width, depth, and cross sectional area of the weld pool decrease with increasing welding speed. It is observed that the weld pool geometry does not change significantly when the beam defocusing is in the range of -3 mm to +3 mm, which corresponds to an average laser power density in the range of  $1.2 \times 10^5$  to  $5.3 \times 10^5$  W/cm<sup>2</sup>. The deep penetration of these weld pool indicates that a keyhole was formed during the welding. When the beam defocus values are higher than +3 mm or less than -3 mm, i.e. the laser power density is smaller than  $1.2 \times 10^5$  W/cm<sup>2</sup>, the weld pool depth reduces more significantly than the weld pool width, resulting in shallow weld pool shape that is characteristic of conduction mode of welding. Therefore, the threshold laser power density for keyhole formation for this alloy is about  $1.2 \times 10^5$  W/cm<sup>2</sup>. This is much smaller than that for laser welding of 5000 series automotive aluminum alloys where the threshold values were in the range of  $3.7 \times 10^5$  to  $8.4 \times 10^5$  W/cm<sup>2</sup> [12]. This difference can be attributed to the much higher equilibrium vapor pressure of magnesium than that of aluminum.



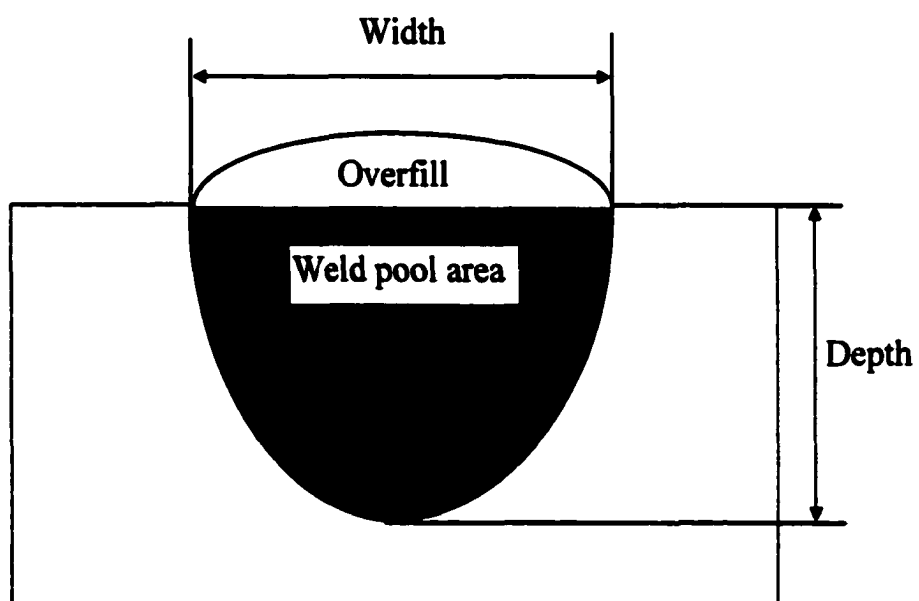


**Fig. 5.9 Measurement of weld pool width, depth, and cross section area.**

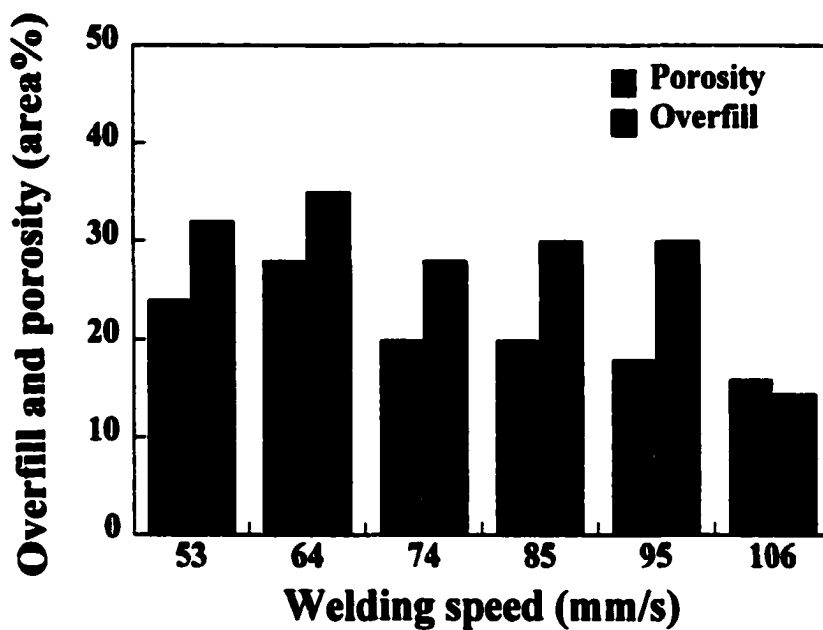


Fig. 5.10(a) Area percent of porosity (gray bars) and area percent of overfill (black bars) in laser welds of AM60B alloy at several welding speeds for 2 mm-thick plates. Nominal laser power: 3 kW, laser beam: at focus, and shielding gas flow rate: 200 ft<sup>3</sup>/h (5.7 m<sup>3</sup>/h) of helium.

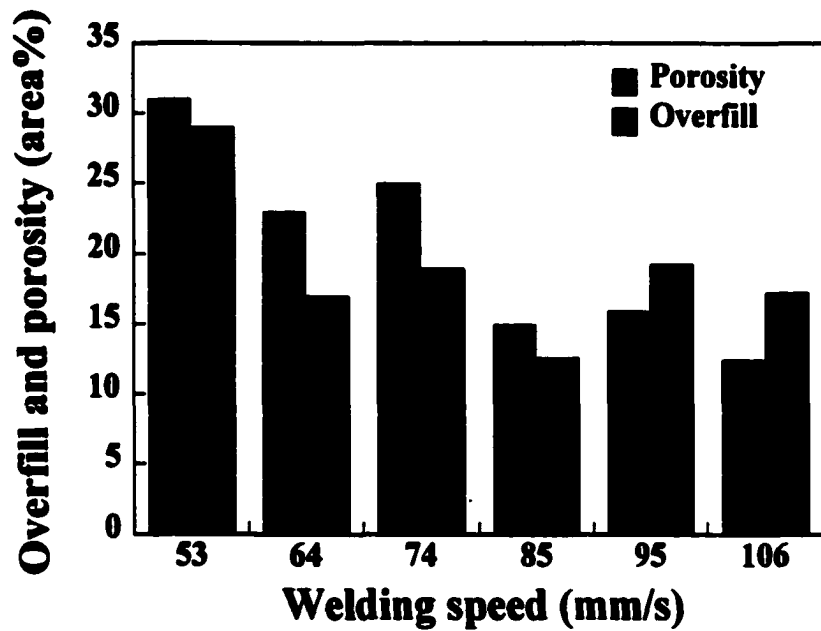


Fig. 5.10(b) Area percent of porosity (gray bars) and area percent of overfill (black bars) in laser welds of AM60B alloy at several welding speeds for 6 mm-thick plates. Nominal laser power: 3 kW, laser beam: at focus, and shielding gas flow rate: 200 ft<sup>3</sup>/h (5.7 m<sup>3</sup>/h) of helium.

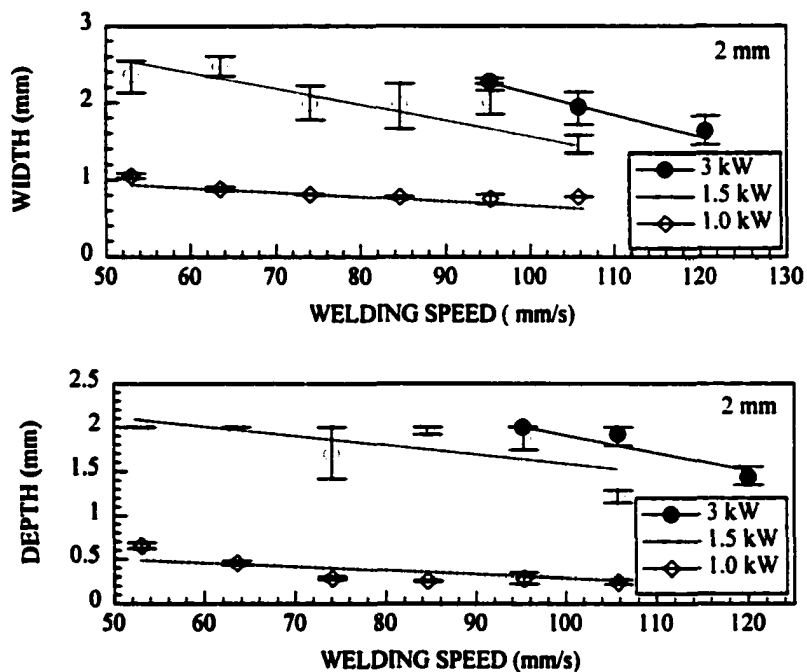


Fig. 5.11(a) Width and depth of the weld pools produced at several welding speeds and laser powers in AM60B alloy for 2 mm-thick plates. Laser beam: at focus, shielding gas flow rate: 200 ft<sup>3</sup>/h (5.7 m<sup>3</sup>/h) of helium.

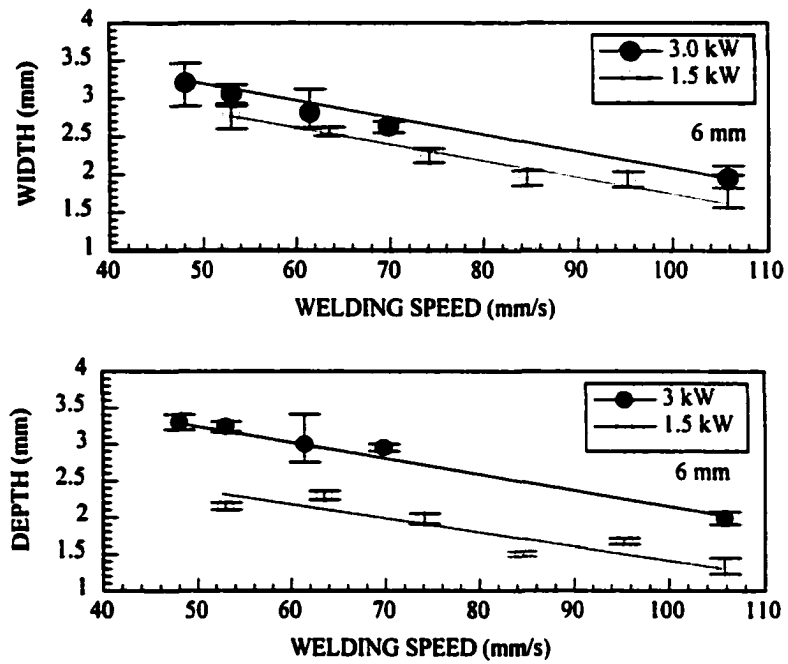


Fig. 5.11(b) Width and depth of the weld pools produced at several welding speeds and laser powers in AM60B alloy for 6 mm-thick plates. Laser beam: at focus, shielding gas flow rate: 200 ft<sup>3</sup>/h (5.7 m<sup>3</sup>/h) of helium.

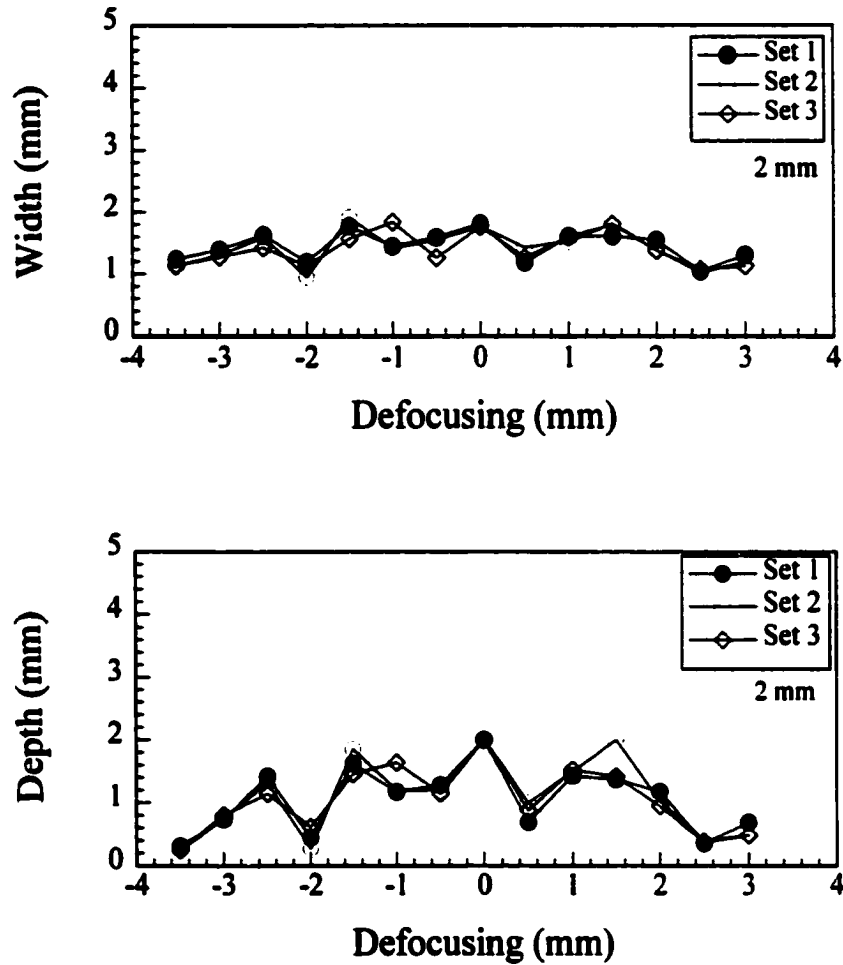


Fig. 5.12(a) Width and depth of the weld pools produced at several beam defocus values in AM60B alloy for 2 mm-thick plates. Nominal power: 1.5 kW, welding speed: 105.8 mm/s, and shielding gas flow rate: 200 ft<sup>3</sup>/h (5.7 m<sup>3</sup>/h) of helium.

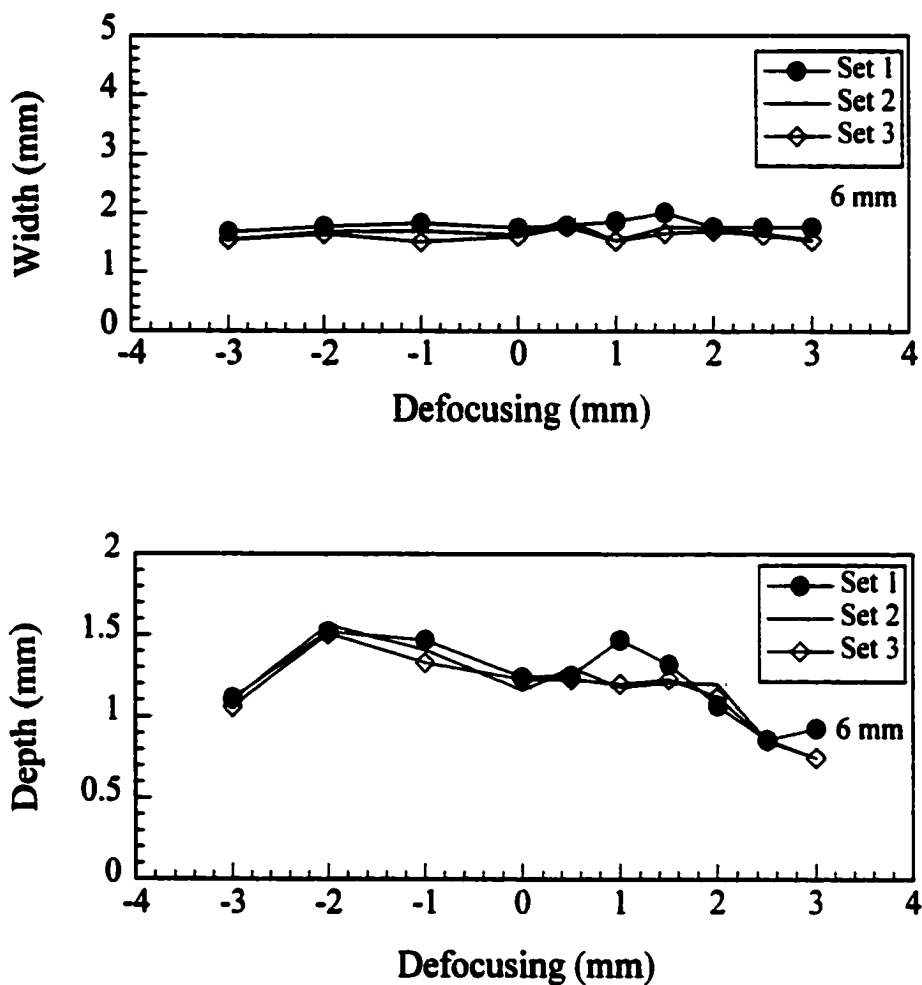


Fig. 5.12(b) Width and depth of the weld pools produced at several beam defocus values in AM60B alloy for 6 mm-thick plates. Nominal power: 1.5 kW, welding speed: 105.8 mm/s, and shielding gas flow rate: 200 ft<sup>3</sup>/h (5.7 m<sup>3</sup>/h) of helium.

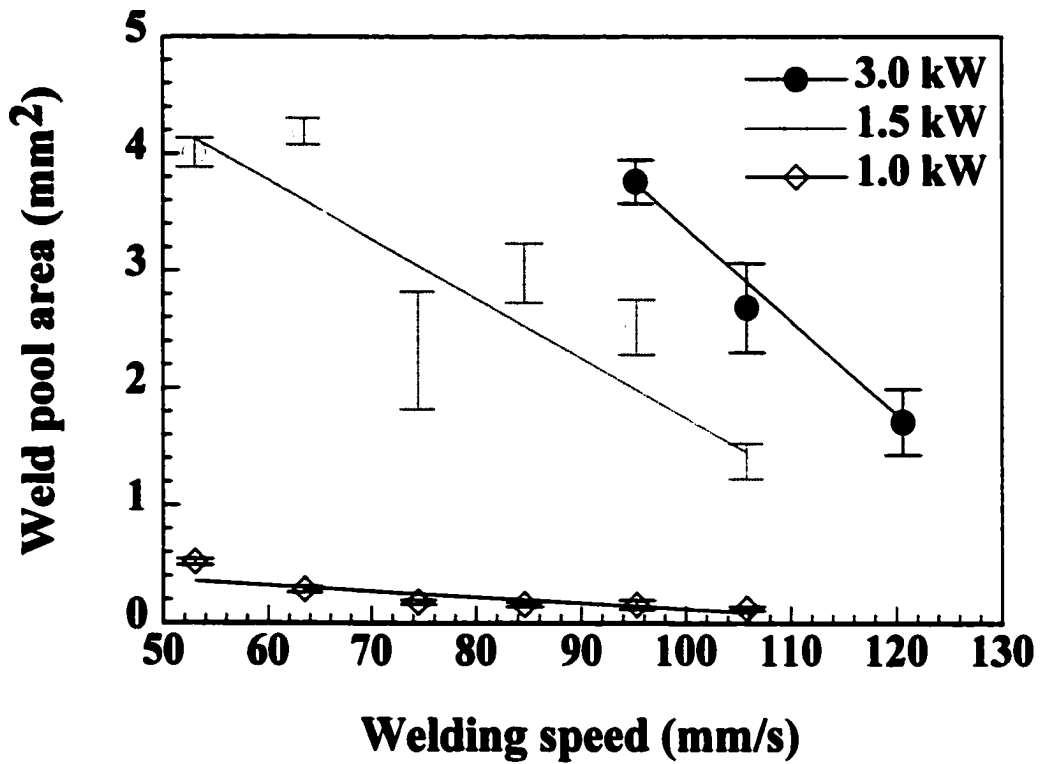


Fig. 5.13(a) Weld pool area produced in laser welds of 2 mm-thick alloy AM60B plates for different welding speeds and laser powers using focused beam and shielding gas flow rate 200 ft<sup>3</sup>/h (5.7 m<sup>3</sup>/h) of helium.



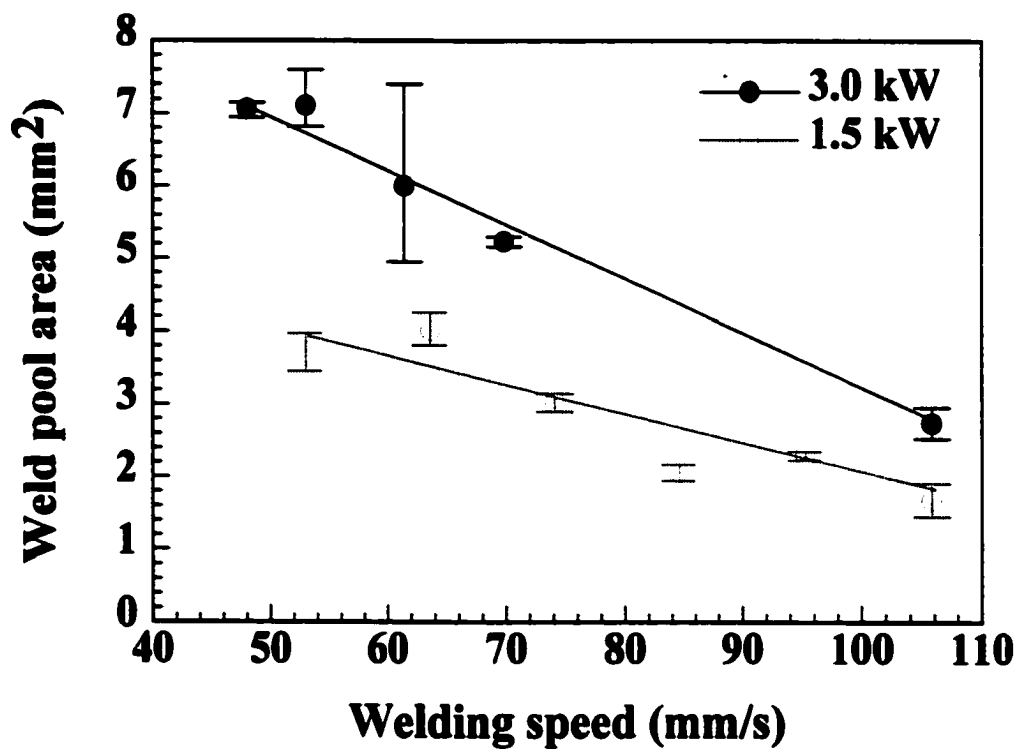
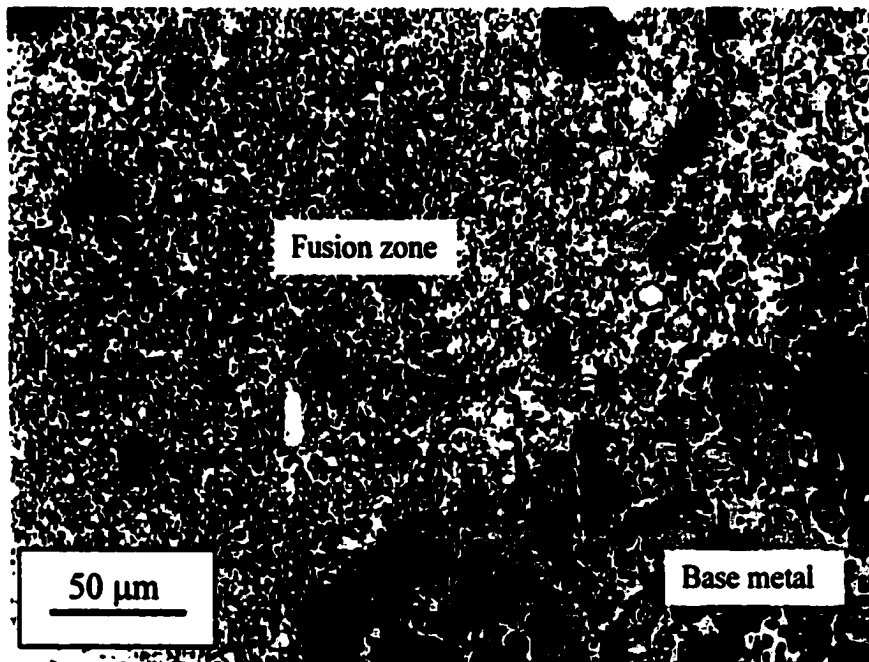


Fig. 5.13(b) Weld pool area produced in laser welds of 6 mm-thick alloy AM60B plates for different welding speeds and laser powers using focused beam and shielding gas flow rate 200 ft<sup>3</sup>/h (5.7 m<sup>3</sup>/h) of helium.

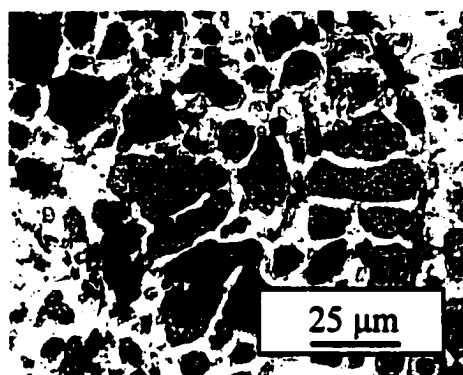
## 2) Microstructure and Microhardness

Fig. 5.14 shows the typical microstructures of the fusion zone and the base metal near the fusion plane. Heat affected zone is very small in the welds, which is characteristic of high power density laser welding. It is observed that the microstructures in both fusion zone and base metal consist of cored grains of magnesium-rich solid solution (gray) surrounded by  $Mg_{17}Al_{12}$  (unetched) intermetallic compound at the grain boundaries. The volume fraction of  $Mg_{17}Al_{12}$  intermetallic phase in the fusion zone is somewhat higher than that in the base metal, caused by the non-equilibrium solidification during the welding. Porosity (black) is present in both the fusion zone and the base metal. More porosity is observed near the fusion boundary than in the interior, indicating pronounced rejection of hydrogen along the solid-liquid interface.

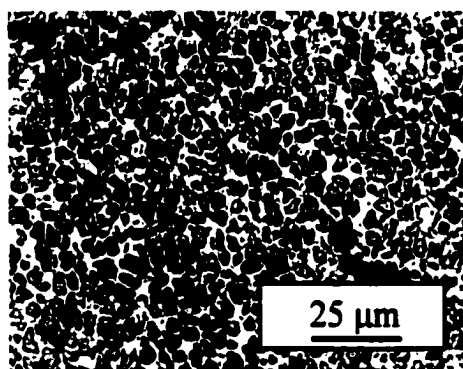
The solid solution phase has equiaxed morphology in the base metal and the fusion zone of low-speed welds as shown in figures 5.15(a) and 5.15(b). However, the morphology became dendritic in the fusion zone of 6 mm-thick plates at welding speeds higher than 74 mm/s as shown in Fig. 5.15(c). The grain size in the base metal is much larger than that in the fusion zone. The average grain size in the base metal was about 30  $\mu\text{m}$  while the average grain size in the fusion zone as a function of the welding speed is shown in Fig. 5.16. It is observed that for the 2 mm-thick plates, the average grain size in the fusion zone decreases as the welding speed increases as expected. For the 6 mm-thick plates, the grain size in the fusion zone also decreases with increasing welding speed of up to 74 mm/s. However, when the welding speed is higher than 74 mm/s, the morphology changes from equiaxed to dendritic and therefore, the grain size can not be measured in terms of grain diameter. It is also observed that the grain size in the fusion zone of the 6 mm-thick plates is much smaller than that in the 2 mm-thick plates. The difference in grain size and grain morphology between these plates indicates that the cooling rate in the weld pool of 2 mm-thick plates was smaller than that of 6 mm-thick plates.



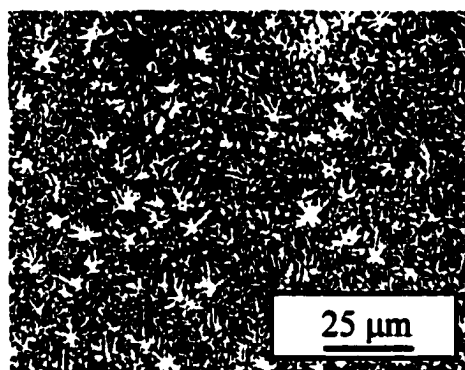
**Fig. 5.14** Microstructures in the fusion zone and base metal of laser welded alloy AM60B. The Microstructures consist of cored grains of magnesium-rich solid solution (gray) surrounded by Mg<sub>17</sub>Al<sub>12</sub> intermetallic (unetched) in both the fusion zone and the base metal. Porosity (black) is also observed. Nominal power: 1.5 kW, welding speed: 74.1 mm/s. Chemically etched with 10% HF aqueous solution.



(a)



(b)



(c)

**Fig. 5.15** Grain morphologies of magnesium-rich solid solution (gray) in (a) the base metal, (b) the fusion zone welded at a welding speed lower than 74 mm/s, and (c) the fusion zone produced at a welding speed higher than 74 mm/s. Specimen thickness: 6 mm, nominal power: 1.5 kW. Chemically etched with 10% HF aqueous solution.

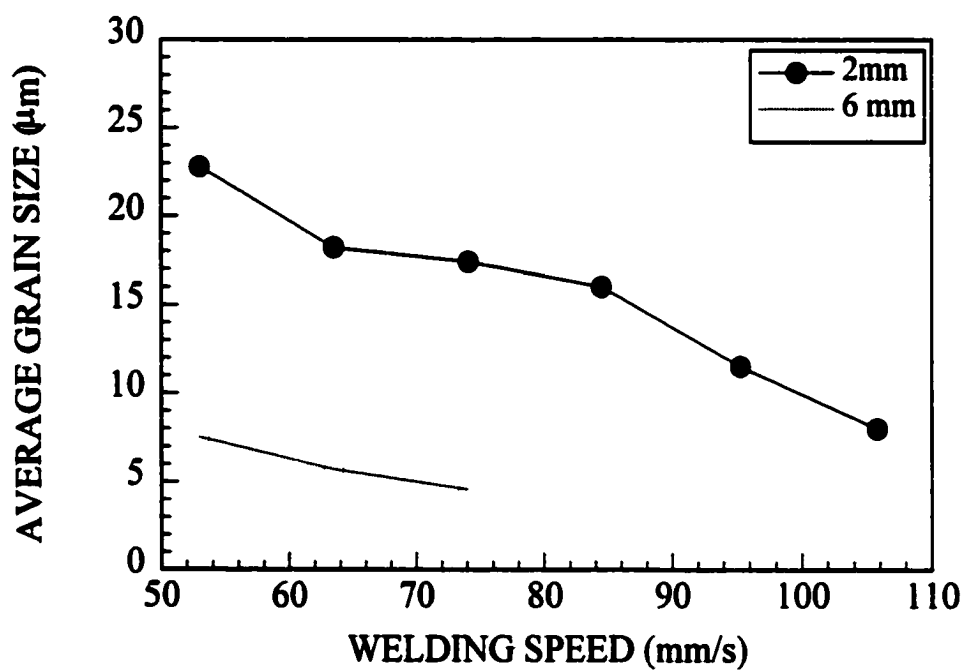


Fig. 5.16 Variation of the grain size in the fusion zone as a function of the welding speed for laser welds of AM60B alloy. Nominal power: 1.5 kW, shielding gas flow rate: 200 ft<sup>3</sup>/h (5.7 m<sup>3</sup>/h) of helium.

Vickers microhardness profile across the weld is shown in Fig. 5.17. This figure depicts an average hardness of about 53 HV in the base metal and 63 HV in the fusion zone. The small grain size and high volume fraction of  $Mg_{17}Al_{12}$  intermetallic phase in the fusion zone are considered to be the main causes of hardening in the fusion zone. There is a narrow region in the base metal adjacent to the fusion line where the average hardness is lower than both the base metal and the fusion zone. The average hardness obtained from 10 indentations in a region within 100  $\mu\text{m}$  from the fusion plane was about 47 HV. The low hardness is considered to be caused by the accumulation of pores in this region. As shown in Fig. 5.18, large indentations (or low hardness values) were obtained in regions of high porosity. Thus, the presence of porosity weakens the weldment.

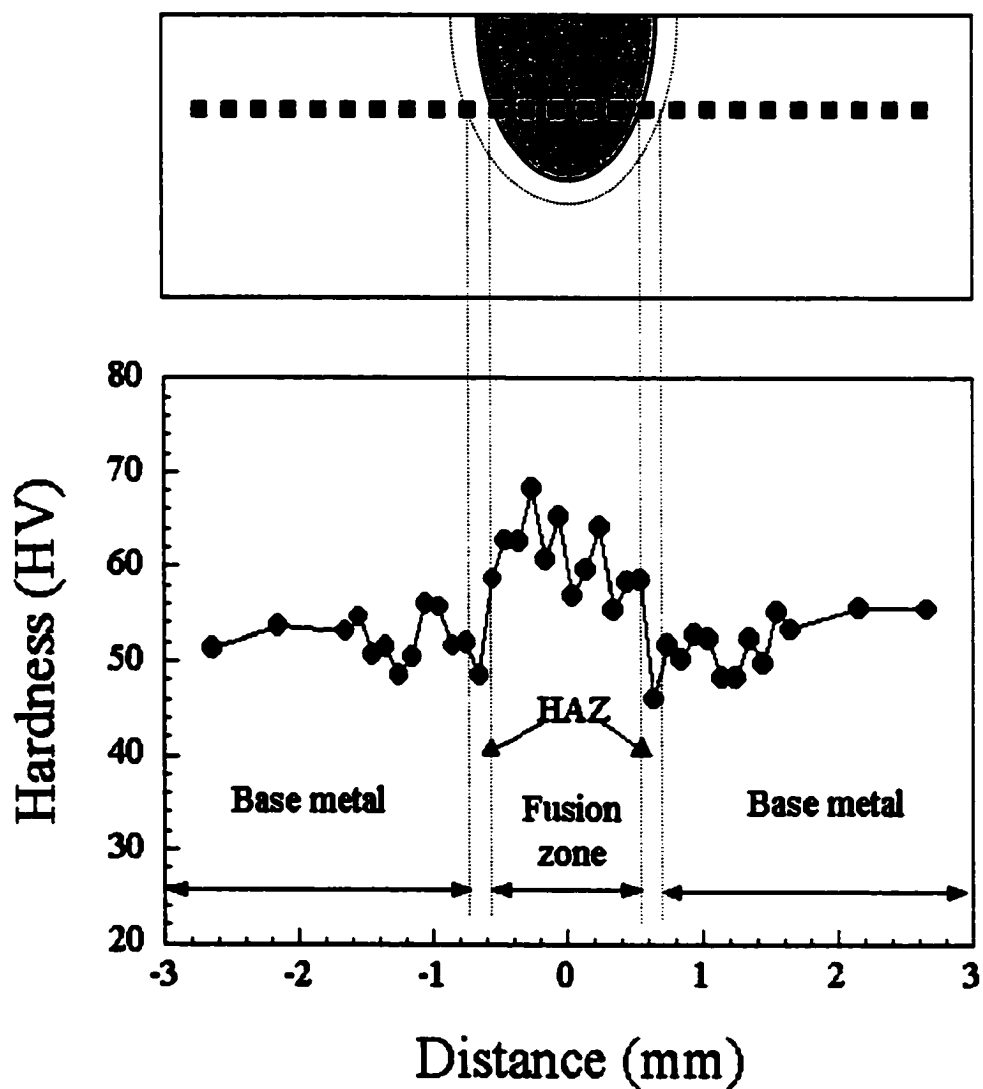
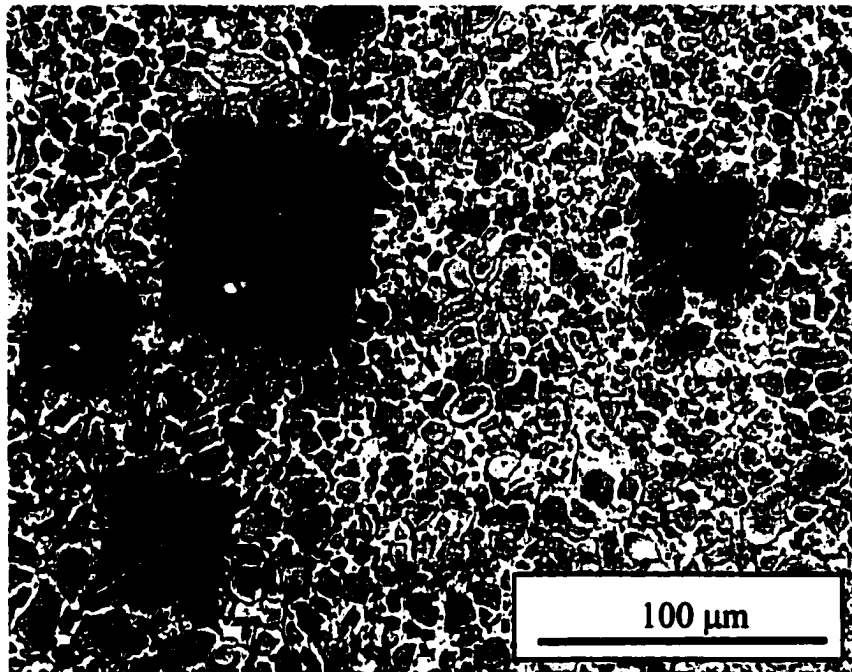


Fig. 5.17 Microhardness profile across the fusion zone of laser welded AM60B alloy. Nominal power: 1.5 kW, laser beam: at focus, welding speed: 105.8 mm/s, and shielding gas flow rate: 200 ft<sup>3</sup>/h (5.7 m<sup>3</sup>/h) of helium. Test load: 100 g, time of loading 15 s.



**Fig. 5.18 Dents (black) of microhardness test showing the influence of porosity on hardness. The regions with the presence of porosity have larger dent sizes and smaller hardness readings than the regions without porosity.**



## **Chapter 6**

### **CONCLUDING REMARKS**

The present work addressed the quality issues in laser welding of automotive aluminum and magnesium alloys, including composition change and porosity formation in the weld metal.

Weld metal composition change caused by selective vaporization of volatile alloying elements can be affected by many factors. In order to control alloying element loss in the weld metal, a quantitative understanding of the effects of various factors is needed. In this study, the first three dimensional comprehensive model was developed for this purpose. The model integrated the calculations of heat transfer and fluid flow in the weld pool and the rates of vaporization and alloying element loss occurring during conduction mode laser welding. The weld pool temperature is the most important factor in determining the rates of vaporization. In this study, the weld pool temperature field was calculated considering the effect of turbulence on heat transfer and fluid flow in the weld pool. The evaporative heat loss due to vaporization of alloying elements was taken into account. Such detailed considerations ensured accurate prediction of weld pool size and temperature. The vaporization rates of alloying elements were calculated based on principles of gasdynamics and mass transfer considering pressure gradient and concentration gradient at the weld pool surface. The calculations of weld pool temperature field and rates of vaporization were coupled to determine alloying element loss in the weld metal.

The model predictions of weld pool geometry, vaporization rates, and composition changes agreed well with the corresponding experimental results for laser welding of aluminum alloy 5182. The good agreement between the calculated and experimental results indicates that the model can serve as a basis for the quantitative understanding of

influences of various welding parameters on fluid flow and heat transfer, vaporization of alloying elements, and weld metal composition changes during laser welding.

The formation of macroporosity has been linked to the instability of the keyhole during laser welding of thin plates of automotive aluminum alloys 5182 and 5754. Porosity was minimum when welding was conducted in either keyhole or conduction mode. In contrast, high porosity in the weld metal was observed in the intermediate transition region where the beam intensity was just above the threshold value for keyhole formation. The keyhole was not stable in this region. Very small disturbances in the system caused the welding mode to shift between keyhole and conduction mode. In order to avoid macroporosity formation, it is essential to choose proper welding parameters to avoid the formation of an unstable keyhole. In this study, a mathematical model was developed to predict the mode of welding based on the welding parameters used. The model was applied to understand the effects of welding variables on the formation of macroporosity during laser welding of aluminum alloys 5182 and 5754. The calculated welding mode and fusion zone geometry agreed well with the corresponding experimental results. Moreover, the model also helped to understand the different keyhole behaviors between using divergent and convergent laser beams. This study showed that the model can be used to determine the operating window of welding parameters where a stable keyhole can be formed and macroporosity could be avoided.

A large amount of macroporosity was observed in the fusion zone of laser welded die-cast magnesium alloy AM60B. The mechanism of porosity formation in the weld metal was determined in this study. Unlike aluminum alloys, pre-existing pores existed in the base metal of alloy AM60B. Experimental observations and theoretical analysis revealed that the coalescence and expansion of the small pre-existing pores in the base metal caused the formation of macro-pores in the fusion zone. The coalescence of small pores was accompanied by an increase in total pore volume due to the reduced internal pressure in the large pores formed. The thermal cycle during the welding also caused the pores to expand.

The keyhole formed during welding of alloy AM60B was more stable than that formed in aluminum alloys 5182 and 5754. The stability of the keyhole depends on a balance between surface tension pressure and vapor pressure. The surface tension pressure tends to close the keyhole while the vaporization tends to keep it open. Aluminum alloys have higher surface tension and much lower vapor pressure than magnesium alloys. Therefore, it is easier to maintain a keyhole for the welding of magnesium alloys than aluminum alloys. Experimental results showed that the stability of the keyhole was not a major factor in the pore formation in the fusion zone during laser welding of alloy AM60B.

Decrease in heat input, i.e. increase in welding speed or decrease in laser power, was found to alleviate porosity formation during laser welding of alloy AM60B. However, a more practical method was developed in this study to reduce porosity by remelting of the fusion zone. Well controlled remelting of the fusion zone, which allowed some of the large pores to be removed by floatation, resulting in reduced porosity in the fusion zone. The reduction in porosity during remelting also indicates that keyhole instability did not contribute significantly to pore formation during laser welding of alloy AM60B.

This study shows that quantitative understanding of quality issues such as weld metal composition change and porosity formation can be achieved based on the fundamental scientific theories. The results obtained in this study provided not only improved understanding of laser welding processes from a scientific point of view but also a guideline for practical welding applications. Taken as a whole, the research presented in this thesis is a contribution to the growing quantitative knowledge base in fusion welding. Expansion of this knowledge base is necessary, if not essential, to solve important quality problems and achieve structurally sound, defect free welds in automotive aluminum and magnesium alloys based on scientific principles.

A list of unsolved important problems in laser welding of automotive aluminum alloys is given below for future research.

### 1) The role of surface active elements

Surface active elements in aluminum alloys [1] such as Bi, Pb, Sb, Ca, and Sn, can potentially affect the laser welding of aluminum alloys in several ways. First, they may significantly influence the fluid flow pattern [2] and the keyhole stability by changing the surface tension of the molten metal. Second, they may affect the vaporization rates of the alloying elements by two opposing effects: a) inhibit vaporization by covering a part of the available vaporizing surface and b) enhance vaporization by causing interface turbulence which increases the surface area. Third, the surface active elements reduce the interfacial energy and aid in the nucleation of hydrogen pores. It is not clear if the surface active elements can be utilized to achieve improved weld penetration, lower vaporization rates of alloying elements, and minimize porosity formation.

### 2) The relationship between microstructure and mechanical behavior

The microstructures in fusion zone and heat affected zone greatly affect the mechanical behavior and formability of the weldment. An improved understanding of the relationship between the microstructures and the mechanical properties of the joints as a whole and the ability to control mechanical properties are much needed. Such researches are critical to the wider use of laser welded automotive aluminum and magnesium alloys, particularly in laser welded tailored blanks that are increasingly used in automotive industry.

### 3) Process robustness

Research to date has indicated that laser welding of automotive aluminum alloys is not a particularly robust process. Small variations in processing parameters often have a major impact on joint properties [3]. For wide spread use in the automotive industry, larger process variable windows are needed. Research on increasing the predictability and robustness of the process in the presence of the disturbances, such as variations in base

metal composition and surface conditions of the workpiece, which commonly occur in a manufacturing environment, is more important to the broader use of this technology than optimizing the process in a very narrow operating region. Research on this topic has not been discussed in the generally available literature.

**References:**

1. J. E. Hatch: '*Aluminum: Properties and Physical Metallurgy*', 1984, ASM, Metal Park, Ohio.
2. W. Pitscheneder, R. Ebner, T. DebRoy, and K. Mundra: *Welding Journal*, 1996, 75, 3, pp. 71s-80s.
3. K. H. Leong, K. R. Sabo, P. G. Sanders, and W. J. Spawr: in '*Laser as Tools for Manufacturing II*', edited by L. R. Miglione and R. D. Schaeffer, SPIE Proceedings 2993, 1997, pp. 37-44, International Society for Optical Engineering, Bellingham, WA.

## **Appendix A**

### **Program for the Calculation of Vaporization Rates and Composition Change during Laser Welding of 5000 Series Aluminum Alloys**

This program is used to calculate the vaporization rates and weld metal composition change during conduction mode laser welding of 5000 series aluminum alloys. There are two files in the program package. The first file is an input data file that stores the weld pool surface temperature data. The default name for this file is "in". The data structure in this file is given in later section. The second one is a window-based executable program named "vap.exe". This executable program calculate the vaporization rates of alloying elements and the weld metal composition changes based on the given weld pool temperature data. The necessary input parameters for the calculation can be provided through several user-friendly dialog boxes.

#### **A1. How to Use the Program**

##### **1) Start up:**

To run the executable file 'vap.exe' under windows environment, the users do not need to have any other compiler or graphics program, just double click the icon for the file and the 'Welcome' window will pop-up on the screen as shown Fig. A1.

##### **2) Modify parameters:**

When the users single click the "Start" button on the 'Welcome' window, the second window 'Input parameters' shows up as shown in Fig. A2. The users can change the default values of all the parameters in the dialog boxes. However, the welding speed and location of the beam on x-axis should be the same as those used in the calculation of surface temperature of the weld pool.

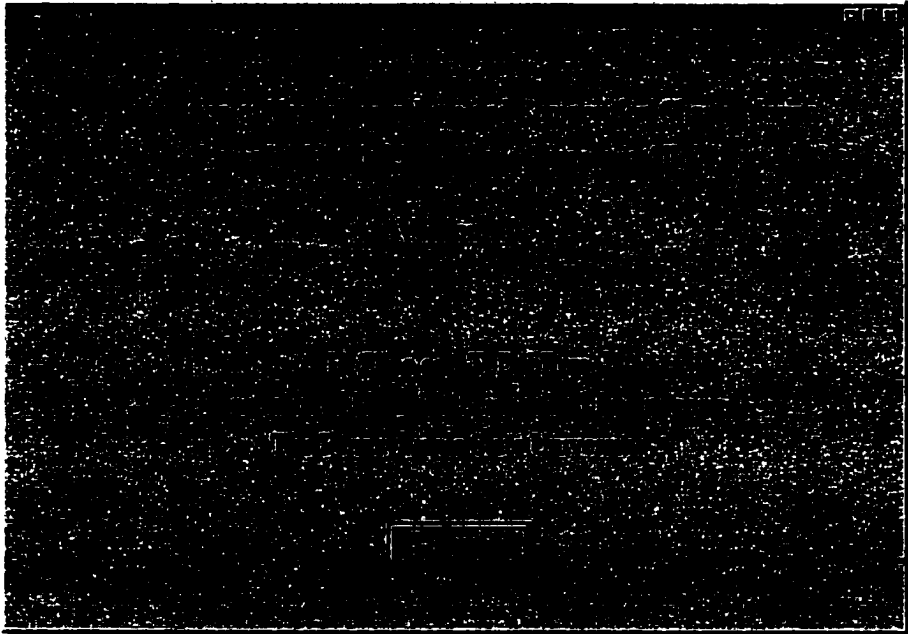


Fig. A1

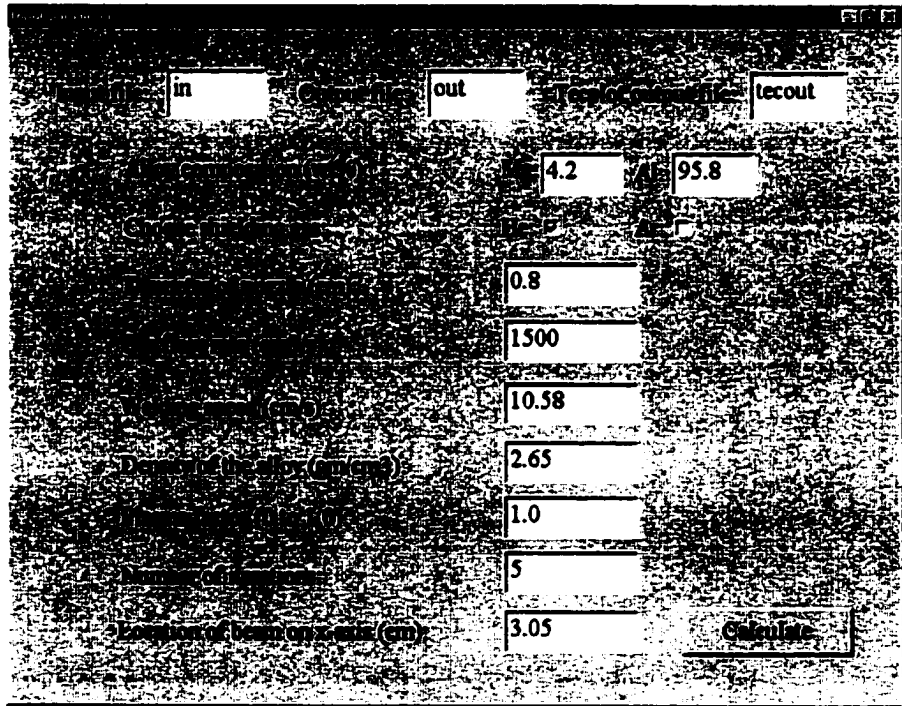


Fig. A2

### 3) Start calculation:

To start the calculations, simply click on the 'Calculate' button in the 'Input parameters' window and the calculation will begin. After a moment, the calculated results will be displayed in the 'Output' window shown in Fig. A3.

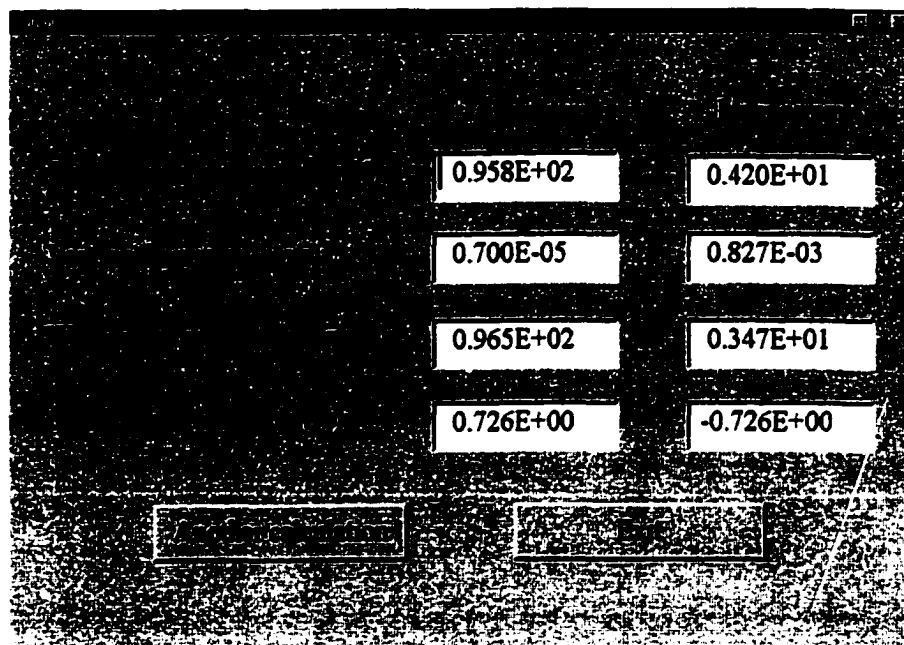


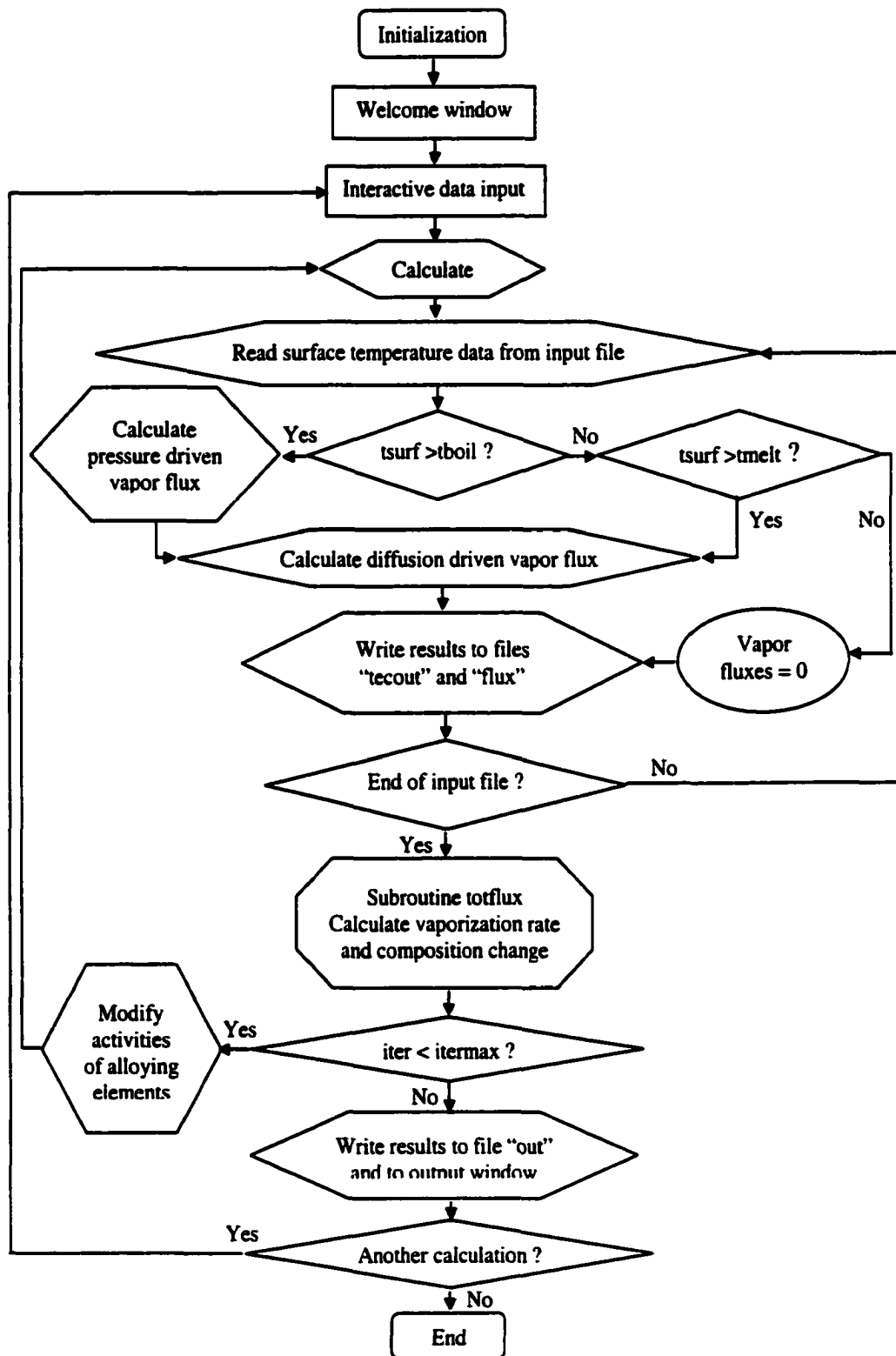
Fig. A3

The results shown in the window will also be stored in an output file with a default name 'out'. Another file with a default name 'tecout' stores the various vapor fluxes on the weld pool surface. This file is specially formatted so that the spatial distributions of various vapor fluxes can be displayed and analyzed on Tecplot data visualization software.

If another calculation is needed, click 'Another calculation' button. If not, click 'Exit' button to quit the program.



## A2. Structure of the Source Code



At the beginning, a welcome window is displayed. This is followed by the second window that displays the default values of various parameters. The users can interactively modify these default values. The input and output file names are also defined here. The input file named 'in' was written in the following fashion:

```

open (unit = 8, file = 'in')
write (8, *) areacs
write (8, *) l1, m1
do 100 j = 1, m1
do 100 i = 1, l1
write (8, *) x, y, xcv, ycv, tsurf
100 continue

```

In the input file, the data on the first line is areacs, the area (in  $\text{cm}^2$ ) of weld pool cross section (y-z plane) vertical to the welding direction (i.e. x direction). The two quantities, l1 and m1, are the numbers of grids in x and y directions, respectively on the surface of the calculation domain as shown in Fig. A4.

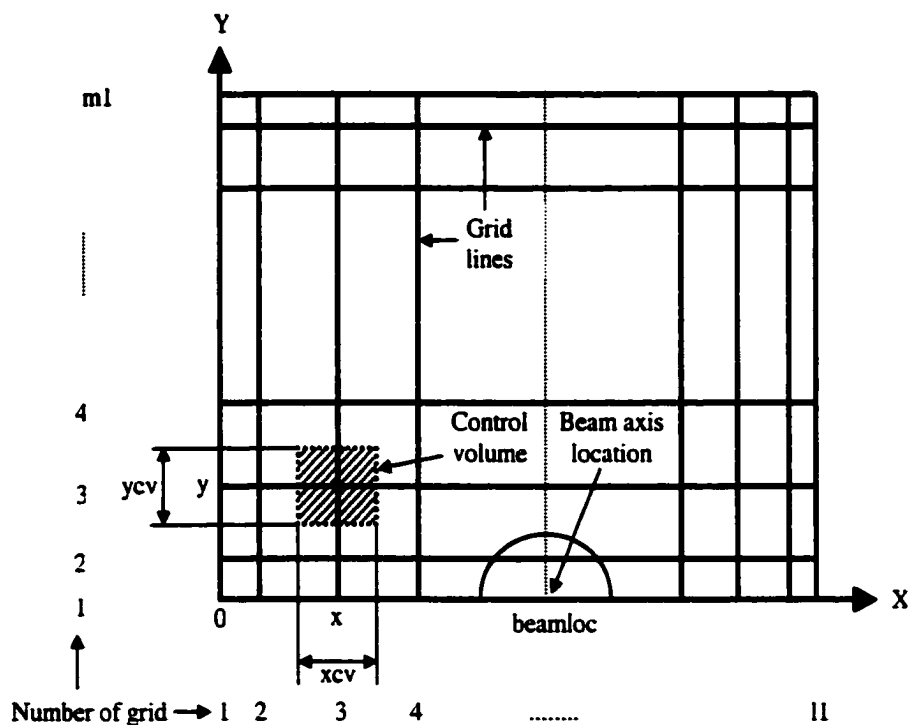


Fig. A4

Due to the symmetry, the temperature data on half of the weld pool surface are provided. The laser beam axis is vertical to the x-y plane and is located at  $x = \text{beamloc}$  and  $y = 0$ . The center of the control volume is located at the intersection of the grid lines  $(x, y)$ . The widths of the control volume in x and y directions are  $x_{cv}$  and  $y_{cv}$ , respectively. The temperature at the control volume is  $t_{surf}$ . There are five numbers on each line from the third line to the end of the input file, describing the position, size and temperature of each control volume. These five quantities are x (in cm), y (in cm),  $x_{cv}$  (in cm),  $y_{cv}$  (in cm) and  $t_{surf}$  (in K), respectively. A sample of the input file is shown below:

```
.39170E-02
51 51
.00000E+00 .00000E+00 .00000E+00 .00000E+00 .29800E+03
.36492E+00 .00000E+00 .72984E+00 .00000E+00 .29800E+03
...
.30570E+01 .10929E-01 .33541E-02 .18579E-02 .20099E+04
.30605E+01 .10929E-01 .35892E-02 .18579E-02 .19819E+04
...
.46533E+01 .30000E+01 .69347E+00 .00000E+00 .29800E+03
.50000E+01 .30000E+01 .00000E+00 .00000E+00 .29800E+03
...
...
...
...
...
```

After all the values of parameters are set and assigned to their corresponding variables, the calculation begins. The boiling point of the liquid metal in the weld pool,  $t_{boil}$ , is calculated first. The boiling point varies with composition of the alloy. Since the volatile elements in this case, Mg, is selectively vaporized during welding, the composition and consequently the boiling point of the liquid metal in the weld pool are different from those of the base metal. At the beginning, the composition in the weld pool is not known and  $t_{boil}$  is calculated based on the composition of the base metal. The boiling point of the weld pool is obtained iteratively as described in Chapter 3 of the thesis. The calculations of the boiling point and the composition of the weld metal are repeated several times. Each time the composition of the weld pool is modified based on the calculated value and the previously used input value. After 5 to 15 iterations, the calculated composition in the weld pool is exactly the same as the one used as input. The

default value for the number of iteration is 5. When the iteration number is reached, the various vapor fluxes are stored in an output file named 'tecout' in the following fashion:

```

open (unit=8, file='in')
open (unit=24, file='tecout')
...
read (8, *) areacs
read(8, *) ll, ml
...
write(24,*)'TITLE = vapor flux file'
write(24,*)'VARIABLES="x","y","confl","totdif","totgd","tsurf","al","mg"'
write(24,*)'ZONE I=',ll,' J=',ml,' F=POINT'
...
do 440 i=1,5000
read(8,*,end=201)x, y, xcv, ycv, tsurf
...
(calculat confl, totdif, totgd, total, and totmg)
...
write(24, *)x, y, confl, totdif, totgd, tsurf, total, totmg
440 continue
201 continue

```

The variables confl, totdif, totgd, tsurf, total, totmg are the pressure driven flux, diffusion driven flux, total flux, surface temperature, aluminum flux, and magnesium flux, respectively.

The data in the input file are read one line at a time and the vapor fluxes on the surface of each control volume are calculated. If the temperature of the control volume is higher than the boiling point of the liquid metal in the weld pool, both the pressure driven and diffusion driven vapor fluxes are calculated. Otherwise, the pressure driven vapor flux is not calculated. If the surface temperature is less than the melting point of the alloy, all the vapor fluxes on this control volume are assigned zero values. The calculation proceeds until all the data in the input file are read and the corresponding vapor fluxes are calculated. At this time, the top surface area of the control volume and the vapor flux of each alloying element on it are stored in a file named 'flux'. The program then calls a

subroutine 'totflux' to calculate the vaporization rates of all the alloying elements by integrating the vapor fluxes stored in file 'flux'.

From the calculated vaporization rates of all the alloying elements and the data of weld pool cross section area, welding speed, and density and composition of the base metal, the composition of the weld metal is calculated. The vaporization rate of each alloying element, the composition and its change in the weld pool are stored in an output file named 'out'. These are also displayed in the 'Output' window as shown in Fig. 4. A typical 'out' file is shown below:

	Aluminum	Magnesium
Base metal composition (wt%)	0.958E+02	0.420E+01
Vaporization rates (gm/s)	0.700E-05	0.827E-03
Weld metal composition (wt%)	0.965E+02	0.347E+01
Composition change (wt%)	0.726E+00	-0.726E+00

The whole calculation starting from interactive data input can be repeated for different conditions if necessary.

### A3. Source Code

```

program vaporization
c   This program calculate the vaporization rates and composition
c   change for 5000 series aluminum alloys.
c   The program needs to be compiled together with resource files
c   including 'resource.fd', 'resource.h', and 'vap.rc'.
  use DFLOGM
  include 'resource.fd'
c-----initialization-----
  character*60 filenames(3), val(9)
  dimension valnov(9)
  logical retlog, icheck(2)
  real gastype, dianz, flrate, wtpal, wtpmg, scvel, density, plfac, beamloc
  integer retint, iedit, itermax, imore
  type (dialog) dlg
  data valnov/0.8,1500.,95.8,4.2,1.0,10.58,2.65,5,3.05/
  data gamma1,gamma3,rtemp,pi/1.6667,1.6667,298.0,3.1416/
  data amwtal,amwtmg,tmelt,imore/26.98,24.31,850.,-1/

```

```

c-----Welcome window-----
      retlog=dlginit(dialog1, dlg)
      retint=dlgmodal(dlg)
      call dlguninit(dlg)
c-----Window for modifying parameters-----
5      retlog=dlginit(dialog2, dlg)
      imore=-1
10     retlog=dlgset(dlg, edit_inf, 'in')
      retlog=dlgset(dlg, edit_outf, 'out')
      retlog=dlgset(dlg, edit_tec, 'tecout')
      retlog=dlgset(dlg, check_he, .true.)
      retlog=dlgset(dlg, check_ar, .false.)
      retlog=dlgset(dlg, edit_nozzle, '0.8')
      retlog=dlgset(dlg, edit_gasflow, '1500')
      retlog=dlgset(dlg, edit_mg, '4.2')
      retlog=dlgset(dlg, edit_al, '95.8')
      retlog=dlgset(dlg, edit_speed, '10.58')
      retlog=dlgset(dlg, edit_plasma, '1.0')
      retlog=dlgset(dlg, edit_density, '2.65')
      retlog=dlgset(dlg, edit_iteration, '5')
      retlog=dlgset(dlg, edit_beamloc, '3.05')
      retint=dlgmodal(dlg)
      retlog=dlgget(dlg, edit_inf, filenames(1))
      retlog=dlgget(dlg, edit_outf, filenames(2))
      retlog=dlgget(dlg, edit_tec, filenames(3))
      retlog=dlggetlog(dlg, check_he, icheck(1))
      retlog=dlggetlog(dlg, check_ar, icheck(2))
      if (icheck(1).and.icheck(2)) goto 10
      if (icheck(1)) gastype=1.0
      if (icheck(2)) gastype=2.0
      do 11 i=1,9
      iedit=1005+i
      retlog=dlgget(dlg, iedit, val(i))
11     continue
      do 12 i=1,9
      read (val(i),*) valnov(i)
12     continue
      call dlguninit(dlg)
c-----end data input, assign user friendly names for the variable-----
      wtpmg = valnov(1)
      wtpal = valnov(2)
      dianz = valnov(3)
      flrate = valnov(4)
      scvel = valnov(5)
      density = valnov(6)
      plfac = valnov(7)
      itermax = valnov(8)
      beamloc = valnov(9)
      if ((wtpmg+wtpal).ne.100.) wtpal=100.-wtpmg
c-----store original composition data-----
      wtpoldal=wtpal
      wtpoldmg=wtpmg
      actco=1073.*alog(0.88)
c-----pick molecular wt. and room temp. viscosity of the shielding gas--

```

```

if (gastype.lt.1.5) then
  amwtgas=4.0026
  amuroom=1.97391e-4
else
  amwtgas=39.94
  amuroom=2.2527e-4
end if
c-----calculate Reynolds number and its function-----
renno=4.*flrate*(amwtgas*273.)/(22400.*298.)/(amuroom*pi*dianz)
fre=2.*sqrt(renno)*sqrt(1.+renno**0.55/200.)
c-----open input and output files-----
open (unit=8, file=filenames(1))
open (unit=16,file=filenames(2))
open (unit=24,file=filenames(3))
open (unit=30,file='flux')
read(8,*) areacs
read(8,*) l1, m1
write(24,*) 'TITLE = vapor flux file'
write(24,*) 'VARIABLES="x","y","confl","totdif","totgd","tsurf",
1 "al","mg"'
write(24,*) 'ZONE I=',l1,' J=',m1,' F=POINT'
rewind(8)
c-----start of calculations-----
do 1000 iter=1,itermax
c-----calculate composition in mole fraction from weight percent-----
totmol=wtpal/amwtal+wtpmg/amwtmg
amfmg=wtpmg/(totmol*amwtmg)
amfal=wtpal/(totmol*amwtal)
c-----find tboil from equilibrium pressures for the given composition---
c-----above tboil there is vapor flux due to pressure gradient-----
c-----bisection method used: aa & bb are initial guessed values-----
aa=1500.
bb=3000.
110  tboil=(aa+bb)/2.0
    call eqpres(aa,pmg,pal)
    ptaa=amfal*pal+exp(actco/aa)*amfmg*pmg-1.
    call eqpres(tboil,pmg,pal)
    ptboil=amfal*pal+exp(actco/tboil)*amfmg*pmg-1.
    if ((ptaa*ptboil).lt.0) then
      bb=tboil
    else
      aa=tboil
    endif
    if (abs(ptboil).lt.0.001) go to 20
    go to 110
20   continue
    write(*,*) 'wtpmg, tboil= ', wtpmg, tboil
c-----read from input file (data of surface temperature)-----
read(8,*)areacs
read(8,*)l1,m1
do 440 i=1,5000
  read(8,*,end=201)x,y,xcv,ycv,tsurf
  areaxy=xcv*ycv
  rdis=sqrt((x-beamloc)**2+y**2)

```

```

c-----initializing the variables-----
total=0.
totmg=0.
totgd=0.
difal=0.
difmg=0.
totdif=0.
confl=0.
cflal=0.
cflmg=0.
if (tsurf.lt.tmelt) goto 101
c-----calculate thermodynamic pressure, equation (3.37)-----
call eqpres (tsurf,pmg,pal)
act=exp(actco/tsurf)
psp=act*amfmg*pmg+amfal*pal
if (tsurf.lt.tboil) goto 102
c-----pressure gradient driven vaporization flux-----
c-----calculate average molecular weight of vapor, equation(3.38)-----
amwtvap=(amfal*pal*amwtal+act*amfmg*pmg*amwtmg)/psp
c-----speed of sound in vapor at room temperature-----
spedrt=sqrt(1.667*8314.*rtemp/amwtvap)*100.
c-----begin calculation of mach number, equations (3.36) to (3.42)-----
amach=0.0
221 am=amach*sqrt(gamma3/2.)
term1=(gamma3-1.)*am/((gamma3+1.)*2.)
c-----temperature jump condition across Knudsen layer, equation (3.36)--
t3ts=(sqrt(1.+pi*term1*term1)-sqrt(pi)*term1)**2
tt=1./(1.+0.47047*am)
erf=0.34802*tt-0.09588*tt*tt+0.74786*tt*tt*tt
c-----density jump condition across Knudsen layer, equation (3.37)-----
r3rs=sqrt(1./t3ts)*((am**2+0.5)*erf-am/sqrt(pi))
r3rs=r3rs+0.5*(1./t3ts)*(1-sqrt(pi)*am*erf)
c-----pressure jump condition across Knudsen layer, equation (3.37)-----
p3ps=r3rs*t3ts
c-----temperature at edge of Knudsen layer surface, equation (3.36)-----
temp3=tsurf*t3ts
a3a1=sqrt(gamma3*temp3*amwtgas)/sqrt(gamma1*rtemp*amwtvap)
term2=(gamma1+1.)/4.*amach*a3a1
c-----Rankine Hogonoit relation, equation (3.41)-----
p2p1=1.+gamma1*a3a1*amach*(term2+sqrt(1.+term2*term2))
c-----gasdynamic pressure at pool surface -----
psp1=p2p1/p3ps
c-----difference between gasdynamic and thermodynamic pressure-----
resd=abs(psp1/psp-1.)
amach = amach+0.00005
if (resd.gt.0.001) go to 221
c-----end mach number calculation, density at pool surface (ideal)-----
rs=amwtvap*273.*psp/(22400.*tsurf)
c-----density at edge of Knudsen layer-----
rho3=r3rs*rs
c-----velocity of vapor at edge of Knudsen layer-----
sped=spedrt*sqrt(temp3/rtemp)
c-----calculate total flux, equation (3.43)-----
confl=rho3*amach*sped

```



```

        cflal=amfal*confl*pal/psp
        cflmg=act*amfmg*confl*pmg/psp
c-----end calculation of pressure gradient driven vaporization flux-----
102  continue
c-----calculate vaporization flux due to concentration gradient-----
        prsure=1.
        if (tsurf.gt.tboil) prsure=(psp+1.)/2.
c        prsure=(psp+1.)/2.
        avtemp=(tsurf+rtemp)/2.
        call gasprop(gastype,avtemp,prsure,visgas,dalgas,dmggas)
        dengas=amwtgas*273.*prsure/(22400.*avtemp)
        akinvis=visgas/dengas
        rd=rdis/dianz
        rd2=rd*rd
        rd3=0.483-0.108*rd+7.71e-3*rd2
c-----aluminum-----
        scno=akinvis/dalgas
        shno=fre*scno**0.42*rd3
        amasco=shno*dalgas/dianz
        difal=amasco*pal*amwtal*amfal/(82.0594*tsurf)
c-----magnesium-----
        scno=akinvis/dmggas
        shno=fre*scno**0.42*rd3
        amasco=shno*dmggas/dianz
        difmg=amasco*pmg*amwtmg*act*amfmg/(82.0594*tsurf)
c-----calculate vapor fluxes consider suppressing effect of plasma-----
        totdif=(difal+difmg)*plfac
        confl=confl*plfac
        total=(cflal+difal)*plfac
        totmg=(cflmg+difmg)*plfac
        totgd=totdif+confl
c-----write the local vaporization flux into a file. The data in this
c        file are used for calculating composition change in a subroutine---
101  write(30,999) areaxy,total,totmg
        if(iter.lt.itermax) goto 440
c-----write output files-----
        write(24,998)x,y,confl,totdif,totgd,tsurf,total,totmg
998  format(8e14.6)
999  format(3e14.6)
440  continue
201  continue
        rewind(8)
        rewind(30)
        close(30)
c-----call subroutine to calculate composition change-----
        call totflux(iter,itermax,areacs,scvel,density,
1      wtpal,wtpmg,wtpoldal,wtpoldmg,imore)
1000 continue
1100 if (imore.gt.0) goto 5
        end program vaporization
c-----subroutine to calculate composition change-----
        subroutine totflux(iter,itermax,areacs,scvel,density,
1      wtpal,wtpmg,wtpoldal,wtpoldmg,imore)
        use DFLOGM

```

```

include 'resource.fd'
logical retlog
integer imore
parameter (nj=5000)
character*60 out(8)
dimension areaxy(nj),gdflux(nj,3),tsum(3),wtp(2)
dimension fwtp(2),delwt(2),output(8)
type (dialog) dlg
retlog=dlginit(dialog3,dlg)
open(unit=30,file='flux')
wtp(1)=wtpoldal
wtp(2)=wtpoldmg
c-----read the local temperature,area and vaporization fluxes-----
jmax=0
do 105 j=1,nj
read(30,*,end=200) areaxy(j),gdflux(j,1),gdflux(j,2)
gdflux(j,3)=gdflux(j,1)+gdflux(j,2)
jmax=jmax+1
105 continue
200 continue
rewind(30)
c-----integrate fluxes over the surface to calculate vaporization rates-
do 330 i=1,3
tsum(i)=0.0
do 441 j=1,jmax
tirate=2.0*gdflux(j,i)*areaxy(j)
tsum(i)=tsum(i)+tirate
441 continue
330 continue
c-----calculate weight percent composition change -----
do 111 i=1,2
anum=scvel*areacs*density*wtp(i)/100.0-tsum(i)
denom=scvel*areacs*density-tsum(3)
fwtp(i)=anum/denom*100.0
if (fwtp(i).lt.0.) fwtp(i)=0.
delwt(i)=fwtp(i)-wtp(i)
111 continue
wtpal=(fwtp(1)+wtpal)/2.
wtpmg=(fwtp(2)+wtpmg)/2.
if(iter.lt.itermax) goto 90
fwtp(1)=wtpal
fwtp(2)=wtpmg
c-----write the output in an output file-----
write(16,99)
99 format(61('-',)/38x,'Aluminum',4x,'Magnesium')
write(16,98) (wtp(i),i=1,2)
98 format(2x,'Base metal composition (wt%)',5x,2(2x,e10.3))
write(16,97) (tsum(i),i=1,2)
97 format(2x,'Vaporization rates (gm/s)',8x,2(2x,e10.3))
write(16,95) (fwtp(i),i=1,2)
95 format(2x,'Weld metal composition (wt%)',5x,2(2x,e10.3))
write(16,93) (delwt(i),i=1,2)
93 format(2x,'Composition change (wt%)',9x,2(2x,e10.3))
write(16,91)

```

```

91   format(61('-'))
c-----Output in a window-----
      output(1)=wtp(1)
      output(2)=wtp(2)
      output(3)=tlsum(1)
      output(4)=tlsum(2)
      output(5)=fwtp(1)
      output(6)=fwtp(2)
      output(7)=delwt(1)
      output(8)=delwt(2)
      do 13 i=1,8
        write(out(i),'(e11.3)') output(i)
        iout=1014+i
        retlog=dlgset (dlg,iout,out(i))
13      continue
        retint=dlgmodal(dlg)
        call dlguninit(dlg)
      if (retint.eq.1023) imore=1
90      return
      end
c-----subroutine to calculate the viscosity of the shielding gas and
c      diffusivity of the alloying elements in the shielding gas-----
      subroutine gasprop(gastype,t,prsure,visgas,dalgas,dmggas)
      if (gastype.lt.1.5) then
        visgas=2.2029e-4+2.2171e-7*t
        dalgas=(-1.199+3.858e-3*t+2.0874e-6*t**2)/prsure
        dmggas=(-1.10152+3.5752e-3*t+1.95512e-6*t**2)/prsure
      else
        visgas=2.7373e-4+2.7681e-7*t
        dalgas=(-0.3852+9.3934e-4*t+6.958e-7*t**2)/prsure
        dmggas=(-0.37496+9.12707e-4*t+6.699e-7*t**2)/prsure
      endif
      return
      end
c-----subroutine to calculate equilibrium vapor pressure -----
      subroutine eqpres(t,pmg,pal)
      pmg=10.**(-7.55e3/t-1.41*alog10(t)+12.79-alog10(760.))
c      pal=10.**((10.578-16946./t-1.3133*alog10(t))
      pal=10.**(-1.645e4/t-1.023*alog10(t)+12.36-alog10(760.))
      return
      end
c-----end of the program-----

```

**A4. Nomenclature in the Source Code**

<b>amach:</b>	<b>mach number of the vapor</b>
<b>amfal:</b>	<b>mole fraction of Al</b>
<b>amfmg:</b>	<b>mole fraction of Mg</b>
<b>amwtal:</b>	<b>molecular weight of Al</b>
<b>amwtmg:</b>	<b>molecular weight of Mg</b>
<b>amwtgas:</b>	<b>molecular weight of the shielding gas</b>
<b>amolwt:</b>	<b>average molecular weight of the alloy</b>
<b>amuroom:</b>	<b>viscosity of the shielding gas at room temperature</b>
<b>amwtvap:</b>	<b>average molecular weight of vapor</b>
<b>areacs:</b>	<b>area of the weld cross section vertical to the welding direction</b>
<b>areaxy:</b>	<b>top surface area of the control volume</b>
<b>avtemp:</b>	<b>average temperature of the shielding gas</b>
<b>cfal:</b>	<b>pressure driven Al vapor flux</b>
<b>cfmg:</b>	<b>pressure driven Mg vapor flux</b>
<b>confl:</b>	<b>total pressure driven vapor flux</b>
<b>dalgas:</b>	<b>diffusivity of Al in shielding gas</b>
<b>dmggas:</b>	<b>diffusivity of Mg in shielding gas</b>
<b>delwt(i):</b>	<b>composition change of the alloying element i</b>
<b>density:</b>	<b>density of the alloy</b>
<b>dengas:</b>	<b>density of shielding gas</b>
<b>dianz:</b>	<b>diameter of the shielding gas nozzle</b>
<b>difal:</b>	<b>diffusion driven Al vapor flux</b>
<b>difmg:</b>	<b>diffusion driven Mg vapor flux</b>
<b>flrate:</b>	<b>flow rate of the shielding gas</b>
<b>fwtp(i):</b>	<b>final weight percent of element i</b>
<b>gamma1:</b>	<b>ratio of specific heats of shielding gas</b>
<b>gamma3:</b>	<b>ratio of specific heats of vapor</b>
<b>gastype:</b>	<b>index of shielding gas (gastype = 1 for He, or 2 for Ar)</b>
<b>gdflex(j,i):</b>	<b>vapor flux of element i and total vapor flux (if i=3) on jth control volume</b>

<b>imore:</b>	<b>index for another calculation</b>
<b>iter:</b>	<b>index of iteration number</b>
<b>itermax:</b>	<b>total number of iteration</b>
<b>jmax:</b>	<b>total number of control volumes</b>
<b>ll:</b>	<b>total number of grid lines in x-axis</b>
<b>ml:</b>	<b>total number of grid lines in y-axis</b>
<b>pi:</b>	<b>constant, <math>\pi = 3.1416</math></b>
<b>pal:</b>	<b>equilibrium vapor pressure of Al</b>
<b>pmg:</b>	<b>equilibrium vapor pressure of Mg</b>
<b>plfac:</b>	<b>plasma factor in the suppression of the vaporization rate</b>
<b>prsure:</b>	<b>pressure of the shielding gas</b>
<b>rdis:</b>	<b>radial distance of the weld pool surface to beam axis</b>
<b>renno:</b>	<b>Reynolds number of the shielding gas</b>
<b>rtemp:</b>	<b>room temperature</b>
<b>scno:</b>	<b>Schmidt number, the ratio of kinematic viscosity and diffusivity</b>
<b>scvel:</b>	<b>scanning velocity of the power source</b>
<b>spedrt:</b>	<b>sound speed at room temperature</b>
<b>t:</b>	<b>temperature</b>
<b>tlsum(i):</b>	<b>vaporization rate of element i and total vaporization rate</b>
<b>tmelt:</b>	<b>solidus temperature of the alloy</b>
<b>totmol:</b>	<b>total mole of metal atoms in unit weight of alloy</b>
<b>total:</b>	<b>total Al vapor flux</b>
<b>totmg:</b>	<b>total Mg vapor flux</b>
<b>totdif:</b>	<b>total diffusion driven vapor flux</b>
<b>totgd:</b>	<b>total vapor flux</b>
<b>tboil:</b>	<b>boiling point of the alloy</b>
<b>tsurf:</b>	<b>weld pool surface temperature</b>
<b>visgas:</b>	<b>viscosity of the shielding gas</b>
<b>wtp(i):</b>	<b>initial weight percent of the alloying element i</b>
<b>wtpal:</b>	<b>weight percent Al in the weld pool</b>

<b>wtpmg:</b>	<b>weight percent Mg in the weld pool</b>
<b>wtpoldal:</b>	<b>weight percent Al in the base metal</b>
<b>wtpoldmg:</b>	<b>weight percent Mg in the base metal</b>
<b>x:</b>	<b>grid line position in x-direction</b>
<b>xcv:</b>	<b>x-direction width of the control volume</b>
<b>y:</b>	<b>grid line position in y-direction</b>
<b>ycv:</b>	<b>y-direction width of the control volume</b>

## Appendix B

### Program for the Calculation of Keyhole Geometry and Weld Pool Temperature Field during Laser Welding

This program is used to calculate the keyhole geometry and the three dimensional temperature field of the weld pool in laser beam welding.

#### B1. How to Use the Program

##### 1) Start up:

A window-based executable program named "key.exe" is generated by compiling and building the source code "keylaser.f" together with resource files including 'resource.fd', 'resource.h', and 'resource.rc' in Visual Fortran. To run the program under windows environment, the users do not need to have any other compiler or graphics program, just double click the icon for this file and the 'Welcome' window will pop-up on the screen as shown in Fig. B1.

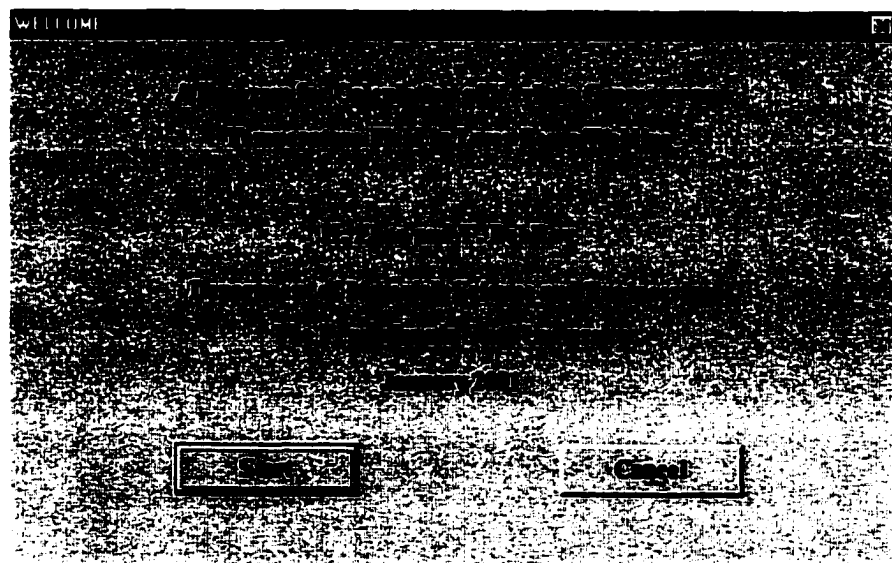
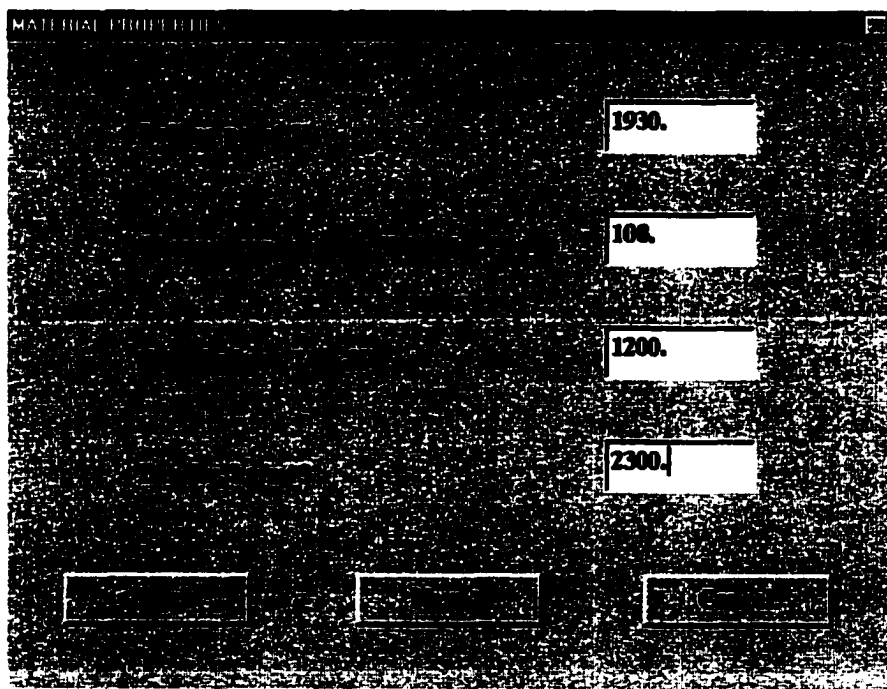


Fig. B1

## 2) Modify parameters:

Click the “Start” button shown in Fig. B1, the window shown in Fig. B2 will appear, where the materials properties, including boiling point, thermal conductivity, specific heat, and density, can be defined in the corresponding edit boxes. Click the buttons “<Back”, “Next>”, or “Cancel” will cause the program to move the previous window, move to the next window, or stop the calculation.



The image shows a window titled "MATERIAL PROPERTIES". It contains four vertically stacked input fields with the following values: 1930., 108., 1200., and 2300. At the bottom of the window, there are three buttons: "<Back", "Next>", and "Cancel".

Fig. B2

To continue the calculation, click the “Next>” button and a third window shown in Fig. B3 will show up where the welding parameters, including beam power, welding speed, absorption coefficient, beam radius, beam focal length, beam defocusing, and preheat temperature, can be defined.



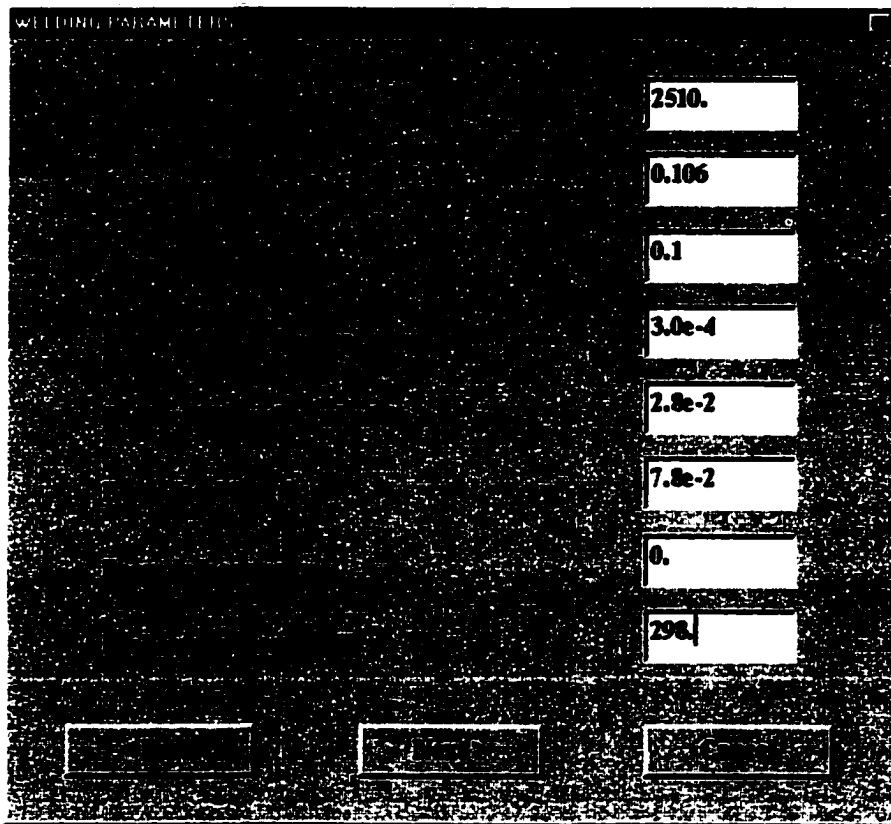


Fig. B3

To continue calculation, click the "Next>" button in the welding parameters window and the window shown in Fig. B4 will appear. In this window, the calculation domain, grid size, and the spatial precision of the keyhole wall can be defined. To start calculation, click the "Calculation" button and the program will calculate the keyhole profile and the temperature field based on the input parameters.

At any stage before clicking the "Calculation" button, the previously defined parameters can be corrected by clicking the "<Back" button to go to the previous window. But please remember that all the defined parameters in the current window will be set back to the default values if the "<Back" button is clicked.

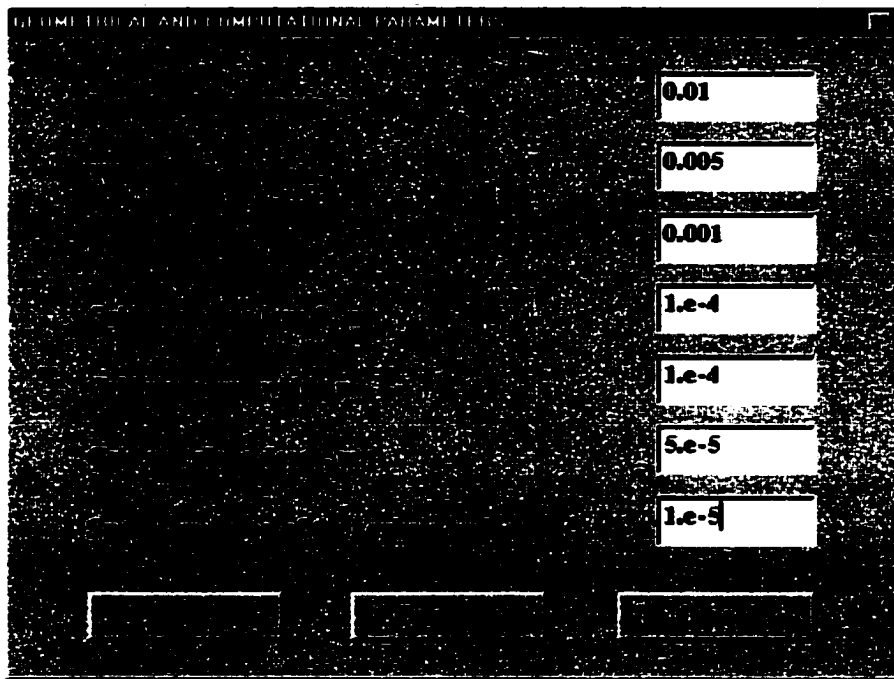
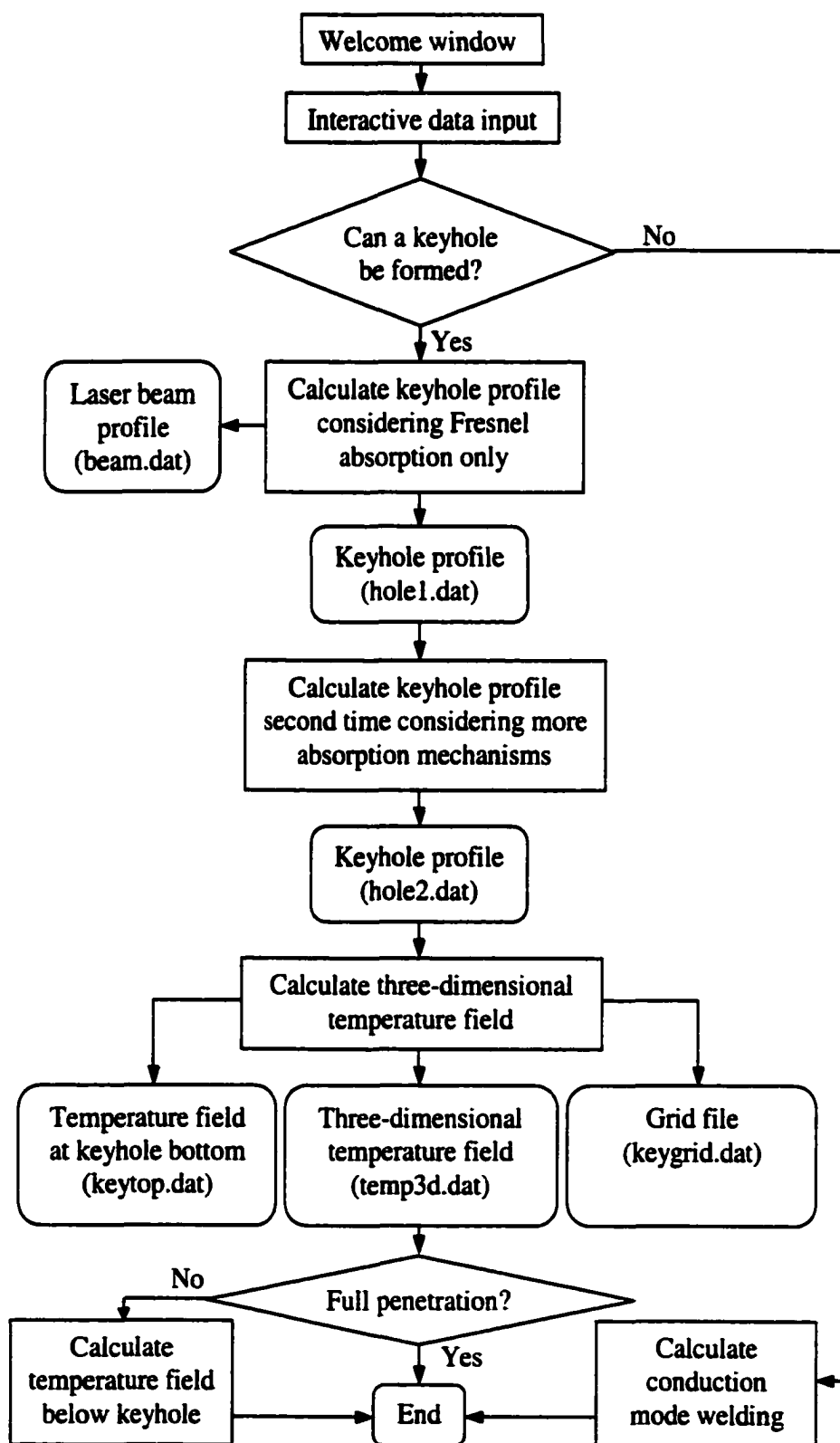


Fig. B4

After the calculation, the output data will be stored in four or six files, depending on the calculated results. The profile the laser beam is stored in file "beam.dat". The keyhole geometries calculated in the first and second round of calculation are stored in file "hole1.dat" and "hole2.dat", respectively. The temperature field of the weld pool is stored in file "temp3d.dat". If the keyhole depth is equal to the thickness of the workpiece, the calculation will stop here. However, if the keyhole depth is less than thickness of the workpiece, another two files "keygrid.dat" and "keytop.dat" will be generated. These two files store the grid information and the temperature field at the bottom plane of the keyhole. These two files together with file "temp3d.dat" will be used by another program "keyadapt" to calculate the heat conduction below the bottom of the keyhole. The source code for the program "keyadapt" is "keyadapt.f". It is a subroutine of a general purpose program "COMPACT3D" running on workstation "flow1". Files "keygrid.dat" and "keytop.dat" are used as input files to define the grid system and boundary condition for the calculation of heat conduction. The calculated temperature field below the keyhole will be appended in file "temp3d.dat". The previously stored temperature field in file "temp3d.dat" is kept untouched.

## B2. Structure of the Source Code





```

if (retint.eq.1008) goto 9998
if (retint.eq.1006) goto 1
tv=valnov(1)
cond=valnov(2)
cp=valnov(3)
dens=valnov(4)
c-----welding parameters-----
c   power:      laser beam power
c   speed:      welding speed
c   absorb:     absorption coefficient, no unit
c   radius:     beam radius at the focal point
c   rlens:     beam radius at the end of the focusing lens
c   f:         focal length
c   defocus:    displacement from workpiece surface to focal point
c               defocus is positive when the focal point is placed
c               above the workpiece surface, and vice versa.
c   ta:        preheat temperature
c   data power,speed,absorb/2510.,0.106,0.1/
c   data radius,rlens,f,defocus,ta/3.e-4,2.8e-2,7.8e-2,0.,298./
c-----open window for welding parameters-----
3   retlog=dlginit(IDD_DIALOG3,dlg)
c-----define default values-----
retlog=dlgset(dlg,fdc_power,'2510.')
retlog=dlgset(dlg,fdc_speed,'0.106')
c   retlog=dlgset(dlg,fdc_speed,'0.0635')
retlog=dlgset(dlg,fdc_absorb,'0.10')
retlog=dlgset(dlg,fdc_radius,'3.0e-4')
retlog=dlgset(dlg,fdc_rlens,'2.8e-2')
retlog=dlgset(dlg,fdc_f,'7.8e-2')
retlog=dlgset(dlg,fdc_defocus,'0.')
retlog=dlgset(dlg,fdc_ta,'298.')
retint=dlgmodal(dlg)
c-----set new values-----
do 20 i=1,8
iedit=1008+i
20  retlog=dlgget(dlg,iedit,val(i))
do 21 i=1,8
21  read(val(i),*) valnov(i)
call dlguninit(dlg)
if (retint.eq.1019) goto 9998
if (retint.eq.1017) goto 2
power=valnov(1)
speed=valnov(2)
absorb=valnov(3)
radius=valnov(4)
rlens=valnov(5)
f=valnov(6)
defocus=valnov(7)
ta=valnov(8)
c-----geometrical and computational parameters-----
c   alength:    length of the calculation domain
c   width:     width of the calculation domain
c   thick:     work-piece thickness
c   depth:     depth of keyhole

```

```

c      dx:          grid size along length
c      dy:          grid size along width
c      dz:          grid size along depth
c      dr:          spatial precision of the keyhole wall profile
c      pi:          constant
data alength,width,thick/0.03,0.01,0.01/
data dx,dy,dz,dr,pi/5.e-4, 5.e-4, 5.e-4, 1.e-5, 3.1416/
c-----open window for geometrical and computational parameters-----
4      retlog=dlginit(IDD_DIALOG4,dlg)
c-----define default values-----
      retlog=dlgset(dlg, IDC_LENGTH, '0.01')
      retlog=dlgset(dlg, IDC_WIDTH, '0.005')
      retlog=dlgset(dlg, IDC_THICK, '0.001')
      retlog=dlgset(dlg, IDC_DX, '1.e-4')
      retlog=dlgset(dlg, IDC_DY, '1.e-4')
      retlog=dlgset(dlg, IDC_DZ, '5.e-5')
      retlog=dlgset(dlg, IDC_DR, '1.e-5')
      retint=dlgmodal(dlg)
c-----set new values-----
do 30 i=1,7
  iedit=1019+i
30      retlog=dlgget(dlg, iedit, val(i))
do 31 i=1,7
31      read(val(i), *) valnov(i)
      call dlguninit(dlg)
      if(retint.eq.1029) goto 9998
      if(retint.eq.1027) goto 3
      alength=valnov(1)
      width=valnov(2)
      thick=valnov(3)
      dx=valnov(4)
      dy=valnov(5)
      dz=valnov(6)
      dr=valnov(7)
      leapz=int(dz/dr)
c-----open file for output data-----
c      temp3d.dat: file for 3D temperature field data
c      cool.dat:   file for cooling rate data
c      beam.dat:   file for beam profile data
c      hole.dat:   file for keyhole wall profile data
      open(unit=10, file='temp3d.dat')
      open(unit=20, file='cool.dat')
      open(unit=22, file='beam.dat')
      open(unit=32, file='hole1.dat')
      open(unit=42, file='hole2.dat')
      open(unit=45, file='hole.dat')
      open (unit=50, file='keygrid.dat')
      open (unit=60, file='keytop.dat')
c-----calculate beam properties-----
      afr=absorb
      v=speed
      z0=defocus
      rf0=radius
      diff=cond/(cp*dens)

```

```

pe=0.5*v/diff
zray=rf0*f/rlens
ai=2.*power/(rf0*rf0*pi)
write(60,*) ta,cond,dens,cp,speed
c-----evaporation flux-----
call eqpres(tv,pal,pmg)
totmol=wtpal/amwtal+wtpmg/amwtmg
amfal=wtpal/(totmol*amwtal)
amfmg=wtpmg/(totmol*amwtmg)
vpal=44.34/7.5*amfal*pal*sqrt(amwtal/tv)
vpmg=44.34/7.5*amfmg*pmg*sqrt(amwtmg/tv)
c-----evaporative heat flux-----
heatv=heatal*vpal+heatmg*vpmg
write(*,*) 'evaporative heat flux= ',heatv,' w/m2'
c-----calculate keyhole front and rear wall profiles-----
dist=1.0
900  xstart=2.0*radius
     xf=xstart
     xr=xstart
     z=0.
     ttp=0.
     nangle=0
     write(*,*) 'Calculating line source...'
     do 1000 i=1,100000
       x=xf+xr
       if (x.lt.0.) goto 1100
       if (z.gt.thick) goto 1100
       x1=0.2*x
       x2=0.5*x
1110  call wall(pe,x1,xrs)
       t1=x1+xrs-x
       call wall(pe,x2,xrs)
       t2=x2+xrs-x
       if (abs(t2).lt.1.e-6) goto 1001
       ax=x2
       x2=x1-t1*(x2-x1)/(t2-t1)
       x1=ax
       goto 1110
1001  xfs=x2
       xs=xf-xfs
       write(32,33) xf,-xr,xs,-z
33    format (4e15.6)
c-----calculate energy balance at the keyhole wall-----
perf=pe*abs(xfs)
call bess0(perf,ak0)
call bess1(perf,ak1)
akf=ak1/ak0
perr=pe*abs(xrs)
call bess0(perr,ak0)
call bess1(perr,ak1)
akr=ak1/ak0
qf=(tv-ta)*cond*pe*(1.+akf)
qr=(tv-ta)*cond*pe*(-1.+akr)
rb=rf0*sqrt(1.+((z+z0)/zray)**2)

```

```

c-----record laser beam profile-----
c   write(22,*) rb, -z
   aif=dist*afr*ai*((rf0/rb)**2)*exp(-2.*(xf/rb)**2)
   air=dist*afr*ai*((rf0/rb)**2)*exp(-2.*(xr/rb)**2)
   tanf=qf/(aif-heatv)
   tanr=qr/(air-heatv)
   if((aif-heatv).lt.0.) then
     dxf=dr
     dxr=dr
     goto 99
   endif
   dxf=dr*tanf
   dxr=dr*tanr
   if(((dxf.gt.dr).or.(dxx.gt.dr)).and.(z.eq.0.)) then
     dxf=dr
     dxr=dr
     goto 99
   endif
   thetaf=thetaf+atan(tanf)
   thetar=thetar+atan(tanr)
   z=z+dr
99  if(z.eq.0.) then
     rewind(32)
     als=0.
     goto 411
   endif
     als=sqrt((xs-xs0)**2+dr*dr)
     xs0=xs
     r0=xf-xs
     per0=pe*abs(r0)
     call bess0(per0,ak0)
     p=(tv-ta)*2.*pi*cond/ak0*exp(per0)
     ttp=ttp+p*als
     nangle=nangle+1
411  xf=xf-dxf
     xr=xr-dxr
1000 continue
1100 continue
     rewind(32)
c-----keyhole depth first round-----
     depth=z
     write(*,*) 'First round line source calculation finished.'
c   write(*,*) 'Line source calculation finished.'
     write(*,*) 'Keyhole depth (mm):', depth*1000.
     write(*,*) 'Absorbed power (W): ', ttp
     write(*,*) 'Input power (W):      ', power
     write(*,*) 'Overall absorption: ', ttp/power
     read(32,*) xf0,xr0
     rewind(32)
c   goto 3001
     if ((depth.eq.0.).and.(dist.gt.1.)) then
       write(*,*) 'Keyhole can not be formed for the given conditions.'
       goto 5000
     else

```



```

    if (depth.gt.0.) goto 901
    if (defocus.le.0.) dist=2.0
    if (defocus.gt.0.) then
write(*,*) 'Keyhole can not be formed for this positive
defocusing.'
    goto 5000
    endif
    goto 900
    endif
c-----Second round calculation consider plasma and multiple
reflection---
901 write(*,*) 'second round calculation'
do 3000 nround=2,2
c   thetaf=thetaf/float(nangle)
c   thetar=thetar/float(nangle)
    thetaf=atan((xf0-xr0)/(2.*depth))
    thetar=thetaf
    refnf=pi/(4.*thetaf)
    refnr=pi/(4.*thetar)
    theta=(thetaf+thetar)/2.
    refn=pi/(4.*theta)
    write(*,*) 'number of reflection = ',refnf, refnr,refn
    dpl=1.2e-3
    aivb=100.
    apl=1.-exp(-aivb*dpl)
    apli=1.-exp(-aivb*0.5*depth)
    amrf=1.-(1.-afr)**(refnf-1.)
    amrr=1.-(1.-afr)**(refnr-1.)
    amr=1.-(1.-afr)**(refn-1.)
    aibmr=1.-exp(-1.5*aivb*depth)
    cofr=(1.-apl)*(1.-apli)*afr
    comrf=(1.-apl)*(1.-apli)*(1.-afr)*amrf
    comrr=(1.-apl)*(1.-apli)*(1.-afr)*amrr
    comr=(1.-apl)*(1.-apli)*(1.-afr)*amr
    coplf=(1.-apl)*(apli+aibmr*(1.-apli)*(1.-afr)*(1.-amrf))
    coplr=(1.-apl)*(apli+aibmr*(1.-apli)*(1.-afr)*(1.-amrr))
    copl=(1.-apl)*(apli+aibmr*(1.-apli)*(1.-afr)*(1.-amr))
c-----find line source positions-----
    xf=xstart
    xr=xstart
    z=0.
    ttp=0.
    nangle=0
    do 2000 i=1,100000
    x=xf+xr
    if (x.lt.0.) goto 2100
    if (z.gt.thick) goto 2100
    x1=0.2*x
    x2=0.5*x
2110 call wall(pe,x1,xrs)
    t1=x1+xrs-x
    call wall(pe,x2,xrs)
    t2=x2+xrs-x
    if (abs(t2).lt.1.e-6) goto 2001

```

```

    ax=x2
    x2=x1-t1*(x2-x1)/(t2-t1)
    x1=ax
    goto 2110
2001 xfs=x2
    xs=xf-xfs
    write(42,33) xf,-xr,xs,-z
    write(45,*) 1000.*xf,-1000.*xr,1000.*xs,-1000.*z
c-----calculate energy balance at the keyhole wall-----
    perf=pe*abs(xfs)
    call bess0(perf,ak0)
    call bess1(perf,ak1)
    akf=ak1/ak0
    perr=pe*abs(xrs)
    call bess0(perr,ak0)
    call bess1(perr,ak1)
    akr=ak1/ak0
    qf=(tv-ta)*cond*pe*(1.+akf)
    qr=(tv-ta)*cond*pe*(-1.+akr)
    rb=rf0*sqrt(1.+((z+z0)/zray)**2)
    aif=ai*((rf0/rb)**2)*exp(-2.*(xf/rb)**2)
    air=ai*((rf0/rb)**2)*exp(-2.*(xr/rb)**2)
    aif2=cofr*aif
    air2=cofr*air
    aimf=comrf*aif
    aimr=comrr*air
    aipf=coplf*aif
    aipr=coplr*air
c    qf2=qf-aimf-aipf
c    qr2=qr-aimr-aipr
    qf2=qf-aipf
    qr2=qr-aipr
c-----with heat of evaporation-----
    tanf2=qf2/(aif2+aimf-heatv)
    tanr2=qr2/(air2+aimr-heatv)
    if((aif2+aimf-heatv).lt.0.) then
    dxf=dr
    dxr=dr
    goto 199
    endif
    dxf=dr*tanf2
    dxr=dr*tanr2
    if(((dxf.gt.dr).or.(dxx.gt.dr)).and.(z.eq.0.)) then
    dxf=dr
    dxr=dr
    goto 199
    endif
    thetaf=thetaf+atan(tanf2)
    thetar=thetar+atan(tanr2)
    z=z+dr
199  if(z.eq.0.) then
    rewind(42)
    als=0.
    goto 511

```

```

endif
als=sqrt((xs-xs0)**2+dr*dr)
xs0=xs
r0=xf-xs
per0=pe*abs(r0)
call bess0(per0,ak0)
p=(tv-ta)*2.*pi*cond/ak0*exp(per0)
ttp=ttp+p*als
nangle=nangle+1
511  xf=xf-dxf
     xr=xr-dxr
     write(22,*) 1000.*rb, 1000*-z
2000 continue
2100 continue
     rewind(42)
c-----keyhole depth second round-----
     depth=z
     if (nround.ne.2) then
       write(*,*) nround,'th round line source calculation finished.'
       goto 3010
     endif
     write(*,*) 'Second round line source calculation finished.'
3010 write(*,*) 'Keyhole depth (mm):', depth*1000.,' mm'
     write(*,*) 'Plate thickness(mm):',thick*1000.,' mm'
     write(*,*) 'Absorbed power (W): ', ttp
     write(*,*) 'Input power (W): ', power
     write(*,*) 'Overall absorption: ', ttp/power
     if (depth.lt.thick) write(*,*) 'Partial penetration, run keyadapt'
     read(42,*) xf0,xr0
     rewind(42)
3000 continue
3001 continue
c-----3D temperatue field-----
     write(*,*) 'Calculating 3D temperature field and cooling rate...'
     xmax=3.e-3
     xmin=xmax-alength
     imax=int(alength/dx)+1
     ymax=width/2.
     ymin=-ymax
     jmax=int(width/dy)+1
     kmax=thick/dz+1
     t0=ta
     write(10,*) 'TITLE = "Temperature field"'
     write(10,*) 'VARIABLES="X (mm)", "Y (mm)", "Z (mm)",
&"Temperature (K)"'
     write(10,*) 'ZONE I=',imax,'J=',jmax,'K=',kmax,'F=POINT'
     write(20,*) 'TITLE = "Cooling rate"'
     write(20,*) 'VARIABLES="X (mm)", "Y (mm)", "Z (mm)",
&"Cooling rate (K/s)"'
     write(20,*) 'ZONE I=',imax,'J=',jmax,'K=',kmax,'F=POINT'
4001 read(42,*,end=4002) xf,xr,xs,zz
     if (zz.eq.0.) then
       ka=1

```

```

        goto 4011
    endif
    ka=ka+1
    if(ka.lt.leapz) goto 4001
    ka=1
4011  xs0=xs
        r0=xf-xs
        per0=pe*abs(r0)
        call bess0(per0,ak0)
        p=(tv-ta)*2.*pi*cond/ak0*exp(per0)
4002  continue
        nz=nz+1
        do 4000 y=ymin,ymax,dy
        do 4000 x=xmin,xmax,dx
        xa=x-xs
        r=sqrt(xa*xa+y*y)
        cos=xa/r
        per=abs(pe*r)
        call bess0(per,ak0)
        t=ta+p/(2.*pi*cond)*ak0*exp(-per*cos)
        if(t .gt. tv) t=tv
        if ((z.le.depth).and.(z.gt.(depth-dz))) then
        write(60,*) t
        write(10,*) 1000.*x,1000.*y,1000.*z,t
        goto 4000
        endif
c-----write data of 3D temperature field-----
        write(10,*) 1000.*x,1000.*y,1000.*z,t
        cool=(t-t0)*v/dx
        t0=t
c-----write data of cooling rate-----
        write(20,*) 1000.*x,1000.*y,1000.*z,cool
4000  continue
9996  rewind(42)
        close(42)
        kmaxb=kmax-nz+1
        depthb=thick-depth
        n=imax*jmax*kmaxb
        write(50,*) alength,width,depthb,imax,jmax,kmaxb,xmax,thick
        goto 9997
5000  write(*,*) 'Calculate weld pool depth for conduction mode welding'
        z=0.
        x=0.
5001  r=sqrt(x*x+z*z)
        expterm=exp(-v*(r+x)/(2.*diff*1.5))
        t=ta+(power*absorb/(2.*pi*cond*r*1.5))*expterm
        if(t .lt. tm) goto 5002
        z=z+1.e-8
        goto 5001
5002  if(tmin .gt. t) goto 5003
        tmin=t
        x=x-1.e-8
        goto 5001
5003  depth=z

```

```

        write(*,*) 'Weld pool depth is:      ',1000.*depth,'mm'
9997 write(*,*) 'Finished all calculations.'
9998 end
c-----main program end here-----
c-----subroutine to find wall position relative to line source-----
      subroutine wall(pe,xfs,xrs)
      real(8) ak0,aka,akb,pet,pet1,pet2
      pet=pe*xfs
      call bess0(pet,ak0)
      confs=exp(pet)/ak0
      g1=2.*xfs
      g2=2.5*xfs
1920  pet1=pe*g1
      pet2=pe*g2
      call bess0(pet1,ak0)
      aka=ak0
      call bess0(pet2,ak0)
      akb=ak0
      var1=aka*exp(pet1)
      var2=akb*exp(pet2)
      v1=confs*var1-1.
      v2=confs*var2-1.
      if (abs(v2).lt.1.e-5) goto 1922
      ag=g2
      g2=g1-v1*(g2-g1)/(v2-v1)
      g1=ag
      goto 1920
1922  xrs=g2
      end
c-----Calculate Modified Bessel Function (2nd kind & 0th order)-----
      subroutine bess0(x,ak0)
      real(8) x,ak0
      data c0 /1.25331414/,c1 /-.07832358/,c2 /.02189568/
      data c3 /-.01062446/,c4 /.00587872/, c5 /-.0025154/
      data c6 /.00053208/
      if (x.gt.2.) goto 100
      gamma=0.5772156649
      call i0(x,fi0,f1)
      ak0=- (dlog(0.5*x)+gamma)*fi0+f1
      goto 101
100  y=2./x
      x2= y*y
      x3=x2*y
      x4=x3*y
      x5=x4*y
      x6=x5*y
      var=c0+c1*y+c2*x2+c3*x3+c4*x4+c5*x5+c6*x6
      ak0=var/(sqrt(x)*exp(x))
101  end
c-----Function I0(x)-----
      subroutine i0(x,fi0,f1)
      real(8) x
      fi0=1.
      f1=0.

```

```

    fac=1.
    p2=0.
    do 200 k=1,100
    oldfi0=fi0
    oldf1=f1
    fac=fac*float(k)
    p1=(0.25*x*x)**k/(fac*fac)
    p2=p2+1./float(k)
    fi0=fi0+p1
    f1=f1+p1*p2
    afi0=abs(fi0-oldfi0)
    af1=abs(f1-oldf1)
    if((afi0.lt.1.e-20).and.(af1.lt.1.e-20)) goto 201
200  continue
201  end
c-----Calculate Modified Bessel Function (2nd Kind & 1st Order)-----
    subroutine bess1(x,ak1)
    real(8) x, ak1
    data a2 /.15443144/,a4 /-.67278579/, a6 /-.18156897/
    data a8 /-.01919402/,a10 /-.00110404/,a12 /-4.686e-5/
    data b0 /1.253314/, b1 /.234986/, b2 /-.0365562/
    data b3 /.0150427/, b4 /-.00780353/, b5 /.00325614/
    data b6 /-.00068245/
    if (x.gt.2.) goto 110
    y=x/2.
    y2=y*y
    y4=y2*y2
    y6=y4*y2
    y8=y6*y2
    y10=y8*y2
    y12=y10*y2
    call funil(x,ai1)
    p=x*alog(y)*ai1+1.
    pp=p+a2*y2+a4*y4+a6*y6+a8*y8+a10*y10+a12*y12
    ak1=pp/x
    goto 111
110  continue
    z=2./x
    z2=z*z
    z3=z2*z
    z4=z3*z
    z5=z4*z
    z6=z5*z
    qq=b0+b1*z+b2*z2+b3*z3+b4*z4+b5*z5+b6*z6
    ak1=qq/(sqrt(x)*exp(x))
111  end
c-----Calculate I1(x) Function-----
    subroutine funil(x,ai1)
    real(8) x
    a=0.5*x
    aa=a*a
    ai1=a
    fack=1.
    do 210 k=1,50

```

```
bb=aa**k
fack=fack*float(k)
fack1=fack*float(k+1)
ai0=aa*bb/(fack*fack1)
ail=ail+ai0
if (ai0.lt.1.e-20) goto 211
210 continue
211 end
c-----Calculate equilibrium vapor pressure-----
subroutine eqpres(t,pal,pmg)
c-----thermodynamic equilibrium vapor pressure-temperature relations-----
pal=10.**(-1.645e4/t-1.023*log10(t)+12.36-log10(760.))
pmg=10.**(-7.55e3/t-1.41*log10(t)+12.79-log10(760.))
end
```

## 2) Fortran code "keyadapt.f":

```

      subroutine adapt
c-----This program continue to calculate the temperature field below the
c-----keyhole bottom
c-----Files 'keygrid.dat', 'keytop.dat', and 'temp3d.dat' are need to run
c-----this program
      parameter(ni=150,nj=60,nk=20,nfmax=6,idblk=1000,kunstd=0,
      lnzmx=20,nfm2=(1+kunstd)*nfmax,idim=2*(ni*nj+nj*nk+ni*nk))
      include '/home/CFD/COMP3D/ADPT3.FOR'
      include '/home/CFD/COMP3D/COMPRE.FOR'
      dimension t(ni,nj,nk)
      equivalence (f(1,1,1,6),t(1,1,1))
      data ta,cond,dens,cp/298.,108.,2300.,1200./
c-----ah: heat transfer coefficient for free convection, W/m^2-K-----
      data ah/15./
c*****
      entry check
      iread=0
      return
c*****
      entry grid
      open (unit=10, file='keygrid.dat')
      read(10,*) alength,width,depthb,imax,jmax,kmaxb,xmax,thick
      mode=1
      xl=alength
      yl=width
      zl=depthb
      ncvlx=imax
      ncvly=jmax
      ncvlz=kmaxb-2
      call tools(EZGRID)
      write(*,*)'l1,m1,n1= ',l1,m1,n1
      return
c*****
      entry begin
      open (unit=11,file='keytop.dat')
      read(11,*) ta,cond,dens,cp,speed
      diff=cond/(cp*dens)
      do 100 k=1,n1
      do 100 j=1,m1
      do 100 i=1,l1
100    t(i,j,k)=ta
      do 110 j=2,m2
      do 110 i=2,l2
110    read(11,*) t(i,j,1)
      last=50
      ksolve(1)=0
      ksolve(6)=1
      return
c*****
      entry dense
      write(*,*)'iteration= ',iter
      return

```



```

c*****
  entry output
    if(iter.ne.last) goto 310
    open(unit=12, file='temp3d.dat',position='append')
      xcord=length-xmax
      ycord=width/2.
      zcord=thick-depthb
    do 300 k=2,n1
    do 300 j=2,m2
    do 300 i=2,l2
300  write(12,*) 1000.*(x(i)-xcord),1000.*(y(j)-ycord),
1  1000.*(z(k)+zcord),t(i,j,k)
310  return
c*****
  entry outflo
  return
c*****
  entry phi
    do 200 i=2,l2
      vdx=speed/xcv(i)
    do 200 j=2,m2
    do 200 k=2,n2
      gam(i,j,k)=diff
      sc(i,j,k)=vdx*t(i-1,j,k)
200  sp(i,j,k)=-vdx
c-----boundary condition: bottom boundary-----
      kbcn1(i,j)=2
    do 210 i=2,l2
    do 210 j=2,m2
      flxc(i,j,n1)=ah*ta
210  flxp(i,j,n1)=-ah
      write(*,*)'t(70,25,2)= ',t(70,25,2)
    return
c*****
  entry lc
  return
c*****
  include '/home/CFD/COMP3D/FINISH3.FOR'
end

```

## Appendix C

### Animation of Transient Weld Pool Temperature Field during Laser Welding

#### C1. Description of the Movie

A useful way to demonstrate the computed temperature field is to show the results in the form of a movie. For example, the movie may show the instantaneous temperature distributions on three planes on the workpiece vertical to the welding direction as the laser beam move from the right to the left as shown in Fig. C1.

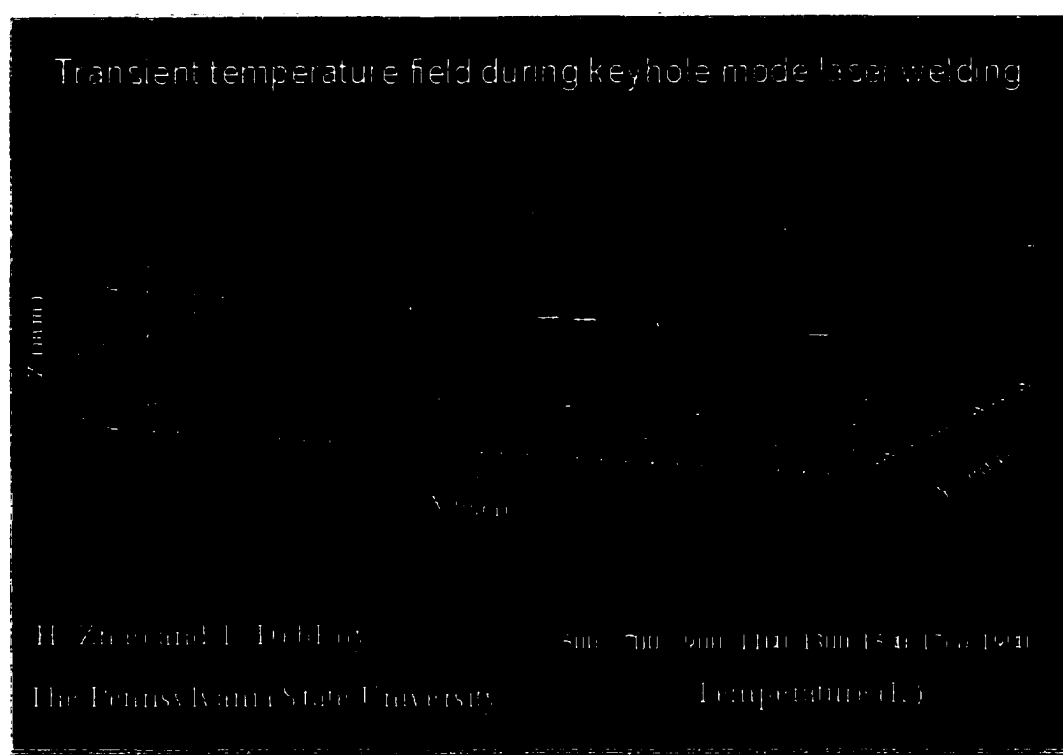


Fig. C1

#### C2. Files Needed to Make the Movie

Five files are needed to make this movie. They are plane1.plt, plane2.plt, plane3.plt, temp3d.lay, and mv.mcr (mvavi.mcr or mvrn.mcr). The first three files store the temperature data on the three planes to be shown in the movie. The file "temp3d.lay"

is edited on Tecplot 8.0. This file determines all the general features of the film as shown above. The file "mv.mcr" is a Tecplot macro file that coordinates the three data files and "temp3d.lay" by showing one frame at a time and records all the frames in sequence. The recorded frames are stored in a movie file "movie.avi". The movie can be played on Windows Media Player or Real Player.

### C3. Procedure to Make the Movie

1) Make the three data files: plane1.plt, plane2.plt, and plane3.plt:

The three planes chosen are vertical to x-axis and are located at  $x = 2, 4, 6$  mm, respectively. The following three block of codes are added to the source code "keylaser.f" presented in Appendix B to make the three data files:

```

... ..
... ..
open(unit=11,file='plane1.dat')
open(unit=12,file='plane2.dat')
open(unit=13,file='plane3.dat')
... ..
... ..
do 4000 z=zmin,zmax,dz
4001 read(42,*,end=4002) xf,xr,xs,zz
    if(zz.eq.0.) then
        ka=1
        goto 4011
    endif
    ka=ka+1
    if(ka.lt.leapz) goto 4001
    ka=1
4011 xs0=xs
    r0=xf-xs
    per0=pe*abs(r0)
    call bess0(per0,ak0)
    p=(tv-ta)*2.*pi*cond/ak0*exp(per0)
    do 4000 y=ymin,ymax,dy
    do 4000 x=xmin,xmax,dx
... ..
... ..
c-----temperature calculation for the first plane-----
xa=2./1000.-x-xs
r=sqrt(xa*xa+y*y)

```

```

cos=xa/r
per=abs(pe*r)
call bess0(per,ak0)
t=ta+p/(2.*pi*cond)*ak0*exp(-per*cos)
if(t .gt. tv) t=tv
c-----write data for the animation in the first plane--
write(11,*) 2.,1000.*y,1000.*z, t
c-----temperature calculation for the second plane-----
xb=4./1000.-x-xs
r=sqrt(xb*xb+y*y)
cos=xb/r
per=abs(pe*r)
call bess0(per,ak0)
t=ta+p/(2.*pi*cond)*ak0*exp(-per*cos)
if(t .gt. tv) t=tv
c-----write data for the animation in the second plane--
write(12,*) 4.,1000.*y,1000.*z, t
c-----temperature calculation for the second plane-----
xc=6./1000.-x-xs
r=sqrt(xc*xc+y*y)
cos=xc/r
per=abs(pe*r)
call bess0(per,ak0)
t=ta+p/(2.*pi*cond)*ak0*exp(-per*cos)
if(t .gt. tv) t=tv
c-----write data for the animation in the third plane--
4000 write(13,*) 6.,1000.*y,1000.*z, t
4002 continue
.....

```

The three data files plane1.dat, plane2.dat, and plane3.dat obtained can be converted to binary files plane1.plt, plane2.plt, and plane3.plt by running “preplot filename” in MS-DOS environment, for example, type in “preplot plane1.dat” will obtain file “plane1.plt” in the same directory.

## 2) Make the file temp3d.lay:

Open Tecplot 8.0, load data file “plane1.plt”, and edit the frame so that it has the features shown in Fig. C2.

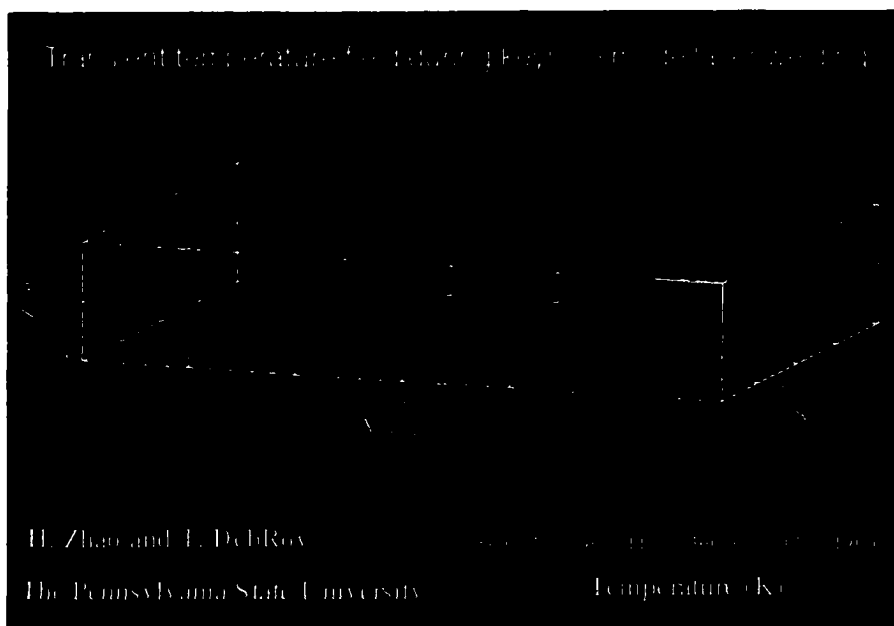


Fig. C2

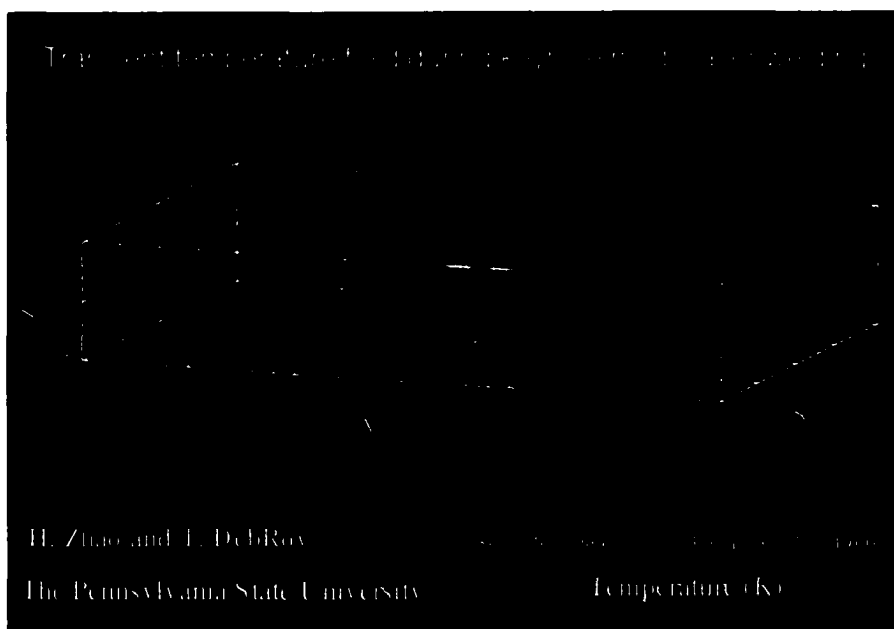


Fig. C3

Then in the tecplot click “File”, choose “Load DataFiles(s)”, choose “Add to Current Dataset”, and open file “plane2.plt”. Activate the new added zone by going “Field”, “Contour Attributes”, “Countour”, and make sure all the zones in “Zone Show” are

showing “Yes”. Also make sure the “IJK Mode” is “Planes”. Now the frame obtained has the features shown in Fig. C3. Similarly, the third plane can be added and the final picture is shown in Fig. C4. Finally, save the file as “temp3d.lay” and close the tecplot.

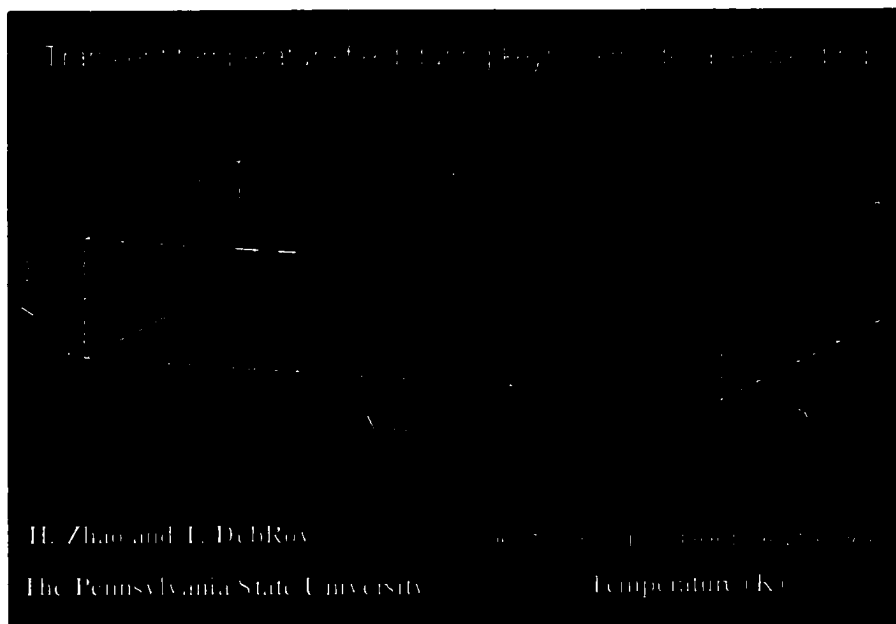


Fig. C4

### 3) Edit the macro file:

The macro file ‘mvavi.mcr’ for making a movie in avi format is as follows:

```

#!MC 800
$!VARSET |I| = 1
$!VARSET |N| = 0
$!LOOP 70
$!OPENLAYOUT "c:\movies\temp3d.lay"
  ALTDATALOADINSTRUCTIONS =
  ' "c:\movies\plane1.plt"+"c:\movies\plane2.plt"+"c:\movies\p
  lane3.plt" '
$!INTERFACE SHOWFRAMEBORDERSWHENOFF = NO
$!FIELD
  IJKMODE
  {CELLTYPE = PLANES
  PLANES = I
  IRANGE{MIN = |I|}

```

```

    IRANGE{MAX = |I|}
  }
$!ATTACHGEOM
  XYZPOS
  {
    X = |N|
    Y = 0
    Z = 0
  }
  GEOMTYPE = LINESEGS3D
  ARROWHEADATTACHMENT =ATBEGINNING
  ARROWHEADSTYLE=FILLED
  COLOR = RED
  LINETHICKNESS = 0.5
  ARROWHEADSIZE = 15
  ARROWHEADANGLE = 3
  RAWDATA
1
2
0 0 0
0 0 -0.5
$!REDRAW
$!EXPORTSETUP EXPORTFNAME = "c:\movies\movie.avi"
  EXPORTFORMAT = AVI
  ANIMATIONSPEED = 5.0
$!EXPORT
  APPEND = YES
$!VARSET |I| += 1
$!VARSET |N| += 0.1
$!ENDLOOP

```

The macro file 'mvrn.mcr' for making a movie in rm format is as follows:

```

#!MC 800
$!VARSET |I| = 1
$!VARSET |N| = 0
$!EXPORTSETUP EXPORTFNAME = "c:\movies\movie.rm"
  EXPORTFORMAT = RASTERMETAFILE
$!EXPORT
$!LOOP 70
$!OPENLAYOUT "c:\movies\temp3d.lay"

```

```

ALTDATALOADINSTRUCTIONS = 'c:\movies\plane1.plt"+
"c:\movies\plane2.plt"+"c:\movies\plane3.plt"'
$!INTERFACE SHOWFRAMEBORDERSWHENOFF = NO
$!FIELD
  IJKMODE
  {CELLTYPE = PLANES
  PLANES = I
  IRANGE{MIN = |I|}
  IRANGE{MAX = |I|}
  }
$!ATTACHGEOM
  XYZPOS
  {
  X = |N|
  Y = 0
  z = 0
  }
  GEOMTYPE = LINESEGS3D
  ARROWHEADATTACHMENT =ATBEGINNING
  ARROWHEADSTYLE=FILLED
  COLOR = RED
  LINETHICKNESS = 0.5
  ARROWHEADSIZE = 15
  ARROWHEADANGLE = 3
  RAWDATA
1
2
0 0 0
0 0 -0.5
$!REDRAW
$!EXPORTSETUP EXPORTFNAME = "c:\movies\movie.rm"
  EXPORTFORMAT = RASTERMETAFILE
$!EXPORT
  APPEND = YES
$!VARSET |I| += 1
$!VARSET |N| += 0.1
$!ENDLOOP

```

In the above examples, all the files are kept in directory c:\movies. If the files are kept in a different directory, the appropriate directory should be specified in the macro files (\*.mcr).



#### 4) Make the movie

Click “Start” at the lower-left corner of the screen, click run, type in “tecplot c:\movies\mvavi.mcr, and click “OK”. Tecplot 8.0 will be opened and the movie named “movie.avi” as defined in file “mvavi.mcr” will be made automatically. Similarly, the movie named “movie.rm” as defined in file “mvrn.mcr” can be made. Depending on the size of the data files and speed of the computer, it will usually take several minutes to tens of minutes to finish.

### C4. Play the Movie

#### 1) Play the movie “movie.avi”:

- a) Play in windows environment: double click the file “movie.avi”.
- b) Play with specified player: open Window Media Player or Real Player, open the file “movie.avi” from the menu “File”, then “Open” or “Open Files”.
- c) Play the movie in PowerPoint presentation: there are two ways of doing this.
  - i) Open the presentation file, and move to the slide where the movie is intended to be shown. Click “Insert”, “Movies and Sounds”, “Movie from File”, and select the movie file to shown and click “OK”. You will have the options of showing the movie automatically or showing by a click on it. The first frame of the movie will be shown in the slide. During presentation with “slide show”, movie will either play automatically or play by a mouse click.
  - ii) Open the presentation file, chose a symbol where you want to show the movie by clicking it during the presentation, click the button on the right side of the mouse, and a list of menu will show up. Choose “Action Settings”, then “Mouse Click” and click “Run Program”. In the edit box for “Run Program, type in the complete directory and name of the .exe file for the movie-playing software, followed by a space and then the complete directory and the name of the movie file. For example,

**“c:\Program Files\Real\RealPlayer\realplay.exe c:\movie\movie.avi”**

**During presentation with “Slide Show”, the movie can be played with a click on the symbol.**

## **2) Play the movie “movie.rm”**

**This movie needs the Framer post-processor and viewer supplied with Tecplot to play. The command is “framer movie.rm”.**

## Appendix D

### Programs for the Calculation of Turbulent Fluid Flow and Heat Transfer during Laser Welding

Three programs are used in the calculation of turbulent fluid flow and heat transfer in laser welding. The calculations are separated in three stages using the three programs. In the first stage, the first program 'turb0.f' is used where the effect of turbulence is not calculated. The calculation is continued in the second stage where the second program 'turb.f' is used and the effect of turbulence is calculated. In the final stage, the calculation considers both the effect of turbulence and evaporative heat loss using the third program 'turbvaploss.f'.

#### D1. Source Code

##### 1) Program turb0.f

```

subroutine adapt
parameter(ni=70,nj=70,nk=70,nfmax=11,idblk=100,kunstd=1,
infm2=(1+kunstd)*nfmax, nzm=10, idim=2*(ni*nj+nj*nk+ni*nk))
c   nx: maximum of nzx,nzy and nzz (number of zones in three
directions)
parameter(nog=5,nz=8,nq=14,np=19,nu=11,no=21,nbg=10,nzmax=10,ng=5)
include '/home/CFD/COMP3D/ADPT3.FOR'
include '/home/CFD/COMP3D/COMP3D.FOR'
save
dimension igroup(nog),valpro(nq),valphy(np),valnsp(nu),
ivalbou(nbg),valout(no)
dimension amuff(ni,nj,nk),diff(ni,nj,nk),dudy1(ni,nj,nk)
dimension t(ni,nj,nk),h(ni,nj,nk),frac1(ni,nj,nk),hold(ni,nj,nk),
1frac1old(ni,nj,nk),apsum(ni,nj,nk)
dimension heatin(ni,nj),qin(ni,nj,nk),factor2(ni,nj,nk),
luv(ni,nj,nk)
dimension scemfx(ni,nj,nk),scemfy(ni,nj,nk),scemfz(ni,nj,nk)
dimension xyzo(nzmax,3),nxyz(nzmax,3),pxyz(nzmax,3),nzone(3)
dimension renew(ni,nj,nk),width1(ni,nk)
dimension ake(ni,nj,nk),dis(ni,nj,nk),amut(ni,nj,nk)
equivalence (f(1,1,1,6),t(1,1,1)),(f(1,1,1,7),h(1,1,1)),
1(f(1,1,1,nfmax+7),hold(1,1,1)),(f(1,1,1,8),frac1(1,1,1)),
1(f(1,1,1,nfmax+8),frac1old(1,1,1)),(f(1,1,1,9),
1ake(1,1,1)),(f(1,1,1,10),dis(1,1,1)),(f(1,1,1,11),amut(1,1,1))

```

```

c-----nzone(i or j or k): number of zones in i or j or k direction
c-----xyzo(i or j or k): length of different zones in i or j or k
direction
c-----nxyz(i or j or k): number of control volumes in different zones
c-----pxyz(i or j or k): exponential factor for different zones
equivalence (nzone(1),nzx), (nzone(2),nzy), (nzone(3),nzz),
1(xyzo(1,1),xzone(1)), (xyzo(1,2),yzone(1)), (xyzo(1,3),zzone(1)),
2(nxyz(1,1),ncvx(1)), (nxyz(1,2),ncvy(1)), (nxyz(1,3),ncvz(1)),
3(pxyz(1,1),powrx(1)), (pxyz(1,2),powry(1)), (pxyz(1,3),powrz(1))
character*60 grname(nog), strfile(nz), strpro(nq),
1strphy(np), strnsp(nu), strgeom(ng), strout(no), strbou(nbg)
character*30 filenames(nz)
data igrp/nz,nq,np,nu,nbg/
data grname/'filenames', 'processes parameters', 'material propertie
ls', 'numerical scheme parameters', 'boundary conditions'/
c----group 1 input data-----
data strfile/'output file name', 'plot file name', 'print file name'
1,'start file name', 'save file name', 'grid input filename', 'tecplot
1 file name', 'emf field file name'/
data filenames/'output', 'plot', 'print', 'start', 'start', 'grid',
1'tecout', 'field'/
c----group 2 input data: process parameters and their default values----
data strpro/'laser power (Watts)', 'absorption coefficient', 'beam/a
lrc radius (cm)', 'scanning velocity (cm/sec)', 'starting location of
1 beam', 'to arc welding (yes:1, no:0)', 'arc current (Amp)', 'arc vol
tage (Volts)', 'arc efficiency (%)', 'starting emf field (yes:1,no:0
1)', 'fraction of energy received from arc', 'radius of volumetric he
at source (cm)', 'height of volumetric heat source (cm)', '# of iter
ls after which power is set to 0'/
data valpro/60.,.2,.25,0.17,4.7,1,150.,11.0,75.,0,1.0,.1,.3,2000./
c-- Group 3 input data: material properties and their default values ---
data strphy/'liquidus temperature (K)', 'density of liquid metal (g
lm/cm**3)', 'enthalpy of solid at mp (cal/gm)', 'enthalpy of liquid a
lt mp (cal/gm)', 'specific heat of solid (cal/gm-K)', 'specific heat
lof liquid (cal/gm-K)', 'thermal cond of solid (cal/cm-sec-K)', 'ther
mal cond of liq (cal/cm-sec-K)', 'viscosity of liquid (gm/cm-sec)',
1'viscosity & liq cond enhancement factor', 'd(gamma)/dT, pure mat (
ldynes/cm-K)', 'conc. of surface active species (wt%)', 'enthalpy of
l segregation (J/mole)', 'surface excess at sat (mole/cm**2)', 'entrop
ly factor', 'to variable properties (yes:1, no:0)', 'coeff of thermal
l expansion (1/K)', 'solidus temperature (K)', 'emissivity of the mat
erial'/
data valphy/1785.0,7.2,250.76,314.76,0.168,0.193,0.06,0.2,0.06,
15.0,0.43,0.0,-1.66e5,1.30e-9,0.00318,0.0,1.0e-5,1745.0,0.0/
c-- Group 4 input data: default values of numerical scheme parameters---
data strnsp/'velocity relaxation parameter', 'pressure relaxation p
l parameter', 'enthalpy relaxation parameter', 'latent heat relaxation
l parameter', 'time increment', 'number of iterations', 'maximum number
l of cycles per time step', 'iter interval for overall heat balance'
1,'index to start from oldfile(yes:1,no:0)', 'index to solve momentu
lm eqns(yes:1,no:0)', 'index to write tecplot file(yes:1,no:0)'/
data valnsp/.8,.8,1.,.8,1e20,40,1.,5.,.0,1.,1./
c----group 5 input data : default values of the boundary conditions----
data strbou/'temperature at i=1 boundary (K)', 'temperature at i=11

```

```

1 boundary (K)', 'temperature at j=m1 boundary', 'temperature at k=n1
1 boundary (k)', 'heat transfer coeff at i=1(cal/cm2-s-K)', 'heat tra
nsfer coeff at i=l1(cal/cm2-s-K)', 'heat transfer coeff at j=m1(cal
1/cm2-s-K)', 'heat transfer coeff at k=n1(cal/cm2-s-K)', 'heat transf
ler coeff at k=1(cal/(cm2-s-k)', 'preheat temperature (K)'/
  data valbou/298.0,298.0,298.0,298.0,100.0,100.0,100.0,100.0,00.0,
  1298.0/
c---group 6: grid data-----
  data strgeom/'zone(', 'number of zones', ' )length', ' )number of con
  trol volumes', ' )exponential factor'/
c---Group 7: output data-----
  data strout/'depth of the pool (cm)', 'width of the pool (cm)', 'len
  lgth of the pool', 'peak temperature', 'heat input rate (cal/s)', 'hea
  lt output rate (cal/s)', 'heat flow at n1', 'heat flow at m1', 'heat f
  llow at i1', 'heat flow at l1', 'RSMAX', 'SMAX', 'SSUM', 'UMAX', 'VMAX',
  'IWMAX', 'IMIN', 'IMAX', 'JMAX', 'KMAX', 'ratio (Heat In/Heat Out)'/
  entry check
  iread=0
  return
  entry grid
10  nogpl=nog+1
  do 11 i=1,nog
11  write(6,99) 'Enter',i, 'to change/view ', grname(i)
  write(6,69) 'Enter',nogpl, 'to do calculations with current values'
c-- Select a data group to view/change data -----
  write(6,4)
  write(*,*) '          Please enter your choice (1 to 6):'
  read(*,*) igrop
  if(igrop.eq.nogpl) go to 51
c-- On screen viewing of parameter values in a selected data group -----
  write (6,79) grname(igrop)
  imax=igroup(igrop)
21  write(6,4)
  do 40 i=1,imax
  goto(31,32,33,34,35)igrop
31  write(*,30) 'Enter',i, 'to change',strfile(i), '(' ,filenames(i), ')'
  go to 40
32  write(*,59) 'Enter',i, 'to change',strpro(i), '(' ,valpro(i), ')'
  go to 40
33  write(*,59) 'Enter',i, 'to change',strphy(i), '(' ,valphy(i), ')'
  go to 40
34  write(*,59) 'Enter',i, 'to change',strnsp(i), '(' ,valnsp(i), ')'
  go to 40
35  write(*,59) 'Enter',i, 'to change',strbou(i), '(' ,valbou(i), ')'
40  continue
  imaxpl=imax+1
  write(6,49) 'Enter',imaxpl, 'if all values in this group are ok'
c-- Decide if some of the values need to be changed -----
  write(6,39) 'Please enter your choice (1 to',imaxpl,'):'
  read(*,*)  ichange
  if(ichange.eq.imaxpl) go to 10
c-- Change parameter value -----
  goto (41,42,43,44,45) igrop
41  write(6,29) 'Enter',strfile(ichange), ':'

```

```

        read(5,89) filenames(ichange)
        go to 21
42    write(6,19)'Enter',strpro(ichange),': '
        read(5,*)valpro(ichange)
        go to 21
43    write(6,19)'Enter',strphy(ichange),': '
        read(5,*)valphy(ichange)
        go to 21
44    write(6,19)'Enter',strnsp(ichange),': '
        read(5,*)valnsp(ichange)
        go to 21
45    write(6,19)'Enter',strbou(ichange),': '
        read(5,*)valbou(ichange)
        go to 21
c-- end data input -----
51    call name3(plotf,filenames(2),startf,filenames(4),
        lsavef,filenames(5))
c---user friendly names for process parameters-----
        call data7(power,valpro(1),abscof,valpro(2),rb,valpro(3),scanvel,
        lvalpro(4),xstart,valpro(5),yesarc,valpro(6),arccur,valpro(7))
        call data5(arcvol,valpro(8),yesoldf,valpro(10),fracg,valpro(11),
        lrbt,valpro(12),htv,valpro(13))
        call inta1(ifinish,int(valpro(14)))
        if (yesarc.lt.0.5) go to 12
        abscof=valpro(9)/100.0
        power=arccur*arcvol
c--user friendly names for physical properties -----
12    call data3(tliquid,valphy(1),rhoref,valphy(2),ac,valphy(11))
        call data3(wtpct,valphy(12),enthse,valphy(13),gamsat,valphy(14))
        call data3(entfac,valphy(15),yvarpr,valphy(16),beta,valphy(17))
        call data3(hsmelt,valphy(3),hlfriz,valphy(4),acp,valphy(5))
        call data3(acpl,valphy(6),amuf,valphy(9),factor,valphy(10))
        call data3(tsolid,valphy(18),dgdtd,valphy(11),emiss,valphy(19))
        difs=valphy(7)/acp
        difl=valphy(8)/acpl
c-- user friendly names for numerical scheme parameters -----
        call data6(relax(1),valnsp(1),relax(2),valnsp(1),relax(3),valnsp(1)
        1),relax(4),valnsp(2),relax(7),valnsp(3),relax(8),valnsp(4))
        call data2(dt,valnsp(5),yesold,valnsp(9))
        call inta5(last,int(valnsp(6)),itmax,int(valnsp(7)),iwrite,
        lint(valnsp(8)),isol,int(valnsp(10)),itecplt,int(valnsp(11)))
c---user friendly names for geometric parameters-----
        call inta2(mode,1,kdisk,1)
        call data3(xu(2),0.,yv(2),0.,zw(2),0.)
c---user friendly names for boundary conditions-----
        call data3(til,valbou(1),t1l,valbou(2),tml,valbou(3))
        call data3(tnl,valbou(4),htcil,valbou(5),htcll,valbou(6))
        call data3(htcml,valbou(7),htcnl,valbou(8),htckl,valbou(9))
        call data1(ti,valbou(10))
c----open required files-----
        open (unit=41,file=filenames(1))
        open (unit=7,file=filenames(3))
        open (unit=42,file=filenames(6))
        if (yesarc.gt.0.5) open (unit=43,file=filenames(8))

```

```

c-----grid generation-----
      do 910 ijk=1,3
      read(42,*)nzone(ijk)
      read(42,*) (xyzo(i,ijk),i=1,nzone(ijk))
      read(42,*) (nxyz(i,ijk),i=1,nzone(ijk))
910      read(42,*) (pxyz(i,ijk),i=1,nzone(ijk))
      call tools(zgrid)
c-----default starting location of the beam-----
      if (xstart.eq.0) xstart=xzone(2)+xzone(1)
      valpro(5)=xstart
      return
      entry begin
      call data2(relax(9),0.01,relax(10),0.01)
      call inta4(kprint(1),1,kprint(2),1,kprint(6),1)
      call inta3(kpmax,2,kpln(1),1,kpln(2),4)
      call name2(title(6),' temperature ',title(7),' enthalpy')
      call namel(title(8),'fraction liquid  ')
c-----calculation of some constant parameters-----
      restd=1.0e-7
      crit(7)=1.0e-7
      pi=3.1415297
      kord = 2
      rb2 = rb**2
      rbt2 = rbt**2
      pkint = fracg*2.0*power*abscof*0.239/(pi*rb2)
c      pkint = fracg*3.0*power*abscof*0.239/(pi*rb2)
c      pkint = fracg*power*abscof*0.239/(2.0*pi*rb2)
      deltemp = tliquid - tsolid
      cpavg = (acp+acpl)/2.0
      hlcal = hsmelt+cpavg*deltemp
      hlatnt = hlfriz - hlcal
      boufac = rhoref*980.0*beta
      rhoscan = rhoref*scanvel
      sigems = emiss*5.67E-12*0.239
      tamb4 = 298.0**4
      acpl4 = acpl**4
      acp4 = acp**4
c      nvk=9
c      nvd=10
c      call inta2(ksolve(9),1,ksolve(10),1)
      if (isol.ne.1) go to 111
      do 110 nff=1,8
      ksolve(nff)=1
110      kbloc(nff)=1
111      call inta3(ksolve(6),0,ksolve(8),0,ksolve(7),1)
      hi = (ti-tsolid)*acp+hsmelt
      h11 = (t11-tsolid)*acp+hsmelt
      h1l = (t1l-tsolid)*acp+hsmelt
      hm1 = (tm1-tsolid)*acp+hsmelt
      hn1 = (tn1-tsolid)*acp+hsmelt
      do 102 i=1,l1
      do 102 j=1,m1
      do 102 k=1,n1
      u(i,j,k)=0.0

```

```

v(i,j,k)=0.0
w(i,j,k)=0.0
rho(i,j,k)=rhoref
amut(i,j,k)=amuf
diff(i,j,k)=difl
ake(i,j,k)=0.1
dis(i,j,k)=0.1
h(i,j,k)=hi
hold(i,j,k)=hi
102  t(i,j,k)=ti
c-----find  istart:  istart is i index closest to the beam location--
      call findindx(x,11,xstart,istart)
C-----heat input on top surface, -----
      do 6001 i = 1,11
          xdist =xstart - x(i)
          do 6001 j = 1,m1
              dist = xdist**2+y(j)**2
              heatin(i,j) = pkint*exp(-2.0*dist/rb2)
c          heatin(i,j) = pkint*exp(-3.0*dist/rb2)
c          heatin(i,j) = pkint*exp(-dist/(2.0*rb2))
6001  topfl1 = topfl1 + xcv(i)*ycv(j)*heatin(i,j)
C-----define volumetric heat source-----
      call findindx(zw,n1,htv,khdep)
      call findindx(yv,m1,rbt,jhrad)
      xmxt = xstart+rbt
      call findindx(xu,11,xmxt,imxrad)
      xnxt = xstart-rbt
      call findindx(xu,11,xnxt,imnrad)
      do 6059 k=1,khdep-1
          do 6059 j=1,jhrad
              do 6059 i=imnrad,imxrad
                  xydist = sqrt(abs(x(i)-xstart)**2+y(j)**2)
                  if (xydist.le.rbt) volheat = volheat + xcv(i)*ycv(j)*zcv(k)
6059  continue
          denv=(1.0-fracg)*power*abscof/(volheat*2.0)
          do 6051 k=1,khdep-1
              do 6051 j=1,jhrad
                  do 6051 i=imnrad,imxrad
                      qin(i,j,k)=0.0
                      xydist = sqrt(abs(x(i)-xstart)**2+y(j)**2)
                      if (xydist.le.rbt) qin(i,j,k) = denv
6051  volheatin = volheatin+qin(i,j,k)*xcv(i)*ycv(j)*zcv(k)
c-----calculate emf field-----
          if ((yesarc.gt.0.5).and.(float(ksolve(1)).gt.0.9))
              1call emf(x,y,z,11,m1,n1,arccur,rb,scemfx,scemfy,scemfz,yesoldf,
                  lxstart,43,ni,nj,nk)
c-- write data used output in a file -----
          do 2400 igrop=1,nog
              imax=igroup(igrop)
              write (41,79) grname(igrop)
              write(41,4)
              do 2400 ii=1,imax
                  go to (241,242,243,244,245)igrop
241  write(41,279) ii,strfile(ii),filenames(ii)

```



```

    go to 2400
242  write(41,269)ii, strpro(ii), valpro(ii)
    go to 2400
243  write(41,269)ii, strphy(ii), valphy(ii)
    go to 2400
244  write(41,269)ii, strnsp(ii), valnsp(ii)
    go to 2400
245  write(41,269)ii, strbou(ii), valbou(ii)
2400  continue
c-----grid related output-----
    write(41,5)
    write(41,*)'x direction'
    write(41,166)strgeom(2),nzx
    do 1099 j=1,nzx
        write(41,169)strgeom(1),j, strgeom(3),xzone(j)
        write(41,168)strgeom(1),j, strgeom(4),ncvx(j)
1099  write(41,169)strgeom(1),j, strgeom(5),powrx(j)
        write(41,*)'y direction'
        write(41,166)strgeom(2),nzy
        do 1098 j=1,nzy
            write(41,169)strgeom(1),j, strgeom(3),yzone(j)
            write(41,168)strgeom(1),j, strgeom(4),ncvy(j)
1098  write(41,169)strgeom(1),j, strgeom(5),powry(j)
            write(41,*)'z direction'
            write(41,166)strgeom(2),nzz
            do 1097 j=1,nzz
                write(41,169)strgeom(1),j, strgeom(3),zzone(j)
                write(41,168)strgeom(1),j, strgeom(4),ncvz(j)
1097  write(41,169)strgeom(1),j, strgeom(5),powrz(j)
                iunit=41
                call tableout(l1,x,xu,' i=', ' x=', 'xu=',iunit)
                call tableout(m1,y,yv,' j=', ' y=', 'yv=',iunit)
                call tableout(n1,z,zw,' k=', ' z=', 'zw=',iunit)
            if (yesold.ge.0.5) call tools(start)
            do 6999 i=1,l1
                do 6999 j=1,m1
                    do 6999 k=1,n1
                        ake(i,j,k)=1
                        dis(i,j,k)=100
6999  continue
    return
c-- Variable density and other properties -----
    entry dense
    do 6002 i=1,l1-1
        do 6002 j=1,m1-1
            do 6002 k=1,n1-1
                if (yvarpr.gt.0.5) go to 7001
c Constant properties -----
-----
c-----thermal diffusivity-----
    if(t(i,j,k).ge.tliquid)diff(i,j,k)=factor*difl
    if(t(i,j,k).le.tsolid)diff(i,j,k)=difs
    if((t(i,j,k).lt.tliquid) .and. (t(i,j,k).gt.tsolid))
1diff(i,j,k)=frac1(i,j,k)*difl+(1.0-frac1(i,j,k))*difs

```

```

c-----viscosity-----
c-----turbulence amut=diff*prantle=diff*0.9
      amut(i,j,k)=amuf+difl*0.9
c      amut(i,j,k)=10.*amuf
      go to 6002
7001 continue
      xx=t(i,j,k)
c---viscosity-----
      amut(i,j,k)=factor*(0.030325-2.017e-5*xx+3.5417e-9*xx*xx)*10.0
c---thermal conductivity, specific heat and k/Cp of solid and liquid---
      if (h(i,j,k).le.hlfriz) then
        tks=(0.016*xx+8.8)*0.00239
        cps=(0.1357*xx+459.28)*0.239/1000
        diff(i,j,k)=tks/cps
      else
        tk1=(0.0036*xx+11.81)*0.00239
        cpl=790.0*0.239/1000
        diff(i,j,k)=tk1/cpl
      endif
6002 continue
c-- temperature calculation from the enthalpy values for iron block-----
      do 8001 i=1,11
        do 8001 j=1,m1
          do 8001 k=1,n1
            if (h(i,j,k)-hlcal)8002,8002,8003
8003   fracl(i,j,k)=1.0
            t(i,j,k)=(h(i,j,k)-hlcal)/acpl+tliquid
            go to 8001
8002   if(h(i,j,k).le.hsmelt) then
            fracl(i,j,k)=0.0
            t(i,j,k)=tsolid-(hsmelt-h(i,j,k))/acp
          else
            fracl(i,j,k)=(h(i,j,k)-hsmelt)/(hlcal-hsmelt)
            t(i,j,k)=deltemp*fracl(i,j,k) + tsolid
          endif
8001   continue
        return
      entry output
c      if(iter.eq.10)call tools(print)
      if (iter.le.ifinish) go to 3901
      topfl1=0.0
      do 3902 i=1,11
        do 3902 j=1,m1
          heatin(i,j)=0.0
          do 3902 k=1,11
3902   qin(i,j,k)=0.0
3901   continue
c-----length of the pool; includes both liq and liq+sol, i.e., mushy
region-
      do 9055 i=istart,11
        if (t(i,1,1).lt.tsolid) go to 9056
        imax=i
9055   continue
9056   dtbox = (t(imax,1,1)-t(imax+1,1,1))/(x(imax)-x(imax+1))

```

```

xxmax = (tsolid - t(imax,1,1))/dtdxx + x(imax)
do 9006 i=istart,1,-1
if (t(i,1,1).lt.tsolid) go to 9066
imin=i
9006 continue
9066 dtdxx = (t(imin,1,1)-t(imin-1,1,1))/(x(imin)-x(imin-1))
xxmin = (tsolid - t(imin,1,1))/dtdxx+x(imin)
alen=xxmax-xxmin
c-----depth of the pool-----
kmax = 0
do 9014 i=istart-5,imax
do 9024 k=2,n2
if (t(i,1,k).lt.tsolid) go to 9014
kmax=max(kmax,k)
9024 continue
9014 continue
depth = 0.0
do 9077 i=istart-5,imax
if (t(i,1,kmax).lt.tsolid) go to 9077
dtdzz = (t(i,1,kmax)-t(i,1,kmax+1))/(z(kmax)-z(kmax+1))
dep = (tsolid - t(i,1,kmax))/dtdzz+z(kmax)
depth=amax1(dep,depth)
9077 continue
c-----width of the pool-----
jmax = 0
do 9007 i=istart-5,imax
do 9008 j=2,m2
if (t(i,j,1).lt.tsolid) go to 9007
jmax=max(jmax,j)
9008 continue
9007 continue
width = 0.0
do 9017 i=istart-5,imax
if (t(i,jmax,1).lt.tsolid) go to 9017
dtdyy = (t(i,jmax,1)-t(i,jmax+1,1))/(y(jmax)-y(jmax+1))
wid = (tsolid - t(i,jmax,1))/dtdyy+y(jmax)
width=amax1(wid,width)
9017 continue
width = width*2.0
if (yvarpr.ge.0.5) then
C-----calculation of depths at different locations-----
do 9991 i=imin-3,imax+3
do 9991 j=2,jmax+3
do 9991 k=2,kmax+3
if ((t(i,j-1,k).gt.tsolid).and.(t(i,j+1,k).lt.tsolid)) then
width1(i,k)=y(j)
C write(*,*)i,j,k,depth1(i,j)
endif
9991 continue
endif
c-----end calculation of geometric parameters,calculate peak temp-----
tpeak=0.0
do 8005 i=1,11
do 8005 j=1,m1

```

```

8005  tpeak=amax1(tpeak,t(i,j,1))
      write(*,8089)iter,tpeak,rsmax,residu(7),depth,alen,width
c     lentmax,sument
c     write(*,*)inew,jnew,knew,entmax1,t(inew,jnew,knew)
c     l,h(inew,jnew,knew)
      open(unit=56,file='akeel')
      write(56,*)"iter,amut(14,3,3),ake(14,3,3),dis(14,3,3),u(14,3,3)"
      write(56,*)"iter,amut(14,3,3),ake(14,3,3),dis(14,3,3),u(14,3,3)"
      if ((iter/iwrite)*iwrite.ne.iter) go to 8006
c-----heat balance-----
      call data6(botfl,0.,frofl,0.,bacfl,0.,alefl,0.,rigfl,0.,topfl1,0.)
      do 8007 i=1,l1
      do 8007 j=1,m1
      botfl = botfl + xcv(i)*ycv(j)*fluxn1(i,j,7)
8007  topfl1 = topfl1 + xcv(i)*ycv(j)*heatin(i,j)
      topfl=topfl1+volheatin
      do 8008 i=1,l1
      do 8008 k=1,n1
      frofl = frofl + xcv(i)*zcv(k)*fluxj1(i,k,7)
8008  bacfl = bacfl + xcv(i)*zcv(k)*fluxm1(i,k,7)
      do 8009 j=1,m1
      do 8009 k=1,n1
      alefl = alefl + ycv(j)*zcv(k)*fluxi1(j,k,7)
8009  rigfl = rigfl + ycv(j)*zcv(k)*fluxl1(j,k,7)
      heatout = botfl+frofl+bacfl+alefl+rigfl
      ratio = heatout/topfl
      write(*,*)'-----'
      write(*,*)'HEAT OUT = ', heatout, 'IN = ',topfl,' RATIO = ',ratio
      write(*,*)'-----'
      write(*,8099)
8006  continue
      do 1066 i=1,l1
      do 1066 j=1,m1
      do 1066 k=1,n1
      if (t(i,j,k).gt.tsolid) go to 1066
      u(i,j,k)=0.0
      u(i+1,j,k)=0.0
      v(i,j,k)=0.0
      v(i,j+1,k)=0.0
      w(i,j,k)=0.0
      w(i,j,k+1)=0.0
1066  continue
      if (iter.ne.last) return
c-----tecplot output-----
      if (itecplt.eq.1) then
      open(unit=71,file=filenames(7))
      write(71,*) 'TITLE = "FLUID FLOW AND HEAT TRANSFER IN WELD POOL"'
      write(71,*) 'VARIABLES = "X", "Y", "Z", "TEM", "U", "V", "W",
1  "amut", "ake", "dis", "gen"'
      write(71,*) 'ZONE I=',l1,' J=',m1,' K=',n1,' F=POINT'
      do 9001 k=1,n1
      do 9001 j=1,m1
      do 9001 i=1,l1
9001  write(71,9099)x(i),y(j),z(k),t(i,j,k),u(i,j,k),v(i,j,k),w(i,j,k)

```

```

1  ,amut(i,j,k),ake(i,j,k),dis(i,j,k),gen(i,j,k)
endif
c-----maximum velocities-----
do 9010 i=imin,imax
do 9010 j=1,jmax
do 9010 k=1,kmax
umax=amax1(umax,abs(u(i,j,k)))
vmax=amax1(vmax,abs(v(i,j,k)))
9010 wmax=amax1(wmax,abs(w(i,j,k)))
call data5(valout(1),depth,valout(2),width,valout(3),alen,
lvalout(4),tpeak,valout(5),topfl)
call data5(valout(6),heatout,
lvalout(7),botfl,valout(8),bacfl,valout(9),alefl,valout(10),rigfl)
call data3(valout(11),rsmax,valout(12),smax,valout(13),ssum)
call data3(valout(14),umax,valout(15),vmax,valout(16),wmax)
call data2(valout(17),float(imin),valout(18),float(imax))
call data2(valout(19),float(jmax),valout(20),float(kmax))
call data1(valout(21),ratio)
write(41,4)
write(41,*)'          output'
write(41,4)
do 251 i=1,no
251 write(41,269)i, strout(i),valout(i)
write(41,4)
call tools(save)
4   format(2x,79('-'))
5   format(2x,79('-'),/15x,'grid related output',/2x,79('-'))
19  format(2x,a5,2x,a60,a2)
29  format(2x,a5,2x,a20,a2)
30  format(2x,a5,1x,i2,1x,a9,1x,a29,1x,a1,a8,a1)
39  format(2x,a30,1x,i2,a2)
49  format(2x,a5,1x,i2,1x,a34,/2x,79('-'))
59  format(2x,a5,1x,i2,1x,a9,1x,a40,a1,1pe10.3,a1)
69  format(2x,a5,1x,i1,1x,a38)
79  format(2x,79('-'),/15x,a40)
89  format(a30)
99  format(2x,a5,1x,i1,1x,a15,a40)
166 format(2x,a50,2x,i5)
168 format(2x,a5,i2,a40,2x,i5)
169 format(2x,a5,i2,a40,2x,e10.4)
269 format(2x,i5,2x,a50,2x,e12.6)
279 format(2x,i5,2x,a30,2x,a15)
8089 format(2x,i4,8(2x,1pe10.3))
8099 format('  ITER',5x,'TPEAK',7x,'RSMAX',7x,'RES(7)      Depth',
1  Length      Width')
9099 format(11(e14.4))
return
entry outflo
return
entry phi
c-----define gam(i,j) for enthalpy equation-----
if (nf.ne.7) go to 5200
do 5001 i=2,12
rhoscx=rhoscans/xcv(i)

```

```

do 5001 j=2,m2
do 5001 k=2,n2
gam(i,j,k)=diff(i,j,k)
c-----enthalpy equation time independent source terms, source term (1)
sc(i,j,k)=rhoscx*h(i-1,j,k)
sp(i,j,k)=-rhoscx
c-----source term (2) -----
rlbdx=rhoref*hlatnt/xcv(i)
rlbdy=rhoref*hlatnt/ycv(j)
rlbdz=rhoref*hlatnt/zcv(k)
flw=frac1(i,j,k)*fx(i)+frac1(i-1,j,k)*fxm(i)
fle=frac1(i+1,j,k)*fx(i+1)+frac1(i,j,k)*fxm(i+1)
fls=frac1(i,j,k)*fz(k)+frac1(i,j,k-1)*fzm(k)
fln=frac1(i,j,k+1)*fz(k+1)+frac1(i,j,k)*fzm(k+1)
flb=frac1(i,j,k)*fy(j)+frac1(i,j-1,k)*fym(j)
flf=frac1(i,j+1,k)*fy(j+1)+frac1(i,j,k)*fym(j+1)
sc(i,j,k)=sc(i,j,k)+rlbdx*(u(i,j,k)*flw-u(i+1,j,k)*fle)+
1 rlbdy*(v(i,j,k)*flb-v(i,j+1,k)*flf)+
1 rlbz*(w(i,j,k)*fls-w(i,j,k+1)*fln)
c-----source term (3) -----
5001 sc(i,j,k)=sc(i,j,k)+(flw-fle)*hlatnt*rhoscx
c-----source term due to droplet transfer-----
do 5044 i=2,l2
do 5044 j=2,m2
do 5044 k=2,n2
5044 sc(i,j,k)=sc(i,j,k)+qin(i,j,k)
c-----end source terms, begin boundary conditions--(front boundary)-----
do 5004 i=2,l2
do 5004 k=2,n2
kbcj1(i,k)=2
flxp(i,1,k)=0.0
flxc(i,1,k)=0.0
c-----back boundary----known temperature if kbcml = 1 -----
if (htcm1.gt.10.0) then
kbcml(i,k)=1
h(i,m1,k)=hml
else
kbcml(i,k)=2
flxc(i,m1,k)=-htcm1*(tsolid-298.0)+htcm1*hsmelt/acp
flxp(i,m1,k)=-htcm1/acp
endif
5004 continue
c-----left boundary-----
do 5003 j=2,m2
do 5003 k=2,n2
if (htcil.gt.10.0) then
kbcil(j,k)=1
h(1,j,k)=hil
else
kbcil(j,k)=2
flxc(1,j,k)=-htcil*(tsolid-298.0)+htcil*hsmelt/acp
flxp(1,j,k)=-htcil/acp
endif
c-----right boundary-----

```

```

    if (htcl1.gt.10.0) then
      kbcl1(j,k)=1
      h(l1,j,k)=h11
    else
      kbcl1(j,k)=2
      flxc(l1,j,k)=-htcl1*(tsolid-298.0)+htcl1*hsmelt/acp
      flxp(l1,j,k)=-htcl1/acp
    endif
5003 continue
c-----top boundary-----
do 5002 i=2,l2
do 5002 j=2,m2
  kbck1(i,j)=2
c-----energy from the heat source (F1)-----
  flxc(i,j,1) = heatin(i,j)
  flxp(i,j,1) = 0.0
c-----radiative heat loss (F2)-----
  if (emiss.gt.1.0e-3) then
    if (h(i,j,1).ge.hlcal) then
      const1 = sigems/acpl**4
      const2 = (tliquid - hlcal/acpl)*acpl
      terma = (h(i,j,1)+const2)**4
      termb = (h(i,j,1)+const2)**3
      fluxc = sigems*tamb4-const1*terma+4.0*const1*termb*h(i,j,1)
      fluxp = -4.0*const1*termb
    else
      if (h(i,j,1).lt.hsmelt) then
        const1 = sigems/acp**4
        const2 = (tsolid-hsmelt/acp)*acp
        terma = (h(i,j,1)+const2)**4
        termb = (h(i,j,1)+const2)**3
        fluxc = sigems*tamb4-const1*terma+4.0*const1*termb*h(i,j,1)
        fluxp = -4.0*const1*termb
      else
        cpavg = (acpl+acp)/2.0
        const1 = sigems/cpavg**4
        const2 = tsolid*cpavg
        terma = (h(i,j,1)+const2)**4
        termb = (h(i,j,1)+const2)**3
        fluxc = sigems*tamb4-const1*terma+4.0*const1*termb*h(i,j,1)
        fluxp = -4.0*const1*termb
      endif
    endif
    flxc(i,j,1)=flxc(i,j,1)+fluxc
    flxp(i,j,1)=flxp(i,j,1)+fluxp
  endif
c-----convective heat loss (F3)-----
  if (htck1.lt.10.) then
    if (h(i,j,1).ge.hlcal) then
      flxc(i,j,1)=-htck1*(tliquid-298.)+htck1*hlcal/acpl+flxc(i,j,1)
      flxp(i,j,1)=-htck1/acpl+flxp(i,j,1)
    else
      if (h(i,j,1).lt.hsmelt) then
        flxc(i,j,1)=-htck1*(tsolid-298.)+htck1*hsmelt/acp+flxc(i,j,1)

```

```

    flxp(i,j,1)=-htck1/acp+flxp(i,j,1)
  else
    flxc(i,j,1)= -htck1*(tsolid-298.0) + flxc(i,j,1)
    flxp(i,j,1) = -htck1/cpavg + flxp(i,j,1)
  endif
endif
endif
c-----bottom boundary-----
  if (htcn1.gt.10.0) then
    kbcn1(i,j)=1
    h(i,j,n1)=hn1
  else
    kbcn1(i,j)=2
    flxc(i,j,n1)=-htcn1*(tsolid-298.0)+htcn1*hsmelt/acp
    flxp(i,j,n1)=-htcn1/acp
  endif
5002 continue
c-----edge boundary: intersecting front and top plane-----
do 5033 i=2,12
5033 h(i,1,1)=h(i,2,1)
5200 continue
c---- define gam(i,j,k) for momentum equations-----
  if (nf.gt.3) goto 6000
  do 5501 i=2,12
  do 5501 j=2,m2
  do 5501 k=2,n2
5501 gam(i,j,k)=amut(i,j,k)
c-----source term for mushy resgion:Karman-Kauzeny approximation-----
  do 5400 k=kst,n2
  do 5400 j=jst,m2
  do 5400 i=ist,12
5400 sp(i,j,k)=-1.6e4*(1.0-fracl(i,j,k))**2/(fracl(i,j,k)**3+1.0e-3)
c-----boundary conditions for u momentum equation, source term-----
  if (nf.ne.1) go to 5500
  call tools(usor)
  do 1004 i=ist,12
  do 1004 j=jst,m2
  do 1004 k=kst,n2
  rsarea = rhoscan/xdif(i)
  asc =rsarea*u(i-1,j,k)
  asp = -rsarea
  if(u(i,j,k).ge.0.0)go to 1003
  asp =0.
  asc=rsarea*(u(i,j,k)-u(i+1,j,k))
1003 sc(i,j,k) = sc(i,j,k) + asc
1004 sp(i,j,k) = sp(i,j,k) + asp
c-----electromagnetic force-----
  if (yesarc.gt.0.5) then
  do 5402 i=imin-2,imax+2
  do 5402 j=jst,jmax+2
  do 5402 k=kst,kmax+2
5402 sc(i,j,k)=sc(i,j,k)+scemfx(i,j,k)
  endif
c-----top boundary (u momentum, shear stress, kbck1 = 1 by default)--

```



```

do 5404 i=imin-2,imax+2
do 5404 j=2,jmax+2
dtdx = (t(i,j,1)-t(i-1,j,1))/xdif(i)
if (wtpct.gt.1e-5) then
tav=t(i,j,1)*fx(i)+t(i-1,j,1)*fxm(i)
if(tav.gt.tsolid) dgdt=surten(tav,wtpct,ac,gamsat,entfac,enthse)
endif
5404 u(i,j,1)=u(i,j,2)+frac1(i,j,1)*dgdt*dtdx*zdif(2)/amut(i,j,2)
c- ---front boundary (plane of symmetry)-----
do 5403 i=1,l1
do 5403 k=1,n1
5403 kbcj1(i,k)=2
5500 continue
c-----v momentum boundary conditions-----
if (nf.ne.2) go to 4001
call tools(vsor)
do 1006 i=ist,l2
do 1006 j=jst,m2
do 1006 k=kst,n2
rsarea = rhoscan/xcv(i)
asc = rsarea*(v(i+1,j,k)-v(i,j,k))
asp = 0.
sc(i,j,k) = sc(i,j,k) + asc
1006 sp(i,j,k) = sp(i,j,k) + asp
c-----electromagnetic field-----
do 502 i=imin-2,imax+2
do 502 j=jst,jmax
do 502 k=kst,kmax
502 sc(i,j,k)=sc(i,j,k)+scemfy(i,j,k)
c-----top boundary (shear stress, kbck1 = 1 by default)-----
do 504 i=imin-2,imax+2
do 504 j=2,jmax+2
dtdy = (t(i,j,1)-t(i,j-1,1))/ydif(j)
if (wtpct.gt.1e-5) then
tav=t(i,j,1)*fy(j)+t(i,j-1,1)*fym(j)
if(tav.gt.tsolid) dgdt=surten(tav,wtpct,ac,gamsat,entfac,enthse)
endif
504 v(i,j,1)=v(i,j,2)+frac1(i,j,1)*dgdt*dtdy*zdif(2)/amut(i,j,2)
c-----front boundary (v momentum, by default kbcj1 = 1)-----
4001 continue
c-----w momentum source terms and boundary conditions-----
if (nf.ne.3) goto 6000
call tools(wsor)
do 1008 i=ist,l2
do 1008 j=jst,m2
do 1008 k=kst,n2
rsarea = rhoscan/xcv(i)
asc = rsarea*(w(i+1,j,k)-w(i,j,k))
asp = 0.
sc(i,j,k) = sc(i,j,k)+asc
1008 sp(i,j,k) = sp(i,j,k)+asp
c-----electromagnetic source-----
do 602 i=imin-2,imax+2
do 602 j=jst,jmax+2

```

```

do 602 k=kst,kmax+2
c-----bouyancy source-----
602  sc(i,j,k)=sc(i,j,k)+scemfz(i,j,k)-boufac*(t(i,j,k)-tsolid)
c-----top boundary (w momentum, kbcnl=1 by default)-----
c-----front boundary (w momentum)-----
do 604 i=imin-2,imax+2
do 604 k=2,kmax+2
604  kbcj1(i,k)=2
6000 continue
if (nf.ne.9) goto 7000
call tools(ksor)
do 5111 k=kst,n2
do 5111 j=jst,m2
do 5111 i=ist,l2
amutt=0.09*rhoref*ake(i,j,k)**2/dis(i,j,k)
amut(i,j,k)=amut(i,j,k)+0.1*(amutt-amut(i,j,k))
if(frac1(i,j,k).gt.0.001) then
gam(i,j,k)=amut(i,j,k)/1.0
sc(i,j,k)=amut(i,j,k)*gen(i,j,k)
sp(i,j,k)=-rhoref*dis(i,j,k)/ake(i,j,k)
else
gam(i,j,k)=1.0e30
sc(i,j,k)=0
sp(i,j,k)=0
c  sp(i,j,k)=-1.6e4*(1.0-frac1(i,j,k))**2/(frac1(i,j,k)**3+1.0e-3)
endif
5111 continue
write(*,*)"gam(14,3,3),ake(14,3,3),sc(14,3,3),sp(14,3,3),
1gen(14,3,3),amut(14,3,3),dis(14,3,3),u(14,3,3)"
write(*,*)gam(14,3,3),ake(14,3,3),sc(14,3,3),sp(14,3,3),
1gen(14,3,3),amut(14,3,3),dis(14,3,3),u(14,3,3)
do 5103 i=1,l1
do 5103 k=1,n1
5103 kbcj1(i,k)=2
do 5104 i=1,l1
do 5104 j=1,m1
ake(i,j,1)=0.5*0.03*(u(i,j,1)**2+v(i,j,1)**2)
5104 kbck1(i,j)=1
7000 continue
if (nf.ne.10) return
call tools(esor)
do 5112 k=kst,n2
do 5112 j=jst,m2
do 5112 i=ist,l2
amutt=0.09*rhoref*ake(i,j,k)**2/dis(i,j,k)
amut(i,j,k)=amut(i,j,k)+0.1*(amutt-amut(i,j,k))
if(frac1(i,j,k).gt.0.001) then
gam(i,j,k)=amut(i,j,k)/1.3
sc(i,j,k)=1.44*amut(i,j,k)*gen(i,j,k)*dis(i,j,k)/ake(i,j,k)
sp(i,j,k)=-1.92*rhoref*dis(i,j,k)/ake(i,j,k)
else
gam(i,j,k)=1.0e30
sc(i,j,k)=0
sp(i,j,k)=0

```

```

c      sp(i,j,k)=-1.6e4*(1.0-fracl(i,j,k))**2/(fracl(i,j,k)**3+1.0e-3)
      endif
5112 continue
      write(*,*)"dis(14,3,3),sc(14,3,3),sp(14,3,3),ake(14,3,3)"
      write(*,*) dis(14,3,3),sc(14,3,3),sp(14,3,3),ake(14,3,3)
      do 5102 i=1,l1
      do 5102 k=1,n1
5102 kbcj1(i,k)=2
      do 5105 i=1,l1
      do 5105 j=1,m1
      dis(i,j,1)=ake(i,j,1)**1.5/(0.3*0.7)
5105 kbck1(i,j)=1
      write(*,*)"ake(14,3,1),dis(14,3,1),u(14,3,1),v(14,3,1)"
      write(*,*)ake(14,3,1),dis(14,3,1),u(14,3,1),v(14,3,1)
      return
      entry lc
      if (nf.ne.7) return
      sument=0.0
      entmax=0.0
      entmax1=0.0
      do 1091 i=ist,l2
      do 1091 j=jst,m2
      do 1091 k=kst,n2
      term1=aip(i,j,k)*h(i+1,j,k)+ajp(i,j,k)*h(i,j+1,k)
1      +akp(i,j,k)*h(i,j,k+1)
      term2=aim(i,j,k)*h(i-1,j,k)+ajm(i,j,k)*h(i,j-1,k)
1+akm(i,j,k)*h(i,j,k-1)
      term3=con(i,j,k)-ap(i,j,k)*h(i,j,k)
      renew(i,j,k)=term1+term2+term3
      entmax=amax1(entmax,abs(renew(i,j,k)))
      sument=sument+abs(renew(i,j,k))
1091 continue
c      do 1092 i=imin-5,imax+5
c      do 1092 j=2,jmax+4
c      do 1092 k=2,kmax+4
      do 1092 i=2,l2
      do 1092 j=2,m2
      do 1092 k=2,n2
      if (abs(renew(i,j,k)).gt.entmax1) then
          entmax1=abs(renew(i,j,k))
          inew=i
          jnew=j
          knew=k
      endif
1092 continue
      return
      include '/home/CFD/COMP3D/FINISH3.FOR'
      end

```

## 2) Program turb.f

```

      subroutine adapt
      parameter(ni=70,nj=70,nk=70,nfmax=11,idblk=100,kunstd=1,
1nf2=(1+kunstd)*nfmax, nzm=10,idim=2*(ni*nj+nj*nk+ni*nk))
c      nx: maximum of nzx,nzy and nzz (number of zones in three
directions)
      parameter(nog=5,nz=8,nq=14,np=18,nu=13,no=26,nbg=10,nzmax=10,ng=5)
      include '/home/CFD/COMP3D/ADPT3.FOR'
      include '/home/CFD/COMP3D/COMP3D.FOR'
      save
      dimension igrp(nog),valpro(nq),valphy(np),valnsp(nu),
1valbou(nbg),valout(no)
      dimension amuff(ni,nj,nk),diff(ni,nj,nk),dudy1(ni,nj,nk)
      dimension t(ni,nj,nk),h(ni,nj,nk),frac1(ni,nj,nk),hold(ni,nj,nk),
1frac1old(ni,nj,nk),apsum(ni,nj,nk)
      dimension heatin(ni,nj),qin(ni,nj,nk),factor2(ni,nj,nk),
1luv(ni,nj,nk)
      dimension scemfx(ni,nj,nk),scemfy(ni,nj,nk),scemfz(ni,nj,nk)
      dimension xyzo(nzmax,3),nxyz(nzmax,3),pxyz(nzmax,3),nzone(3)
      dimension renew(ni,nj,nk),width1(ni,nk),r1(ni,nj,nk),r2(ni,nj,nk)
      dimension ake(ni,nj,nk),dis(ni,nj,nk),amut(ni,nj,nk)
      equivalence (f(1,1,1,6),t(1,1,1)),(f(1,1,1,7),h(1,1,1)),
1(f(1,1,1,nfmax+7),hold(1,1,1)),(f(1,1,1,8),frac1(1,1,1)),
1(f(1,1,1,nfmax+8),frac1old(1,1,1)),(f(1,1,1,9),
1ake(1,1,1)),(f(1,1,1,10),dis(1,1,1)),(f(1,1,1,11),amut(1,1,1))
c-----nzone(i or j or k): number of zones in i or j or k direction
c-----xyzo(i or j or k): length of different zones in i or j or k
direction
c-----nxyz(i or j or k): number of control volumes in different zones
c-----pxyz(i or j or k): exponential factor for different zones
      equivalence (nzone(1),nzx),(nzone(2),nzy),(nzone(3),nzz),
1(xyzo(1,1),xzone(1)),(xyzo(1,2),yzone(1)),(xyzo(1,3),zzone(1)),
2(nxyz(1,1),ncvx(1)),(nxyz(1,2),ncvy(1)),(nxyz(1,3),ncvz(1)),
3(pxyz(1,1),powrx(1)),(pxyz(1,2),powry(1)),(pxyz(1,3),powrz(1))
      character*60 grname(nog),strfile(nz),strpro(nq),
1strphy(np),strnsp(nu),strgeom(ng),strout(no),strbou(nbg)
      character*30 filenames(nz)
      data igrp/nz,nq,np,nu,nbg/
      data grname/'filenames','processes parameters','material propertie
1s','numerical scheme parameters','boundary conditions'/
c-----group 1 input data-----
      data strfile/'output file name','plot file name','print file name'
1,'start file name','save file name','grid input filename','tecplot
1 file name','emf field file name'/
      data filenames/'output','plot','print','start','start','grid',
1'tecout','field'/
c-----group 2 input data: process parameters and their default values-----
      data strpro/'laser power (Watts)','absorption coefficient','beam/a
1rc radius (cm)','scanning velocity (cm/sec)','starting location of
1 beam','to arc welding (yes:1, no:0)','arc current (Amp)','arc vol
1tage (Volts)','arc efficiency (%)','starting emf field (yes:1,no:0
1)','fraction of energy received from arc','radius of volumetric he
1at source (cm)','height of volumetric heat source (cm)','# of iter

```

```

ls after which power is set to 0'/
  data valpro/60..2,.25,0.17,4.7,1,150.,11.0,75.,0,1.0,.1,.3,2000./
c-- Group 3 input data: material properties and their default values ---
  data strphy/'liquidus temperature (K)', 'density of liquid metal (g
  lm/cm**3)', 'enthalpy of solid at mp (cal/gm)', 'enthalpy of liquid a
  lt mp (cal/gm)', 'specific heat of solid (cal/gm-K)', 'specific heat
  lof liquid (cal/gm-K)', 'thermal cond of solid (cal/cm-sec-K)', 'ther
  mal cond of liq (cal/cm-sec-K)', 'viscosity of liquid (gm/cm-sec)',
  1'd(gamma)/dT, pure mat ( dynes/cm-K)', 'conc. of surface active
species
  1(wt%)', 'enthalpy of segregation (J/mole)', 'surface excess at sat
  1(mole/cm**2)', 'entropy factor', 'to variable properties (yes:1, no:
  10)', 'coeff of thermal expansion (1/K)', 'solidus temperature (K)'
  1, 'emissivity of the material'/
  data valphy/1785.0,7.2,250.76,314.76,0.168,0.193,0.06,0.2,0.06,
  10.43,0.0,-1.66e5,1.30e-9,0.00318,0.0,1.0e-5,1745.0,0.0/
c-- Group 4 input data: default values of numerical scheme parameters---
  data strnsp/'velocity relaxation parameter', 'pressure relaxation p
  larameter', 'enthalpy relaxation parameter', 'latent heat relaxation
  lparameter', 'k relaxiation parameter', 'e relaxation parameter',
  1'time increment', 'number of iterations', 'maximum number
  1 of cycles per time step', 'iter interval for overall heat balance'
  1, 'index to start from oldfile(yes:1,no:0)', 'index to solve momentu
  lm eqns(yes:1,no:0)', 'index to write tecplot file(yes:1,no:0)'/
  data valnsp/.8,.8,1.,.8,0.5,0.5,1e20,40,1.,5.,.0,1.,1./
c----group 5 input data : default values of the boundary conditions-----
  data strbou/'temperature at i=1 boundary (K)', 'temperature at i=11
  1 boundary (K)', 'temperature at j=m1 boundary', 'temperature at k=n1
  1 boundary (k)', 'heat transfer coeff at i=1(cal/cm2-s-K)', 'heat tra
  nsfer coeff at i=11(cal/cm2-s-K)', 'heat transfer coeff at j=m1(cal
  1/cm2-s-K)', 'heat transfer coeff at k=n1(cal/cm2-s-K)', 'heat transf
  ler coeff at k=1(cal/(cm2-s-k)', 'preheat temperature (K)'/
  data valbou/298.0,298.0,298.0,298.0,100.0,100.0,100.0,100.0,00.0,
  1298.0/
c----group 6: grid data-----
-----
  data strgeom/'zone(', 'number of zones', ' )length', ' )number of con
  trol volumes', ' )exponential factor'/
c----Group 7: output data-----
  data strout/'depth of the pool (cm)', 'width of the pool (cm)', 'len
  lgth of the pool (cm)', 'cross section area (cm2)', 'peak temperature
  1', 'heat input rate (cal/s)', 'heat output rate (cal/s)', 'heat flow
  lat n1', 'heat flow at m1', 'heat flow at i1', 'heat flow at l1', 'RSMA
  1X', 'SMAX', 'SSUM', 'UMAX', 'VMAX', 'WMAX', 'IMIN', 'IMAX', 'JMAX', 'KMAX',
  1'ratio(Heat In/Heat Out)', 'ratio1(Ave. (amut/amuf))', 'ratio2(Ave. (d
  lift/difl))', 'maxr1(max amut/amuf)', 'maxr2(max dift/difl)'/
  entry check
  iread=0
  return
  entry grid
10  nogpl=nog+1
    do 11 i=1,nog
11  write(6,99)'Enter',i,'to change/view ',grname(i)
    write(6,69)'Enter',nogpl,'to do calculations with current values'

```

```

c-- Select a data group to view/change data -----
  write(6,4)
  write(*,*)'      Please enter your choice (1 to 6):'
  read(*,*) igrop
  if(igrop.eq.nogp1) go to 51
c-- On screen viewing of parameter values in a selected data group -----
  write (6,79) grname(igrop)
  imax=igroup(igrop)
21  write(6,4)
  do 40 i=1,imax
  goto(31,32,33,34,35)igrop
31  write(*,30)'Enter',i,'to change',strfile(i),'(',filenames(i),')'
  go to 40
32  write(*,59)'Enter',i,'to change',strpro(i),'(',valpro(i),')'
  go to 40
33  write(*,59)'Enter',i,'to change',strphy(i),'(',valphy(i),')'
  go to 40
34  write(*,59)'Enter',i,'to change',strnsp(i),'(',valnsp(i),')'
  go to 40
35  write(*,59)'Enter',i,'to change',strbou(i),'(',valbou(i),')'
40  continue
  imaxpl=imax+1
  write(6,49)'Enter',imaxpl,'if all values in this group are ok'
c-- Decide if some of the values need to be changed -----
  write(6,39) 'Please enter your choice (1 to',imaxpl,'):'
  read(*,*)  ichange
  if(ichange.eq.imaxpl) go to 10
c-- Change parameter value -----
  goto (41,42,43,44,45) igrop
41  write(6,29)'Enter',strfile(ichange),': '
  read(5,89) filenames(ichange)
  go to 21
42  write(6,19)'Enter',strpro(ichange),': '
  read(5,*)valpro(ichange)
  go to 21
43  write(6,19)'Enter',strphy(ichange),': '
  read(5,*)valphy(ichange)
  go to 21
44  write(6,19)'Enter',strnsp(ichange),': '
  read(5,*)valnsp(ichange)
  go to 21
45  write(6,19)'Enter',strbou(ichange),': '
  read(5,*)valbou(ichange)
  go to 21
c-- end data input -----
51  call name3(plotf,filenames(2),startf,filenames(4),
  lsavef,filenames(5))
c---user friendly names for process parameters-----
  call data7(power,valpro(1),abscof,valpro(2),rb,valpro(3),scanvel,
  lvalpro(4),xstart,valpro(5),yesarc,valpro(6),arccur,valpro(7))
  call data5(arcvol,valpro(8),yesoldf,valpro(10),fracg,valpro(11),
  lrbt,valpro(12),htv,valpro(13))
  call intal(ifinish,int(valpro(14)))
  if (yesarc.lt.0.5) go to 12

```

```

      abscof=valpro(9)/100.0
      power=arccur*arcvol
c---user friendly names for physical properties -----
12   call data3(tliquid, valphy(1), rhoref, valphy(2), ac, valphy(10))
      call data3(wtpct, valphy(11), enthse, valphy(12), gamsat, valphy(13))
      call data3(entfac, valphy(14), yvarpr, valphy(15), beta, valphy(16))
      call data3(hsmelt, valphy(3), hlfriz, valphy(4), acp, valphy(5))
      call data2(acpl, valphy(6), amuf, valphy(9))
      call data3(tsolid, valphy(17), dgdt, valphy(10), emiss, valphy(18))
      difs=valphy(7)/acp
      if (yvarpr.lt.0.5) then
        difl=valphy(8)/acpl
      else
        difl=valphy(8)/acpl
      endif
c-- user friendly names for numerical scheme parameters -----
      call data6(relax(1), valnsp(1), relax(2), valnsp(1), relax(3), valnsp(1),
        relax(4), valnsp(2), relax(7), valnsp(3), relax(8), valnsp(4))
      call data2(relax(9), valnsp(5), relax(10), valnsp(6))
      call data2(dt, valnsp(7), yesold, valnsp(11))
      call inta5(last, int(valnsp(8)), itmax, int(valnsp(9)), iwrite,
        lint(valnsp(10)), isol, int(valnsp(12)), itecplt, int(valnsp(13)))
c---user friendly names for geometric parameters-----
      call inta2(mode, 1, kdisk, 1)
      call data3(xu(2), 0., yv(2), 0., zw(2), 0.)
c---user friendly names for boundary conditions-----
      call data3(til, valbou(1), t11, valbou(2), tml, valbou(3))
      call data3(tnl, valbou(4), htcl1, valbou(5), htcl1, valbou(6))
      call data3(htcm1, valbou(7), htcn1, valbou(8), htck1, valbou(9))
      call data1(ti, valbou(10))
c-----open required files-----
      open (unit=41, file=filenames(1))
      open (unit=7, file=filenames(3))
      open (unit=42, file=filenames(6))
      if (yesarc.gt.0.5) open (unit=43, file=filenames(8))
c-----grid generation-----
      do 910 ijk=1,3
        read(42,*)nzone(ijk)
        read(42,*) (xyzo(i,ijk), i=1,nzone(ijk))
        read(42,*) (nxyz(i,ijk), i=1,nzone(ijk))
910    read(42,*) (pxyz(i,ijk), i=1,nzone(ijk))
        call tools(zgrid)
c-----default starting location of the beam-----
      if (xstart.eq.0) xstart=xzone(2)+xzone(1)
      valpro(5)=xstart
      return
      entry begin
      call inta4(kprint(1), 1, kprint(2), 1, kprint(6), 1, kprint(11), 1)
      call inta3(kpmax, 2, kpln(1), 1, kpln(2), 2)
      call name2(title(6), ' temperature ', title(7), ' enthalpy')
      call name1(title(8), 'fraction liquid ')
c-----calculation of some constant parameters-----
      restd=1.0e-7
      crit(7)=1.0e-7

```

```

pi=3.1415297
kord = 2
rb2 = rb**2
rbt2 = rbt**2
pkint = fracg*2.0*power*abscof*0.239/(pi*rb2)
c   pkint = fracg*3.0*power*abscof*0.239/(pi*rb2)
c   pkint = fracg*power*abscof*0.239/(2.0*pi*rb2)
deltemp = tliquid - tsolid
cpavg = (acp+acpl)/2.0
hlcal = hsmelt+cpavg*deltemp
hlatnt = hlfriz - hlcal
boufac = rhoref*980.0*beta
rhoscan = rhoref*scanvel
sigems = emiss*5.67E-12*0.239
tamb4 = 298.0**4
acpl4 = acpl**4
acp4 = acp**4
nvk=9
nvd=10
if (isol.ne.1) go to 111
do 110 nff=1,10
ksolve(nff)=1
110 kbloc(nff)=1
111 call inta3(ksolve(6),0,ksolve(8),0,ksolve(7),1)
hi = (ti-tsolid)*acp+hsmelt
hl1 = (tl1-tsolid)*acp+hsmelt
hil = (til-tsolid)*acp+hsmelt
hml = (tml-tsolid)*acp+hsmelt
hnl = (tnl-tsolid)*acp+hsmelt
do 102 i=1,11
do 102 j=1,m1
do 102 k=1,n1
u(i,j,k)=0.0
v(i,j,k)=0.0
w(i,j,k)=0.0
rho(i,j,k)=rhoref
amut(i,j,k)=amuf
amuff(i,j,k)=amuf
diff(i,j,k)=difl
ake(i,j,k)=1
dis(i,j,k)=10
h(i,j,k)=hi
hold(i,j,k)=hi
102 t(i,j,k)=ti
c-----find  istart:  istart is i index closest to the beam location--
call findindx(x,11,xstart,istart)
C-----heat input on top surface, -----
do 6001 i = 1,11
xdist =xstart - x(i)
do 6001 j = 1,m1
dist = xdist**2+y(j)**2
heatin(i,j) = pkint*exp(-2.0*dist/rb2)
c   heatin(i,j) = pkint*exp(-3.0*dist/rb2)
c   heatin(i,j) = pkint*exp(-dist/(2.0*rb2))

```



```

6001 topfl1 = topfl1 + xcv(i)*ycv(j)*heatin(i,j)
C-----define volumetric heat source-----
    call findindx(zw,n1,htv,khdep)
    call findindx(yv,m1,rbt,jhrad)
    xmxt = xstart+rbt
    call findindx(xu,l1,xmxt,imxrad)
    xnxt = xstart-rbt
    call findindx(xu,l1,xnxt,imnrad)
    do 6059 k=1,khdep-1
    do 6059 j=1,jhrad
    do 6059 i=imnrad,imxrad
    xydist = sqrt(abs(x(i)-xstart)**2+y(j)**2)
    if (xydist.le.rbt) volheat = volheat + xcv(i)*ycv(j)*zcv(k)
6059 continue
    denv=(1.0-fracg)*power*abscof*0.239/(volheat*2.0)
    do 6051 k=1,khdep-1
    do 6051 j=1,jhrad
    do 6051 i=imnrad,imxrad
    qin(i,j,k)=0.0
    xydist = sqrt(abs(x(i)-xstart)**2+y(j)**2)
    if (xydist.le.rbt) qin(i,j,k) = denv
6051 volheatin = volheatin+qin(i,j,k)*xcv(i)*ycv(j)*zcv(k)
c----calculate emf field-----
    if ((yesarc.gt.0.5).and.(float(ksolve(1)).gt.0.9))
    lcall emf(x,y,z,l1,m1,n1,arccur,rb,scemfx,scemfy,scemfz,yesoldf,
    lxstart,43,ni,nj,nk)
c-- write data used output in a file -----
    do 2400 igrop=1,nog
    imax=igroup(igrop)
    write(41,79) grname(igrop)
    write(41,4)
    do 2400 ii=1,imax
    go to (241,242,243,244,245) igrop
241 write(41,279) ii, strfile(ii), filenames(ii)
    go to 2400
242 write(41,269) ii, strpro(ii), valpro(ii)
    go to 2400
243 write(41,269) ii, strphy(ii), valphy(ii)
    go to 2400
244 write(41,269) ii, strnsp(ii), valnsp(ii)
    go to 2400
245 write(41,269) ii, strbou(ii), valbou(ii)
2400 continue
c-----grid related output-----
    write(41,5)
    write(41,*) 'x direction'
    write(41,166) strgeom(2), nzx
    do 1099 j=1,nzx
    write(41,169) strgeom(1), j, strgeom(3), xzone(j)
    write(41,168) strgeom(1), j, strgeom(4), ncvx(j)
1099 write(41,169) strgeom(1), j, strgeom(5), powrx(j)
    write(41,*) 'y direction'
    write(41,166) strgeom(2), nzy
    do 1098 j=1,nzy

```

```

write(41,169)strgeom(1),j,strgeom(3),yzone(j)
write(41,168)strgeom(1),j,strgeom(4),ncvy(j)
1098 write(41,169)strgeom(1),j,strgeom(5),powry(j)
write(41,*)'z direction'
write(41,166)strgeom(2),nzz
do 1097 j=1,nzz
write(41,169)strgeom(1),j,strgeom(3),zzone(j)
write(41,168)strgeom(1),j,strgeom(4),ncvz(j)
1097 write(41,169)strgeom(1),j,strgeom(5),powrz(j)
iunit=41
call tableout(11,x,xu,' i=', ' x=', 'xu=',iunit)
call tableout(m1,y,yv,' j=', ' y=', 'yv=',iunit)
call tableout(n1,z,zw,' k=', ' z=', 'zw=',iunit)
if (yesold.ge.0.5) call tools(start)
return
c-- Variable density and other properties -----
entry dense
do 6002 i=1,l1-1
do 6002 j=1,m1-1
do 6002 k=1,n1-1
if (yvarpr.gt.0.5) go to 7001
c Constant properties -----
amuff(i,j,k)=amuf
if(t(i,j,k).ge.tliquid)diff(i,j,k)=difl
if(t(i,j,k).le.tsolid)diff(i,j,k)=difs
if((t(i,j,k).lt.tliquid) .and. (t(i,j,k).gt.tsolid))
ldiff(i,j,k)=frac1(i,j,k)*difl+(1.0-frac1(i,j,k))*difs
go to 6002
7001 continue
c Variable properties -----
c---Turbulent viscosity -----
amutt=0.09*rhoref*ake(i,j,k)**2/(dis(i,j,k)+1.0e-15)
amut(i,j,k)=amut(i,j,k)+0.3*(amutt-amut(i,j,k))
amuff(i,j,k)=amuf+amut(i,j,k)
c---thermal conductivity, specific heat and k/Cp of solid and liquid----
if(frac1(i,j,k).le.0.001) then
tk=(0.016*T(i,j,k)+8.8)*0.00239
cps=(0.1357*T(i,j,k)+459.28)*0.239/1000.0
diff(i,j,k)=difs
else
difftt=amut(i,j,k)/0.9
diff(i,j,k)=diff(i,j,k)+0.8*(difftt-diff(i,j,k))
diff(i,j,k)=difl+diff(i,j,k)
endif
6002 continue
c-- temperature calculation from the enthalpy values for iron block-----
do 8001 i=1,l1
do 8001 j=1,m1
do 8001 k=1,n1
if (h(i,j,k)-hlcal)8002,8002,8003
8003 frac1(i,j,k)=1.0
t(i,j,k)=(h(i,j,k)-hlcal)/acpl+tliquid
go to 8001
8002 if(h(i,j,k).le.hsmelt) then

```

```

      fracl(i,j,k)=0.0
      t(i,j,k)=tsolid-(hsmelt-h(i,j,k))/acp
      else
      fracl(i,j,k)=(h(i,j,k)-hsmelt)/(hcal-hsmelt)
      t(i,j,k)=deltemp*fracl(i,j,k) + tsolid
      endif
8001  continue
      return
      entry output
      if (iter.le.ifinish) go to 3901
      topfl1=0.0
      do 3902 i=1,11
      do 3902 j=1,m1
      heatin(i,j)=0.0
      do 3902 k=1,11
3902  qin(i,j,k)=0.0
3901  continue
c-----length of the pool; includes both liq and liq+sol, i.e., mushy
region-
      do 9055 i=istart,11
      if (t(i,1,1).lt.tsolid) go to 9056
      imax=i
9055  continue
9056  dtdxx = (t(imax,1,1)-t(imax+1,1,1))/(x(imax)-x(imax+1))
      xxmax = (tsolid - t(imax,1,1))/dtdxx + x(imax)
      do 9006 i=istart,1,-1
      if (t(i,1,1).lt.tsolid) go to 9066
      imin=i
9006  continue
9066  dtdxx = (t(imin,1,1)-t(imin-1,1,1))/(x(imin)-x(imin-1))
      xxmin = (tsolid - t(imin,1,1))/dtdxx+x(imin)
      alen=xxmax-xxmin
c-----depth of the pool-----
      kmax = 0
      do 9014 i=istart-5,imax
      do 9024 k=2,n2
      if (t(i,1,k).lt.tsolid) go to 9014
      kmax=max(kmax,k)
9024  continue
9014  continue
      depth = 0.0
      do 9077 i=istart-5,imax
      if (t(i,1,kmax).lt.tsolid) go to 9077
      dtdzz = (t(i,1,kmax)-t(i,1,kmax+1))/(z(kmax)-z(kmax+1))
      dep = (tsolid - t(i,1,kmax))/dtdzz+z(kmax)
      depth=amax1(dep,depth)
9077  continue
c-----width of the pool-----
      jmax = 0
      do 9007 i=istart-5,imax
      do 9008 j=2,m2
      if (t(i,j,1).lt.tsolid) go to 9007
      jmax=max(jmax,j)
9008  continue

```

```

9007 continue
width = 0.0
do 9017 i=istart-5,imax
if (t(i,jmax,1).lt.tsolid) go to 9017
dtdyy = (t(i,jmax,1)-t(i,jmax+1,1))/(y(jmax)-y(jmax+1))
wid = (tsolid - t(i,jmax,1))/dtdyy+y(jmax)
width=amax1(wid,width)
9017 continue
width = width*2.0
c-----across section area of the pool-----
areacs=0.0
do 9029 i=istart-5,imax
areacs0=0.0
do 9019 j=2,m2
do 9019 k=2,n2
if (t(i,j,k).lt.tsolid) go to 9019
areacs0=areacs0+ycv(j)*zcv(k)
9019 continue
areacs=amax1(areacs,areacs0)
9029 continue
areacs=areacs*2.0
c-----end calculation of geometric parameters,calculate peak temp-----
tpeak=0.0
do 8005 i=1,l1
do 8005 j=1,m1
8005 tpeak=amax1(tpeak,t(i,j,1))
write(*,8089)iter,tpeak,rsmx,residu(7),depth,alen,width,areacs
c lentmax,sument
c write(*,*)inew,jnew,knew,entmax1,t(inew,jnew,knew)
c 1,h(inew,jnew,knew)
if ((iter/iwrite)*iwrite.ne.iter) go to 8006
c-----heat balance-----
call data6(botfl,0.,frofl,0.,bacfl,0.,alefl,0.,rigfl,0.,topfl1,0.)
do 8007 i=1,l1
do 8007 j=1,m1
botfl = botfl + xcv(i)*ycv(j)*fluxm1(i,j,7)
8007 topfl1 = topfl1 + xcv(i)*ycv(j)*heatin(i,j)
topfl=topfl1+volheatin
do 8008 i=1,l1
do 8008 k=1,n1
frofl = frofl + xcv(i)*zcv(k)*fluxj1(i,k,7)
8008 bacfl = bacfl + xcv(i)*zcv(k)*fluxm1(i,k,7)
sou5=0
do 8009 j=1,m1
do 8009 k=1,n1
sou5 = sou5 + (h(l1,j,k)-h(1,j,k))*ycv(j)*zcv(k)*rhoscan
alefl = alefl + ycv(j)*zcv(k)*fluxi1(j,k,7)
8009 rigfl = rigfl + ycv(j)*zcv(k)*fluxl1(j,k,7)
heatout = botfl+frofl+bacfl+alefl+rigfl+sou5
ratio = heatout/topfl
write(*,*)'-----'
write(*,*)'HEAT OUT = ', heatout, 'IN = ',topfl,' RATIO = ',ratio
write(*,*)'-----'
write(*,8099)

```

```

8006 continue
c      do 1066 i=1,l1
c      do 1066 j=1,m1
c      do 1066 k=1,n1
c        if (t(i,j,k).gt.tliquid) go to 1066
c        u(i,j,1)=0.0
c        v(i,j,1)=0.0
c        w(i,j,1)=0.0
c        u(i,j,k)=0.0
c        u(i+1,j,k)=0.0
c        v(i,j,k)=0.0
c        v(i,j+1,k)=0.0
c        w(i,j,k)=0.0
c        w(i,j,k+1)=0.0
1066 continue
      if (iter.ne.last) return
      call tools(print)
      do 1077 i=1,l1
      do 1077 j=1,m1
      do 1077 k=1,n1
      amuff(i,1,1)=(amuff(i,2,1)+amuff(i,1,2))/2.0
      diff(i,1,1)=(diff(i,2,1)+diff(i,1,2))/2.0
      ake(i,1,1)=(ake(i,2,1)+ake(i,1,2))/2.0
      dis(i,1,1)=(dis(i,2,1)+dis(i,1,2))/2.0
      u(i,1,1)=(u(i,2,1)+u(i,1,2))/2.0
      v(i,1,1)=(v(i,2,1)+v(i,1,2))/2.0
      r1(i,j,k)=(amuff(i,j,k)-amuf)/amuf
      r2(i,j,k)=(diff(i,j,k)-difl)/difl
      if (t(i,j,k).gt.tsolid) go to 1077
      r1(i,j,k)=0.0
      r2(i,j,k)=0.0
1077 continue
C-----calculation of average vis. and thermal dif.-----
      voll=0.0
      sumvoll=0.0
      sumamuf=0.0
      sumdiff=0.0
      r11max=0.0
      r22max=0.0
      do 9991 i=imin,imax
      do 9991 j=2,jmax
      do 9991 k=2,kmax
      if (t(i,j,k).lt.tliquid) goto 9991
      voll=xcv(i)*ycv(j)*zcv(k)
      sumvoll=sumvoll+voll
      amutt=amuff(i,j,k)-amuf
      diftt=diff(i,j,k)-difl
      sumamuf=sumamuf+voll*amutt
      sumdiff=sumdiff+voll*diftt
      r11max=amax1(r11max,amutt)
      r22max=amax1(r22max,diftt)
9991 continue
      aveamuf=sumamuf/sumvoll
      avediff=sumdiff/sumvoll

```

```

        ratio1=aveamuf/amuf
        ratio2=avediff/difl
        r1max=r1lmax/amuf
        r2max=r22max/difl
c-----write across section area and surface temperature-----
        open(unit=20,file='tsurf.dat')
        write(20,993)areacs
        write(20,*)l1,m1
        do 7009 j=1,m1
        do 7009 i=1,l1
        write(20,992)x(i),y(j),xcv(i),ycv(j),t(i,j,2)
7009  continue
992  format(5(1x,e10.5))
993  format(1x,e10.5)
c-----tecplot output-----
        if (itecplt.eq.1) then
        open(unit=71,file=filenames(7))
        write(71,*) 'TITLE = "FLUID FLOW AND HEAT TRANSFER IN WELD POOL"'
        write(71,*) 'VARIABLES = "X", "Y", "Z", "TEM", "U", "V", "W",
1  "amut","diff","ake","dis"'
        write(71,*) 'ZONE I=',l1,'J=',m1,'K=',n1,'F=POINT'
        do 9001 k=1,n1
        do 9001 j=1,m1
        do 9001 i=1,l1
9001  write(71,9099)x(i),y(j),z(k),t(i,j,k),u(i,j,k),v(i,j,k),w(i,j,k)
1  ,r1(i,j,k),r2(i,j,k),ake(i,j,k),dis(i,j,k)
        endif
c-----maximum velocities-----
        do 9010 i=imin,imax
        do 9010 j=1,jmax
        do 9010 k=1,kmax
        umax=amax1(umax,abs(u(i,j,k)))
        vmax=amax1(vmax,abs(v(i,j,k)))
9010  wmax=amax1(wmax,abs(w(i,j,k)))
        call data6(valout(1),depth,valout(2),width,valout(3),alen,
1valout(4),areacs,valout(5),tpeak,valout(6),topfl)
        call data5(valout(7),heatout,
1valout(8),botfl,valout(9),bacfl,valout(10),alefl,valout(11),rigfl)
        call data3(valout(12),rsmx,valout(13),smx,valout(14),ssum)
        call data3(valout(15),umax,valout(16),vmax,valout(17),wmax)
        call data2(valout(18),float(imin),valout(19),float(imax))
        call data2(valout(20),float(jmax),valout(21),float(kmax))
        call data1(valout(22),ratio)
        call data4(valout(23),ratio1,valout(24),ratio2,valout(25),
1r1max,valout(26),r2max)
        write(41,4)
        write(41,*) '          output'
        write(41,4)
        do 251 i=1,no
251  write(41,269)i,strout(i),valout(i)
        write(41,4)
        call tools(save)
4  format(2x,79('-'))
5  format(2x,79('-'),/15x,'grid related output',/2x,79('-'))

```

```

19  format (2x,a5,2x,a60,a2)
29  format (2x,a5,2x,a20,a2)
30  format (2x,a5,1x,i2,1x,a9,1x,a29,1x,a1,a8,a1)
39  format (2x,a30,1x,i2,a2)
49  format (2x,a5,1x,i2,1x,a34,/2x,79('-'))
59  format (2x,a5,1x,i2,1x,a9,1x,a40,a1,1pe10.3,a1)
69  format (2x,a5,1x,i1,1x,a38)
79  format (2x,79('-'),/15x,a40)
89  format (a30)
99  format (2x,a5,1x,i1,1x,a15,a40)
166 format (2x,a50,2x,i5)
168 format (2x,a5,i2,a40,2x,i5)
169 format (2x,a5,i2,a40,2x,e10.4)
269 format (2x,i5,2x,a50,2x,e12.6)
279 format (2x,i5,2x,a30,2x,a15)
8089 format (2x,i4,8(2x,1pe10.3))
8099 format (' ITER',5x,'TPEAK',7x,'RSMAX',7x,'RES(7)      Depth','
1  Length      Width      Area')
9099 format (11(e14.4))
      return
      entry outflo
      return
      entry phi
c-----define gam(i,j) for enthalpy equation-----
      if (nf.ne.7) go to 5200
      do 5001 i=2,12
          rhoscx=rhoscax/xcv(i)
      do 5001 j=2,m2
          do 5001 k=2,n2
              gam(i,j,k)=diff(i,j,k)
c-----enthalpy equation time independent source terms, source term (1)
      sc(i,j,k)=rhoscx*h(i-1,j,k)
      sp(i,j,k)=-rhoscx
c-----source term (2) -----
      rlbdx=rhoref*hlatnt/xcv(i)
      rlbdy=rhoref*hlatnt/ycv(j)
      rlbz=rhoref*hlatnt/zcv(k)
      flw=frac1(i,j,k)*fx(i)+frac1(i-1,j,k)*fxm(i)
      fle=frac1(i+1,j,k)*fx(i+1)+frac1(i,j,k)*fxm(i+1)
      fls=frac1(i,j,k)*fz(k)+frac1(i,j,k-1)*fzm(k)
      fln=frac1(i,j,k+1)*fz(k+1)+frac1(i,j,k)*fzm(k+1)
      flb=frac1(i,j,k)*fy(j)+frac1(i,j-1,k)*fym(j)
      flf=frac1(i,j+1,k)*fy(j+1)+frac1(i,j,k)*fym(j+1)
      sc(i,j,k)=sc(i,j,k)+rlbdx*(u(i,j,k)*flw-u(i+1,j,k)*fle)+
1      rlbdy*(v(i,j,k)*flb-v(i,j+1,k)*flf)+
1      rlbz*(w(i,j,k)*fls-w(i,j,k+1)*fln)
c-----source term (3) -----
5001 sc(i,j,k)=sc(i,j,k)+(flw-fle)*hlatnt*rhoscx
c-----source term due to droplet transfer-----
      do 5044 i=2,12
          do 5044 j=2,m2
              do 5044 k=2,n2
5044 sc(i,j,k)=sc(i,j,k)+qin(i,j,k)
c-----end source terms, begin boundary conditions--(front boundary)-----

```

```

do 5004 i=2,12
do 5004 k=2,n2
kbcj1(i,k)=2
flxp(i,1,k)=0.0
flxc(i,1,k)=0.0
c-----back boundary-----known temperature if kbcml = 1 -----
if (htcml.gt.10.0) then
kbcml(i,k)=1
h(i,m1,k)=hml
else
kbcml(i,k)=2
flxc(i,m1,k)=-htcml*(tsolid-298.0)+htcml*hsmelt/acp
flxp(i,m1,k)=-htcml/acp
endif
5004 continue
c-----left boundary-----
do 5003 j=2,m2
do 5003 k=2,n2
if (htcil.gt.10.0) then
kbcil(j,k)=1
h(1,j,k)=hil
else
kbcil(j,k)=2
flxc(1,j,k)=-htcil*(tsolid-298.0)+htcil*hsmelt/acp
flxp(1,j,k)=-htcil/acp
endif
c-----right boundary-----
if (htcl1.gt.10.0) then
kbc11(j,k)=1
h(11,j,k)=h11
else
kbc11(j,k)=2
flxc(11,j,k)=-htcl1*(tsolid-298.0)+htcl1*hsmelt/acp
flxp(11,j,k)=-htcl1/acp
endif
5003 continue
c-----top boundary-----
do 5002 i=2,12
do 5002 j=2,m2
kbck1(i,j)=2
c-----energy from the heat source (F1)-----
flxc(i,j,1) = heatin(i,j)
flxp(i,j,1) = 0.0
c-----radiative heat loss (F2)-----
if (emiss.gt.1.0e-3) then
if (h(i,j,1).ge.hlcal) then
const1 = sigems/acpl**4
const2 = (tliquid - hlcal/acpl)*acpl
terma = (h(i,j,1)+const2)**4
termb = (h(i,j,1)+const2)**3
fluxc = sigems*tamb4-const1*terma+4.0*const1*termb*h(i,j,1)
fluxp = -4.0*const1*termb
else
if (h(i,j,1).lt.hsmelt) then

```



```

const1 = sigems/acp**4
const2 = (tsolid-hsmelt/acp)*acp
terma = (h(i,j,1)+const2)**4
termb = (h(i,j,1)+const2)**3
fluxc = sigems*tamb4-const1*terma+4.0*const1*termb*h(i,j,1)
fluxp = -4.0*const1*termb
else
cpavg = (acpl+acp)/2.0
const1 = sigems/cpavg**4
const2 = tsolid*cpavg
terma = (h(i,j,1)+const2)**4
termb = (h(i,j,1)+const2)**3
fluxc = sigems*tamb4-const1*terma+4.0*const1*termb*h(i,j,1)
fluxp = -4.0*const1*termb
endif
endif
flxc(i,j,1)=flxc(i,j,1)+fluxc
flxp(i,j,1)=flxp(i,j,1)+fluxp
endif
c-----convective heat loss (F3)-----
if (htck1.lt.10.) then
if (h(i,j,1).ge.hlcal) then
flxc(i,j,1)=-htck1*(tliquid-298.)+htck1*hlcal/acpl+flxc(i,j,1)
flxp(i,j,1)=-htck1/acpl+flxp(i,j,1)
else
if (h(i,j,1).lt.hsmelt) then
flxc(i,j,1)=-htck1*(tsolid-298.)+htck1*hsmelt/acp+flxc(i,j,1)
flxp(i,j,1)=-htck1/acp+flxp(i,j,1)
else
flxc(i,j,1)= -htck1*(tsolid-298.0) + flxc(i,j,1)
flxp(i,j,1) = -htck1/cpavg + flxp(i,j,1)
endif
endif
endif
c-----bottom boundary-----
if (htcn1.gt.10.0) then
kbcn1(i,j)=1
h(i,j,n1)=hn1
else
kbcn1(i,j)=2
flxc(i,j,n1)=-htcn1*(tsolid-298.0)+htcn1*hsmelt/acp
flxp(i,j,n1)=-htcn1/acp
endif
5002 continue
c-----edge boundary: intersecting front and top plane-----
do 5033 i=2,12
5033 h(i,1,1)=h(i,2,1)
5200 continue
c----- define gam(i,j,k) for momentum equations-----
if (nf.gt.3) goto 6000
do 5501 i=2,12
do 5501 j=2,m2
do 5501 k=2,n2
5501 gam(i,j,k)=amuff(i,j,k)

```

```

c-----source term for mushy resgion:Karman-Kauzeny approximation-----
      do 5400 k=kst,n2
      do 5400 j=jst,m2
      do 5400 i=ist,l2
5400  sp(i,j,k)=-1.6e4*(1.0-fracl(i,j,k))**2/(fracl(i,j,k)**3+1.0e-3)
c-----boundary conditions for u momentum equation, source term-----
      if (nf.ne.1) go to 5500
      call tools(usor)
      do 1004 i=ist,l2
      do 1004 j=jst,m2
      do 1004 k=kst,n2
      rsarea = rhoscan/xdif(i)
      asc =rsarea*u(i-1,j,k)
      asp = -rsarea
      if(u(i,j,k).ge.0.0)go to 1003
      asp =0.
      asc=rsarea*(u(i,j,k)-u(i+1,j,k))
1003  sc(i,j,k) = sc(i,j,k) + asc
1004  sp(i,j,k) = sp(i,j,k) + asp
c-----electromagnetic force-----
      if (yesarc.gt.0.5) then
      do 5402 i=imin-2,imax+2
      do 5402 j=jst,jmax+2
      do 5402 k=kst,kmax+2
5402  sc(i,j,k)=sc(i,j,k)+scemfx(i,j,k)
      endif
c-----top boundary (u momentum, shear stress, kbck1 = 1 by default)--
-
      do 5404 i=imin-2,imax+2
      do 5404 j=2,jmax+2
      dtdx = (t(i,j,1)-t(i-1,j,1))/xdif(i)
      if (wtpct.gt.1e-5) then
      tav=t(i,j,1)*fx(i)+t(i-1,j,1)*fxm(i)
      if(tav.gt.tsolid) dgdt=surten(tav,wtpct,ac,gamsat,entfac,enthse)
      endif
5404  u(i,j,1)=u(i,j,2)+fracl(i,j,1)*dgdt*dtdx*zdif(2)/amuff(i,j,2)
c- ---front boundary (plane of symmetry)-----
      do 5403 i=1,l1
      do 5403 k=1,n1
5403  kbcj1(i,k)=2
5500  continue
c-----v momentum boundary conditions-----
      if (nf.ne.2) go to 4001
      call tools(vsor)
      do 1006 i=ist,l2
      do 1006 j=jst,m2
      do 1006 k=kst,n2
      rsarea = rhoscan/xcv(i)
      asc = rsarea*(v(i+1,j,k)-v(i,j,k))
      asp = 0.
      sc(i,j,k) = sc(i,j,k) + asc
1006  sp(i,j,k) = sp(i,j,k) + asp
c-----electromagnetic field-----
      do 502 i=imin-2,imax+2

```

```

do 502 j=jst,jmax
do 502 k=kst,kmax
502  sc(i,j,k)=sc(i,j,k)+scemfy(i,j,k)
c-----top boundary (shear stress, kbck1 = 1 by default)-----
do 504 i=imin-2,imax+2
do 504 j=2,jmax+2
dtdy = (t(i,j,1)-t(i,j-1,1))/ydif(j)
if (wtpct.gt.1e-5) then
tav=t(i,j,1)*fy(j)+t(i,j-1,1)*fym(j)
if(tav.gt.tsolid) dgdt=surten(tav,wtpct,ac,gamsat,entfac,enthse)
endif
504  v(i,j,1)=v(i,j,2)+frac1(i,j,1)*dgdt*dtdy*zdif(2)/amuff(i,j,2)
c-----front boundary (v momentum, by default kbcj1 = 1)-----
4001 continue
c-----w momentum source terms and boundary conditions-----
if (nf.ne.3) goto 6000
call tools(wsor)
do 1008 i=ist,l2
do 1008 j=jst,m2
do 1008 k=kst,n2
rsarea = rhoscan/xcv(i)
asc = rsarea*(w(i+1,j,k)-w(i,j,k))
asp = 0.
sc(i,j,k) = sc(i,j,k)+asc
1008  sp(i,j,k) = sp(i,j,k)+asp
c-----electromagnetic source-----
do 602 i=imin-2,imax+2
do 602 j=jst,jmax+2
do 602 k=kst,kmax+2
c-----bouyancy source-----
602  sc(i,j,k)=sc(i,j,k)+scemfz(i,j,k)-boufac*(t(i,j,k)-tsolid)
c-----top boundary (w momentum, kbcn1=1 by default)-----
c-----front boundary (w momentum)-----
do 604 i=imin-2,imax+2
do 604 k=2,kmax+2
604  kbcj1(i,k)=2
6000 continue
if (nf.ne.9) goto 7000
call tools(ksor)
do 5111 k=kst,n2
do 5111 j=jst,m2
do 5111 i=ist,l2
amutt=0.09*rhoref*ake(i,j,k)**2/(dis(i,j,k)+1.0e-15)
amut(i,j,k)=amut(i,j,k)+0.3*(amutt-amut(i,j,k))
amuff(i,j,k)=amuf+amut(i,j,k)
if(frac1(i,j,k).gt.0.001) then
gam(i,j,k)=amuff(i,j,k)/1.0
sc(i,j,k)=amut(i,j,k)*gen(i,j,k)
sp(i,j,k)=-rhoref*dis(i,j,k)/(ake(i,j,k)+1.0e-15)
else
gam(i,j,k)=1.0e30
sc(i,j,k)=0
sp(i,j,k)=0
endif

```

```

5111 continue
c   write(*,*)"amuff(23,3,3),diff(23,3,3),dis(23,3,3),ake(23,3,3)"
c   write(*,9998)amuff(23,3,3),diff(23,3,3),dis(23,3,3),ake(23,3,3)
9998 format(4(e12.4))
do 5103 i=1,l1
do 5103 k=1,n1
5103 kbcj1(i,k)=2
do 5104 i=1,l1
do 5104 j=1,m1
5104 kbck1(i,j)=2
7000 continue
if (nf.ne.10) return
call tools(esor)
do 5112 k=kst,n2
do 5112 j=jst,m2
do 5112 i=ist,l2
amutt=0.09*rhoref*ake(i,j,k)**2/(dis(i,j,k)+1.0e-15)
amut(i,j,k)=amut(i,j,k)+0.3*(amutt-amut(i,j,k))
amuff(i,j,k)=amuf+amut(i,j,k)
if(frac1(i,j,k).gt.0.001) then
gam(i,j,k)=amuff(i,j,k)/1.3
sc(i,j,k)=1.44*amut(i,j,k)*gen(i,j,k)*dis(i,j,k)/(ake(i,j,k)
1 +1.0e-15)
sp(i,j,k)=-1.92*rhoref*dis(i,j,k)/(ake(i,j,k)+1.0e-15)
else
gam(i,j,k)=1.0e30
sc(i,j,k)=0
sp(i,j,k)=0
endif
5112 continue
do 5102 i=1,l1
do 5102 k=1,n1
5102 kbcj1(i,k)=2
do 5105 i=1,l1
do 5105 j=1,m1
5105 kbck1(i,j)=2
return
entry lc
if (nf.ne.7) return
sument=0.0
entmax=0.0
entmax1=0.0
do 1091 i=ist,l2
do 1091 j=jst,m2
do 1091 k=kst,n2
term1=aip(i,j,k)*h(i+1,j,k)+ajp(i,j,k)*h(i,j+1,k)
1 +akp(i,j,k)*h(i,j,k+1)
term2=aim(i,j,k)*h(i-1,j,k)+ajm(i,j,k)*h(i,j-1,k)
1+akm(i,j,k)*h(i,j,k-1)
term3=con(i,j,k)-ap(i,j,k)*h(i,j,k)
renew(i,j,k)=term1+term2+term3
entmax=amax1(entmax,abs(renew(i,j,k)))
sument=sument+abs(renew(i,j,k))
1091 continue

```

```

c      do 1092 i=imin-5,imax+5
c      do 1092 j=2,jmax+4
c      do 1092 k=2,kmax+4
          do 1092 i=2,l2
          do 1092 j=2,m2
          do 1092 k=2,n2
            if (abs(renew(i,j,k)).gt.entmax1) then
              entmax1=abs(renew(i,j,k))
              inew=i
              jnew=j
              knew=k
            endif
1092    continue
          return
          include '/home/CFD/COMP3D/FINISH3.FOR'
        end

```

### 3) Program turbvaploss.f

```

      subroutine adapt
      parameter (ni=70,nj=70,nk=70,nfmax=11,idblk=100,kunstd=1,
1nfm2=(1+kunstd)*nfmax, nzm=10, idim=2*(ni*nj+nj*nk+ni*nk))
c      nx: maximum of nzx,nzy and nzz (number of zones in three
directions)
      parameter (nog=5,nz=8,nq=14,np=18,nu=13,no=26,nbg=10,nzmax=10,ng=5)
      include '/home/CFD/COMP3D/ADPT3.FOR'
      include '/home/CFD/COMP3D/COMP3D.FOR'
      save
      dimension igroup(nog),valpro(nq),valphy(np),valnsp(nu),
1valbou(nbg),valout(no)
      dimension amuff(ni,nj,nk),diff(ni,nj,nk),dudy1(ni,nj,nk)
      dimension t(ni,nj,nk),h(ni,nj,nk),frac1(ni,nj,nk),hold(ni,nj,nk),
1frac1old(ni,nj,nk),apsum(ni,nj,nk)
      dimension heatin(ni,nj),qin(ni,nj,nk),factor2(ni,nj,nk),
1uv(ni,nj,nk)
      dimension scemfx(ni,nj,nk),scemfy(ni,nj,nk),scemfz(ni,nj,nk)
      dimension xyzo(nzmax,3),nxyz(nzmax,3),pxyz(nzmax,3),nzone(3)
      dimension renew(ni,nj,nk),width1(ni,nk),r1(ni,nj,nk),r2(ni,nj,nk)
      dimension ake(ni,nj,nk),dis(ni,nj,nk),amut(ni,nj,nk)
      equivalence (f(1,1,1,6),t(1,1,1)),(f(1,1,1,7),h(1,1,1)),
1(f(1,1,1,nfmax+7),hold(1,1,1)),(f(1,1,1,8),frac1(1,1,1)),
1(f(1,1,1,nfmax+8),frac1old(1,1,1)),(f(1,1,1,9),
1ake(1,1,1)),(f(1,1,1,10),dis(1,1,1)),(f(1,1,1,11),amut(1,1,1))
c-----nzone(i or j or k): number of zones in i or j or k direction
c-----xyzo(i or j or k): length of different zones in i or j or k
direction
c-----nxyz(i or j or k): number of control volumes in different zones
c-----pxyz(i or j or k): exponential factor for different zones
      equivalence (nzone(1),nzx),(nzone(2),nzy),(nzone(3),nzz),
1(xyzo(1,1),xzone(1)),(xyzo(1,2),yzone(1)),(xyzo(1,3),zzone(1)),
2(nxyz(1,1),ncvx(1)),(nxyz(1,2),ncvy(1)),(nxyz(1,3),ncvz(1)),
3(pxzy(1,1),powrx(1)),(pxzy(1,2),powry(1)),(pxzy(1,3),powrz(1))

```

```

character*60 grname(nog),strfile(nz),strpro(nq),
lstrphy(np),strnsp(nu),strgeom(ng),strout(no),strbou(nbg)
character*30 filenames(nz)
data igrp/nz,nq,np,nu,nbg/
data grname/'filenames','processes parameters','material propertie
ls','numerical scheme parameters','boundary conditions'/
c----group 1 input data-----
data strfile/'output file name','plot file name','print file name'
1,'start file name','save file name','grid input filename','tecplot
1 file name','emf field file name'/
data filenames/'output','plot','print','start','start','grid',
1'tecout','field'/
c----group 2 input data: process parameters and their default values----
data strpro/'laser power (Watts)','absorption coefficient','beam/a
lrc radius (cm)','scanning velocity (cm/sec)','starting location of
l beam','to arc welding (yes:1, no:0)','arc current (Amp)','arc vol
ltage (Volts)','arc efficiency (%)','starting emf field (yes:1,no:0
1)','fraction of energy received from arc','radius of volumetric he
lat source (cm)','height of volumetric heat source (cm)','# of iter
ls after which power is set to 0'/
data valpro/60.,.2,.25,0.17,4.7,1,150.,11.0,75.,0,1.0,.1,.3,2000./
c-- Group 3 input data: material properties and their default values ---
data strphy/'liquidus temperature (K)','density of liquid metal (g
lm/cm**3)','enthalpy of solid at mp (cal/gm)','enthalpy of liquid a
lt mp (cal/gm)','specific heat of solid (cal/gm-K)','specific heat
lof liquid (cal/gm-K)','thermal cond of solid (cal/cm-sec-K)','ther
lmal cond of liq (cal/cm-sec-K)','viscosity of liquid (gm/cm-sec)',
1'd(gamma)/dT, pure mat ( dynes/cm-K)','conc. of surface active
species
1(wt%)','enthalpy of segregation (J/mole)','surface excess at sat
1(mole/cm**2)','entropy factor','to variable properties (yes:1, no:
10)','coeff of thermal expansion (1/K)','solidus temperature (K)'
1,'emissivity of the material'/
data valphy/1785.0,7.2,250.76,314.76,0.168,0.193,0.06,0.2,0.06,
10.43,0.0,-1.66e5,1.30e-9,0.00318,0.0,1.0e-5,1745.0,0.0/
c-- Group 4 input data: default values of numerical scheme parameters---
data strnsp/'velocity relaxation parameter','pressure relaxation p
lparameter','enthalpy relaxation parameter','latent heat relaxation
lparameter','k relaxation parameter','e relaxation parameter',
1'time increment','number of iterations','maximum number
1 of cycles per time step','iter interval for overall heat balance'
1,'index to start from oldfile(yes:1,no:0)','index to solve momentu
lm eqns(yes:1,no:0)','index to write tecplot file(yes:1,no:0)'/
data valnsp/.8,.8,1.,.8,0.5,0.5,1e20,40,1.,5.,0,1.,1./
c----group 5 input data : default values of the boundary conditions----
data strbou/'temperature at i=1 boundary (K)','temperature at i=11
1 boundary (K)','temperature at j=m1 boundary','temperature at k=n1
1 boundary (k)','heat transfer coeff at i=1(cal/cm2-s-K)','heat tra
lnsfer coeff at i=11(cal/cm2-s-K)','heat transfer coeff at j=m1(cal
1/cm2-s-K)','heat transfer coeff at k=n1(cal/cm2-s-K)','heat transf
ler coeff at k=1(cal/(cm2-s-k)','preheat temperature (K)'/
data valbou/298.0,298.0,298.0,298.0,100.0,100.0,100.0,100.0,00.0,
1298.0/
c---group 6: grid data-----

```

```

      data strgeom/'zone(','number of zones',' )length',' )number of con
      trol volumes',' )exponential factor'/
c---Group 7: output data-----
      data strout/'depth of the pool (cm)', 'width of the pool (cm)', 'len
      lgth of the pool (cm)', 'cross section area (cm2)', 'peak temperature
      1', 'heat input rate (cal/s)', 'heat output rate (cal/s)', 'heat flow
      lat n1', 'heat flow at m1', 'heat flow at i1', 'heat flow at l1', 'RSMA
      1X', 'SMAX', 'SSUM', 'UMAX', 'VMAX', 'WMAX', 'IMIN', 'IMAX', 'JMAX', 'KMAX',
      1'ratio(Heat In/Heat Out)', 'ratio1(Ave.(amut/amuf))', 'ratio2(Ave.(d
      lift/difl))', 'maxr1(max amut/amuf)', 'maxr2(max dift/difl)'/
      entry check
      iread=0
      return
      entry grid
10   nogp1=nog+1
      do 11 i=1,nog
11   write(6,99)'Enter',i,'to change/view ',grname(i)
      write(6,69)'Enter',nogp1,'to do calculations with current values'
c-- Select a data group to view/change data -----
      write(6,4)
      write(*,*)          Please enter your choice (1 to 6):'
      read(*,*) igrop
      if(igrop.eq.nogp1) go to 51
c-- On screen viewing of parameter values in a selected data group -----
      write (6,79) grname(igrop)
      imax=igroup(igrop)
21   write(6,4)
      do 40 i=1,imax
      goto(31,32,33,34,35)igrop
31   write(*,30)'Enter',i,'to change',strfile(i),'(',filenames(i),')'
      go to 40
32   write(*,59)'Enter',i,'to change',strpro(i),'(',valpro(i),')'
      go to 40
33   write(*,59)'Enter',i,'to change',strphy(i),'(',valphy(i),')'
      go to 40
34   write(*,59)'Enter',i,'to change',strnsp(i),'(',valnsp(i),')'
      go to 40
35   write(*,59)'Enter',i,'to change',strbou(i),'(',valbou(i),')'
40   continue
      imaxp1=imax+1
      write(6,49)'Enter',imaxp1,'if all values in this group are ok'
c-- Decide if some of the values need to be changed -----
      write(6,39) 'Please enter your choice (1 to',imaxp1,'):'
      read(*,*)  ichange
      if(ichange.eq.imaxp1) go to 10
c-- Change parameter value -----
      goto (41,42,43,44,45) igrop
41   write(6,29)'Enter',strfile(ichange),':'
      read(5,89) filenames(ichange)
      go to 21
42   write(6,19)'Enter',strpro(ichange),':'
      read(5,*)valpro(ichange)
      go to 21
43   write(6,19)'Enter',strphy(ichange),':'
```

```

        read(5,*)valphy(ichange)
        go to 21
44    write(6,19)'Enter',strnsp(ichange),':'
        read(5,*)valnsp(ichange)
        go to 21
45    write(6,19)'Enter',strbou(ichange),':'
        read(5,*)valbou(ichange)
        go to 21
c-- end data input -----
51    call name3(plotf,filenames(2),startf,filenames(4),
        isavef,filenames(5))
c---user friendly names for process parameters-----
        call data7(power,valpro(1),abscof,valpro(2),rb,valpro(3),scanvel,
        lvalpro(4),xstart,valpro(5),yesarc,valpro(6),arccur,valpro(7))
        call data5(arcvol,valpro(8),yesoldf,valpro(10),fracg,valpro(11),
        lrbt,valpro(12),htv,valpro(13))
        call intal(ifinish,int(valpro(14)))
        if (yesarc.lt.0.5) go to 12
        abscof=valpro(9)/100.0
        power=arccur*arcvol
c--user friendly names for physical properties -----
12    call data3(tliquid,valphy(1),rhoref,valphy(2),ac,valphy(10))
        call data3(wtpct,valphy(11),enthse,valphy(12),gamsat,valphy(13))
        call data3(entfac,valphy(14),yvarpr,valphy(15),beta,valphy(16))
        call data3(hsmelt,valphy(3),hlfriz,valphy(4),acp,valphy(5))
        call data2(acpl,valphy(6),amuf,valphy(9))
        call data3(tsolid,valphy(17),dgdtd,valphy(10),emiss,valphy(18))
        difs=valphy(7)/acp
        if (yvarpr.lt.0.5) then
            difl=valphy(8)/acpl
        else
            difl=valphy(8)/acpl
        endif
c-- user friendly names for numerical scheme parameters -----
        call data6(relax(1),valnsp(1),relax(2),valnsp(1),relax(3),valnsp(1)
        1),relax(4),valnsp(2),relax(7),valnsp(3),relax(8),valnsp(4))
        call data2(relax(9),valnsp(5),relax(10),valnsp(6))
        call data2(dt,valnsp(7),yesold,valnsp(11))
        call inta5(last,int(valnsp(8)),itmax,int(valnsp(9)),iwrite,
        lint(valnsp(10)),isol,int(valnsp(12)),itecplt,int(valnsp(13)))
c---user friendly names for geometric parameters-----
        call inta2(mode,1,kdisk,1)
        call data3(xu(2),0.,yv(2),0.,zw(2),0.)
c---user friendly names for boundary conditions-----
        call data3(ti1,valbou(1),tl1,valbou(2),tml,valbou(3))
        call data3(tn1,valbou(4),htci1,valbou(5),htcl1,valbou(6))
        call data3(htcm1,valbou(7),htcn1,valbou(8),htck1,valbou(9))
        call data1(ti,valbou(10))
c----open required files-----
        open (unit=41,file=filenames(1))
        open (unit=7,file=filenames(3))
        open (unit=42,file=filenames(6))
        if (yesarc.gt.0.5) open (unit=43,file=filenames(8))
c-----grid generation-----

```



```

do 910 ijk=1,3
  read(42,*)nzone(ijk)
  read(42,*)(xyzo(i,ijk),i=1,nzone(ijk))
  read(42,*)(nxyz(i,ijk),i=1,nzone(ijk))
910  read(42,*)(pxyz(i,ijk),i=1,nzone(ijk))
      call tools(zgrid)
c-----default starting location of the beam-----
  if (xstart.eq.0) xstart=xzone(2)+xzone(1)
  valpro(5)=xstart
  return
  entry begin
  call inta4(kprint(1),1,kprint(2),1,kprint(6),1,kprint(11),1)
  call inta3(kpmax,2,kpln(1),1,kpln(2),2)
  call name2(title(6),' temperature ',title(7),' enthalpy')
  call name1(title(8),' fraction liquid ')
c----calculation of some constant parameters-----
  restd=1.0e-7
  crit(7)=1.0e-7
  pi=3.1415297
  kord = 2
  rb2 = rb**2
  rbt2 = rbt**2
  pkint = fracg*2.0*power*abscof*0.239/(pi*rb2)
c  pkint = fracg*3.0*power*abscof*0.239/(pi*rb2)
c  pkint = fracg*power*abscof*0.239/(2.0*pi*rb2)
  deltemp = tliquid - tsolid
  cpavg = (acp+acpl)/2.0
  hlcal = hsmelt+cpavg*deltemp
  hlatnt = hlfriz - hlcal
  rhoref = rhoref*980.0*beta
  rhoscan = rhoref*scanvel
  sigems = emiss*5.67E-12*0.239
  tamb4 = 298.0**4
  acpl4 = acpl**4
  acp4 = acp**4
  nvk=9
  nvd=10
  if (isol.ne.1) go to 111
  do 110 nff=1,10
  ksolve(nff)=1
110  kbloc(nff)=1
111  call inta3(ksolve(6),0,ksolve(8),0,ksolve(7),1)
      hi = (ti-tsolid)*acp+hsmelt
      hli = (tli-tsolid)*acp+hsmelt
      hil = (til-tsolid)*acp+hsmelt
      hml = (tml-tsolid)*acp+hsmelt
      hnl = (tnl-tsolid)*acp+hsmelt
      do 102 i=1,11
      do 102 j=1,m1
      do 102 k=1,n1
      u(i,j,k)=0.0
      v(i,j,k)=0.0
      w(i,j,k)=0.0
      rho(i,j,k)=rhoref

```

```

    amut(i,j,k)=amuf
    amuff(i,j,k)=amuf
    diff(i,j,k)=difl
    ake(i,j,k)=1
    dis(i,j,k)=10
    h(i,j,k)=hi
    hold(i,j,k)=hi
102  t(i,j,k)=ti
c-----find  istart:  istart is i index closest to the beam location--
    call findindx(x,ll,xstart,istart)
C-----heat input on top surface, -----
    do 6001 i = 1,ll
        xdist =xstart - x(i)
        do 6001 j = 1,m1
            dist = xdist**2+y(j)**2
            heatin(i,j) = pkint*exp(-2.0*dist/rb2)
c        heatin(i,j) = pkint*exp(-3.0*dist/rb2)
c        heatin(i,j) = pkint*exp(-dist/(2.0*rb2))
6001  topfll = topfll + xcv(i)*ycv(j)*heatin(i,j)
C-----define volumetric heat source-----
    call findindx(zw,n1,htv,khdep)
    call findindx(yv,m1,rbt,jhrad)
    xmxt = xstart+rbt
    call findindx(xu,ll,xmxt,imxrad)
    xnxt = xstart-rbt
    call findindx(xu,ll,xnxt,imnrad)
    do 6059 k=1,khdep-1
        do 6059 j=1,jhrad
            do 6059 i=imnrad,imxrad
                xydist = sqrt(abs(x(i)-xstart)**2+y(j)**2)
                if (xydist.le.rbt) volheat = volheat + xcv(i)*ycv(j)*zcv(k)
6059  continue
            denv=(1.0-fracg)*power*abscof*0.239/(volheat*2.0)
            do 6051 k=1,khdep-1
                do 6051 j=1,jhrad
                    do 6051 i=imnrad,imxrad
                        qin(i,j,k)=0.0
                        xydist = sqrt(abs(x(i)-xstart)**2+y(j)**2)
                        if (xydist.le.rbt) qin(i,j,k) = denv
6051  volheatin = volheatin+qin(i,j,k)*xcv(i)*ycv(j)*zcv(k)
c-----calculate emf field-----
    ---
        if ((yesarc.gt.0.5).and.(float(ksolve(1)).gt.0.9))
            lcall emf(x,y,z,ll,m1,n1,arccur,rb,scemfx,scemfy,scemfz,yesoldf,
                lxstart,43,ni,nj,nk)
c-- write data used output in a file -----
        do 2400 igrop=1,nog
            imax=igroup(igrop)
            write (41,79) gname(igrop)
            write(41,4)
            do 2400 ii=1,imax
                go to (241,242,243,244,245)igrop
241  write(41,279)ii,strfile(ii),filenames(ii)
            go to 2400

```

```

242  write(41,269)ii,strpro(ii),valpro(ii)
      go to 2400
243  write(41,269)ii,strphy(ii),valphy(ii)
      go to 2400
244  write(41,269)ii,strnsp(ii),valnsp(ii)
      go to 2400
245  write(41,269)ii,strbou(ii),valbou(ii)
2400  continue
c-----grid related output-----
      write(41,5)
      write(41,*)'x direction'
      write(41,166)strgeom(2),nzx
      do 1099 j=1,nzx
        write(41,169)strgeom(1),j,strgeom(3),xzone(j)
        write(41,168)strgeom(1),j,strgeom(4),ncvx(j)
1099  write(41,169)strgeom(1),j,strgeom(5),powrx(j)
        write(41,*)'y direction'
        write(41,166)strgeom(2),nzy
        do 1098 j=1,nzy
          write(41,169)strgeom(1),j,strgeom(3),yzone(j)
          write(41,168)strgeom(1),j,strgeom(4),ncvy(j)
1098  write(41,169)strgeom(1),j,strgeom(5),powry(j)
          write(41,*)'z direction'
          write(41,166)strgeom(2),nzz
          do 1097 j=1,nzz
            write(41,169)strgeom(1),j,strgeom(3),zzone(j)
            write(41,168)strgeom(1),j,strgeom(4),ncvz(j)
1097  write(41,169)strgeom(1),j,strgeom(5),powrz(j)
            iunit=41
            call tableout(11,x,xu,' i=', ' x=', 'xu=',iunit)
            call tableout(m1,y,yv,' j=', ' y=', 'yv=',iunit)
            call tableout(n1,z,zw,' k=', ' z=', 'zw=',iunit)
            if (yesold.ge.0.5) call tools(start)
            return
c-- Variable density and other properties -----
-----
      entry dense
      do 6002 i=1,l1-1
      do 6002 j=1,m1-1
      do 6002 k=1,n1-1
      if (yvarpr.gt.0.5) go to 7001
c Constant properties -----
-----
      amuff(i,j,k)=amuf
      if(t(i,j,k).ge.tliquid)diff(i,j,k)=difl
      if(t(i,j,k).le.tsolid)diff(i,j,k)=difs
      if((t(i,j,k).lt.tliquid) .and. (t(i,j,k).gt.tsolid))
1diff(i,j,k)=frac1(i,j,k)*difl+(1.0-frac1(i,j,k))*difs
      go to 6002
7001  continue
c Variable properties -----
c---Turbulent viscosity -----
      amutt=0.09*rhoref*ake(i,j,k)**2/(dis(i,j,k)+1.0e-15)
      amut(i,j,k)=amut(i,j,k)+0.3*(amutt-amut(i,j,k))

```

```

      amuff(i,j,k)=amuf+amut(i,j,k)
c---thermal conductivity, specific heat and k/Cp of solid and liquid----
      if(frac1(i,j,k).le.0.001) then
        tks=(0.016*T(i,j,k)+8.8)*0.00239
        cps=(0.1357*T(i,j,k)+459.28)*0.239/1000.0
        diff(i,j,k)=difs
      else
        diftt=amut(i,j,k)/0.9
        diff(i,j,k)=diff(i,j,k)+0.8*(diftt-diff(i,j,k))
        diff(i,j,k)=difl+diff(i,j,k)
      endif
6002 continue
c-- temperature calculation from the enthalpy values for iron block-----
      do 8001 i=1,11
        do 8001 j=1,m1
          do 8001 k=1,n1
            if (h(i,j,k)-hlcal)8002,8002,8003
8003   frac1(i,j,k)=1.0
            t(i,j,k)=(h(i,j,k)-hlcal)/acpl+tliquid
            go to 8001
8002   if(h(i,j,k).le.hsmelt) then
            frac1(i,j,k)=0.0
            t(i,j,k)=tsolid-(hsmelt-h(i,j,k))/acp
          else
            frac1(i,j,k)=(h(i,j,k)-hsmelt)/(hlcal-hsmelt)
            t(i,j,k)=deltemp*frac1(i,j,k) + tsolid
          endif
8001   continue
        return
      entry output
      if (iter.le.ifinish) go to 3901
      topfl1=0.0
      do 3902 i=1,11
        do 3902 j=1,m1
          heatin(i,j)=0.0
          do 3902 k=1,11
8002   qin(i,j,k)=0.0
3901   continue
c-----length of the pool; includes both liq and liq+sol, i.e., mushy
region-
      do 9055 i=istart,11
        if (t(i,1,1).lt.tsolid) go to 9056
        imax=i
9055   continue
9056   dtddxx = (t(imax,1,1)-t(imax+1,1,1))/(x(imax)-x(imax+1))
        xxmax = (tsolid - t(imax,1,1))/dtddxx + x(imax)
        do 9006 i=istart,1,-1
          if (t(i,1,1).lt.tsolid) go to 9066
          imin=i
9006   continue
9066   dtddxx = (t(imin,1,1)-t(imin-1,1,1))/(x(imin)-x(imin-1))
        xxmin = (tsolid - t(imin,1,1))/dtddxx+x(imin)
        alen=xxmax-xxmin
c-----depth of the pool-----

```

```

      kmax = 0
      do 9014 i=istart-5,imax
      do 9024 k=2,n2
      if (t(i,1,k).lt.tsolid) go to 9014
      kmax=max(kmax,k)
9024  continue
9014  continue
      depth = 0.0
      do 9077 i=istart-5,imax
      if (t(i,1,kmax).lt.tsolid) go to 9077
      dtdzz = (t(i,1,kmax)-t(i,1,kmax+1))/(z(kmax)-z(kmax+1))
      dep = (tsolid - t(i,1,kmax))/dtdzz+z(kmax)
      depth=amax1(dep,depth)
9077  continue
c-----width of the pool-----
      jmax = 0
      do 9007 i=istart-5,imax
      do 9008 j=2,m2
      if (t(i,j,1).lt.tsolid) go to 9007
      jmax=max(jmax,j)
9008  continue
9007  continue
      width = 0.0
      do 9017 i=istart-5,imax
      if (t(i,jmax,1).lt.tsolid) go to 9017
      dtdyy = (t(i,jmax,1)-t(i,jmax+1,1))/(y(jmax)-y(jmax+1))
      wid = (tsolid - t(i,jmax,1))/dtdyy+y(jmax)
      width=amax1(wid,width)
9017  continue
      width = width*2.0
c-----across section area of the pool-----
      areacs=0.0
      do 9029 i=istart-5,imax
      areacs0=0.0
      do 9019 j=2,m2
      do 9019 k=2,n2
      if (t(i,j,k).lt.tsolid) go to 9019
      areacs0=areacs0+ycv(j)*zcv(k)
9019  continue
      areacs=amax1(areacs,areacs0)
9029  continue
      areacs=areacs*2.0
c-----end calculation of geometric parameters,calculate peak temp-----
      tpeak=0.0
      do 8005 i=1,l1
      do 8005 j=1,m1
8005  tpeak=amax1(tpeak,t(i,j,1))
      write(*,8089)iter,tpeak,rsmax,residu(7),depth,alen,width,areacs
c      lentmax,sument
c      write(*,*)inew,jnew,knew,entmax1,t(inew,jnew,knew)
c      l,h(inew,jnew,knew)
      if ((iter/iwrite)*iwrite.ne.iter) go to 8006
c-----heat balance-----
      call data6(botfl,0.,frofl,0.,bacfl,0.,alefl,0.,rigfl,0.,topfl1,0.)

```

```

do 8007 i=1,l1
do 8007 j=1,m1
botfl = botfl + xcv(i)*ycv(j)*fluxml(i,j,7)
8007 topfl1 = topfl1 + xcv(i)*ycv(j)*heatin(i,j)
topfl=topfl1+volheatin
do 8008 i=1,l1
do 8008 k=1,n1
frofl = frofl + xcv(i)*zcv(k)*fluxjl(i,k,7)
8008 bacfl = bacfl + xcv(i)*zcv(k)*fluxml(i,k,7)
sou5=0
do 8009 j=1,m1
do 8009 k=1,n1
sou5 = sou5 + (h(11,j,k)-h(1,j,k))*ycv(j)*zcv(k)*rhoscan
alefl = alefl + ycv(j)*zcv(k)*fluxil(j,k,7)
8009 rigfl = rigfl + ycv(j)*zcv(k)*fluxll(j,k,7)
heatout = botfl+frofl+bacfl+alefl+rigfl+sou5
ratio = heatout/topfl
write(*,*)'-----'
write(*,*)'HEAT OUT = ', heatout, 'IN = ',topfl,' RATIO = ',ratio
write(*,*)'-----'
write(*,*,8099)
8006 continue

c do 1066 i=1,l1
c do 1066 j=1,m1
c do 1066 k=1,n1
c if (t(i,j,k).gt.tliquid) go to 1066
c u(i,j,1)=0.0
c v(i,j,1)=0.0
c w(i,j,1)=0.0
c u(i,j,k)=0.0
c u(i+1,j,k)=0.0
c v(i,j,k)=0.0
c v(i,j+1,k)=0.0
c w(i,j,k)=0.0
c w(i,j,k+1)=0.0
1066 continue
if (iter.ne.last) return
call tools(print)
do 1077 i=1,l1
do 1077 j=1,m1
do 1077 k=1,n1
amuff(i,1,1)=(amuff(i,2,1)+amuff(i,1,2))/2.0
diff(i,1,1)=(diff(i,2,1)+diff(i,1,2))/2.0
ake(i,1,1)=(ake(i,2,1)+ake(i,1,2))/2.0
dis(i,1,1)=(dis(i,2,1)+dis(i,1,2))/2.0
u(i,1,1)=(u(i,2,1)+u(i,1,2))/2.0
v(i,1,1)=(v(i,2,1)+v(i,1,2))/2.0
r1(i,j,k)=(amuff(i,j,k)-amuf)/amuf
r2(i,j,k)=(diff(i,j,k)-difl)/difl
if (t(i,j,k).gt.tsolid) go to 1077
r1(i,j,k)=0.0
r2(i,j,k)=0.0
1077 continue

```

```

C-----calculation of average vis. and thermal dif.-----
  voll=0.0
  sumvoll=0.0
  sumamuf=0.0
  sumdiff=0.0
  r1lmax=0.0
  r22max=0.0
  do 9991 i=imin,imax
  do 9991 j=2,jmax
  do 9991 k=2,kmax
  if (t(i,j,k).lt.tliquid) goto 9991
  voll=xcv(i)*ycv(j)*zcv(k)
  sumvoll=sumvoll+voll
  amutt=amuff(i,j,k)-amuf
  diftt=diff(i,j,k)-difl
  sumamuf=sumamuf+voll*amutt
  sumdiff=sumdiff+voll*difft
  r1lmax=amax1(r1lmax,amutt)
  r22max=amax1(r22max,diftt)
9991  continue
      aveamuf=sumamuf/sumvoll
      avediff=sumdiff/sumvoll
      ratio1=aveamuf/amuf
      ratio2=avediff/difl
      r1max=r1lmax/amuf
      r2max=r22max/difl
c-----write across section area and surface temperature-----
  open(unit=20,file='tsurf.dat')
  write(20,993)areacs
  write(20,*)l1,m1
  do 7009 j=1,m1
  do 7009 i=1,l1
  write(20,992)x(i),y(j),xcv(i),ycv(j),t(i,j,2)
7009  continue
992  format(5(1x,e10.5))
993  format(1x,e10.5)
c-----tecplot output-----
  if (itecplt.eq.1) then
  open(unit=71,file=filenames(7))
  write(71,*) 'TITLE = "FLUID FLOW AND HEAT TRANSFER IN WELD POOL"'
  write(71,*) 'VARIABLES = "X", "Y", "Z", "TEM", "U", "V", "W",
1  "amut", "diff", "ake", "dis"
  write(71,*) 'ZONE I=',l1,'J=',m1,'K=',n1,'F=POINT'
  do 9001 k=1,n1
  do 9001 j=1,m1
  do 9001 i=1,l1
  if (t(i,j,k).lt.850.) then
  u(i,j,k)=0.
  v(i,j,k)=0.
  w(i,j,k)=0.
  endif
9001  write(71,9099)x(i),y(j),z(k),t(i,j,k),u(i,j,k),v(i,j,k),w(i,j,k)
1  ,r1(i,j,k),r2(i,j,k),ake(i,j,k),dis(i,j,k)
  endif

```

```

c-----maximum velocities-----
      do 9010 i=imin,imax
      do 9010 j=1,jmax
      do 9010 k=1,kmax
          umax=amax1(umax,abs(u(i,j,k)))
          vmax=amax1(vmax,abs(v(i,j,k)))
9010    wmax=amax1(wmax,abs(w(i,j,k)))
      call data6(valout(1),depth,valout(2),width,valout(3),alen,
1valout(4),areacs,valout(5),tpeak,valout(6),topfl)
      call data5(valout(7),heatout,
1valout(8),botfl,valout(9),bacfl,valout(10),alefl,valout(11),rigfl)
      call data3(valout(12),rsmax,valout(13),smax,valout(14),ssum)
      call data3(valout(15),umax,valout(16),vmax,valout(17),wmax)
      call data2(valout(18),float(imin),valout(19),float(imax))
      call data2(valout(20),float(jmax),valout(21),float(kmax))
      call data1(valout(22),ratio)
      call data4(valout(23),ratiol,valout(24),ratio2,valout(25),
1r1max,valout(26),r2max)
      write(41,4)
      write(41,*)'                output'
      write(41,4)
      do 251 i=1,no
251    write(41,269)i,strout(i),valout(i)
      write(41,4)
      call tools(save)
4      format(2x,79('-'))
5      format(2x,79('-'),/15x,'grid related output',/2x,79('-'))
19     format(2x,a5,2x,a60,a2)
29     format(2x,a5,2x,a20,a2)
30     format(2x,a5,1x,i2,1x,a9,1x,a29,1x,a1,a8,a1)
39     format(2x,a30,1x,i2,a2)
49     format(2x,a5,1x,i2,1x,a34,/2x,79('-'))
59     format(2x,a5,1x,i2,1x,a9,1x,a40,a1,1pe10.3,a1)
69     format(2x,a5,1x,i1,1x,a38)
79     format(2x,79('-'),/15x,a40)
89     format(a30)
99     format(2x,a5,1x,i1,1x,a15,a40)
166    format(2x,a50,2x,i5)
168    format(2x,a5,i2,a40,2x,i5)
169    format(2x,a5,i2,a40,2x,e10.4)
269    format(2x,i5,2x,a50,2x,e12.6)
279    format(2x,i5,2x,a30,2x,a15)
8089   format(2x,i4,8(2x,1pe10.3))
8099   format('  ITER',5x,'TPEAK',7x,'RSMAX',7x,'RES(7)    Depth',
1  Length      Width      Area')
9099   format(11(e14.4))
      return
      entry outflo
      return
      entry phi
c-----define gam(i,j) for enthalpy equation-----
      if (nf.ne.7) go to 5200
      do 5001 i=2,12
          rhoscx=rhoscan/xcv(i)

```



```

do 5001 j=2,m2
do 5001 k=2,n2
gam(i,j,k)=diff(i,j,k)
c-----enthalpy equation time independent source terms, source term (1)
sc(i,j,k)=rhoscx*h(i-1,j,k)
sp(i,j,k)=-rhoscx
c-----source term (2) -----
rlbdx=rhoref*hlatnt/xcv(i)
rlbdy=rhoref*hlatnt/ycv(j)
rlbdz=rhoref*hlatnt/zcv(k)
flw=frac1(i,j,k)*fx(i)+frac1(i-1,j,k)*fxm(i)
fle=frac1(i+1,j,k)*fx(i+1)+frac1(i,j,k)*fxm(i+1)
fls=frac1(i,j,k)*fz(k)+frac1(i,j,k-1)*fzm(k)
fln=frac1(i,j,k+1)*fz(k+1)+frac1(i,j,k)*fzm(k+1)
flb=frac1(i,j,k)*fy(j)+frac1(i,j-1,k)*fym(j)
flf=frac1(i,j+1,k)*fy(j+1)+frac1(i,j,k)*fym(j+1)
sc(i,j,k)=sc(i,j,k)+rlbdx*(u(i,j,k)*flw-u(i+1,j,k)*fle)+
1   rlbdy*(v(i,j,k)*flb-v(i,j+1,k)*flf)+
1   rlbz*(w(i,j,k)*fls-w(i,j,k+1)*fln)
c-----source term (3) -----
5001 sc(i,j,k)=sc(i,j,k)+(flw-fle)*hlatnt*rhoscx
c-----source term due to droplet transfer-----
do 5044 i=2,l2
do 5044 j=2,m2
do 5044 k=2,n2
5044 sc(i,j,k)=sc(i,j,k)+qin(i,j,k)
c-----end source terms, begin boundary conditions--(front boundary)-----
do 5004 i=2,l2
do 5004 k=2,n2
kbcj1(i,k)=2
flxp(i,1,k)=0.0
flxc(i,1,k)=0.0
c-----back boundary----known temperature if kbcml = 1 -----
if (htcml.gt.10.0) then
kbcml(i,k)=1
h(i,m1,k)=hml
else
kbcml(i,k)=2
flxc(i,m1,k)=-htcml*(tsolid-298.0)+htcml*hsmelt/acp
flxp(i,m1,k)=-htcml/acp
endif
5004 continue
c-----left boundary-----
do 5003 j=2,m2
do 5003 k=2,n2
if (htcil.gt.10.0) then
kbcil(j,k)=1
h(1,j,k)=hil
else
kbcil(j,k)=2
flxc(1,j,k)=-htcil*(tsolid-298.0)+htcil*hsmelt/acp
flxp(1,j,k)=-htcil/acp
endif
c-----right boundary-----

```

```

      if (htcl1.gt.10.0) then
        kbcl1(j,k)=1
        h(l1,j,k)=hl1
      else
        kbcl1(j,k)=2
        flxc(l1,j,k)=-htcl1*(tsolid-298.0)+htcl1*hsmelt/acp
        flxp(l1,j,k)=-htcl1/acp
      endif
5003 continue
c-----top boundary-----
      do 5002 i=2,l2
        do 5002 j=2,m2
          kbck1(i,j)=2
c-----energy from the heat source (F1)-----
          flxc(i,j,1) = heatin(i,j)
          flxp(i,j,1) = 0.0
c-----radiative heat loss (F2)-----
          if (emiss.gt.1.0e-3) then
            if (h(i,j,1).ge.hlcal) then
              const1 = sigems/acpl**4
              const2 = (tliquid - hlcal/acpl)*acpl
              terma = (h(i,j,1)+const2)**4
              termb = (h(i,j,1)+const2)**3
              fluxc = sigems*tamb4-const1*terma+4.0*const1*termb*h(i,j,1)
              fluxp = -4.0*const1*termb
            else
              if (h(i,j,1).lt.hsmelt) then
                const1 = sigems/acp**4
                const2 = (tsolid-hsmelt/acp)*acp
                terma = (h(i,j,1)+const2)**4
                termb = (h(i,j,1)+const2)**3
                fluxc = sigems*tamb4-const1*terma+4.0*const1*termb*h(i,j,1)
                fluxp = -4.0*const1*termb
              else
                cpavg = (acpl+acp)/2.0
                const1 = sigems/cpavg**4
                const2 = tsolid*cpavg
                terma = (h(i,j,1)+const2)**4
                termb = (h(i,j,1)+const2)**3
                fluxc = sigems*tamb4-const1*terma+4.0*const1*termb*h(i,j,1)
                fluxp = -4.0*const1*termb
              endif
            endif
          flxc(i,j,1)=flxc(i,j,1)+fluxc
          flxp(i,j,1)=flxp(i,j,1)+fluxp
        endif
c-----convective heat loss (F3)-----
          if (htck1.lt.10.) then
            if (h(i,j,1).ge.hlcal) then
              flxc(i,j,1)=-htck1*(tliquid-298.0)+htck1*hlcal/acpl+flxc(i,j,1)
              flxp(i,j,1)=-htck1/acpl+flxp(i,j,1)
            else
              if (h(i,j,1).lt.hsmelt) then
                flxc(i,j,1)=-htck1*(tsolid-298.0)+htck1*hsmelt/acp+flxc(i,j,1)

```

```

    flxp(i,j,1)=-htck1/acp+flxp(i,j,1)
  else
    flxc(i,j,1)= -htck1*(tsolid-298.0) + flxc(i,j,1)
    flxp(i,j,1) = -htck1/cpavg + flxp(i,j,1)
  endif
endif
endif
endif
c-----heat loss due to vaporization-----
c-----the vapor fluxes was obtained from another model based on
3.5wt%Mg--
  if (t(i,j,1).gt.1990.) then
    fluxmg=16.508+0.00576468*t(i,j,1)-3.63366e-5*t(i,j,1)**2+
1 1.97815e-8*t(i,j,1)**3-2.54498e-12*t(i,j,1)**4
    fluxal=118.282-0.228514*t(i,j,1)+1.66567e-4*t(i,j,1)**2-
1 5.43307e-8*t(i,j,1)**3+6.69533e-12*t(i,j,1)**4
    vaploss = -fluxmg*1388.25-fluxal*2576.5
    flxc(i,j,1) = vaploss + flxc(i,j,1)
  endif
c-----bottom boundary-----
  if (htcn1.gt.10.0) then
    kbcn1(i,j)=1
    h(i,j,n1)=hnl
  else
    kbcn1(i,j)=2
    flxc(i,j,n1)=-htcn1*(tsolid-298.0)+htcn1*hsmelt/acp
    flxp(i,j,n1)=-htcn1/acp
  endif
5002 continue
c-----edge boundary: intersecting front and top plane-----
  do 5033 i=2,12
5033 h(i,1,1)=h(i,2,1)
5200 continue
c----- define gam(i,j,k) for momentum equations-----
  if (nf.gt.3) goto 6000
  do 5501 i=2,12
  do 5501 j=2,m2
  do 5501 k=2,n2
5501 gam(i,j,k)=amuff(i,j,k)
c-----source term for mushy resgion:Karman-Kauzeny approximation-----
  do 5400 k=kst,n2
  do 5400 j=jst,m2
  do 5400 i=ist,12
5400 sp(i,j,k)=-1.6e4*(1.0-fracl(i,j,k))**2/(fracl(i,j,k)**3+1.0e-3)
c-----boundary conditions for u momentum equation, source term-----
  if (nf.ne.1) go to 5500
  call tools(usor)
  do 1004 i=ist,12
  do 1004 j=jst,m2
  do 1004 k=kst,n2
  rsarea = rhoscan/xdif(i)
  asc =rsarea*u(i-1,j,k)
  asp = -rsarea
  if(u(i,j,k).ge.0.0)go to 1003
  asp =0.

```

```

        asc=rsarea*(u(i,j,k)-u(i+1,j,k))
1003  sc(i,j,k) = sc(i,j,k) + asc
1004  sp(i,j,k) = sp(i,j,k) + asp
c-----electromagnetic force-----
        if (yesarc.gt.0.5) then
        do 5402 i=imin-2,imax+2
        do 5402 j=jst,jmax+2
        do 5402 k=kst,kmax+2
5402  sc(i,j,k)=sc(i,j,k)+scemfx(i,j,k)
        endif
c-----top boundary (u momentum, shear stress, kbck1 = 1 by default)--
        do 5404 i=imin-2,imax+2
        do 5404 j=2,jmax+2
        dtdx = (t(i,j,1)-t(i-1,j,1))/xdif(i)
        if (wtpct.gt.1e-5) then
        tav=t(i,j,1)*fx(i)+t(i-1,j,1)*fxm(i)
        if(tav.gt.tsolid) dgdt=surten(tav,wtpct,ac,gamsat,entfac,enthse)
        endif
5404  u(i,j,1)=u(i,j,2)+frac1(i,j,1)*dgdt*dtdx*zdif(2)/amuff(i,j,2)
c- ---front boundary (plane of symmetry)-----
        do 5403 i=1,l1
        do 5403 k=1,n1
5403  kbcj1(i,k)=2
5500  continue
c-----v momentum boundary conditions-----
        if (nf.ne.2) go to 4001
        call tools(vsor)
        do 1006 i=ist,l2
        do 1006 j=jst,m2
        do 1006 k=kst,n2
        rsarea = rhoscan/xcv(i)
        asc = rsarea*(v(i+1,j,k)-v(i,j,k))
        asp = 0.
        sc(i,j,k) = sc(i,j,k) + asc
1006  sp(i,j,k) = sp(i,j,k) + asp
c-----electromagnetic field-----
        do 502 i=imin-2,imax+2
        do 502 j=jst,jmax
        do 502 k=kst,kmax
502  sc(i,j,k)=sc(i,j,k)+scemfy(i,j,k)
c-----top boundary (shear stress, kbck1 = 1 by default)-----
        do 504 i=imin-2,imax+2
        do 504 j=2,jmax+2
        dtdy = (t(i,j,1)-t(i,j-1,1))/ydif(j)
        if (wtpct.gt.1e-5) then
        tav=t(i,j,1)*fy(j)+t(i,j-1,1)*fym(j)
        if(tav.gt.tsolid) dgdt=surten(tav,wtpct,ac,gamsat,entfac,enthse)
        endif
504  v(i,j,1)=v(i,j,2)+frac1(i,j,1)*dgdt*dtdy*zdif(2)/amuff(i,j,2)
c-----front boundary (v momentum, by default kbcj1 = 1)-----
4001  continue
c-----w momentum source terms and boundary conditions-----
        if (nf.ne.3) goto 6000
        call tools(wsor)

```

```

do 1008 i=ist,12
do 1008 j=jst,m2
do 1008 k=kst,n2
  rsarea = rhoscan/xcv(i)
  asc = rsarea*(w(i+1,j,k)-w(i,j,k))
  asp = 0.
  sc(i,j,k) = sc(i,j,k)+asc
1008  sp(i,j,k) = sp(i,j,k)+asp
c-----electromagnetic source-----
do 602 i=imin-2,imax+2
do 602 j=jst,jmax+2
do 602 k=kst,kmax+2
c----bouyancy source-----
602  sc(i,j,k)=sc(i,j,k)+scemfz(i,j,k)-boufac*(t(i,j,k)-tsolid)
c-----top boundary (w momentum, kbcnl=1 by default)-----
c-----front boundary (w momentum)-----
do 604 i=imin-2,imax+2
do 604 k=2,kmax+2
604  kbcj1(i,k)=2
6000 continue
if (nf.ne.9) goto 7000
call tools(ksor)
do 5111 k=kst,n2
do 5111 j=jst,m2
do 5111 i=ist,12
amutt=0.09*rhoref*ake(i,j,k)**2/(dis(i,j,k)+1.0e-15)
amut(i,j,k)=amut(i,j,k)+0.3*(amutt-amut(i,j,k))
amuff(i,j,k)=amuf+amut(i,j,k)
if(frac1(i,j,k).gt.0.001) then
gam(i,j,k)=amuff(i,j,k)/1.0
sc(i,j,k)=amut(i,j,k)*gen(i,j,k)
sp(i,j,k)=-rhoref*dis(i,j,k)/(ake(i,j,k)+1.0e-15)
else
gam(i,j,k)=1.0e30
sc(i,j,k)=0
sp(i,j,k)=0
endif
5111 continue
c  write(*,*)"amuff(23,3,3),diff(23,3,3),dis(23,3,3),ake(23,3,3)"
c  write(*,9998)amuff(23,3,3),diff(23,3,3),dis(23,3,3),ake(23,3,3)
9998 format(4(e12.4))
do 5103 i=1,11
do 5103 k=1,n1
5103  kbcj1(i,k)=2
do 5104 i=1,11
do 5104 j=1,m1
5104  kbck1(i,j)=2
7000 continue
if (nf.ne.10) return
call tools(esor)
do 5112 k=kst,n2
do 5112 j=jst,m2
do 5112 i=ist,12
amutt=0.09*rhoref*ake(i,j,k)**2/(dis(i,j,k)+1.0e-15)

```

```

    amut(i,j,k)=amut(i,j,k)+0.3*(amutt-amut(i,j,k))
    amuff(i,j,k)=amuf+amut(i,j,k)
    if(frac1(i,j,k).gt.0.001) then
    gam(i,j,k)=amuff(i,j,k)/1.3
    sc(i,j,k)=1.44*amut(i,j,k)*gen(i,j,k)*dis(i,j,k)/(ake(i,j,k)
1 +1.0e-15)
    sp(i,j,k)=-1.92*rhoref*dis(i,j,k)/(ake(i,j,k)+1.0e-15)
    else
    gam(i,j,k)=1.0e30
    sc(i,j,k)=0
    sp(i,j,k)=0
    endif
5112 continue
    do 5102 i=1,l1
    do 5102 k=1,n1
5102 kbcj1(i,k)=2
    do 5105 i=1,l1
    do 5105 j=1,m1
5105 kbck1(i,j)=2
    return
    entry lc
    if (nf.ne.7) return
    sument=0.0
    entmax=0.0
    entmax1=0.0
    do 1091 i=ist,l2
    do 1091 j=jst,m2
    do 1091 k=kst,n2
    term1=aip(i,j,k)*h(i+1,j,k)+ajp(i,j,k)*h(i,j+1,k)
1 +akp(i,j,k)*h(i,j,k+1)
    term2=aim(i,j,k)*h(i-1,j,k)+ajm(i,j,k)*h(i,j-1,k)
1+akm(i,j,k)*h(i,j,k-1)
    term3=con(i,j,k)-ap(i,j,k)*h(i,j,k)
    renew(i,j,k)=term1+term2+term3
    entmax=amax1(entmax,abs(renew(i,j,k)))
    sument=sument+abs(renew(i,j,k))
1091 continue
c do 1092 i=imin-5,imax+5
c do 1092 j=2,jmax+4
c do 1092 k=2,kmax+4
    do 1092 i=2,l2
    do 1092 j=2,m2
    do 1092 k=2,n2
    if (abs(renew(i,j,k)).gt.entmax1) then
        entmax1=abs(renew(i,j,k))
        inew=i
        jnew=j
        knew=k
    endif
1092 continue
    return
    include '/home/CFD/COMP3D/FINISH3.FOR'
    end

```

## D2. Calculation Procedure

The calculation is done on the workstation 'flow1' under the directory: /usr/local/ads3/hailiang/ALVAP. The calculation procedure is separated in three stages as described below:

### 1) First stage

The program 'turb0.f' is run with the following batch file:

```
turb0<map0a>0a.prot
mv output out0a
mv tecout tec0a
turb0<map0b>0b.prot
mv output out0b
mv tecout tec0b
```

where the input files map0a and map0b are given below:

#### map0a

```
5
1
298
2
298
3
298
4
298
5
100
6
100
7
100
10
298
8
100
9
0
11
4
1
0.1
2
0.6
3
0.6
4
0.6
```

5  
0.1  
6  
0.1  
8  
50  
11  
1  
12  
1  
14  
3  
1  
911  
2  
2.3  
3  
172.3  
4  
266.7  
5  
0.215  
6  
0.281  
7  
0.402  
8  
0.258  
9  
0.011  
10  
-0.35  
11  
0.0  
15  
1.0  
17  
850  
19  
2  
5  
3.05  
6  
0  
1  
3000  
2  
0.20  
3  
0.05  
4  
10.58  
15  
1



4  
start  
5  
start  
6  
algrid1  
9  
6

map0b

5  
1  
298  
2  
298  
3  
298  
4  
298  
5  
100  
6  
100  
7  
100  
10  
298  
8  
100  
9  
0  
11  
4  
1  
0.9  
2  
0.9  
3  
1.0  
4  
0.9  
6  
80  
9  
1  
10  
1  
11  
1  
12  
3  
1  
911

```
2
2.3
3
172.3
4
266.7
5
0.215
6
0.281
7
0.402
8
0.258
9
0.011
10
1.8
11
-0.35
12
0
18
850
20
2
1
3000
2
0.20
5
3.05
6
0
3
0.05
4
10.58
15
1
4
start
5
start
6
algrid1
9
6
```

**The grid file 'algrid1' for all the calculations is given below:**

```

7
  2.5  0.48  0.05  0.02  0.02  0.13  1.8
   4   5   12   6   6   13   3
-1.2 -1.2 -1.2 -1.2  1.2  1.2  1.2
5
0.01  0.08  0.41  0.5  2.0
   6   23   10   4   6
  1.2  1.2  1.2  1.2  1.2
3
2.e-3  0.05  0.05
   1   17   11
  1.0   1.2  1.2

```

## 2) Second stage

The program 'turb.f' is run with the following batch file:

```

turb<mapa>a.prot
turb<mapb>b.prot
turb<mapc>c.prot
turb<mapd>d.prot
mv tecout tec1
mv output out1
mv tsurf.dat tsurf1.dat

```

where the input files are given below:

### mapa

```

5
1
298
2
298
3
298
4
298
5
100
6
100
7
100
10
298
8
100
9
0
11
4
1

```

0.1  
2  
0.6  
3  
0.6  
4  
0.6  
5  
0.1  
6  
0.1  
8  
50  
11  
1  
12  
1  
14  
3  
1  
911  
2  
2.3  
3  
172.3  
4  
266.7  
5  
0.215  
6  
0.281  
7  
0.402  
8  
0.258  
9  
0.011  
10  
-0.35  
11  
0.0  
15  
1.0  
17  
850  
19  
2  
5  
3.05  
6  
0  
1  
3000  
2

0.20  
3  
0.05  
4  
10.58  
15  
1  
4  
start  
5  
start  
6  
algrid1  
9  
6

mapb

5  
1  
298  
2  
298  
3  
298  
4  
298  
5  
100  
6  
100  
7  
100  
10  
298  
8  
100  
9  
0  
11  
4  
1  
0.4  
2  
0.6  
3  
0.6  
4  
0.6  
5  
0.4  
6  
0.4  
8

50  
11  
1  
12  
1  
14  
3  
1  
911  
2  
2.3  
3  
172.3  
4  
266.7  
5  
0.215  
6  
0.281  
7  
0.402  
8  
0.258  
9  
0.007  
10  
-0.35  
11  
0.0  
15  
1.0  
17  
850  
19  
2  
5  
3.05  
6  
0  
1  
3000  
2  
0.20  
3  
0.05  
4  
10.58  
15  
1  
4  
start  
5  
start  
6

algrid1

9  
6

mapc

5  
1  
298  
2  
298  
3  
298  
4  
298  
5  
100  
6  
100  
7  
100  
10  
298  
8  
100  
9  
0  
11  
4  
1  
0.6  
2  
0.6  
3  
0.85  
4  
0.8  
5  
0.6  
6  
0.6  
8  
50  
11  
1  
12  
1  
14  
3  
1  
911  
2  
2.3  
3

172.3  
4  
266.7  
5  
0.215  
6  
0.281  
7  
0.402  
8  
0.258  
9  
0.011  
10  
-0.35  
11  
0.0  
15  
1.0  
17  
850  
19  
2  
5  
3.05  
6  
0  
1  
3000  
2  
0.20  
3  
0.05  
4  
10.58  
15  
1  
4  
start  
5  
start  
6  
algrid1  
9  
6

mapd

5  
1  
298  
2  
298  
3



298  
4  
298  
5  
100  
6  
100  
7  
100  
10  
298  
8  
100  
9  
0  
11  
4  
1  
0.8  
2  
0.8  
3  
0.85  
4  
0.8  
5  
0.8  
6  
0.8  
8  
50  
11  
1  
12  
1  
14  
3  
1  
911  
2  
2.3  
3  
172.3  
4  
266.7  
5  
0.215  
6  
0.281  
7  
0.402  
8  
0.258  
9

```

0.011
10
-0.35
11
0.0
15
1.0
17
850
19
2
5
3.05
6
0
1
3000
2
0.20
3
0.05
4
10.58
15
1
4
start
5
start
6
algrid1
9
6

```

### 3) Third stage

The program 'turbvaploss.f' is run with the following batch file:

```
turbvaploss<mapvap>v.prot
```

where the input file mapvap is given below:

#### mapvap

```

5
1
298
2
298
3
298
4

```

298  
5  
100  
6  
100  
7  
100  
10  
298  
8  
100  
9  
0  
11  
4  
1  
0.8  
2  
0.8  
3  
0.85  
4  
0.8  
5  
0.8  
6  
0.8  
8  
50  
11  
1  
12  
1  
14  
3  
1  
911  
2  
2.3  
3  
172.3  
4  
266.7  
5  
0.215  
6  
0.281  
7  
0.402  
8  
0.258  
9  
0.011  
10

```

-0.35
11
0.0
15
1.0
17
850
19
2
5
3.05
6
0
1
3000
2
0.20
3
0.05
4
10.58
15
1
4
start
5
start
6
algrid1
9
6

```

### D3. Output Files

There are three output files from the calculation: tecout, output, and tsurf.dat. File 'tecout' stores the temperature and velocity fields of the weld metal, and the distributions of turbulence quantities. The format of this file is shown below. The variables X, Y, Z are the three coordinators of the grid in cm, TEM is the temperature in K, U, V, and W are the three velocity components in X, Y, and Z directions, respectively, with unit of cm/s, amut is the ratio of turbulent viscosity to molecular viscosity, diff is the ratio of turbulent thermal conductivity to molecular thermal conductivity, ake is the turbulent kinetic energy in  $\text{cm}^2/\text{s}^2$ , dis is the dissipation rate of turbulent kinetic energy in  $\text{cm}^2/\text{s}^3$ .

```

TITLE = "FLUID FLOW AND HEAT TRANSFER IN WELD POOL"
VARIABLES = "X", "Y", "Z", "TEM", "U", "V", "W", "amut", "diff", "ake", "dis"
ZONE I= 51 J= 51 K= 31 F=POINT

```

```

.000E+00 .000E+00 .000E+00 .298E+03 .000E+00 .000E+00 .000E+00 .000E+00 .000E+00 .100E+01 .100E+03
.3649E+00 .000E+00 .000E+00 .2981E+03 .000E+00 .000E+00 .000E+00 .000E+00 .000E+00 .1000E+01 .1000E+03
.1071E+01 .000E+00 .000E+00 .2981E+03 .000E+00 .000E+00 .000E+00 .000E+00 .000E+00 .1000E+01 .1000E+03
.1719E+01 .000E+00 .000E+00 .2981E+03 .000E+00 .000E+00 .000E+00 .000E+00 .000E+00 .1000E+01 .1000E+03
.2263E+01 .000E+00 .000E+00 .2981E+03 .000E+00 .000E+00 .000E+00 .000E+00 .000E+00 .1000E+01 .1000E+03
.2556E+01 .000E+00 .000E+00 .2981E+03 .000E+00 .000E+00 .000E+00 .000E+00 .000E+00 .1001E+01 .1021E+03
.2666E+01 .000E+00 .000E+00 .2984E+03 .000E+00 .000E+00 .000E+00 .000E+00 .000E+00 .1006E+01 .1119E+03
...
3010E+01 .1920E-02 .000E+00 .1234E+04 -.6787E+02 .2716E+01 .000E+00 .9594E+02 .1063E+01 .8186E+04 .2065E+08
3015E+01 .1920E-02 .000E+00 .1369E+04 -.8049E+02 .3151E+01 .000E+00 .1052E+03 .1141E+01 .8314E+04 .1944E+08
3019E+01 .1920E-02 .000E+00 .1500E+04 -.8848E+02 .3544E+01 .000E+00 .1099E+03 .1181E+01 .8207E+04 .1812E+08
3022E+01 .1920E-02 .000E+00 .1621E+04 -.9200E+02 .3904E+01 .000E+00 .1120E+03 .1199E+01 .8013E+04 .1695E+08
3026E+01 .1920E-02 .000E+00 .1730E+04 -.9163E+02 .4214E+01 .000E+00 .1126E+03 .1204E+01 .7786E+04 .1592E+08
3029E+01 .1920E-02 .000E+00 .1816E+04 -.8832E+02 .4450E+01 .000E+00 .1125E+03 .1203E+01 .7564E+04 .1504E+08
3032E+01 .1920E-02 .000E+00 .1904E+04 -.8325E+02 .4653E+01 .000E+00 .1118E+03 .1197E+01 .7312E+04 .1414E+08
...

```

The file 'output' gives the major features of the calculation and its format is give below:

```

-----
                        filenames
-----
1  output file name          output
2  plot file name           plot
3  print file name          print
4  start file name          start
5  save file name           start
6  grid input filename      algridi
7  tecplot file name        tecout
8  emf field file name      field
-----
                        processes parameters
-----
1  laser power (Watts)              .251000E+04
2  absorption coefficient            .215000E+00
3  beam/arc radius (cm)             .423000E-01
4  scanning velocity (cm/sec)       .105800E+02
5  starting location of beam        .305000E+01
6  to arc welding (yes:1, no:0)    .000000E+00
7  arc current (Amp)                .150000E+03
8  arc voltage (Volts)              .110000E+02
9  arc efficiency (%)               .750000E+02
10 starting emf field (yes:1,no:0)  .000000E+00
11 fraction of energy received from arc .100000E+01
12 radius of volumetric heat source (cm) .100000E+00
13 height of volumetric heat source (cm) .300000E+00
14 # of iters after which power is set to 0 .200000E+04
-----
                        material properties
-----
1  liquidus temperature (K)         .911000E+03
2  density of liquid metal (gm/cm**3) .230000E+01
3  enthalpy of solid at mp (cal/gm)  .172300E+03
4  enthalpy of liquid at mp (cal/gm) .266700E+03
5  specific heat of solid (cal/gm-K) .215000E+00
6  specific heat of liquid (cal/gm-K) .281000E+00
7  thermal cond of solid (cal/cm-sec-K) .402000E+00

```

8	thermal cond of liq (cal/cm-sec-K)	.258000E+00
9	viscosity of liquid (gm/cm-sec)	.110000E-01
10	d(gamma)/dT, pure mat ( dynes/cm-K)	-.350000E+00
11	conc. of surface active spe(wt%)	.000000E+00
12	enthalpy of segregation (J/mole)	-.166000E+06
13	surface excess at sat (mole/cm**2)	.130000E-08
14	entropy factor	.318000E-02
15	to variable properties (yes:1, no:0)	.100000E+01
16	coeff of thermal expansion (1/K)	.100000E-04
17	solidus temperature (K)	.850000E+03
18	emissivity of the material	.000000E+00
-----		
numerical scheme parameters		
-----		
1	velocity relaxation parameter	.800000E+00
2	pressure relaxation parameter	.800000E+00
3	enthalpy relaxation parameter	.950000E+00
4	latent heat relaxation parameter	.800000E+00
5	k relaxation parameter	.800000E+00
6	e relaxation parameter	.800000E+00
7	time increment	.100000E+21
8	number of iterations	.400000E+02
9	maximum number of cycles per time step	.100000E+01
10	iter interval for overall heat balance	.500000E+01
11	index to start from oldfile(yes:1,no:0)	.100000E+01
12	index to solve momentum eqns(yes:1,no:0)	.100000E+01
13	index to write tecplot file(yes:1,no:0)	.100000E+01
-----		
boundary conditions		
-----		
1	temperature at i=1 boundary (K)	.298000E+03
2	temperature at i=11 boundary (K)	.298000E+03
3	temperature at j=m1 boundary	.298000E+03
4	temperature at k=n1 boundary (k)	.298000E+03
5	heat transfer coeff at i=1(cal/cm2-s-K)	.100000E+03
6	heat transfer coeff at i=11(cal/cm2-s-K)	.100000E+03
7	heat transfer coeff at j=m1(cal/cm2-s-K)	.100000E+03
8	heat transfer coeff at k=n1(cal/cm2-s-K)	.100000E+03
9	heat transfer coeff at k=1(cal/(cm2-s-k)	.000000E+00
10	preheat temperature (K)	.298000E+03
-----		
grid related output		
-----		
x direction		
number of zones		7
zone( 1 )length		.2500E+01
zone( 1 )number of control volumes		4
zone( 1 )exponential factor		-.1200E+01
zone( 2 )length		.4800E+00
zone( 2 )number of control volumes		5
zone( 2 )exponential factor		-.1200E+01
zone( 3 )length		.5000E-01
zone( 3 )number of control volumes		12
zone( 3 )exponential factor		-.1200E+01
zone( 4 )length		.2000E-01
zone( 4 )number of control volumes		6
zone( 4 )exponential factor		-.1200E+01
zone( 5 )length		.2000E-01
zone( 5 )number of control volumes		6
zone( 5 )exponential factor		.1200E+01
zone( 6 )length		.1300E+00
zone( 6 )number of control volumes		13
zone( 6 )exponential factor		.1200E+01
zone( 7 )length		.1800E+01
zone( 7 )number of control volumes		3
zone( 7 )exponential factor		.1200E+01
y direction		
number of zones		5

```

zone( 1 )length                .1000E-01
zone( 1 )number of control volumes      6
zone( 1 )exponential factor          .1200E+01
zone( 2 )length                .8000E-01
zone( 2 )number of control volumes     23
zone( 2 )exponential factor          .1200E+01
zone( 3 )length                .4100E+00
zone( 3 )number of control volumes     10
zone( 3 )exponential factor          .1200E+01
zone( 4 )length                .5000E+00
zone( 4 )number of control volumes      4
zone( 4 )exponential factor          .1200E+01
zone( 5 )length                .2000E+01
zone( 5 )number of control volumes      6
zone( 5 )exponential factor          .1200E+01
z direction
number of zones                  3
zone( 1 )length                .2000E-02
zone( 1 )number of control volumes      1
zone( 1 )exponential factor          .1000E+01
zone( 2 )length                .5000E-01
zone( 2 )number of control volumes     17
zone( 2 )exponential factor          .1200E+01
zone( 3 )length                .5000E-01
zone( 3 )number of control volumes     11
zone( 3 )exponential factor          .1200E+01

  i=   1     2     3     4     5     6     7     8
  x=  0.00E+00 3.65E-01 1.07E+00 1.72E+00 2.26E+00 2.56E+00 2.67E+00 2.77E+00
 xu=  0.00E+00 0.00E+00 7.30E-01 1.41E+00 2.03E+00 2.50E+00 2.61E+00 2.72E+00

  i=   9    10    11    12    13    14    15    16
  x=  2.87E+00 2.95E+00 2.98E+00 2.99E+00 2.99E+00 3.00E+00 3.00E+00 3.01E+00
 xu=  2.82E+00 2.91E+00 2.98E+00 2.98E+00 2.99E+00 2.99E+00 3.00E+00 3.00E+00

  i=  17    18    19    20    21    22    23    24
  x=  3.01E+00 3.01E+00 3.02E+00 3.02E+00 3.03E+00 3.03E+00 3.03E+00 3.04E+00
 xu=  3.01E+00 3.01E+00 3.02E+00 3.02E+00 3.02E+00 3.03E+00 3.03E+00 3.03E+00

  i=  25    26    27    28    29    30    31    32
  x=  3.04E+00 3.04E+00 3.05E+00 3.05E+00 3.05E+00 3.05E+00 3.06E+00 3.06E+00
 xu=  3.04E+00 3.04E+00 3.04E+00 3.05E+00 3.05E+00 3.05E+00 3.06E+00 3.06E+00

  i=  33    34    35    36    37    38    39    40
  x=  3.06E+00 3.07E+00 3.07E+00 3.08E+00 3.09E+00 3.10E+00 3.11E+00 3.12E+00
 xu=  3.06E+00 3.07E+00 3.07E+00 3.08E+00 3.08E+00 3.09E+00 3.10E+00 3.11E+00

  i=  41    42    43    44    45    46    47    48
  x=  3.13E+00 3.14E+00 3.15E+00 3.16E+00 3.17E+00 3.18E+00 3.19E+00 3.44E+00
 xu=  3.12E+00 3.13E+00 3.14E+00 3.15E+00 3.16E+00 3.18E+00 3.19E+00 3.20E+00

  i=  49    50    51
  x=  3.99E+00 4.65E+00 5.00E+00
 xu=  3.68E+00 4.31E+00 5.00E+00

  j=   1     2     3     4     5     6     7     8
  y=  0.00E+00 5.82E-04 1.92E-03 3.51E-03 5.25E-03 7.09E-03 9.02E-03 1.09E-02
 yv=  0.00E+00 0.00E+00 1.16E-03 2.68E-03 4.35E-03 6.15E-03 8.03E-03 1.00E-02

  j=   9    10    11    12    13    14    15    16
  y=  1.31E-02 1.56E-02 1.84E-02 2.13E-02 2.44E-02 2.76E-02 3.09E-02 3.42E-02
 yv=  1.19E-02 1.43E-02 1.69E-02 1.98E-02 2.28E-02 2.60E-02 2.92E-02 3.25E-02

  j=  17    18    19    20    21    22    23    24
  y=  3.77E-02 4.12E-02 4.48E-02 4.85E-02 5.22E-02 5.60E-02 5.98E-02 6.37E-02
 yv=  3.59E-02 3.94E-02 4.30E-02 4.66E-02 5.03E-02 5.41E-02 5.79E-02 6.18E-02

  j=  25    26    27    28    29    30    31    32

```

```

y= 6.76E-02 7.16E-02 7.56E-02 7.77E-02 8.38E-02 8.79E-02 1.03E-01 1.33E-01
yv= 6.57E-02 6.96E-02 7.36E-02 7.76E-02 8.17E-02 8.58E-02 9.00E-02 1.16E-01

j= 33 34 35 36 37 38 39 40
y= 1.68E-01 2.07E-01 2.48E-01 2.90E-01 3.35E-01 3.80E-01 4.27E-01 4.76E-01
yv= 1.49E-01 1.87E-01 2.27E-01 2.68E-01 3.12E-01 3.57E-01 4.04E-01 4.51E-01

j= 41 42 43 44 45 46 47 48
y= 5.47E-01 6.56E-01 7.86E-01 9.27E-01 1.12E+00 1.38E+00 1.70E+00 2.05E+00
yv= 5.00E-01 5.95E-01 7.18E-01 8.54E-01 1.00E+00 1.23E+00 1.54E+00 1.87E+00

j= 49 50 51
y= 2.42E+00 2.80E+00 3.00E+00
yv= 2.23E+00 2.61E+00 3.00E+00

k= 1 2 3 4 5 6 7 8
z= 0.00E+00 1.00E-03 2.83E-03 4.75E-03 7.04E-03 9.52E-03 1.22E-02 1.49E-02
zw= 0.00E+00 0.00E+00 2.00E-03 3.67E-03 5.83E-03 8.24E-03 1.08E-02 1.35E-02

k= 9 10 11 12 13 14 15 16
z= 1.78E-02 2.07E-02 2.38E-02 2.69E-02 3.01E-02 3.33E-02 3.66E-02 3.99E-02
zw= 1.63E-02 1.92E-02 2.22E-02 2.53E-02 2.85E-02 3.17E-02 3.49E-02 3.82E-02

k= 17 18 19 20 21 22 23 24
z= 4.33E-02 4.68E-02 5.02E-02 5.34E-02 5.66E-02 6.05E-02 6.47E-02 6.91E-02
zw= 4.16E-02 4.50E-02 4.85E-02 5.20E-02 5.48E-02 5.85E-02 6.25E-02 6.69E-02

k= 25 26 27 28 29 30 31
z= 7.38E-02 7.86E-02 8.36E-02 8.87E-02 9.39E-02 9.93E-02 1.02E-01
zw= 7.14E-02 7.62E-02 8.11E-02 8.61E-02 9.13E-02 9.66E-02 1.02E-01

```

-----  
output  
-----

```

1 depth of the pool (cm) .400128E-01
2 width of the pool (cm) .125840E+00
3 length of the pool (cm) .136961E+00
4 cross section area (cm2) .385319E-02
5 peak temperature .214518E+04
6 heat input rate (cal/s) .643260E+02
7 heat output rate (cal/s) -.631432E+02
8 heat flow at n1 -.631413E+02
9 heat flow at m1 -.112279E-02
10 heat flow at i1 -.514793E-03
11 heat flow at l1 .221019E-03
12 RSMAX .297171E-03
13 SMAX .536791E-06
14 SSUM .567694E-09
15 UMAX .921510E+02
16 VMAX .909727E+02
17 WMAX .370505E+02
18 IMIN .150000E+02
19 IMAX .410000E+02
20 JMAX .230000E+02
21 KMAX .160000E+02
22 ratio(Heat In/Heat Out) -.981612E+00
23 ratio1(Ave. (amut/amuf)) .761642E+02
24 ratio2(Ave. (dift/difl)) .895197E+00
25 maxr1(max amut/amuf) .115255E+03
26 maxr2(max dift/difl) .122635E+01
-----

```

Output file 'tsurf.dat' gives the distribution of temperature on the weld pool surface. This file is used as a input file in program 'vap.f' where the vaporization rates



and weld metal composition change are calculated. Detailed description for the format of file 'tsurf.dat' is given in Appendix A.

## VITA

Hailiang Zhao was born in Shanxi province, China, on October 22, 1967. He obtained Bachelor and Master degrees of engineering in Materials Engineering at Shanghai Jiao Tong University in 1989 and 1994, respectively. In the spring of 1997, he joined the Pennsylvania State University to pursue doctoral study in Materials Science and Engineering. He is a member of American Welding Society and American Society of Metals. He has authored or co-authored the following papers:

1. H. Zhao, D. R. White, and T. DebRoy, "Current Issues and Problems in Laser Welding of Automotive Aluminum Alloys", *International Materials Reviews*, 1999, 44(6), pp. 238-266.
2. H. Zhao and T. DebRoy, "Weld Metal Composition Change during Conduction Mode Laser Welding of 5182 Aluminum Alloy", *Metallurgical and Materials Transactions B*, 2001, 32B(1), pp. 163-172.
3. H. Zhao and T. DebRoy, "Pore Formation during Laser Welding of Die-cast Magnesium Alloy AM60B - Mechanism and Remedy", *Welding Journal*, 2001, 80(8), pp. 204s-210s.
4. M. Pastor, H. Zhao, and T. DebRoy, "Pore Formation during C.W. Nd:YAG Laser Welding of Aluminum Alloys for Automotive Applications", *Revista de Metalurgia* (Spain), 2000, 36(2), pp. 108-117.
5. M. Pastor, H. Zhao, and T. DebRoy, "Continuous Wave Nd:YAG Laser Welding of AM60B Magnesium Alloy", *Journal of Laser Applications*, 2000, 12(3), pp. 91-100.
6. M. Pastor, H. Zhao, R. P. Martukanitz, and T. DebRoy, "Porosity, Underfill and Magnesium Loss during Continuous Wave Nd:YAG Laser Welding of Thin Plates of Aluminum Alloys 5182 and 5754", *Welding Journal*, 1999, 78(6), pp. 207s-216s.
7. M. Pastor, H. Zhao, and T. DebRoy, "Pore Formation and Composition Change during Continuous Wave Nd:YAG Laser Welding of Aluminum Alloys 5182 and 5754", *Trends in Welding Research*, Proceedings of 5th International Conference, Pine Mountain, GA, June 1-5, 1998, edited by J. M. Vitek et al., ASM International, Materials Park, OH, 1999, pp. 455-460.
8. M. Pastor, H. Zhao, and T. DebRoy, "Porosity and Alloying Element Loss during Laser Welding of 5754 Aluminum Alloy", *Proceedings of the National Welding Seminar '97*, Indian Institute of Welding, held in Bangalore, India, December 11-13, 1997, published by the Indian Institute of Welding, Bangalore, India, pp. 31-46, 1997.